UNIVERSITY OF CALIFORNIA
SANTA CRUZ

OBSERVATIONS OF GAMMA-RAY BURSTS AT EXTREME ENERGIES

A dissertation submitted in partial satisfaction of the
requirements for the degree of

DOCTOR OF PHILOSOPHY

in

PHYSICS

by

Taylor Aune

June 2012

The Dissertation of Taylor Aune
is approved:

Professor Steven Ritz, Chair

Professor David Williams

Professor Enrico Ramirez-Ruiz

Dean Tyrus Miller
Vice Provost and Dean of Graduate Studies

Table of Contents

List of Figures **vi**

List of Tables **xvi**

Abstract **xvii**

Dedication **xix**

Acknowledgments **xx**

1 Gamma-Ray Bursts **1**
1.1 Introduction 1
1.2 GRBs in the *Swift*/*Fermi* Era 10
1.2.1 GRB Distances 11
1.2.2 Temporal Properties 13
1.2.3 Spectral Properties 16
1.2.4 Correlations 19
1.2.5 Early-afterglow Emission 21
1.3 GRB Physics 24
1.3.1 Radiation Processes 25
1.3.2 Accretion and the Central Engine 27
1.3.3 Jet Formation and Confinement 28
1.3.4 Radiation, Cooling, and Afterglows 29
1.4 VHE Emission from GRBs 31
1.5 GRBs and the Extragalactic Background Light 37
1.6 Constraining GRB physics with VHE observations 43
1.7 Results of this work 49

2 The Milagro Gamma-Ray Observatory **51**
2.1 Introduction 51
2.2 Extensive Air Showers 52

2.3 The Milagro Detector and Data-Acquisition System 56
2.3.1 The Detector 56
2.3.2 Data Acquisition System 61
2.4 Standard Methods of Signal Reconstruction and Background Rejection 62

3 The Single-Particle (Scaler) Analysis Technique 65
3.1 Introduction & Application to Milagro 65
3.2 The Scaler Data Acquisition System 68
3.3 Improved Sensitivity and Data Cleaning 72
3.3.1 Reducing Instrumental Effects 73
3.3.2 Correcting for Environmental Conditions 77
3.4 Determining the Statistical Significance of Rate Fluctuations in the Presence of Systematic Effects 81

4 Satellite-Triggered Search for Prompt VHE Emission from GRBs with Milagro 87
4.1 Satellite-detected GRBs Observed with Milagro 88
4.2 Milagro Detector Response in Scaler Mode 94
4.3 Calculation of Flux Upper Limits from Scaler Data 100

5 Results from GRB Observations with Milagro 104
5.1 Milagro Observations of GRBs from 2000 – 2008 105
5.2 The "naked-eye" burst: GRB 080319B 114
5.3 Constraints on the synchrotron self-Compton model of prompt GRB Emission 121

6 Very Energetic Radiation Imaging Telescope Array System (VERITAS) 126
6.1 Introduction 126
6.2 The Imaging Atmospheric Cherenkov Technique 128
6.3 The Telescopes and Data Acquisition System 132
6.3.1 Telescopes 132
6.3.2 Trigger and Data Acquisition Systems 138

7 Rapid Follow-Up Observations of GRB Afterglows with VERITAS 144
7.1 Satellite-triggered Observations 145
7.2 The VERITAS GRB Alert and Tracking Subsystems 149
7.3 Observing GRBs under non-optimal conditions 154
7.4 Improving GRB Observations with VERITAS 159

8 Analysis of VERITAS GRB Data 164
8.1 VERITAS Data Analysis – Event Reconstruction & Background Rejection 165

8.1.1 Pixel Calibration & Image Cleaning 165
8.1.2 Image Parameterization & Shower Reconstruction 169
8.1.3 Gamma-Hadron Separation 174
8.1.4 Background Estimation & Signal Extraction 177
8.2 Low-Elevation Observations: The "Displacement" Reconstruction Method 181
8.3 Spectral Reconstruction and Upper Limit Calculations 187
8.4 Correcting the Absorption of VHE Gamma-Rays by the EBL 190

9 Results from GRB Observations with VERITAS 193
9.1 VERITAS Observations of GRBs: 2007 – 2012 193
9.2 Search for VHE Gamma-Ray Emission Optimized on the *Fermi* "Super-Bursts" 199
9.3 Looking for VHE Gamma-Rays from X-Ray Flares During GRB Afterglows 202
9.4 Constraints on VHE Emission During the Early Afterglow Phase of GRBs 204

10 Discussion 208
10.1 Constraints from VHE Observations on GRB Environment, Particle Populations, & Shock Acceleration 208
10.2 Sensitivity of Current-Generation Ground-Based VHE Observatories to GRBs 211
10.3 Prospects For Future VHE GRB Observations 215
10.3.1 High Altitude Water Cherenkov (HAWC) Observatory 216
10.3.2 The Cherenkov Telescope Array (CTA) 219

List of Figures

1.1 Two example GRB spectra (GRB 910503, GRB 980425) plotted in conventional νF_ν coordinates which correspond to the energy radiated in per logarithmic frequency interval alongside the galactic black hole candidate Cyg X-1 and the well-known Crab nebula – a pulsar wind nebula generated by a historically documented supernova in 1054 AD (Gehrels *et al.*, 2009). 3

1.2 The distribution of BATSE-measured burst durations (T_{90}'s – see text) for photon energies > 20 keV (Mallozzi, 2010). 4

1.3 A plot, in galactic coordinates, of 2704 BATSE-detected GRBs. The isotropic distribution provided strong evidence of the extragalactic nature of GRBs (Mallozzi, 2010). 6

1.4 Late-time photometry of GRB 080319B across several wavelengths. The steepening of the light curve at $\sim 10^6$ s is reflective of the geometry of the GRB. The green dashed line is the estimated magnitude of the host galaxy, the blue line the afterglow model, the red line is a model SN light curve, and the black line is the sum of the SN and GRB afterglow models (Tanvir *et al.*, 2010). 8

1.5 Redshift distribution of *Swift*-detected bursts (blue) compared with pre-*Swift* GRB redshifts (gray). The red solid line is the comoving volume derivative ($H_0^3 \frac{dV}{dz d\Omega}$) and the red dotted line is the comoving volume derivative convolved with the star-formation rate from Porciani and Madau (2001). Figure from Gehrels *et al.* (2009). 12

1.6 GRB angular distributions and durations as measured by the *Fermi*-GBM over the first two years of its operation. Both figures from Paciesas *et al.* (2012). 14

1.7 Example light curves obtained by the *Fermi*-GBM illustrating the characteristic diversity of the prompt phase of GRBs. The top two rows are light curves from long GRBs while the last row is data obtained from short GRBs (Bhat and Guiriec, 2011). 15

1.8 The joint *Fermi*-GBM-LAT unfolded νF_ν spectrum of GRB 090902B showing the extra power-law component which is dominant at both high and low energies (Abdo *et al.*, 2009b). 17
1.9 The integrated (top) and time-resolved (bottom) spectra showing the evolution of the power-law component during the prompt phase of the GRB 090926A (Ackermann *et al.*, 2011). 18
1.10 The light curve of the prompt phase of GRB 080916C across different energy bands. The high-energy emission detected by the LAT is delayed and long-lasting compared to the GBM-detected emission, a characteristic common to many of the bright, LAT-detected GRBs (Abdo *et al.*, 2009c). 20
1.11 The large X-ray flare associated with GRB 050502B as measured by the *Swift*-XRT. The flare intensity is nearly three orders of magnitude above the underlying afterglow (Burrows *et al.*, 2005). 22
1.12 GeV emission detected by the *Fermi*-LAT associated with X-ray flaring in GRB 100728A. The high-energy emission is consistent within 3σ with the extrapolation of the *Swift*-detected emission. Considered alone, the LAT-detected emission is best fit with a power-law spectral index of $\Gamma = 1.4 \pm 0.2$ (Abdo *et al.*, 2011). 23
1.13 Diagrams of the common processes producing gamma rays in GRBs. . 25
1.14 Figure 14 from Gehrels *et al.* (2009): Snapshots of the GRB lifecycle depicted at relevant length scales. Details in the text. 28
1.15 Internal and external shocks in the relativistic outflow of a GRB. Figure from Piran (2003). 31
1.16 SSC emission predicted from the forward shock assuming a constant-density ISM (Fan *et al.*, 2008). Figure1.16(a) shows the light curve in the central 20 MeV – 300 GeV band as well as the broader 200 eV – 100 TeV energy range. Figure 1.16(b) shows the predicted spectra at 200 s (black), 5.5 hours (red), and 23 days (blue) after the GRB. The thin lines show the synchrotron component, while the thick lines show the total synchrotron + SSC emission. For comparison, the VERITAS IACT array has a median response time of ~ 5 min., an average energy threshold of ~ 250 GeV (6.3×10^{25} Hz) and a typical νF_ν sensitivity of 10^{-11} erg cm^{-2} s^{-1} for GRB observations (before consideration of EBL absorption). 35
1.17 Models of the EBL energy density as a function of energy. The models listed are obtained using a variety of methods and are explained in their respective publications: Finke *et al.* (2010), Kneiske *et al.* (2004), Franceschini *et al.* (2008), Gilmore *et al.* (2009), Stecker *et al.* (2006), and Razzaque *et al.* (2009). The light gray points represent measurements or upper limits from experiment and are explained in the caption of Figure 4 of Finke *et al.* (2010) from which this figure is adapted. . 39

1.18 The attenuation as a function of gamma-ray energy for sources at a variety of redshifts. The black line represents the fiducial model and is what is used in this work to calculate EBL attenuation of GRBs observed by Milagro and VERITAS. The colored dashed lines represent attenuation from varying some of the model parameters such as the star formation rate and quasar contributions. Explained in detail in Gilmore *et al.* (2009), from which this figure is taken. 40
1.19 The gamma-ray energy and redshift values at which the Universe becomes opaque ($\tau_{\gamma\gamma} = 1$) for a variety of models (see Figure 1.17). Also included are the relevant energy ranges for the *Fermi*-LAT and several IACT instruments as well as the highest measured photon energies and redshifts for number of blazers and GRBs. Figure adapted from Finke *et al.* (2010). 42
1.20 The dependence of the prompt GRB spectrum on the fraction of thermal energy carried by the magnetic field (ϵ_B). The solid, dashed, and dotted lines are for ϵ_B=0.33, 0.01, 0.0001, respectively. Figure from Pe'er and Waxman (2004). 45
1.21 Predicted photon spectra during the early afterglow phase for different ISM characteristics. The solid line represents a constant-density ISM ($n = 1$ cm^{-3}), while the dashed and dotted lines represent an explosion into a particle wind including and excluding the proton contribution to the flux, respectively. Figure from Pe'er and Waxman (2005). . . . 47

2.1 Extensive air showers simulated using the CORSIKA Monte Carlo code (Heck *et al.*, 1998). Left: A 100 GeV proton-initiated air shower. Right: a 100 GeV gamma ray-initiated air shower. Red: e^+, e^-, and photons, Green: muons, Blue: hadrons. Color scale is logarithmic. The first interaction height is fixed at 30 km a.s.l. Only leptons and gamma rays above 100 keV and hadrons above 100 MeV are plotted. z scale is 0 – 30 km a.s.l. and x,y scales are ±5 km around the shower core. (Schmidt, 2009) 55
2.2 A view of the Milagro pond with the light-tight top cover inflated for maintenance and repairs. Clearly visible are the AS layer and Mu layer PMTs and the weighted lattice to which they are anchored. 58
2.3 Left: A cut-away view of one of the Milagro outrigger tanks partially emptied of water but with the PMT still mounted inside. Right: An overhead view of the Milagro Observatory. The covered pond is in the center and the locations of the outrigger tanks marked in red. 60
2.4 A simplified schematic of the Milagro standard DAQ pipeline 61

3.1 The Milagro triggered and scaler gamma-ray effective areas plotted as a function of energy. Both effective areas asymptotically approach a constant at high energies and are essentially flat above the maximum energy shown here. This is because the area on the ground covered by gamma ray-induced air showers is approximately independent of the primary gamma-ray energy and all showers at these energies are bright enough to be detected by Milagro. 67
3.2 The PMT layout for a representative group of 16 tubes sharing the same front-end board. The colors indicate the four-fold logical-OR combination of the low-threshold DFEB output. The high-threshold output was simply a logical-OR of all 16 PMTs in the group. A diagram of how the outputs were combined and connected to the CAMAC scalers can be found in Figure 3.3. 69
3.3 A diagram of the connections between the DFEB and the CAMAC scalers. The colored boxes represent the discriminator output from each PMT and their relative location in the group of sixteen PMTs sharing a front-end board (see Figure 3.2). The low-threshold output is combined into either 8 (AS) or 16 (Mu, Outrigger) PMTs per channel, while the high-threshold output contains all 16 OR-combined PMTs per scaler channel. The masked output was normally set to measure the rate from one PMT in the group at a time. 71
3.4 *Top:* Raw scaler rate from a functioning OR-group over the course of a day. *Bottom:* Raw scaler rate from an OR-group with one or more malfunctioning PMTs as is evident by the 161 kHz noise. Such an OR-group would be removed from the scaler analysis. 75
3.5 The removal of noisy PMT OR-groups based on a automated procedure for maximizing of array sensitivity. The blue histogram represents the subset of OR-groups which comprise the most-sensitive combination for this particular event. 77
3.6 Plots showing the effect of environmental corrections on the raw scaler data (red). *Top:* The measured outside temperatures and pressures over the course of 4 July, 2006. *Bottom:* Raw and corrected scaler rates from the AS low-threshold array. Corrections were made based on the above temperature and pressure measurements. 80
3.7 Orientation and durations of the background regions relative to the signal region for a transient analysis. 82
3.8 Distribution of significances for $\sim$ 1370 uncorrelated data intervals. The red line is the fit of a Gaussian that shows by the long tails that the fluctuations are not purely statistical but influenced by some systematic effects. 83

3.9 Illustration of how the test intervals are distributed around the true signal/background interval. For a standard transient analysis, roughly 15,000 test intervals are used to calculate the significance distribution (3.8). 84

4.1 The median energy of detected events as a function of zenith angle for the Milagro scaler system. An intrinsic spectrum of $\frac{dN}{dE} \propto E^{-2}$ is assumed. This spectrum is then attenuated by the EBL using the model of Gilmore *et al.* (2009) assuming four different redshifts. . . . 98

5.1 A histogram of the statistical significances of scaler rate fluctuations coincident with the prompt phase of GRBs observed with Milagro. The distribution is consistent with a unit normal distribution, indicating that the scaler rate fluctuations during the observations were purely background in nature. 106

5.2 The background-subtracted gamma-ray light curve as measured by Konus (black; 181,160 keV), plotted relative to the GRB trigger time measured with *Swift*-BAT. Optical data from Pi of the Sky (blue) and TORTORA (red) are also plotted. The optical emission begins within seconds of the onset of the burst and ends at roughly the same time, providing strong evidence that both originate at the same site. Figure from Racusin *et al.* (2008). 115

5.3 Light curve of both the scaler and reconstructed air shower count rates coincident with GRB 080319B and the time immediately before and after the prompt phase of the burst. The lightcurve is binned in intervals of the burst duration, which for GRB 080319B was 60 seconds. No significant excess of events associated with the prompt phase of GRB 080319B is observed. 117

5.4 99% confidence-level upper limits on the integral photon flux above various values of $E_{\rm th}$ assuming a monochromatic (δ-function) intrinsic GRB spectrum at $E_{\rm th}$. This spectrum is then attenuated by the EBL using the model of Gilmore *et al.* (2009). The upper limits from both the scaler and standard analyses are plotted here. 118

5.5 99% confidence-level upper limits on the prompt νF_ν flux obtained using the scaler analysis method described in the text. The limits are quoted at $E = E_{\rm p,GeV}$ where $E_{\rm p,GeV}$ is the peak energy for various intrinsic Band-function GRB spectra. Also shown are the data obtained simultaneously by Konus and TORTORA. The dotted lines show three assumed synchrotron spectra ($E_{\rm p,syn} = 1, 2.26, 5.1$ eV). The corresponding second-order IC spectral features predicted by the SSC model are shown with dashed lines. The Milagro upper limits are compared to the unattenuated second-order IC spectral components since the limits plotted here already account for gamma-ray attenuation from both Klein-Nishina suppression and attenuation via pair production with the EBL. 120
5.6 SSC-model-predicted prompt νF_ν flux at $E = E_{\rm p,GeV}$ (open points) plotted for several assumed values of $E_{\rm p,GeV}$ and the corresponding 99% confidence level upper limits obtained with Milagro using the scaler method described in the text (filled points). The Milagro limits account for attenuation of the high-energy gamma-ray flux by both Klein-Nishina suppression at the source and from the EBL using the model of Gilmore *et al.* (2009). 123

6.1 The VERITAS array at the Fred Lawrence Whipple Observatory. The array configuration seen here is the new (post-Summer, 2009) configuration which leads to relatively uniform separation distances (roughly 100 m) between the telescopes. 127
6.2 *Left:* A cartoon illustrating the distribution of Cherenkov light on the from a gamma-ray-generated EAS. The figure is not to scale but it illustrates the effect of the varying refractive index of the atmosphere and the subsequent creation of the Cherenkov ring. *Right:* Resulting camera images from a gamma-ray shower similar to the one shown in the cartoon, that is, with the axis of the shower intersecting the Earth's surface roughly in the middle of the array. 130
6.3 A picture of one of the VERITAS telescopes which shows the segmented mirror facets and the tubular steel OSS. 134
6.4 Reflectivity of the VERITAS telescopes as a function of wavelength (Roache *et al.*, 2008). 135
6.5 Improvement (before: left, after: right) of the VERITAS PSF from mirror alignment. The solid circle represents the size of a VERITAS pixel (McCann *et al.*, 2010) 137
6.6 The VERITAS camera with concentrating light-cones installed (Nagai *et al.*, 2008). 138
6.7 Diagram of the VERITAS trigger levels and data acquisition systems (Weinstein, 2008). The components are described in the text. 139

6.8 Schematic of the pixel-level (L1) trigger, which includes a novel rate-feedback circuit for improved performance in the presence of NSB light (Hall *et al.*, 2003). ZCD and TD are explained in the text. 141

7.1 A diagram illustrating the communication of GRB detections from satellite-based instruments through the Tracking and Data Relay Satellite System (TDRSS), to the ground and through the GCN system to ground-based telescopes including VERITAS. 150
7.2 Diagram of GRB alert processing by the systems at VERITAS. . . . 152
7.3 Plot of observation delays of the VERITAS-observed GRBs listed in Table 7.1. The red diamonds indicate bursts where the delays were affected by elevation, light level, or other environmental factor. The blue dots show unconstrained response times which incorporate time for satellite downlink, GCN distribution, and VERITAS processing of the GRB alert. The grey bands indicate the time during which VERITAS is shut down for the Summer monsoons. 153
7.4 The VERITAS energy threshold as a function of zenith angle. The energy threshold is defined as the maximum of the differential counting rate of a Crab-like ($\frac{dN}{dE} \propto E^{-2.5}$) spectrum. 155
7.5 Angular resolution of VERITAS as a function of energy and zenith angle ($90^\circ -$ elevation). Figure credit: G. Maier 157
7.6 Reconstruction of the Crab spectrum at different elevation ranges. The blue spectrum is a fit of the Crab spectrum as measured by the MAGIC collaboration (Albert *et al.*, 2008) and the red points are the VERITAS measurements. The black line is a power-law fit to the VERITAS points. The VERITAS spectral points are self-consistent and consistent with the MAGIC measurements across all elevations. The analysis cuts used for this study are the same used for GRB analysis. 160
7.7 The VERITAS sensitivity to a 1% Crab Nebula source over various zenith angle ranges. The blue histogram indicates the disp method sensitivity, and the grey histogram the standard reconstruction method. Both methods are described in Section 8.1. 161
7.8 Illustration of the wobble and orbit observing modes employed by VERITAS. In both cases the putative source position is offset from the center of the VERITAS FOV, enabling the simultaneous measurement of signal and background regions at a minimal loss of sensitivity. Figure credit J. Christiansen. 162

8.1 Illustration of the effect of the image cleaning procedure described in the text. Image pixels have a threshold of $5 \times \sigma_i$ and the boundary pixels have a threshold of $2.5 \times \sigma_i$. 168

8.2 A diagram showing the parameterization of a Cherenkov shower image. The quantities noted are defined in Table 8.1. 170
8.3 Reconstruction of the shower source location in the mirror plane using 3 telescope images. The pink star represents the reconstructed position calculated from a weighted minimization of the distance from the 3 shower image major axes. 171
8.4 Reconstruction of the impact point in the telescope mirror plane for an event recorded by all four VERITAS telescopes. The size and color of the circle surrounding each telescope indicates the size of the image measured by that telescope. 173
8.5 Reduced mean scaled width and reduced mean scaled length distributions for hadronic cosmic-ray showers and gamma-ray showers. Image credit: G. Maier. 176
8.6 Smoothed acceptance function for a 20-minute run on GRB 080310. The histogram is plotted as a function of ϕ^2, the squared angle from the center of the FOV. 178
8.7 Relative acceptance map for all runs taken on GRB 080310. The shape of the map is due to the observations being taken over all four wobble positions (Figure 7.4). 179
8.8 The two methods of background estimation and signal extraction used in this work. See text for explanation. 181
8.9 Diagram of the standard shower source location reconstruction involving the three telescopes. The reconstructed source location is determined by a minimization of size-weighted perpendicular distance. . . 183
8.10 Diagrams illustrating the calculation of the image displacement and the use of this information to reconstruct source locations in a stereoscopic event. 184
8.11 A comparison of the angular resolution of VERITAS as a function of zenith angle obtained using the standard reconstruction method and the displacement reconstruction method. 186
8.12 The effective area of VERITAS as a function of energy for several different elevation angles, (θ). These effective areas were generated using cuts optimized for a weak, soft-spectrum point source and the standard shower location reconstruction method. 189
8.13 Effects of EBL attenuation on a hypothetical GRB with a power-law spectrum ($\Gamma = -2.1$) located at a redshift of $z = 1$. The observation elevation when factoring in the VERITAS effective area (Figure 8.13(b)) is assumed to be 70° in this case. 192

9.1 Significance histogram of the 28 GRBs in the sample listed in Table 9.2. Included in the figure is the normalized Gaussian distribution of mean zero and variance one that the significance histograms should follow if no signal is present. The GRB significances are consistent with having been drawn from the aforementioned Gaussian distribution indicating that no VHE gamma-ray emission was observed from this set of GRBs. 196
9.2 Significance histogram obtained from an analysis of the GRBs in the sample over timescales for which VERITAS is maximally sensitive to a burst with a $t^{-1.5}$ power-law afterglow. Included in the figures is the normalized Gaussian distribution of mean zero and variance one that the significance histogram should follow if no signal is present. The GRB significances are consistent with having been drawn from the aforementioned Gaussian distribution. 201
9.3 VERITAS observation window of GRB 080310 superimposed on the *Swift*-XRT lightcurve (Evans *et al.*, 2007, 2009). The inset shows the structure of the X-ray flare (between the dashed lines) and is the time window over which the search for VHE emission was performed. No significant excess of VHE gamma rays coincident with the X-ray flare ($475 \text{ s} < t - \text{T}_{\text{trig}} < 750 \text{ s}$) was found. 203
9.4 (a) EBL-corrected VERITAS integral fluence upper limits above 200 GeV, divided by the fluence measured by the *Swift*-BAT in the 15 – 350 keV energy band as a function of t_{med} as defined in the text. (b) A histogram of the ratio of the VERITAS integral fluence upper limit above 200 GeV, now integrated over the time period $t - \text{T}_{\text{trig}} > 300$ s, to the Swift-BAT fluence. In both figures the red entries indicate GRBs with measured redshifts, while the blue entries represent GRBs without measured redshifts and for which a fiducial redshift of $z = 2.5$ is assumed. 206

10.1 Predicted VERITAS lightcurves for three of the four brightest *Fermi*-LAT GRBs. The fourth, GRB 080916C had a redshift of nearly 4.4 and VHE emission is predicted to be too attenuated by the EBL to be detectable by VERITAS. The EBL model of Gilmore *et al.* (2009) is used to estimate the attenuation of the VHE γ-rays. The elevation of the burst with respect to VERITAS is chosen to be 70° and no intrinsic spectral cutoff of the high energy emission is assumed. Each point signifies a detection of at least three standard deviations (σ) in that time bin. 213

10.2 Senstivity of HAWC to GRBs. Figure 10.2(a) shows the necessary flux at 10 GeV multiplied by the square root of the duration of the GRB required to produce a 5σ detection from the HAWC scaler data. This is for the full HAWC array and for a burst with high elevation. The energies plotted indicate an assumed exponential spectral cutoff. The data from 3 bright LAT-detected GRBs are included. Figure 10.2(b) shows the 5σ detection level (discovery potential) for the HAWC scaler (air-shower reconstruction) analysis as a function of duration for various redshifts. Included is the flux necessary for the observation of 1 photon above 10 GeV by the *Fermi*-LAT. Figures from Abeysekara *et al.* (2011). 218

List of Tables

4.1 Satellite-detected GRBs in the field of view of Milagro. All information taken from GCN circulars. 89

5.1 Upper limits on gamma-ray emission in the 1 – 100 GeV energy range for all satellite-detected GRBs in the Milagro field of view (above 40° elevation). 107

7.1 Details of *Swift*-detected GRBs triggering observations by VERITAS since 2007 January 148

8.1 Image parameters obtained from a moment analysis of light distribution 169

9.1 Analysis Cuts 195
9.2 VERITAS Observations of Gamma-Ray Bursts 197
9.3 Redshift-corrected VERITAS upper limits on VHE emission from nine *Swift*-detected GRBs 198
9.4 A search for VHE emission on timescales optimized on VERITAS sensitivity to a power law afterglow decay $\sim t^{-1.5}$. 200

Abstract

Observations of Gamma-Ray Bursts at Extreme Energies

by

Taylor Aune

Gamma-ray bursts (GRBs), thought to be produced by the core-collapse of massive stars or merging compact objects, are the most luminous events observed since the Big Bang. GRBs are intrinsically interesting as laboratories to study physical processes at energies much higher than can be produced in the largest particle accelerators on Earth. A better understanding of GRBs may also allow for their use as cosmological tools – backlights for the study of the evolution of the Universe back to the era of the first gravitationally-bound structures. In this work, results from observations of satellite-detected GRBs with the Milagro and VERITAS very high energy (VHE, > 100 GeV) gamma-ray telescopes are presented. No significant flux of VHE gamma rays associated with any of the 144 GRBs observed was detected. The limits on VHE gamma-ray emission during the GRB early afterglow phase obtained from the VERITAS observations are among the most constraining to date and the interpretation of these non-detections in the context of GRB emission models is discussed. Results from observation of the "naked-eye burst" GRB 080319B with Milagro are shown to rule out the popular synchrotron self-Compton model of emission over a broad range of energy space. Finally, the prospects for GRB observations with both current and

future-generation VHE observatories are examined.

To Rebekah

Acknowledgments

First and foremost I would like to thank my advisor, David Williams who, over the last six years, has somehow managed to keep me moving in the right direction. With patience, skepticism, and an unwavering attention to detail, he has assisted me greatly with the research presented in this dissertation and he may have finally succeeded in turning me into a scientist. Thanks to the current and former postdocs down the hall in Room 313, Nepomuk, Pablo and Aurelien. They were knowledgeable, helpful, and easy to drink a beer with...all qualities I too strive to possess.

I would also like to thank everyone in the VERITAS and Milagro collaborations. The work I've done over the last several years would not have been possible without the tireless effort of the many many people involved with the construction and operation of these experiments. Thanks to Neil Gehrels and the NASA GSRP for the assistance the helped make my research possible.

Thanks to my office-mates, Brandon and Michael for contributing to a very enjoyable work environment, and Amy for putting up with our nonsense and my occasional(?) surliness.

Thanks to my parents for their love and encouragement. I don't think they had me pegged for a physicist when I was growing up but their support and understanding has made it all possible. Finally, thanks to Bekah, whose patience and love over the last 8+ years has contributed so much to my happiness. Through example she has been an inspiration to me during these years in graduate school and I very much look

forward to what the future will bring.

Chapter 1

Gamma-Ray Bursts

1.1 Introduction

Gamma-ray bursts (GRBs) are one of the most intriguing astrophysical phenomena in the Universe. Observationally they appear as short, bright flashes of photonic radiation with peak energies in the gamma-ray band. Observed GRB durations vary widely from fractions of a second to several tens or even hundreds of seconds. Over this relatively short timescale, GRBs produce a total isotropic equivalent energy output of 10^{53} – 10^{54} ergs, more energy than Earth's sun will produce over its entire lifetime. Apart from the Big Bang, GRBs are the most luminous events known and understanding the physical processes and conditions responsible for producing such phenomena has been a challenge to astrophysicists for decades. Current evidence suggests that GRBs are gravitationally powered and result from the core collapse of

massive stars and subsequent generation of a black hole. It is also suspected that a subgroup of short-duration GRBs may arise from the merger of compact objects such as neutron stars and black holes.

The opacity of Earth's atmosphere to gamma rays all but ensured that the discovery of GRBs would be delayed until the advent of the Space Age. Ten years after the launch of *Sputnik 1*, the first observational evidence for GRBs was provided by the *Vela* satellites on 2 July, 1967 (Klebesadel *et al.*, 1973). The discovery of GRBs was serendipitous, as the *Vela* satellites were designed to monitor Soviet adherence to the Nuclear Test Ban Treaty but instead discovered gamma-ray flashes that did not appear to be terrestrial or solar in origin and did not resemble the gamma-ray signature expected from nuclear weapons. Over the next few decades thousands of GRBs were detected by various gamma-ray-sensitive satellites, the most prolific of these being the Compton Gamma-ray Observatory (CGRO).

The results from the Burst and Transient Source Experiment (BATSE) (Preece *et al.*, 2000) on board CGRO provided much information on the duration, spectral properties, frequency, and angular distribution of GRBs. BATSE detected $\sim$ 3000 bursts, indicating that detectable GRBs are quite common, occurring at a rate of roughly 3 per day. The discovery of a typical spectral energy distribution for GRBs (Figure 1.1) at gamma-ray energies, a distribution fit well by two power-laws smoothly joined by an exponential (the Band function (Band *et al.*, 1993)), was also made by BATSE. The duration of BATSE-detected GRBs shows a bimodal distribution

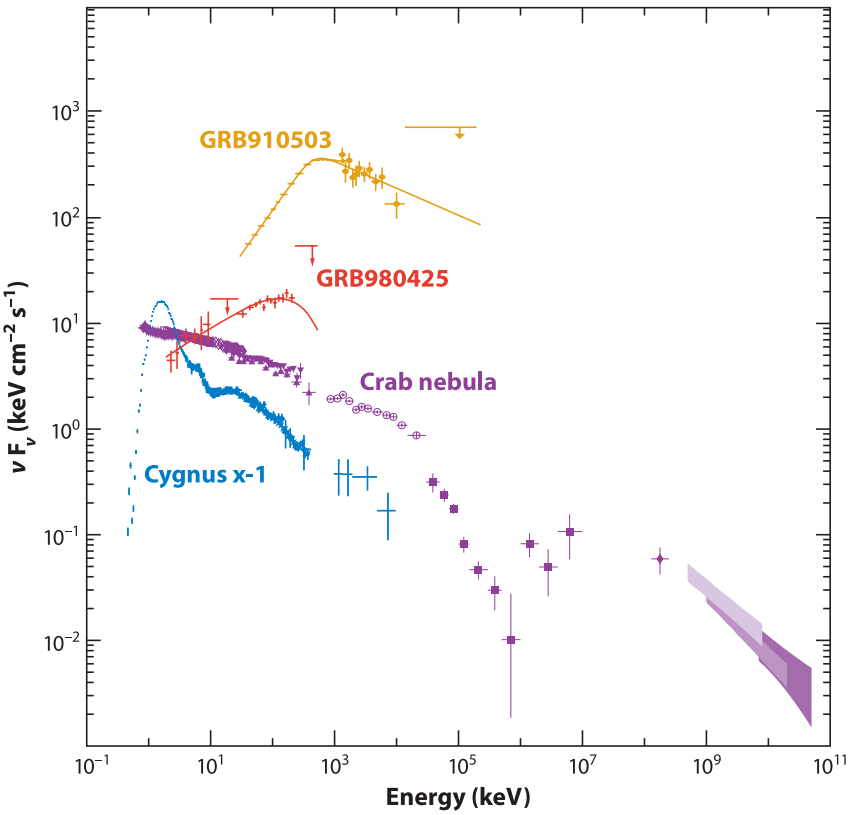

Figure 1.1: Two example GRB spectra (GRB 910503, GRB 980425) plotted in conventional νF_ν coordinates which correspond to the energy radiated in per logarithmic frequency interval alongside the galactic black hole candidate Cyg X-1 and the well-known Crab nebula – a pulsar wind nebula generated by a historically documented supernova in 1054 AD (Gehrels *et al.*, 2009).

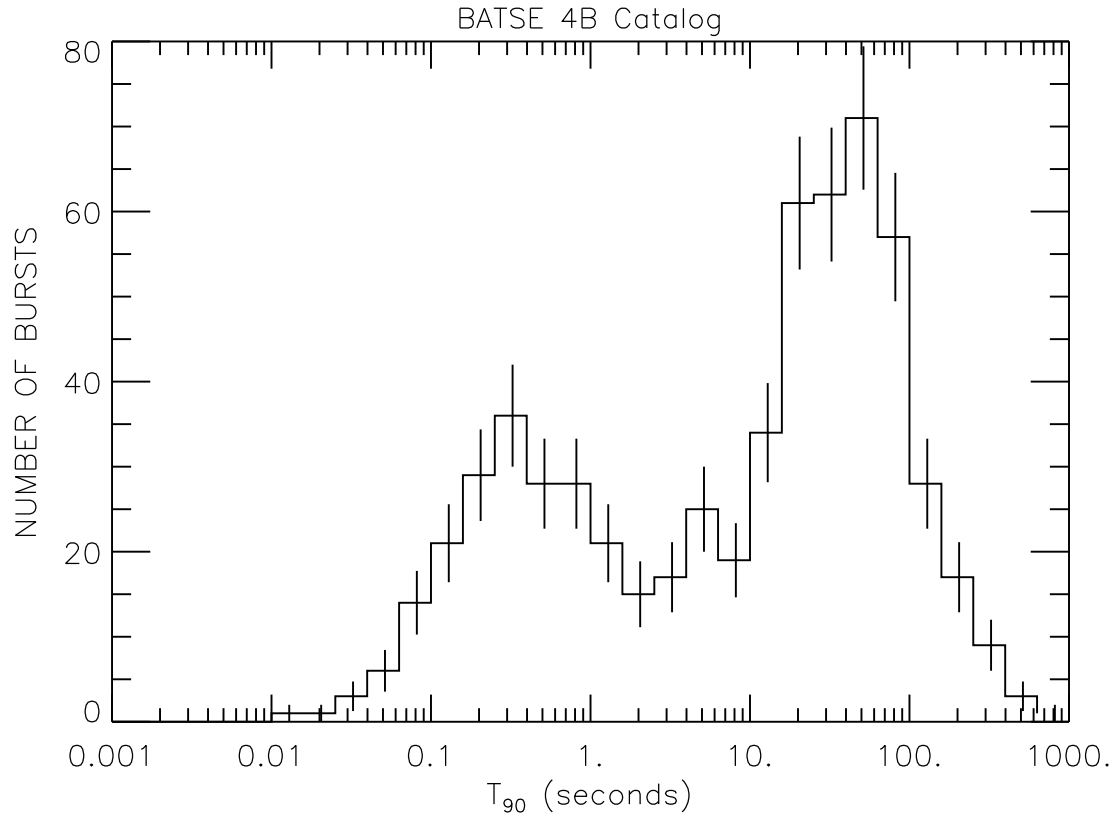

Figure 1.2: The distribution of BATSE-measured burst durations (T_{90}'s – see text) for photon energies > 20 keV (Mallozzi, 2010).

(Figure 1.2) indicating that short ($T_{90} < 2$s) and long ($T_{90} > 2$s) may arise from physically different conditions.[1] Arguably the most important discovery made by BATSE was that the angular distribution of GRBs on the sky appeared to completely isotropic (Figure 1.3). This indicated that GRBs were most likely extragalactic in origin, an unpalatable proposition for some since events observed to be so bright at such great distances would dictate an extremely large release of energy.

For all that BATSE provided to GRB science, its localization of GRBs was not

[1] T_{90} is defined as the time over which the central 90% of the counts above background from a GRB are detected. This duration is energy dependent but is usually quoted over some range between 10 and 500 keV.

sufficient to allow for sensitive, small field of view (FOV) instruments such as optical telescopes, to perform follow-up observations on GRBs. The Dutch-Italian *BeppoSAX* satellite (Boella *et al.*, 1997) was able to acquire arcminute-precision X-ray images of the fading afterglow of GRB 970228,[2] which in turn allowed for followup observations at longer wavelengths. Optical follow-up observations of GRB 970228 (van Paradijs *et al.*, 1997) and later bursts allowed for the identification of host galaxies and subsequently the determination of spectroscopic redshifts which confirmed that GRBs are extragalactic in origin (Metzger *et al.*, 1997).

Due to the energies involved, a natural candidate for GRB progenitors are collapsing massive stars. Such events are also the source for some subclasses of supernovae. The first observation of a GRB possibly associated with a supernova was the case of GRB 980425/SN1998bw (Galama *et al.*, 1998), though the connection between the two was based only on the coincident locations of SN1998bw and GRB 980425. The first GRB to show an unambiguous connection to a supernova was GRB 030329/SN2003dh which showed a typical GRB afterglow decay follow several days later by broad flux peaks characteristic of supernovae (Stanek *et al.*, 2003).

With the launch of the *Swift* GRB mission in 2004 and the launch of the *Fermi* Gamma-ray Space Telescope in 2008 (Atwood *et al.*, 2009, Meegan *et al.*, 2009) the rate and quality of GRB detections have increased dramatically. An overview of the current state of GRB observations and data is provided in Section 1.2. These

[2]GRBs are named based on their year (YY), month (MM), and day (DD), of detection: GRB YYMMDD, followed by a Roman letter: A,B,C to differentiate between bursts detected on the same day. If no Roman-letter-suffix exists it is assumed to be equivalent to A.

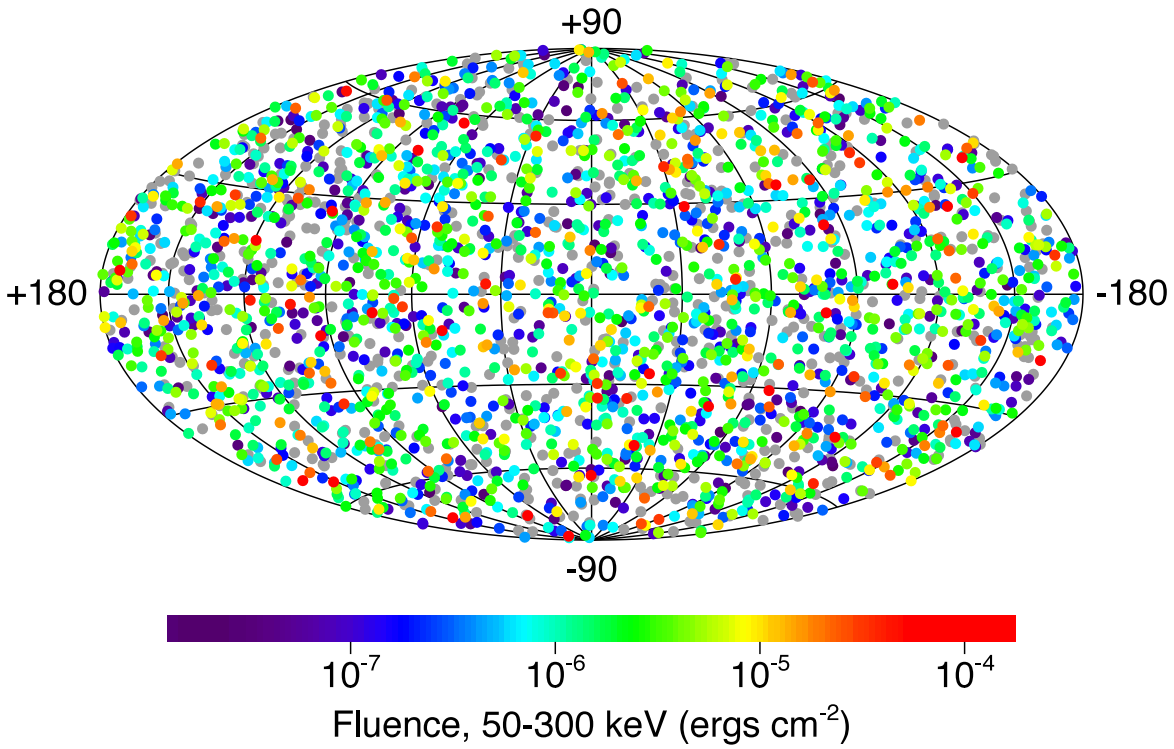

Figure 1.3: A plot, in galactic coordinates, of 2704 BATSE-detected GRBs. The isotropic distribution provided strong evidence of the extragalactic nature of GRBs (Mallozzi, 2010).

satellite missions have provided a trove of data but their facilitation of rapid follow-up observations by other instruments across the electromagnetic spectrum from radio to very high energy (VHE, > 100 GeV) gamma-ray observations (the topic of this thesis) and beyond (neutrinos, gravitational waves) is at least equally important. Only by characterizing the behavior of GRBs across photon energy and particle messengers can we hope to understand the physics of these events.

The gamma rays observed from GRBs exhibit a non-thermal spectrum (Ackermann *et al.*, 2010, Toma *et al.*, 2011) which typically extends above 1 MeV and as high as ~ 30 GeV (Swenson *et al.*, 2010). These observations, combined with the rapid variability of GRBs indicate that the radiating emission region must be expanding relativistically (Paczynski, 1986). The motivation for this conclusion stems from opacity considerations. Absent relativistic effects, GRB variability indicates that the origin of the GRB radiation be only a few hundred kilometers in diameter. In order for the electron density to be low enough for gamma rays to escape, the total mass of baryons surrounding the emission site would have to be very low, an unlikely situation at the center of a collapsing star (Piran and Shemi, 1993). Photon-photon opacity is also a problem in the absence of a relativistic emission region, however large bulk Lorentz factors ($\Gamma = 100 - 1000$) (Lithwick and Sari, 2001) can accommodate the rapid variability observed in GRBs and ameliorate the photon opacity problem (opacity $\propto \Gamma^{-4}$) (Granot *et al.*, 2008).

As the relativistic material expands into the circumburst medium, collisionless

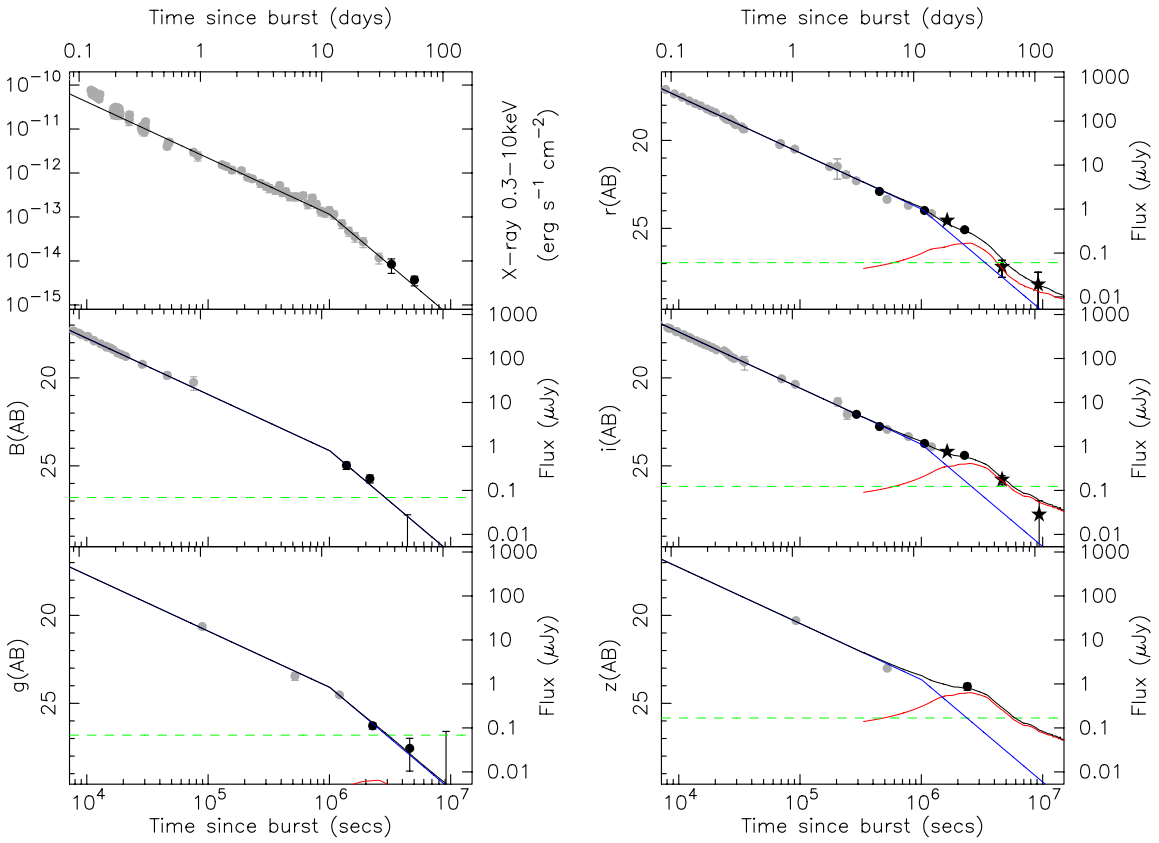

Figure 1.4: Late-time photometry of GRB 080319B across several wavelengths. The steepening of the light curve at $\sim 10^6$ s is reflective of the geometry of the GRB. The green dashed line is the estimated magnitude of the host galaxy, the blue line the afterglow model, the red line is a model SN light curve, and the black line is the sum of the SN and GRB afterglow models (Tanvir *et al.*, 2010).

shocks are formed and the bulk Lorentz factor of the outflow falls. The peak energy of the GRB radiation gradually falls as the burst cools (Mészáros and Rees, 1997). The afterglow time profiles of GRBs, however, are rarely featureless power laws indicating that the central engine may remain active for several minutes after the initial outburst (Falcone *et al.*, 2007). The geometry of the GRB is difficult to determine, but there are clues that indicate GRB radiation is highly collimated and anisotropic. Radiation from a source moving relativistically toward an observer is beamed and the detectable emission emanates from a confined region of angular size Γ^{-1}. As the Lorentz factor decreases, more of the material becomes visible, offsetting the decreased emission per unit solid angle. The observations of achromatic jet-breaks in some GRBs indicate the time when the entire jet becomes visible (Figure 1.4). Such behavior is not possible from a spherically symmetric blast wave and provides strong evidence that the radiation from GRBs is beamed rather that isotropic. Evidence points to jet opening angles of $\sim 15^{\circ}$ or less (Bloom *et al.*, 2003), which significantly reduces the overall energetics of the GRB but also implies that many GRBs are not detected due to the orientation of the jet axis.

While GRBs are inherently interesting events, they can also provide information on other aspects of astrophysical and cosmological importance. GRBs are extremely bright and can be used as probes of the Universe at great distances/early times. Associated with star-forming regions and thought to be triggered by the death of massive stars, GRBs can be used to study the early evolution of star and galaxy

formation at high redshift ($z > 6$). It is theorized that the first luminous objects to form in the Universe were extremely massive (Population III) stars and that the collapse of these stars could give rise to GRBs which would provide information on the nature of the Universe at quite early times ($z > 10$) (Heger *et al.*, 2003, Suwa and Ioka, 2011). GRBs can also be used to probe the fundamental principles of physics such as the invariance of the speed of light in vacuum (Lorentz invariance). Some theories of quantum gravity predict dispersion (Amelino-Camelia *et al.*, 1998) and the short durations, high energies, and extreme distances of GRBs can be used to provide extremely constraining limits on presence of Lorentz invariance violation (LIV) (Abdo *et al.*, 2009a).

This chapter briefly outlines the current state of observational (Section 1.2) and theoretical (Section 1.3) GRB science. A more detailed discussion on gamma-ray emission at the highest energies from GRBs and the physical processes involved follows (Section 1.4). Finally a summary of the characteristics of high-energy-gamma-ray attenuation due to interaction with the extragalactic background light (EBL), an important consideration for GRB observations at high energies, is provided.

1.2 GRBs in the *Swift*/*Fermi* Era

The data provided by the *Swift* and *Fermi* missions have pushed the GRB field forward in the last 8 years due to improved sensitivity, wavelength coverage and localization capabilities. The *Swift* mission was specifically designed to detect, localize,

and characterize the prompt and early afterglow phases of GRBs and in this respect it has been very successful. The *Fermi* mission, and the Large Area Telescope (LAT) instrument in particular, has enabled a vastly more sensitive study of a multitude of astrophysical objects, including GRBs, across an energy range (20 MeV – 300 GeV) that had gone unexplored since the demise of CGRO in 2000. Of relevance to this work, *Fermi* bridges the energy gap between the classical GRB energies (keV – MeV) and the energy range explored by the ground-based VHE gamma-ray telescopes. This section offers an extremely condensed survey of the current state of GRB observations with an emphasis on the behavior of GRBs at the highest energies.

1.2.1 GRB Distances

Before the era of *BeppoSAX* and later *Swift*, GRB redshifts were impossible to determine since localizations were too poor for the small-FOV optical telescopes that are required for redshift measurements. The extremely rapid localization abilities of the *Swift*-BAT (arc minutes) and the *Swift*-XRT (arc seconds), combined with the frequency of *Swift* GRB-detections ($\sim$ 100 yr^{-1}) has led to successful redshift determinations for hundreds of bursts. These distances span nearly three orders of magnitude in redshift from ~ 0.013 (GRB 111005A) (Michalowski *et al.*, 2011) to 9.4 (GRB 090429B) (Cucchiara *et al.*, 2011).

The redshift distribution of *Swift*-detected GRBs peaks around $z \approx 2.5$, higher than determinations from previous instruments (Figure 1.5) and roughly consistent

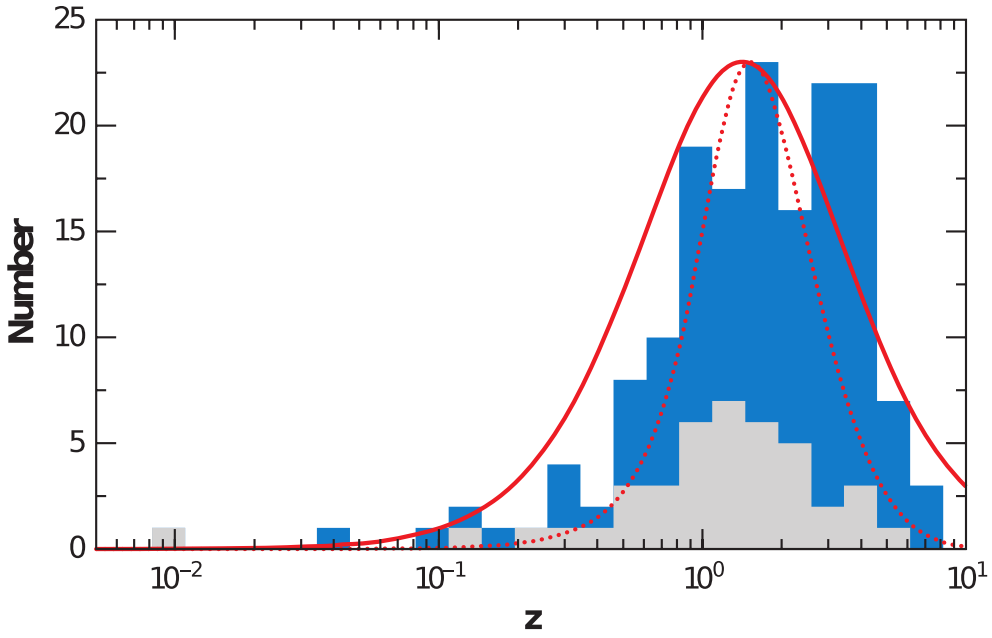

Figure 1.5: Redshift distribution of *Swift*-detected bursts (blue) compared with pre-*Swift* GRB redshifts (gray). The red solid line is the comoving volume derivative ($H_0^3 \frac{dV}{dz d\Omega}$) and the red dotted line is the comoving volume derivative convolved with the star-formation rate from Porciani and Madau (2001). Figure from Gehrels *et al.* (2009).

with what is expected assuming GRB rates trace the star-formation rate. The average redshift before *Swift* was closer to 1 due to the lower sensitivity of previous-generation instruments. Determining the redshift for GRBs is required for understanding nearly any of the fundamental properties of bursts since it affects the interpretation of observed spectra, temporal behavior, and energetics.

1.2.2 Temporal Properties

GRB durations observed by *Fermi* and *Swift* largely confirm what was detected by BATSE, specifically the bimodal distribution. *Swift*, however, detects fewer short bursts than BATSE did, but this can be understood as a consequence of a lower energy range (15 – 150 keV for *Swift* vs. 50 – 2000 keV for BATSE) and triggering algorithm which results in less sensitivity to the lower-fluence, harder-spectrum short GRBs (Barthelmy *et al.*, 2005). With determined redshifts from many *Swift*-detected bursts, the burst durations in the source frame can be computed. The average T_{90} for *Swift*-detected bursts (15 – 150 keV band) is $\sim$ 50 (20) s in the observer (source) frame. The *Fermi*-GBM has much poorer localization capabilities than *Swift* so most GRBs detected by GBM do not have measured redshifts. GBM does detect GRBs at nearly three times the rate of *Swift* and over the first two years of operation detected nearly 500 GRBs. The duration and angular distribution of GRBs measured by GBM is similar to what was detected with BATSE (Figure 1.6).

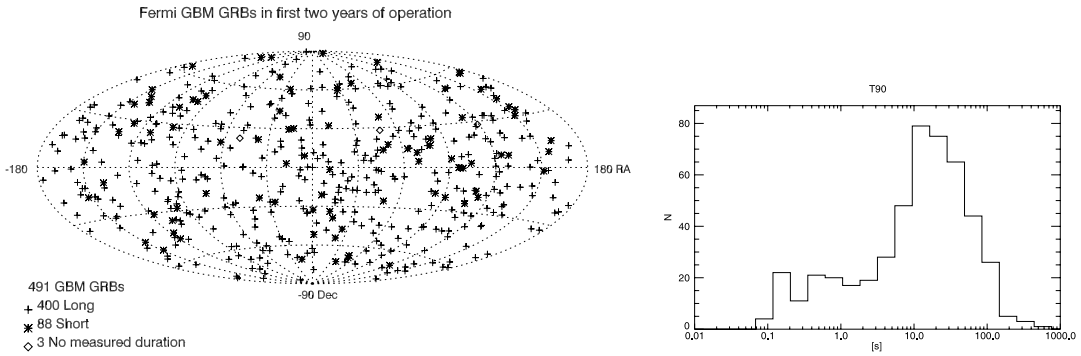

(a) GBM GRB Skymap (b) GBM GRB Durations

Figure 1.6: GRB angular distributions and durations as measured by the *Fermi*-GBM over the first two years of its operation. Both figures from Paciesas *et al.* (2012).

The diversity of GRB light curves during the prompt phase ($t_5 < t < t_{95}$)[3] (Figure 1.7) has led to efforts at characterizing bursts at time scales significantly smaller than the overall duration. In the internal shock model (e.g. Bošnjak *et al.* (2009)) the GRB central engine produces relativistic shells of matter and radiation with a non-uniform distribution of Lorentz factors. The collision of these relativistic shells may be responsible for the individual pulses in the prompt GRB light curves (Nakar and Piran, 2002) and the deconvolution of the GRB light curves can potentially reveal differences in the properties of the central engines of the two populations of GRBs, long and short, that are believed to originate from the deaths of massive stars and compact object-mergers respectively. Studies of the light curves show evidence for discrete, asymmetric, overlapping pulses which are suggestive a stochastic central engine process (Hakkila and Preece, 2011).

[3] t_n is defined to be the time at which n% of the counts above background from the GRB have been detected. The interval defined is equivalent to T_{90}.

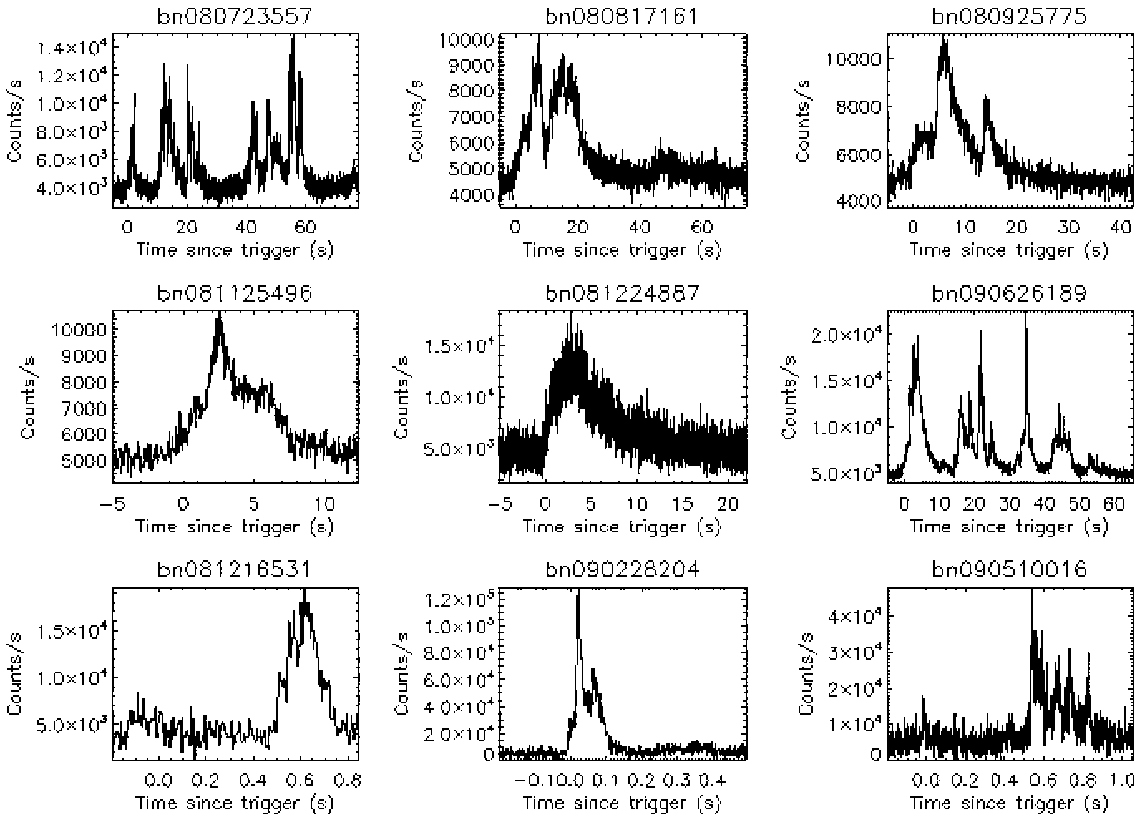

Figure 1.7: Example light curves obtained by the *Fermi*-GBM illustrating the characteristic diversity of the prompt phase of GRBs. The top two rows are light curves from long GRBs while the last row is data obtained from short GRBs (Bhat and Guiriec, 2011).

1.2.3 Spectral Properties

The spectral information on GRBs obtained with *Fermi* covers an energy range largely inaccessible since the end of CGRO. The spectral results on GRB prompt emission obtained with GBM (Bissaldi *et al.*, 2011) generally confirm the BATSE results, specifically that the emission between 8 keV and 40 MeV is usually well-fit by a Band function. Some of the most illuminating results have come from the LAT, which is much more sensitive than its predecessor EGRET on board CGRO. The high-energy spectra of some GRBs have been seen to extend up to rest-frame energies of $\sim$ 90 GeV, a promising development for ground-based VHE gamma-ray experiments. These GRBs' significant high-energy components have been found to be quite rare; the fraction of GBM-detected GRBs also detected by the LAT ($>$ 20 MeV) is only about 5%.

In addition to the high energies detected from GRBs by the LAT, the spectral fits to joint GBM-LAT detected bursts show wide variation and are sometimes inconsistent with the extension of the Band function spectrum to high energies. Several bursts are preferentially fit by an extra power-law component in addition to the Band function, a characteristic first suggested by the analysis of BATSE data from GRB 941017 (Gonzalez *et al.*, 2003). This extra component is seen in both long (Abdo *et al.*, 2009b, Ackermann *et al.*, 2011) and short (Ackermann *et al.*, 2010) bursts and is often the dominant spectral feature at both low and high energies (Figure 1.8). This extra component is usually quite hard (spectral index $\Gamma < 1.9$) which is challenging to

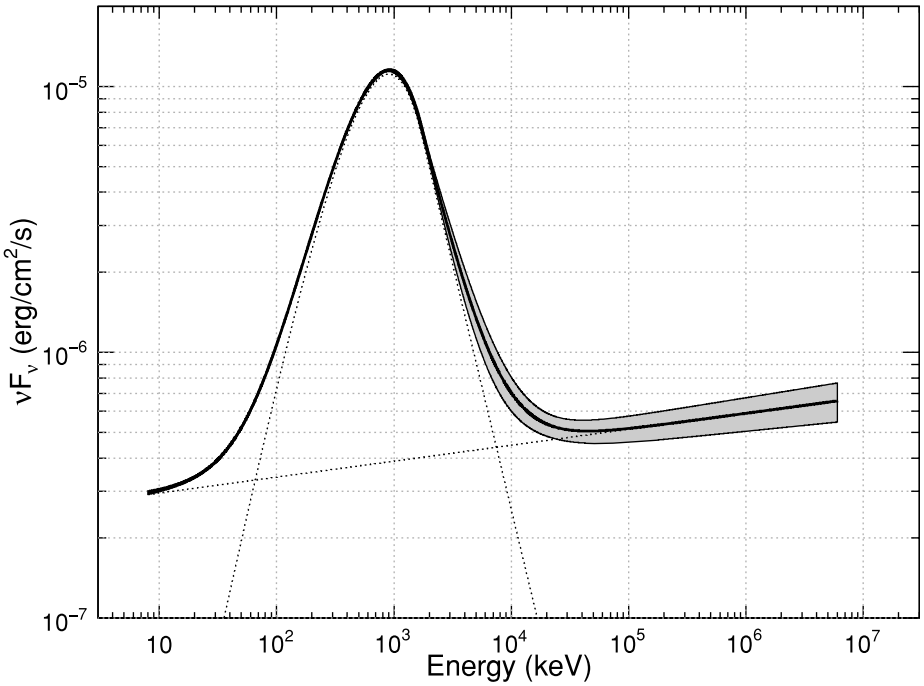

Figure 1.8: The joint *Fermi*-GBM-LAT unfolded νF_ν spectrum of GRB 090902B showing the extra power-law component which is dominant at both high and low energies (Abdo *et al.*, 2009b).

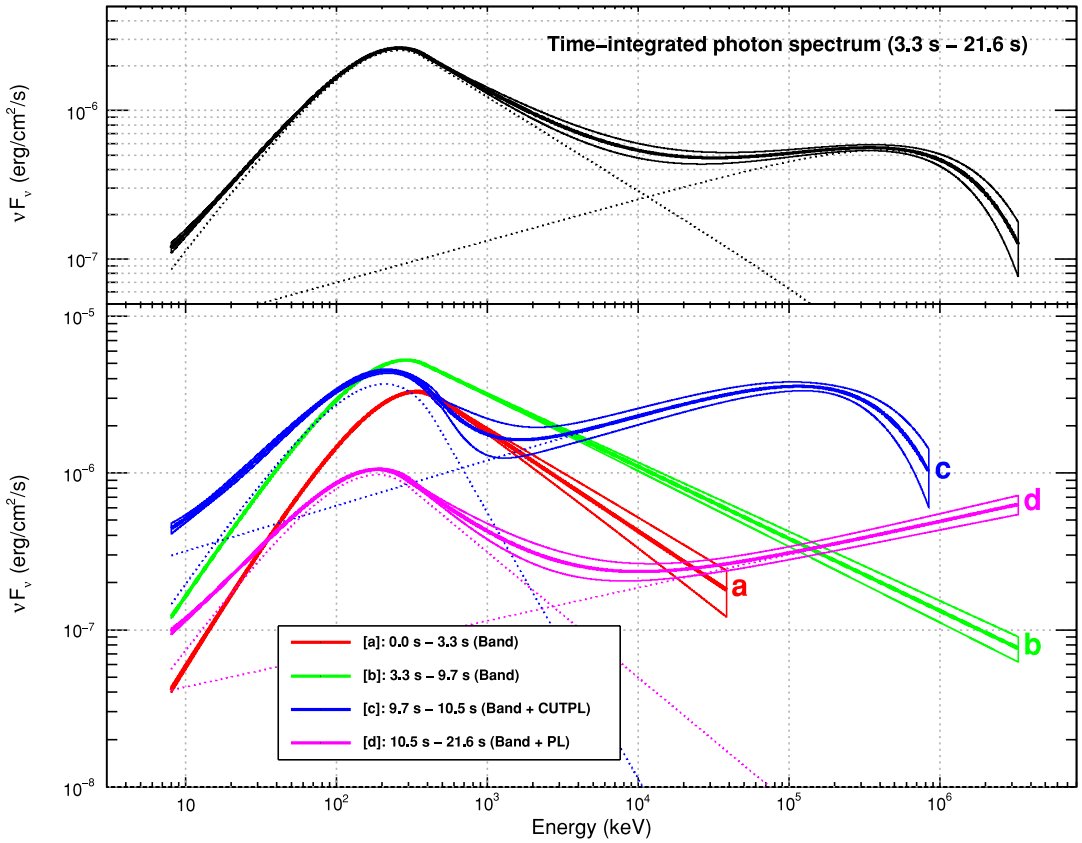

Figure 1.9: The integrated (top) and time-resolved (bottom) spectra showing the evolution of the power-law component during the prompt phase of the GRB 090926A (Ackermann *et al.*, 2011).

explain for both leptonic and hadronic models of gamma-ray production in GRBs (Asano *et al.*, 2009).

Strong evolution in the time-resolved spectra of GRB 090926A (Ackermann *et al.*, 2011), including the appearance of a cutoff in the hard power-law component (Figure 1.9) may be indicative of pair-production ($\gamma\gamma \rightarrow e^+e^-$) or from inverse Compton (IC) scattering in the Klein-Nishina regime. In several *Fermi*-detected bursts the inclusion of a blackbody component in addition to the Band function improved the spectral fit and may be indicative of emission from the photosphere of the GRB jet

(Guiriec *et al.*, 2011). The detailed, time-resolved spectral behavior of GRBs from keV to GeV energies measured by *Fermi* provides a wealth of new information (and questions) regarding the nature of the emission processes occurring in GRBs.

A significant feature of emission from GRBs detected by the LAT is that the high-energy spectral component is often significantly delayed and longer lasting than the lower-energy emission seen by the GBM. This behavior is also seen in both long (e.g. GRB 080916C (Abdo *et al.*, 2009c), Figure 1.10) and short (e.g. GRB 081024B (Abdo *et al.*, 2010a)) GRBs, indicating that it is common in bright LAT-detected GRBs. Explanations for this behavior range from emission due to multiple pairs of colliding relativistic shells (Piran, 1999) or from an expansion of the emitting region which becomes optically thin to high-energy photons later than low-energy photons (Granot *et al.*, 2008). The delayed, long-lasting emission of the high-energy spectral component of the bright, hard, LAT-detected GRBs suggests that some of these bursts may be detectable with ground-based VHE telescopes whose significantly higher sensitivity may be able to shed light on GRB emission at the highest energies.

1.2.4 Correlations

Due to the heterogeneity of GRBs in the prompt phase, significant effort has been made to extract correlations between observed properties of bursts. Many relations concerning measured quantities of duration, spectral hardness, the peak of the spectral energy distribution, the peak luminosity, variability, spectral lag, light curve

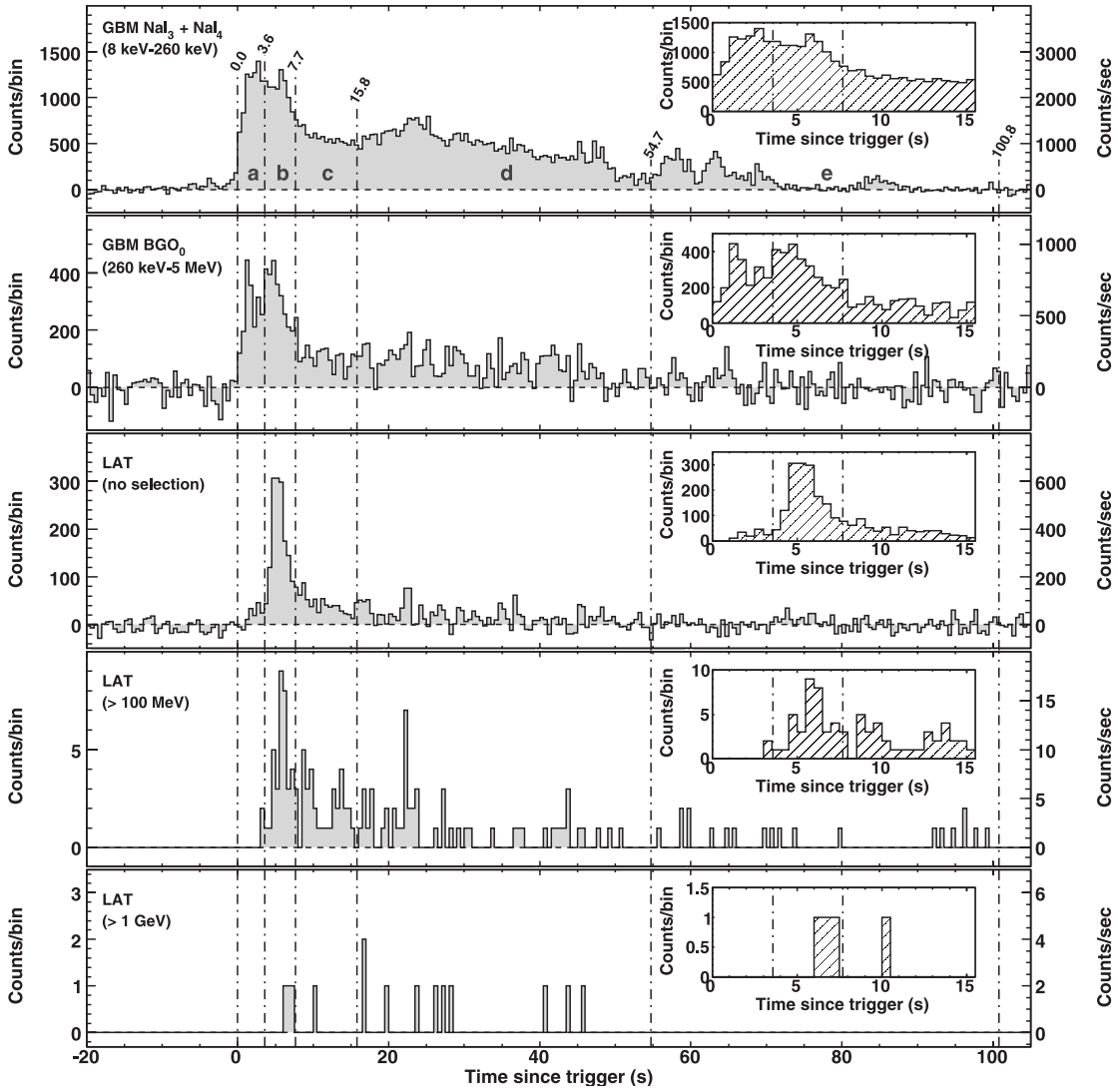

Figure 1.10: The light curve of the prompt phase of GRB 080916C across different energy bands. The high-energy emission detected by the LAT is delayed and long-lasting compared to the GBM-detected emission, a characteristic common to many of the bright, LAT-detected GRBs (Abdo *et al.*, 2009c).

pulse shapes, etc. have been suggested. A summary of several frequently discussed correlations can be found in Figure 5 of Gehrels *et al.* (2009).

The holy grail of such correlation studies is a method to determine reasonably well and independent of a measured redshift, the absolute luminosity of a GRB from the observables discussed above. Other correlations have been proposed (Firmani *et al.*, 2006, Ghirlanda *et al.*, 2004) with this goal in mind. Whether or not any of the correlations will be significantly constraining to attain this goal (Bloom *et al.*, 2003) remains to be seen. If such a relation were found, GRBs could be used as cosmic rulers in much the same fashion that Type Ia supernovae are currently used, with the added benefit of being detectable out to redshifts much greater than is possible with supernovae.

1.2.5 Early-afterglow Emission

Following the prompt gamma-ray emission, GRBs are seen to radiate at longer wavelengths (from X-ray to radio) for days or weeks after the initial burst. The *Swift* satellite was specifically designed to observe these afterglows and results from the *Swift*-BAT and XRT has shown that the prompt emission in the X-ray band undergoes a smooth transition to the decaying afterglow. These X-ray afterglows are interesting insofar as apart from flaring activity seen in some afterglows, nearly all X-ray afterglows follow a template made up of three power-law segments of temporal decay (Nousek *et al.*, 2006). The early, steep decline in the X-ray light curve is

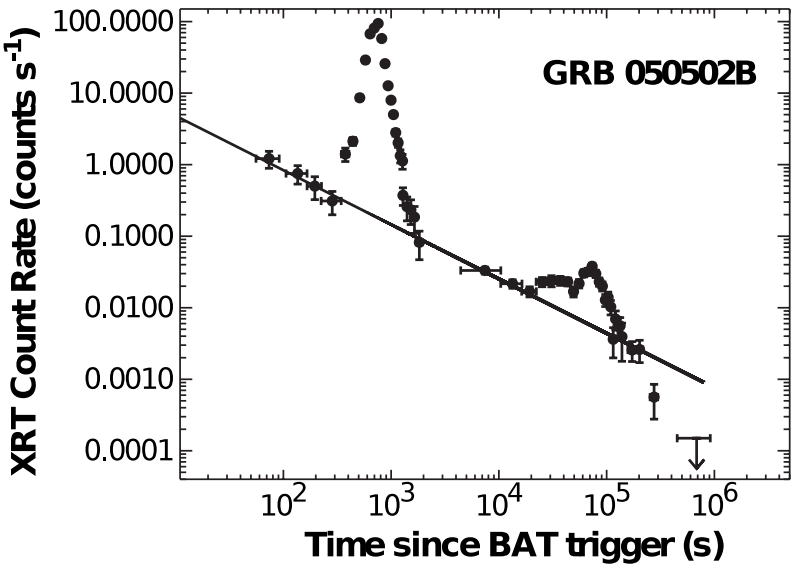

Figure 1.11: The large X-ray flare associated with GRB 050502B as measured by the *Swift*-XRT. The flare intensity is nearly three orders of magnitude above the underlying afterglow (Burrows *et al.*, 2005).

attributed to the prompt gamma rays observed at large emission angles. The transition to the shallow middle phase is thought to reflect the emission from the forward shock becoming dominant (Zhang *et al.*, 2006). Finally a transition to a "classical" afterglow phase occurs. In some cases, achromatic jet breaks are seen at late times which are indicative of the geometry of the GRB jet (Figure 1.4).

In approximately half of the GRB afterglows observed with *Swift*, X-ray flaring activity is seen (Falcone *et al.*, 2007). These X-ray flares occur hundreds to thousands of seconds after the initial GRB and can be very bright, in some cases exceeding the energy released during the prompt phase of the GRB (Figure 1.11). The cause of the X-ray flares remains unknown but the energetics suggest that the central engine powering the initial GRB may also be responsible for the later X-ray flaring

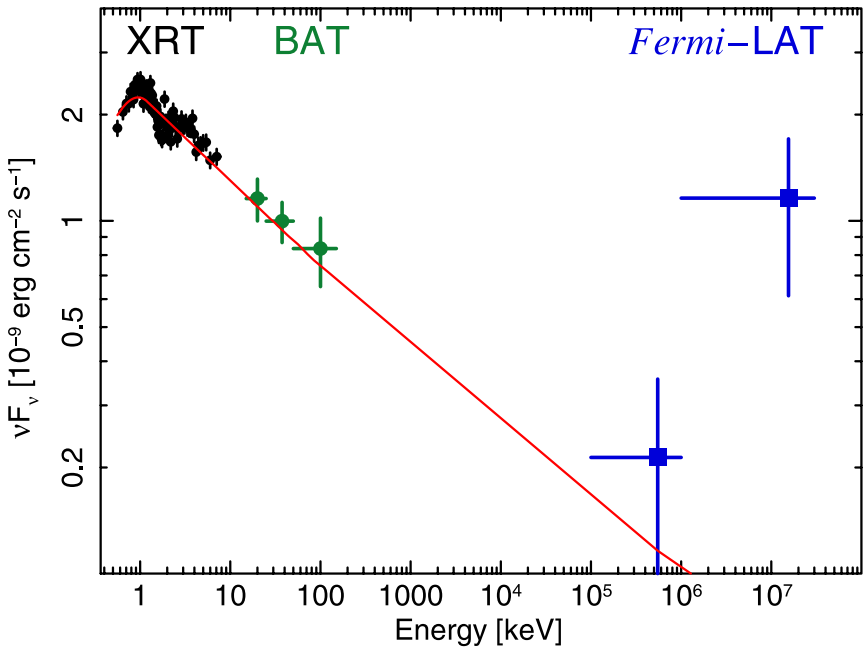

Figure 1.12: GeV emission detected by the *Fermi*-LAT associated with X-ray flaring in GRB 100728A. The high-energy emission is consistent within 3σ with the extrapolation of the *Swift*-detected emission. Considered alone, the LAT-detected emission is best fit with a power-law spectral index of $\Gamma = 1.4 \pm 0.2$ (Abdo *et al.*, 2011).

activity (Falcone *et al.*, 2006). Other theories, such as the production of X-rays by synchrotron emission from electrons in the forward shock (Galli and Piro, 2007), have been advanced to explain the X-ray flares.

Recent results from the *Fermi*-LAT have shown that gamma rays of up to GeV energies are produced coincident with some X-ray flares in GRB afterglows (Abdo *et al.*, 2011). The high-energy emission coupled with the complexity of the flaring light curve for GRB 100728A indicates that the X-ray and GeV late-time flares may originate from internal shocks in a long-lasting relativistic outflow (Zhang *et al.*, 2006). The spectrum of the GeV emission associated with the X-ray flaring in GRB 100728A is not well constrained (Figure 1.12) and may be consistent with an extrapolation of

the X-ray spectrum, but the best-fit spectral index for the LAT-detected emission is a very hard $\Gamma = 1.4 \pm 0.2$. Emission of such high energy and at the later times associated with X-ray flares makes this component an interesting feature to search for with VHE gamma-ray telescopes.

Swift in particular has enabled follow-up observations of GRBs to a degree never before possible. As a result, follow-up observations spanning the electromagnetic spectrum from radio to VHE gamma-rays have become common and much can be learned about GRBs from these observations. The details of VHE gamma-ray observations will be covered in quite some detail in this work, but results of lower-energy and longer-duration observations and their impact on GRB science are omitted here. Recent results from optical and radio observations of GRB afterglows are given in Gehrels *et al.* (2009) and references therein.

1.3 GRB Physics

Most theoretical models of GRBs share some common features: the central engine is gravitationally powered and fueled by the accretion of matter onto a compact object; the outflows generated by this released energy are relativistic and anisotropic; and gamma rays are most likely generated through collisionless shocks inside and at the front of the relativistic material. However there remains many open questions about the details and this section is a brief review of the basic physical processes that are thought to drive GRBs.

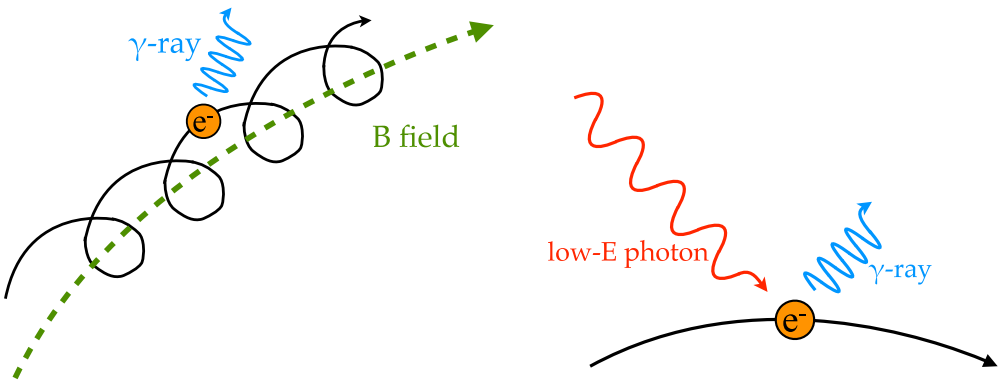

(a) Sychrotron Emission (b) Inverse Compton Scattering

Figure 1.13: Diagrams of the common processes producing gamma rays in GRBs.

1.3.1 Radiation Processes

GRBs are so-named for their production of gamma rays. Gamma rays from GRBs are believed to be produced by some combination of two primary mechanisms. These processes are shown schematically in Figure 1.13. These processes involve electrons and photons and are invoked as the source of gamma rays in the leptonic model of GRBs. Synchrotron radiation is generated by any accelerated charged particle and with sufficient energies, bulk Lorentz factors, and magnetic fields, synchrotron radiation in the gamma-ray energy range (up to GeV energies) in the observer frame can be generated. The second leptonic process for gamma-ray generation is inverse Compton (IC) scattering. IC scattering is simply Compton scattering in the case where high-energy electrons up scatter low-energy photons to higher (gamma-ray) energies.

Synchrotron and IC processes can take place among the same population of elec-

trons. The synchrotron radiation from a population of highly energetic electrons is up scattered to higher energies by the same electron population. This is known as synchrotron self-Compton (SSC) radiation. IC processes are common in active galactic nuclei (AGN) and supernova remnants and are capable of producing photons of very high energies (>TeV). In hadronic models of GRBs, protons are accelerated to high energies and in addition to producing synchrotron radiation, high-energy proton collisions with gamma-rays can produce neutral pions through the delta resonance $p + \gamma \rightarrow \Delta^+ \rightarrow \pi^0 + p$. These pions decay preferentially to pairs of gamma rays ($\pi^0 \rightarrow \gamma\gamma$) and may be responsible for some of the observed properties of GRBs.

One important feature of Compton scattering is the suppression of the electron-photon cross section when photon energies become larger than the electron rest-mass. This reduction of the electron-photon cross-section is commonly referred to as Klein-Nishina (KN) suppression. The integral KN cross section in the rest-frame of a free electron is given by:

$$\sigma = 2\pi r_e^2 \left\{ \frac{1+\gamma}{\gamma^2} \left[\frac{2(1+\gamma)}{1+2\gamma} - \frac{1}{\gamma} \ln(1+2\gamma) \right] + \frac{1}{2\gamma} \ln(1+2\gamma) - \frac{1+3\gamma}{(1+2\gamma)^2} \right\} \quad (1.1)$$

where r_e is the classical electron radius and $\gamma = h\nu/m_e c^2$ is scaled energy of the incident photon. This cross-section was one of the first results obtained with quantum electrodynamics (Klein and Nishina, 1929) and has important implications for the production of VHE gamma-rays in GRBs through IC processes.

1.3.2 Accretion and the Central Engine

Most GRBs are thought to occur from the collapse of the core of a massive star to a neutron star or black hole. Infalling matter accreting onto black hole or neutron star (Figure 1.14(a)) is the most efficient process of extracting energy from matter, more than two orders of magnitude more efficient than thermonuclear reactions. The rate of mass accretion required for generating the luminosities observed from GRBs ($\sim 10^{53}$) erg s^{-1} is extremely large but is predicted to be achievable in core-collapse supernovae (Narayan *et al.*, 2001, Woosley, 1993) and also from compact-object mergers which are suspected to be the source of short GRBs (Lee *et al.*, 2005, Metzger *et al.*, 2008). Under these conditions the densities and temperatures are so large that photons are unable to escape and are effectively coupled to the accreting material. During this time, neutrinos are the dominant source of cooling.

The Eddington luminosity for neutrinos is dependent on the both the energy of the neutrinos produced and the mass of the compact object but is on the order of 10^{54} erg s^{-1}, capable of providing the energy required to produce a GRB. Associated with such a luminosity, the Eddington limit of the blackbody temperature (~ 50 MeV), density ($\sim 10^{11}$ g cm^{-3}) and magnetic field ($\sim 10^{16}$ G) in the vicinity of the compact object can be computed (Ramirez-Ruiz, 2006). These values assume spherical symmetry but in general the material in the collapsing star will have some associated angular momentum. If matter is falling in isotropically from larger radii, then an accretion disk, (Figure 1.14(b)) will form (Lee and Ramirez-Ruiz, 2006).

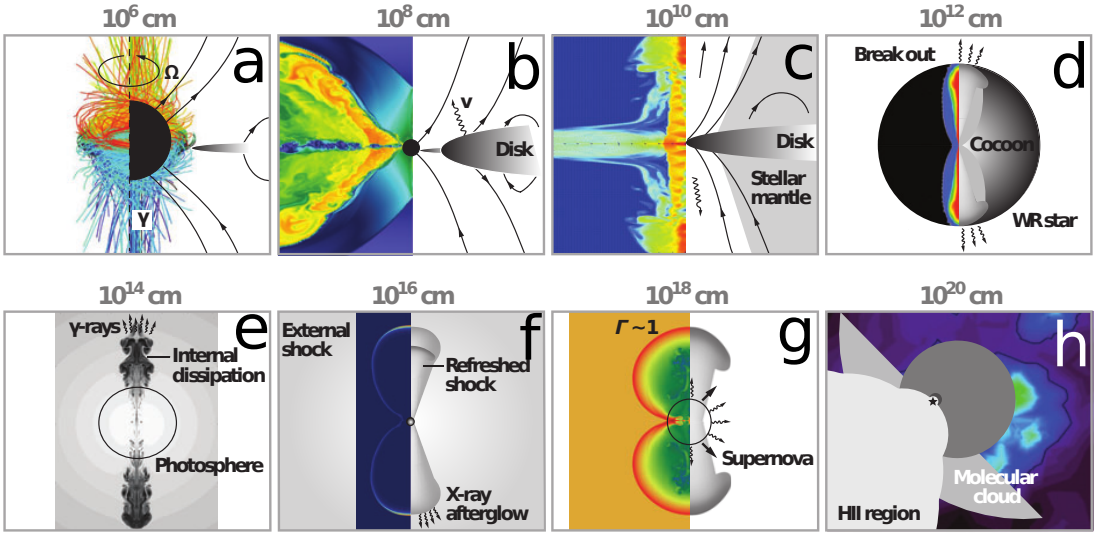

Figure 1.14: Figure 14 from Gehrels *et al.* (2009): Snapshots of the GRB lifecycle depicted at relevant length scales. Details in the text.

1.3.3 Jet Formation and Confinement

As mentioned in the previous section, there are observational clues implying that GRBs are far from isotropic and that radiation may be produced in collimated jets. These jets would presumably be co-linear with the rotation axis of the accretion disk (Levinson and Eichler, 2000) and the accretion, angular momentum and magnetic fields surrounding a spinning neutron star or black hole could conceivably create a collimated outflow (McKinney, 2006). The exact mechanism of how exactly the jets are created is not clear but there are some theories of how jet formation may be accomplished. One general idea involves the creation of electron/positron pairs or photons by the escaping neutrinos which would create a relativistic wind in regions with low baryon densities (i.e. along the rotation axis, away from the accretion disk) (Dessart *et al.*, 2009, Rosswog *et al.*, 2003). Another line of thought is that

extremely large electric fields generated from the rotation of the compact object (an extremely powerful dynamo) serve to create a relativistic jet of electrons and positrons, essentially extracting the spin energy of the black hole or neutron star (Blandford and Payne, 1982) (Figure 1.14(c)).

Assuming that a jet has been formed, another significant challenge is understanding how it can maintain coherence and propagate through and break out of the stellar envelope which remains from the progenitor star (Figure 1.14(d)) and obstructs the progress of the jet (MacFadyen and Woosley, 1999). It is not clear at this time what ingredients in what proportion are required to explain the confinement of the jets in GRBs. The acceleration of the relativistic flows to Lorentz factors of $\Gamma \approx 1000$ does not require very tight collimation of a jet (Zhang *et al.*, 2004), but the region through which the jet propagates must be relatively free of baryons – a situation not easily imagined inside a star.

1.3.4 Radiation, Cooling, and Afterglows

One encounters relativistic jets in various astrophysical systems including low-mass X-ray binaries and AGN, but the bulk Lorentz factors achieved in GRBs ($\Gamma \sim 1000$) (Lithwick and Sari, 2001) are a speed record of sorts and require special consideration. In the relativistic fireball model (Piran, 1999), many features of which have become widely accepted, much of the observed photonic radiation is produced by shocks created by interacting shells of material with relative velocity differentials in-

side the jet (internal shocks, Figures 1.15 and 1.14(e)). These shocks are collisionless; the densities are low enough that the mean free path of the particles is larger than the size of the system. Instead of particle collisions, magnetic fields and/or plasma waves mediate particle interactions in the shock (Piran, 2005). In addition to these collisionless shocks, magnetic reconnection and hydromagnetic turbulence may also account for observed GRB radiation (Rees and Mészáros, 1994). The photosphere of the relativistic flow is a source of thermal radiation which may be directly observable and could also serve as seed photons for IC scattering by the non-thermal electrons in the jet (Ryde and Pe'er, 2009, Thompson *et al.*, 2007). The magnetic fields behind the shocks are highly disordered and the electrons in the jet will produce synchrotron radiation in these conditions. IC and/or SSC processes could create gamma-rays up to GeV – TeV energies, those detected by *Fermi* and searched for with VHE telescopes, e.g. Milagro.

As the material in the jet expands outwards, it gathers up, accelerates, and compresses the external matter, creating a forward shock. A reverse shock is formed by the deceleration of the jet material and propagates back into the relativistic flow. Both the forward and reverse shocks are considered external shocks, as opposed to internal shocks discussed in the previous paragraph (Figure 1.15). The deceleration of the forward external shock occurs when the rest mass energy of the swept up particles equals the injected energy. This sets a deceleration length scale ($\sim 10^{16}$ cm) (Rees and Mészáros, 1992) at which point the slower material in the jet catches up and refreshes

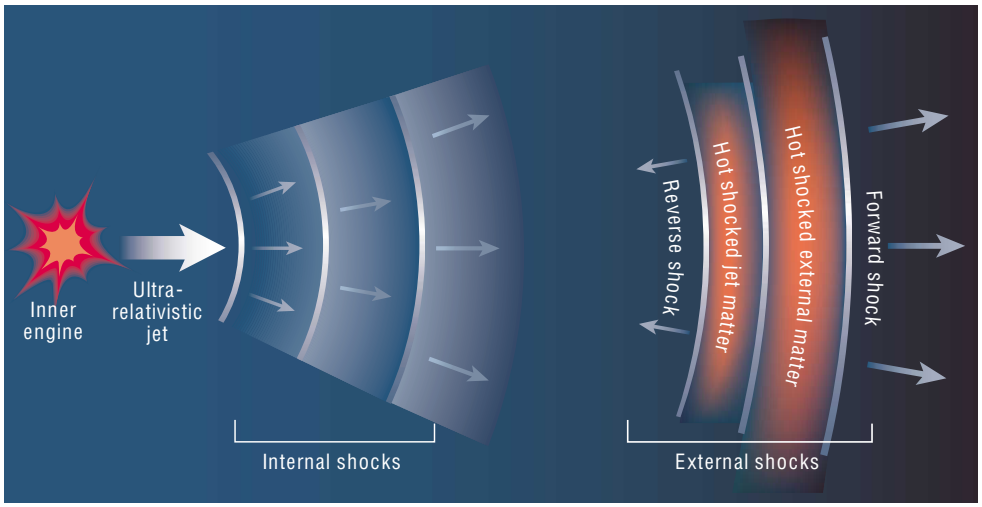

Figure 1.15: Internal and external shocks in the relativistic outflow of a GRB. Figure from Piran (2003).

the reverse shock (Figure 1.14(f)). One problem is that, unless the environment is dominated by electrons, most of the energy in the external shocks will be distributed among the baryons. The efficiency of radiation by electrons is much higher and so somehow much of the energy must be transferred to the electrons. The details of this process remain unclear (Gedalin *et al.*, 2008). The blast wave continues to sweep up matter and slow until it eventually becomes non-relativistic. This typically happens at a radial distance of about a light year (Figure 1.14(g,h)).

1.4 VHE Emission from GRBs

Recent results from the *Fermi*-LAT have shown that GRBs are capable of producing emission of energies up to at least 90 GeV in the source frame (Abdo *et al.*, 2009b, Swenson *et al.*, 2010). From a purely observational standpoint then, it is not

too much of a mystery why it is expected that VHE gamma-ray emission may also be produced. It had been (and continues to be) suggested from a theoretical and/or phenomenological point of view that GRBs could produce GeV – TeV scale radiation at various stages in the GRB development, from both internal and external shocks as well as associated with X-ray flares.

Detections of GRBs with *Fermi*-LAT have been made possible in large part due to its high duty cycle, large FOV, and relative sensitivity at GeV energies and seem to support the hypothesis that at least some of the processes expected to produce VHE gamma-rays in GRBs are occurring. VHE gamma-ray emission has been searched for with ground-based telescopes by a number of experiments yet no conclusive detection of VHE photons from GRBs has been made. The lack of GRB detections by VHE observatories may arise from instrumental considerations (sensitivity, FOV, duty cycle, response times) rather than from inherent emission characteristics of GRBs. In this section the theorized physical mechanisms for VHE gamma-ray production are covered with an emphasis on the detectability of such emission with ground-based VHE gamma-ray observatories. An overview of the prospects for VHE GRB observations from both current- and future-generation experiments can be found in Section 10.2 and Section 10.3, respectively.

It is predicted that high-energy gamma-ray emission can be produced by the collision of thin shells of material with different Lorentz factors interacting in the jet of the GRB (the internal shocks) (Bošnjak *et al.*, 2009). The peak of the Band

function (keV – MeV) emission observed with BATSE and now *Fermi*-GBM during the prompt phase of a GRB can be generated in one of two ways: synchrotron emission of high-energy electrons peaking at keV – MeV energies or IC scattering of photons generated from a synchrotron peak at lower energies (SSC). The synchrotron origin of the BATSE/GBM-detected emission is favored in the case of internal shocks as it better predicts the pulse shapes and spectral evolution in GRB light curves than does the SSC case (Daigne and Mochkovitch, 1998, 2003). The electrons in the synchrotron case will IC scatter photons to high energies easily detectable by the *Fermi*-LAT. KN-suppression of the Compton cross-section at VHE energies will result in a fairly steep cutoff depending on model parameters (see Figure 8 of Bošnjak *et al.* (2009)) but, since ground-based VHE telescopes are much more sensitive than the LAT, a detection of VHE gamma rays is possible.

The SSC case has been invoked to explain the low-energy spectral indices observed by BATSE (Panaitescu and Mészáros, 2000, Stern and Poutanen, 2004) and, due to the bright optical synchrotron emission, it is a natural explanation for the observations of GRB 080319B (Racusin *et al.*, 2008). Depending on the location and relative intensities of the synchrotron and first-order IC spectral peaks, either the direct IC or second-order IC component in the SSC model could be significant and detectable by VHE instruments (Kumar and Panaitescu, 2008). It should be noted, however, that the SSC scenario, at least in the case of GRB 080319B suffers from both theoretical (e.g. (Zou *et al.*, 2009b)) and observational (Chapter 5, (Abdo *et al.*, 2012)) issues.

In addition to prompt emission from internal shocks, VHE gamma rays could be produced at later times in the prompt phase or during the early afterglow phase due to processes in the external (both forward and reverse) shocks. The delayed, long-lasting nature of the high-energy GRB emission detected by the *Fermi*-LAT is well-described assuming that it is synchrotron emission in the external forward shock (Kumar and Barniol Duran, 2009, 2010), and the extension of this synchrotron spectrum up to TeV energies could result in a detectable VHE gamma-ray flux.

IC processes in the forward shock have also been considered by several authors (e.g. Sari *et al.* (1998)) and such processes would contribute strongly to gamma-ray emission in the GeV – TeV regime (Dermer *et al.*, 2000, Mészáros and Rees, 1994, Wang *et al.*, 2001). The dominant IC process in the forward shock is the SSC emission from the population of energetic electrons (Sari and Esin, 2001). Figure 1.16 shows the predicted temporal and frequency dependence of the SSC emission during the afterglow phase of a GRB embedded in a constant-density interstellar medium (ISM). The extended duration and high energies of the SSC component make it a promising target for observation by ground-based IACT instruments (Fan *et al.*, 2008, Xue *et al.*, 2009) which have excellent sensitivity but often have GRB observation delays on the order of a few minutes due to repointing requirements.

Yet another observable VHE signal from GRBs may come from GeV – TeV flares associated with X-ray flares commonly observed accompanying GRB afterglows. The aforementioned detection of GeV emission associated with the X-ray flaring activity

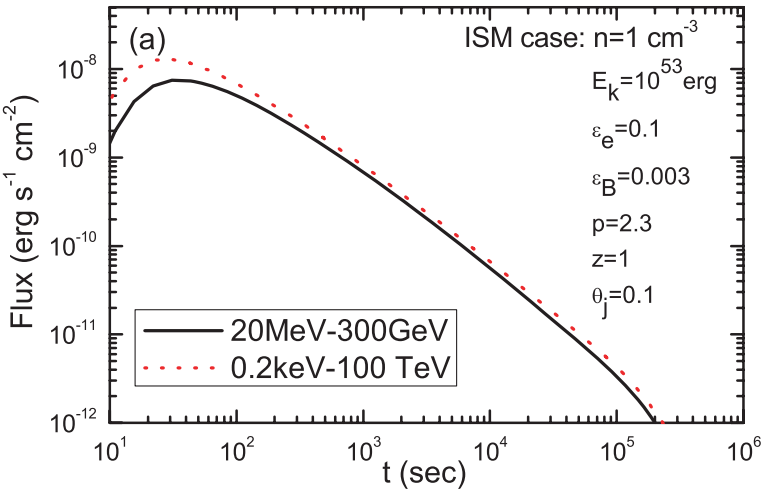

(a) Temporal Characteristics

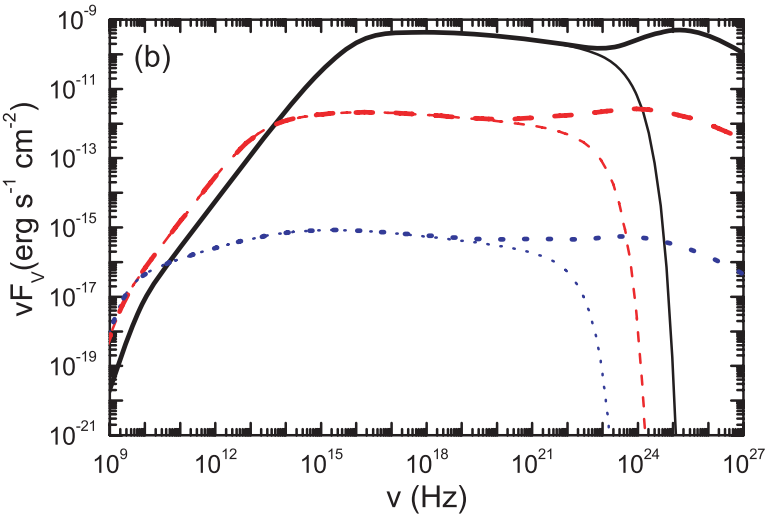

(b) Spectrum

Figure 1.16: SSC emission predicted from the forward shock assuming a constant-density ISM (Fan *et al.*, 2008). Figure1.16(a) shows the light curve in the central 20 MeV – 300 GeV band as well as the broader 200 eV – 100 TeV energy range. Figure 1.16(b) shows the predicted spectra at 200 s (black), 5.5 hours (red), and 23 days (blue) after the GRB. The thin lines show the synchrotron component, while the thick lines show the total synchrotron + SSC emission. For comparison, the VERITAS IACT array has a median response time of $\sim$ 5 min., an average energy threshold of $\sim$ 250 GeV (6.3×10^{25} Hz) and a typical νF_ν sensitivity of 10^{-11} erg cm^{-2} s^{-1} for GRB observations (before consideration of EBL absorption).

in GRB 100728A ((Abdo *et al.*, 2011), Figure 1.12) by *Fermi* hints at this possibility. There are theoretical motivations for such emission as well, in which some of the X-ray photons produced in the flares are IC scattered by the hot forward shock electrons which would result in a detectable photon signal at GeV – TeV energies (Wang *et al.*, 2006). It has also been suggested that X-ray flares may originate from the forward shock itself as it interacts with irregularities in the ISM (Dermer, 2006) in which case VHE emission from SSC processes would also be expected.

Finally, GRBs have been advanced as a possible class of sources that generate ultra-high-energy cosmic rays (Dermer, 2007, Murase *et al.*, 2008, Waxman, 2004). In hadronic or combined leptonic/hadronic models, VHE gamma rays are produced by the energetic leptons that are created from cascades initiated by photopion production (Bottcher and Dermer, 1998). Very recent results from the IceCube neutrino telescope (Abbasi *et al.*, 2012) indicate that either hadronic processes in GRBs are subdominant, or that the current physical models of GRB shocks are incorrect. Currently, leptonic models of gamma-ray production in GRBs are generally preferred, which is the justification for the near-exclusive focus on them in the preceding discussions.

Assuming VHE gamma rays are produced by GRBs, whether these VHE gamma rays make it to Earth is another question. Effects of the EBL on the GeV – TeV component of GRBs can be quite substantial, particularly at high redshifts and energies. A summary of the effects of the EBL on the observability of VHE emission

from GRBs can be found in the following section.

1.5 GRBs and the Extragalactic Background Light

The EBL is thought to be composed of starlight either directly radiated or re-processed through absorption and radiation by dust. The energy and wavelength of light that make up the EBL span from the IR ($E = 10^{-3}$ eV, $\lambda = 1$ mm) to the UV ($E = 10$ eV, $\lambda = 0.1\,\mu$m). The spectrum and intensity of the EBL is of interest in its own right as it reflects much the radiant energy released by the processes of structure formation since photons decoupled from matter after the Big Bang. Measuring the EBL directly is difficult due to foreground contamination from zodiacal light, etc. (a review of the topic can be found in Hauser and Dwek (2001)). However, through a variety of methods outlined below, a general consensus on the properties of the EBL is growing. The EBL is relevant to GRB observations at >GeV energies from the production of electron-positron pairs due to interaction of the high energy photons with the low-energy EBL ($\gamma\gamma \rightarrow e^+e^-$). This process peaks near threshold, which is given by:

$$E_\gamma \epsilon = \frac{2m_e^2c^4}{1+z} \tag{1.2}$$

where ϵ is the energy of the EBL photon and E_γ the energy of the high-energy gamma ray (Gould and Schréder, 1967). Accounting for the effects of the EBL on GRB spectra is critical to the interpretation of VHE GRB observations that are the

topic of this work.

In part due the impact of the EBL on observations of extragalactic sources at high energies, the study and modeling of the EBL has been a very active field over the last decade. There have been several approaches to understanding the EBL and several of the most recent models (Finke *et al.*, 2010, Franceschini *et al.*, 2008, Gilmore *et al.*, 2009) are beginning to converge over the energy range of interest for VHE observations. Some models, less favored now due in part to observations of GeV photons by *Fermi*-LAT from large redshifts (e.g. Abdo *et al.* (2009c)) use IR data from local galaxy observations and extrapolate to larger distances and higher energies (Stecker *et al.*, 2006). The model of Gilmore *et al.* (2009) which is used for EBL attenuation calculations in this work, uses semi-analytic models (SAMs) of galaxy formation to calculate the star formation history of the Universe and evolved to determine the characteristics of the EBL today. Alternatively, using information on star formation rates and stellar properties (Finke *et al.*, 2010, Kneiske *et al.*, 2004) or luminosity data (Franceschini *et al.*, 2008), estimates on the EBL energy density and evolution in time can be made. Figure 1.17 shows several of the models of EBL energy density. The close agreement of several recent models in the near-IR to UV energy range is encouraging as it indicates that the EBL may be well-enough understood at these energy ranges to allow for the correction of high-energy gamma-ray attenuation from sources at cosmological distances.

In addition to the EBL, gamma rays from GRBs can be absorbed by the same

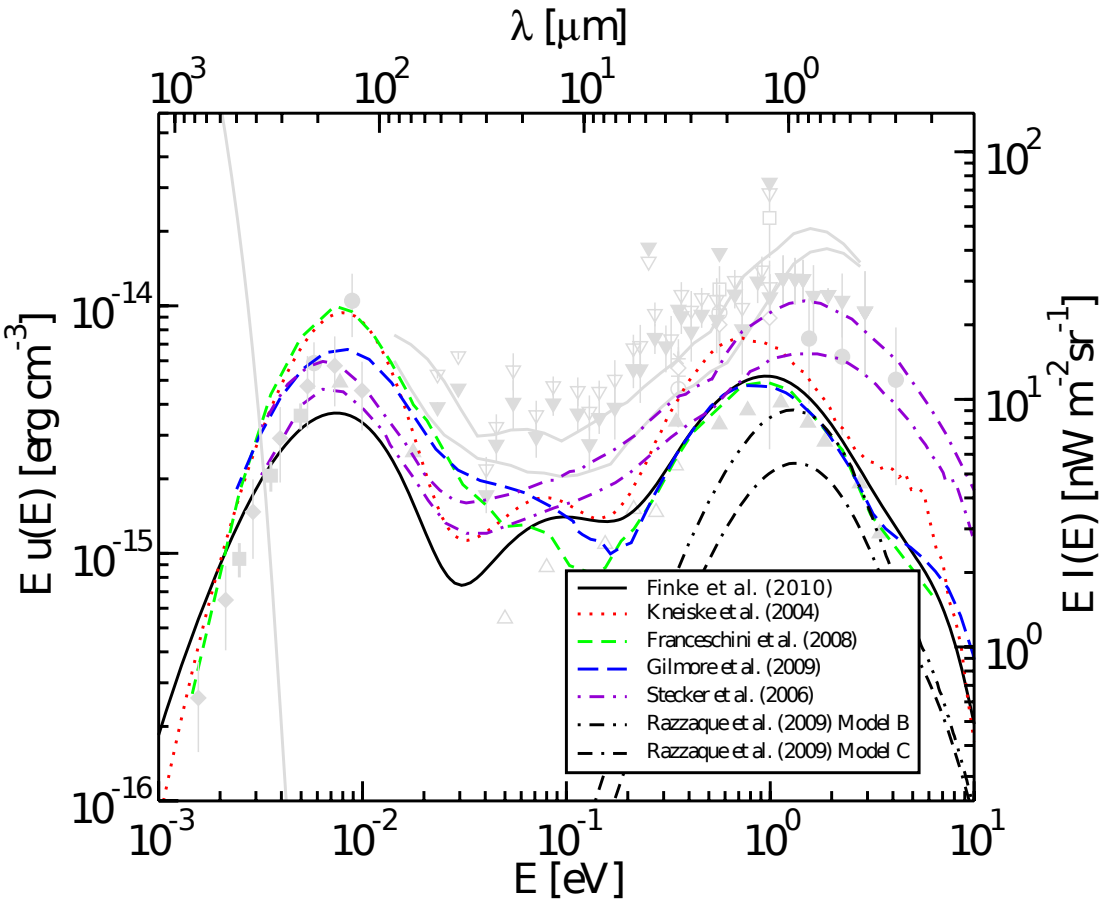

Figure 1.17: Models of the EBL energy density as a function of energy. The models listed are obtained using a variety of methods and are explained in their respective publications: Finke *et al.* (2010), Kneiske *et al.* (2004), Franceschini *et al.* (2008), Gilmore *et al.* (2009), Stecker *et al.* (2006), and Razzaque *et al.* (2009). The light gray points represent measurements or upper limits from experiment and are explained in the caption of Figure 4 of Finke *et al.* (2010) from which this figure is adapted.

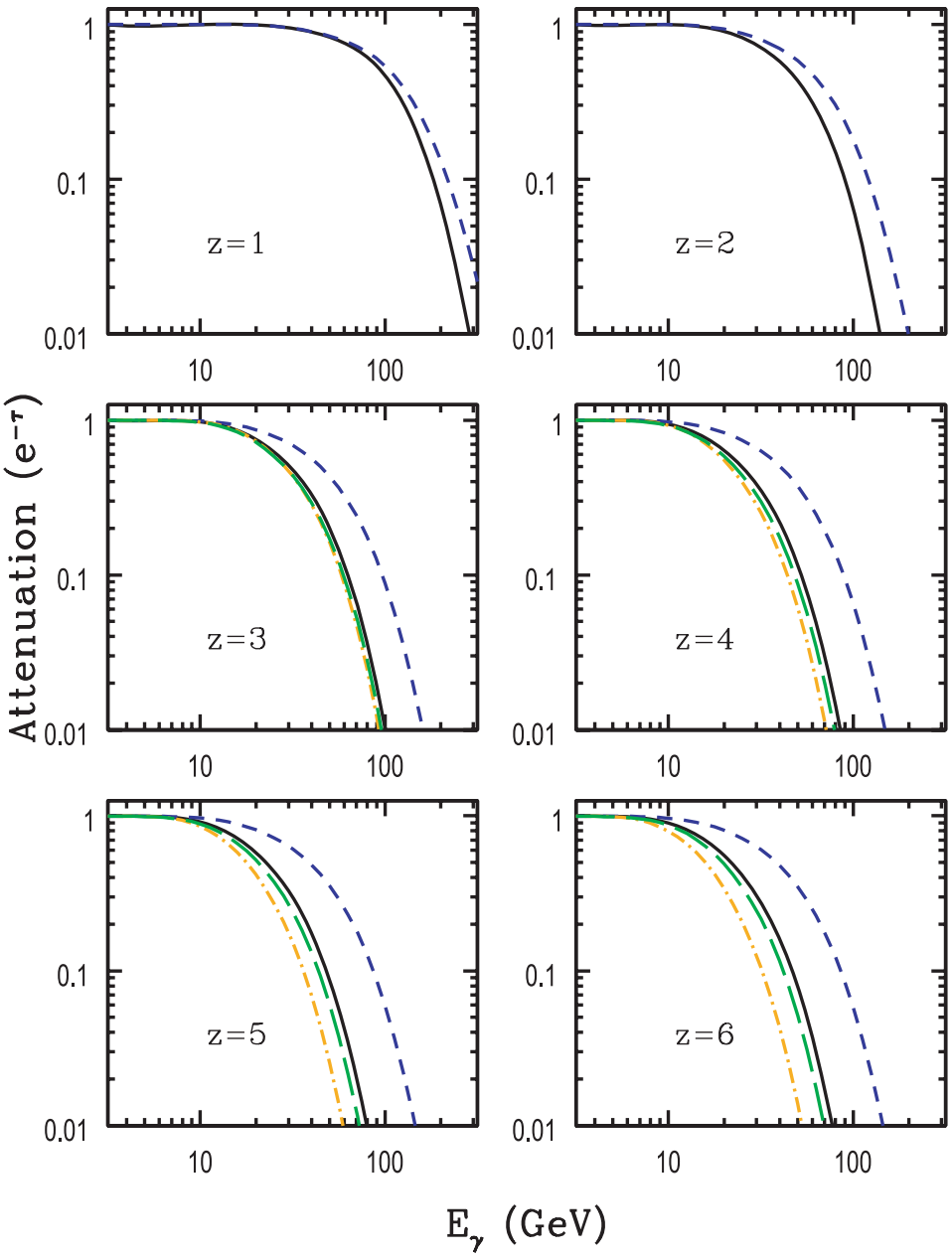

Figure 1.18: The attenuation as a function of gamma-ray energy for sources at a variety of redshifts. The black line represents the fiducial model and is what is used in this work to calculate EBL attenuation of GRBs observed by Milagro and VERITAS. The colored dashed lines represent attenuation from varying some of the model parameters such as the star formation rate and quasar contributions. Explained in detail in Gilmore *et al.* (2009), from which this figure is taken.

$\gamma\gamma \rightarrow e^+e^-$ process through interaction with low-energy photons in the GRB environment. The effect of gamma-ray absorption due to photons from a GRB's binary companion star, the star-forming molecular cloud in which the GRB is likely embedded, and the photon field from the GRB's host galaxy needs also to be considered. Results from Gilmore and Ramirez-Ruiz (2010) show that gamma-ray attenuation due to the first two photon fields (binary companion, molecular cloud) are small and that attenuation due to photons from the host galaxy is also relatively small and may only significantly attenuate GRB spectra at extremely high (> 10 TeV) energies.

Assuming the energy-density of the EBL to be determined (at least in the NIR – UV wavelengths) the absorption of high-energy gamma-rays from distant sources can be computed following the method described in Gould and Schréder (1967). Figure 1.18 shows the attenuation factor as a function of gamma-ray energy at various redshifts using the models of Gilmore *et al.* (2009). As expected, the Universe starts to become very opaque in the > 100 GeV energy range for redshifts larger than ~ 2. The point at which the Universe becomes opaque to gamma rays (optical depth, $\tau = 1$) as a function of energy and redshift is plotted in Figure 1.19. It is discussed in Gilmore *et al.* (2010) how the opacity would affect observations of GRBs with *Fermi* and the MAGIC IACT instrument and it is found that, due to the intrinsic luminosity of GRBs, some may be detectable even out to reasonably high redshifts. This is in agreement with estimates made for the VERITAS IACT array and presented in Chapter 10 and also in Acciari *et al.* (2011).

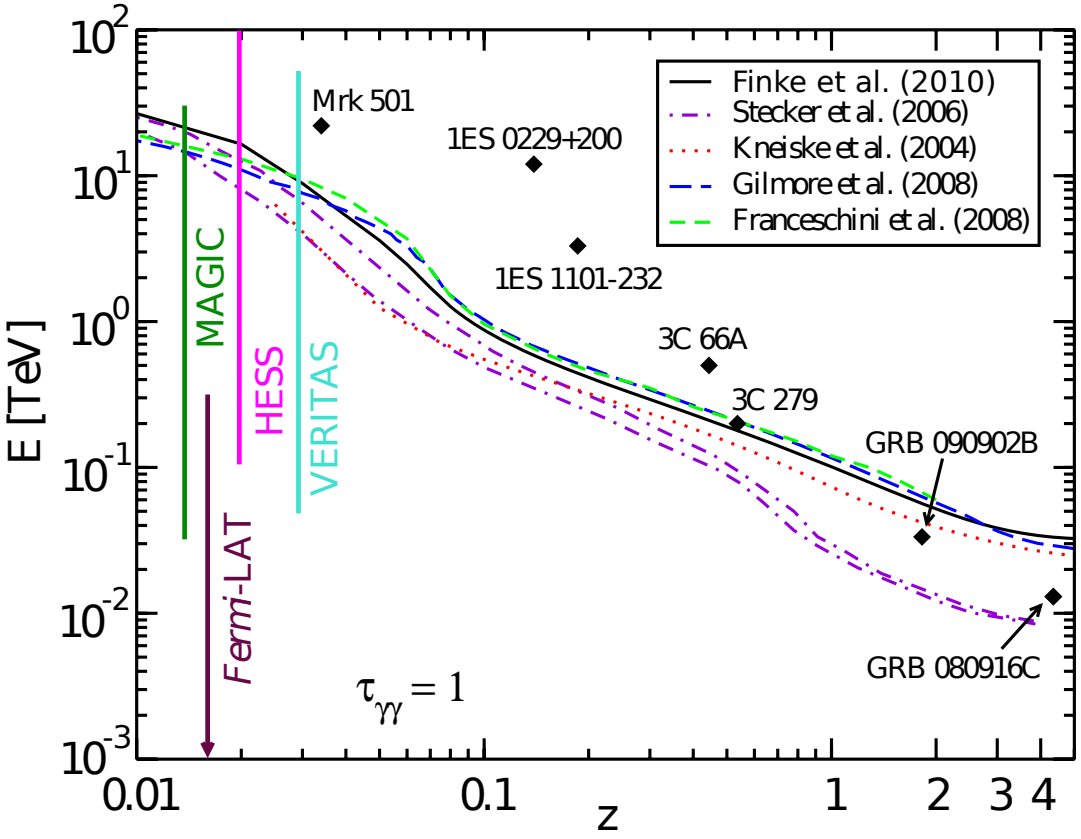

Figure 1.19: The gamma-ray energy and redshift values at which the Universe becomes opaque ($\tau_{\gamma\gamma} = 1$) for a variety of models (see Figure 1.17). Also included are the relevant energy ranges for the *Fermi*-LAT and several IACT instruments as well as the highest measured photon energies and redshifts for number of blazers and GRBs. Figure adapted from Finke *et al.* (2010).

In summary, both the observed and theorized properties of GRBs, make them interesting targets for VHE observations. A VHE detection of a GRB at a typical redshift would place a very substantial constraint on the properties of the EBL. The lack of GRB detections at VHE energies thus far is almost certainly due to instrumental limitations (specifically energy threshold, observation delays and/or FOV sizes). However, the high sensitivity of ground-based gamma-ray observatories make them powerful tools for constraining the emission properties of GRBs at high energies and subsequently the physical processes taking place in the GRB and its surrounding environment. A better understanding the GRB phenomenon will improve our knowledge of the physical processes at energies much higher than can be recreated in even the largest particle accelerators on Earth. Furthermore, it is conceivable that GRBs, once better understood, could be used as cosmological rulers and/or backlights to illuminate the nature of the Universe at extremely large distances and times during which the first gravitationally-bound structures were forming.

1.6 Constraining GRB physics with VHE observations

Results from GRB observations at GeV – TeV energies and above can reveal information about some of the most fundamental characteristics of GRBs and their immediate environment. In addition to constraining overall GRB energetics by quan-

tifying (or limiting) the fraction of the GRB bolometric luminosity at high energies, VHE observations can provide information on the value of the bulk Lorentz factor (Γ) of the GRB outflow, photon opacities and the magnetic field equipartition fraction in the jet as well as the particle density in the circumburst medium. Combining information from contemporaneous lower-energy observations with VHE data can further constrain some of these quantities.

Characterizing the prompt VHE emission from GRBs can provide a measurement of the bulk Lorentz factor (Γ) of the burst outflow. Low values of Γ will result in a high photon opacity ($\gamma\gamma \rightarrow e^+e^-$) in the GRB jet, while high Γ values result in a outflow that is largely transparent to photons up to VHE energies. After taking into account the redshift and variability of the GRB emission, determining the energy and spectrum of the highest-energy photons emitted from GRBs provides a direct measurement of Γ (Baring, 2006), one of the most fundamental quantities in the fireball model (Piran, 1999) of GRBs. Observations of GRBs with Milagro limit the high-energy flux during the prompt phase and so limit Γ.

In addition to Γ, observations of the prompt GRB emission at GeV – TeV energies, coupled with observations of GRBs at classical GRB energies (keV – MeV, around the peak of the Band function) provide a direct measure of the magnetic field equipartition factor (Pe'er and Waxman, 2004). For a magnetic field near equipartition in the GRB outflow, it is predicted that the energy contained in the IC component of the emission spectrum should be comparable to or slightly less than the energy contained in the

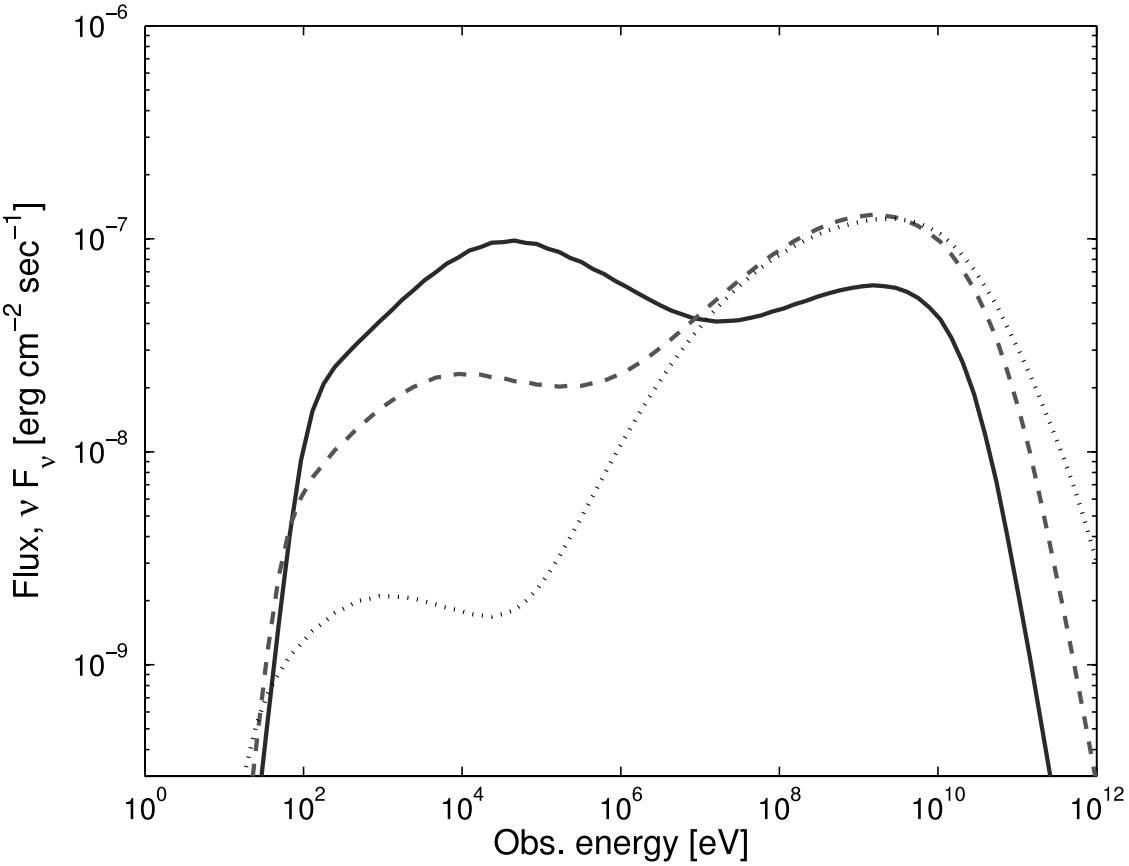

Figure 1.20: The dependence of the prompt GRB spectrum on the fraction of thermal energy carried by the magnetic field (ϵ_B). The solid, dashed, and dotted lines are for ϵ_B=0.33, 0.01, 0.0001, respectively. Figure from Pe'er and Waxman (2004).

synchrotron (keV – MeV) component. However, if the magnetic field is weak, then the synchrotron component will be significantly lower than the IC component (see Figure 1.20). Milagro observations coincident with lower-energy gamma-ray emission by satellites such as *Swift*, directly limit fraction of the GRB jet energy contained in the magnetic field.

While observations during the prompt phase of GRBs shed light on the processes primarily occurring in the relativistic jet (internal shocks), observations of GRBs during their early afterglow phases can be used to understand processes occurring as the GRB interacts with its external environment (external shock), as well as processes that may be associated with late-time internal engine activity such as those thought to be powering X-ray flares. IACT arrays like VERITAS are powerful tools for characterizing emission during the GRB early afterglow due primarily to their high sensitivity relative to both ground-based EAS arrays and satellites.

The spectral characteristics of GRBs at VHE energies during the early afterglow have been shown to directly reflect the conditions of the interstellar medium (ISM) surrounding the GRB progenitor (Pe'er and Waxman, 2005). A significant increase in VHE gamma-ray emission is expected from the forward shock if the jet is propagating into a uniform, low-density medium, as opposed to propagating into a particle wind medium which could be surrounding the GRB progenitor due to mass loss preceding the core collapse (Figure 1.21). Similar considerations to those mentioned previously also indicate that VHE observations during the early afterglow can directly constrain

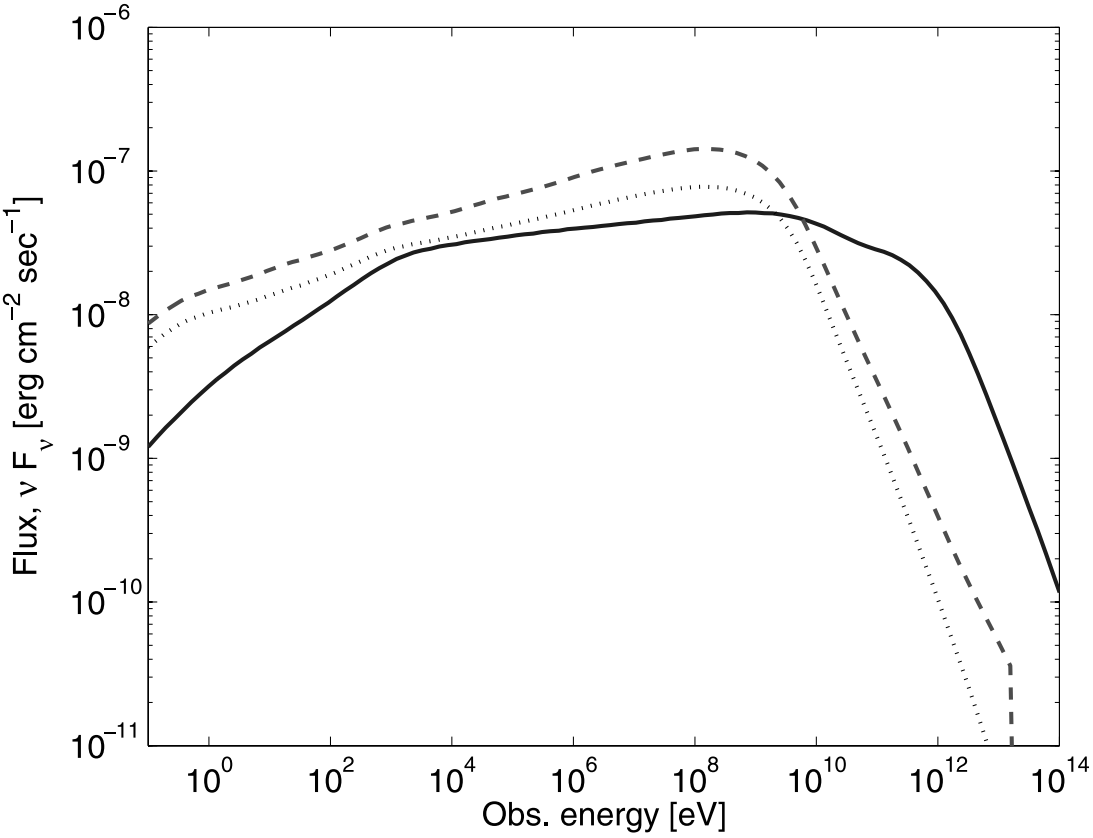

Figure 1.21: Predicted photon spectra during the early afterglow phase for different ISM characteristics. The solid line represents a constant-density ISM ($n = 1$ cm^{-3}), while the dashed and dotted lines represent an explosion into a particle wind including and excluding the proton contribution to the flux, respectively. Figure from Pe'er and Waxman (2005).

the magnetic field equipartition fraction in the explosion. The sensitivity of VERITAS is sufficient to detect the predicted VHE fluxes for several of these scenarios, depending on the conditions under which the GRB observation is made and the redshift of the burst.

As mentioned previously, the *Fermi*-LAT recently detected high energy emission associated with X-ray flaring activity in GRB 100728A (Abdo *et al.*, 2011). This result indicates that the emission is most likely produced by a long-lasting relativistic outflow (Zhang *et al.*, 2006). The *Fermi*-LAT measurement did not conclusively determine whether or not the GeV emission is simply an extension of the synchrotron spectrum up to high energies or if there exists an IC component. VERITAS observations of GRB afterglows concurrent with X-ray flaring activity (as measured by *Swift*) may indicate the high-energy gamma-ray production mechanism responsible for the photons observed by the LAT.

In summary, VHE observations of GRBs during both the prompt and afterglow phases can provide information on some of the most fundamental quantities and processes associated with these events. The Milagro and VERITAS observatories are two of the most sensitive instruments available for measuring the VHE gamma-ray flux from GRBs and the results from observations with these instruments are briefly described in the following section.

1.7 Results of this work

In this work, results from observations of GRBs with the VHE gamma-ray observatories Milagro and VERITAS are presented. GRB observations with both instruments provide no indication of VHE gamma-ray emission from any of the GRBs observed. The results from the Milagro observations are used to limit the gamma-ray fluence in the GeV – TeV energy range during the prompt phase of 115 satellite-detected GRBs. VERITAS, a narrow-field, pointed instrument, is used to perform satellite-triggered follow-up observations of GRBs. These observations are used to constrain the GRB early afterglow emission over several timescales of interest, including intervals optimized to characteristic high-energy afterglow emission as detected by the *Fermi*-LAT as well as time periods coincident with X-ray flares detected by the *Swift* satellite. A brief summary of how the observations from both Milagro and VERITAS are used to constrain GeV – TeV emission from GRBs is presented in this section.

Milagro observed 115 satellite-detected GRBs and using the trigger time and duration (T_{90}) measured by these satellites, limits on the gamma-ray fluence between 1 and 100 GeV are calculated and presented in this work. Many of these limits are not particularly interesting as most emission models predict values of the gamma-ray fluence that fall below the upper limits placed by Milagro. However, in the case of GRB 080319B, Milagro observations are used to directly rule out the most straightforward model, the single-zone SSC model of prompt gamma-ray emission, over a range of energies – a result made possible by the extensive broadband coverage and

unique characteristics of the burst itself. This result is discussed in detail in Section 5.2.

VERITAS performed satellite-triggered follow-up observations on 53 GRBs between January, 2007 and February 2012. In this work, upper limits on the gamma-ray flux from the 28 well-localized (i.e. *Swift*-detected) GRBs are presented. Searches for VHE gamma-ray emission on several timescales during the GRB afterglow are performed. In the case of GRB 080310, a search coincident with a large X-ray flare during the afterglow of the GRB. For many of these bursts a redshift was measured, and using this information, limits on the high-energy emission relative to the prompt gamma-ray flux over the *Swift*-BAT energy range (15 – 350 keV) are calculated and indicate that in at least some cases, the amount of energy released in the VHE band during the early afterglow is constrained to be less than the energy released in the classic GRB energy range (keV – MeV) during the prompt phase. With observation delays on the order of a few hundred seconds, the VERITAS upper limits begin to restrict theoretical models in which SSC processes are expected to produce significant VHE gamma-ray emission from the forward shock.

The results obtained from the VERITAS and Milagro GRB observations comprise one of the most comprehensive searches for VHE gamma-ray emission from GRBs during the afterglow and prompt phases, respectively.

Chapter 2

The Milagro Gamma-Ray Observatory

2.1 Introduction

The Milagro Gamma-Ray Observatory was a large-area, ground-based experiment designed for the indirect detection of VHE photons from astrophysical sources. Constructed at the site of, and using some infrastructure from the former Hot Dry Rock geothermal experiment, Milagro was located in the Jemez Mountains outside of Los Alamos, NM at an elevation of 2600 m above sea level (a.s.l.). The experiment operated almost continuously (total duty cycle of $\sim 95\%$) from 2000 January until it was decommissioned in 2008 May, during which time it surveyed at GeV – TeV energies much of the northern hemisphere.

Milagro is a member of the class of ground-based, high-energy particle detectors referred to extensive air shower (EAS) arrays which operate by the principle of detecting the secondary particles from EASs that are generated by energetic primary particles (including gamma rays) interacting with nuclei high in the Earth's atmosphere.[1] This chapter briefly reviews the physics of EASs and explains how they can be used as a tool to make ground-based gamma ray detection possible. This chapter also describes the Milagro detector, data acquisition systems, standard data analysis methods, and how they are used to do gamma-ray astronomy.

2.2 Extensive Air Showers

For photons of energies above 10 MeV, the predominant mechanism by which they interact with nuclei in the Earth's atmosphere is pair production, $\gamma \rightarrow e^+e^-$. In this process, a photon of sufficient energy is converted to an electron and positron in the electric field of a nucleus which takes up some of the photon's momentum. The leptons produced via pair production by gamma-ray primaries with energies in the GeV – TeV range are highly relativistic and are strongly beamed in the same direction as the parent photon; the angle of emission for these leptonic processes is $\propto m_e c^2/E$ where E is the energy of the particle. These secondary leptons produce high-energy photons via bremsstrahlung which in turn pair-produce and the process continues

[1] The other broad category of ground-based high-energy particle detectors utilize a different, but related method known as the imaging atmospheric Cherenkov technique which is discussed in Section 6.2.

down into the Earth's atmosphere. In this way, a collimated lepton-photon cascade is generated with a longitudinal axis that is co-linear with the primary gamma-ray trajectory and with the number of leptons produced being proportional to primary gamma-ray energy. In addition to the processes described above, many of the charged particles in the shower are moving with velocities greater than the speed of light in the atmosphere. As a result, these particles emit Cherenkov radiation primarily in the UV energy range, which is also strongly beamed in the direction of motion of the relativistic particle.

For photon-induced EASs, the first $e^+ + e^-$ pair is typically produced at an altitude of $10 - 20$ km depending on the primary photon energy. As energy from the primary is partitioned among the secondary particles, the energy per particle decreases until ionization energy losses become dominant, at which point the cascade begins to diminish. The maximum size of the shower, i.e. when radiation and ionization energy losses are equal, occurs between 7 and 12 km a.s.l. Qualitatively, the EAS can be described as a thin (~ 1 m), slightly convex pancake comprised of a core of high-energy particles surrounded by an extended circular sheet of lower-energy particles. The details of the Milagro detector will be discussed in the following section, but in a nutshell it is the Cherenkov light produced by this pancake of particles as it passes through water in the instrument that is used to reconstruct the primary particle direction and energy.

In the energy ranges relevant to VHE gamma-ray astronomers, the gamma-ray-induced EASs are out numbered by charged-particle-induced showers by 3 to 5 orders

of magnitude. The charged particle primaries are largely protons and some He ions though heavier nuclei up to Fe are also present. These hadronic showers are by far the largest background for ground-based VHE gamma-ray instruments and the degree to to which an instrument can distinguish showers produced by gamma-ray primaries from showers initiated by hadronic primaries plays a large part in determining the sensitivity of the instrument. It should be noted that in addition to nucleon and gamma-ray primaries, some showers are produced by high-energy electron primaries. The electron flux at the top of the atmosphere is much lower than the nucleon flux and about the same as the diffuse gamma-ray flux at VHE energies. However, since electrons induce purely electromagnetic cascades just as gamma rays do, they represent an essentially irreducible diffuse background.

Fortunately, there are some significant differences in the shower development between hadronic (proton- and ion-initiated) and leptonic (gamma-ray- and electron-initiated) EASs. One is the shape of the shower. Leptonic showers are relatively compact, both in time and space due to the low mass of the particles involved and the strong relativistic beaming of secondary particles in the electromagnetic interactions. Hadronic showers are much more fragmented as secondary particles from hadronic interactions are emitted at wider angles and produce smaller secondary air showers. This is illustrated by the air shower simulations in Figure 2.1, which shows the difference between a proton-induced and a gamma ray-induced air shower. Another discriminator between hadronic and leptonic showers, particularly for EAS

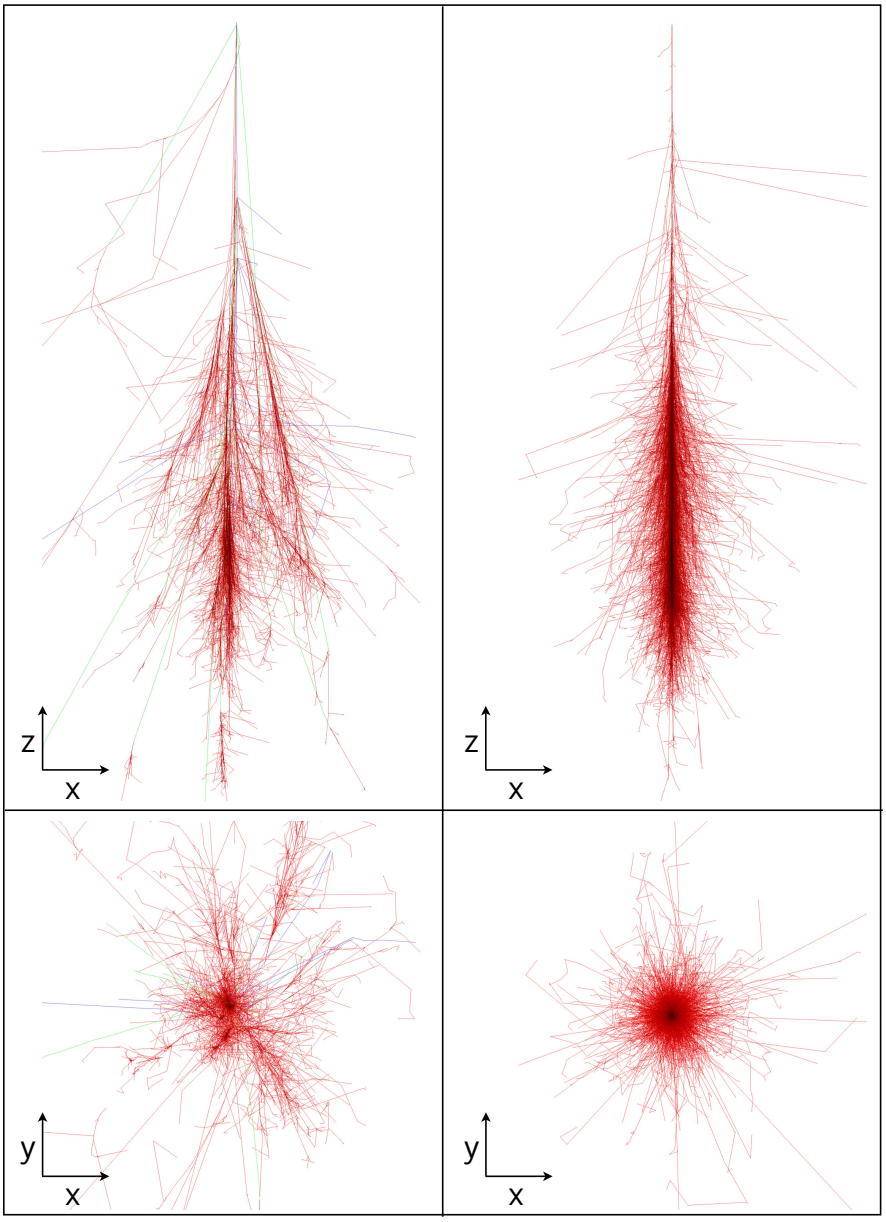

Figure 2.1: Extensive air showers simulated using the CORSIKA Monte Carlo code (Heck *et al.*, 1998). Left: A 100 GeV proton-initiated air shower. Right: a 100 GeV gamma ray-initiated air shower. Red: e^+, e^-, and photons, Green: muons, Blue: hadrons. Color scale is logarithmic. The first interaction height is fixed at 30 km a.s.l. Only leptons and gamma rays above 100 keV and hadrons above 100 MeV are plotted. z scale is 0 – 30 km a.s.l. and x,y scales are ±5 km around the shower core. (Schmidt, 2009)

arrays, is the survival of a larger number of penetrating particles, particularly muons, at ground level in hadronic showers. In hadronic showers, pions, and to a lesser extent high energy particles such as kaons, are produced which decay and produce significant numbers of muons. Muons are extremely penetrating, have a very long lifetime ($\sim 2\mu s$), and reach the Earth's surface (and beyond) in significant numbers after generation by an EAS. Thus the shape, and particle content of EASs can be used to discriminate between hadronic and leptonic initiating particles to a degree that makes ground-based gamma-ray astronomy possible.

2.3 The Milagro Detector and Data-Acquisition System

2.3.1 The Detector

Milagro was a detector that utilized the water-Cherenkov technique. It consisted of large volumes of very pure water instrumented with photomultiplier tubes (PMTs). When the shower front of an EAS passes through the water the relativistic charged particles in the shower produce Cherenkov radiation in the optical and near-UV parts of the spectrum. The PMTs were sensitive to this radiation and these Cherenkov photons were used to reconstruct the properties of the EAS itself and consequently, the primary EAS-initiating particle. The water-Cherenkov technique has an advantage over other EAS detection techniques by virtue of the fact that, in addition to detecting

charged particles in the EAS, secondary gamma rays in the EAS can also be detected as they have very short interaction lengths in water and will convert to e^+e^- pairs which will in turn produce detectable Cherenkov light. Since Milagro was located at an elevation well below shower maximum for virtually all showers, many of the surviving particles in the EAS were secondary gamma rays. The ability of the water to convert this electrically neutral shower component into detectable Cherenkov photons served to significantly reduce the energy threshold below that which would be possible by only measuring the charged particles in the EAS.

The main part of the Milagro detector consisted of a large pool of water dubbed "the pond." The pond was a rectangular frustum 60 m by 80 m at the surface, 30 m by 50 m at the bottom with a depth of 8 m. This pond was formerly a part of the Hot Dry Rock experiment and was subsequently cleaned and lined with black polypropylene for use as part of Milagro. The pond was then filled with $\sim$ 23 million liters of very clean water. Using purified water (and keeping it clean) was important, as impurities would reduce the mean free path of the Cherenkov photons. 723 upward-facing PMTs were anchored to a sand-filled PVC lattice throughout the pond in two layers, both with regular square grid patterns with 2.8 m separation. The top layer of 450 PMTs, called the "air-shower layer" (AS), was located 1.6 m below the surface of the water. The bottom layer of PMTs, referred to as the "muon layer" (Mu) consisted of 273 PMTs located 6 m below the water's surface. The entire pond was covered with a thin (2 mm) light-tight, flexible polypropylene cover which floated on the surface of

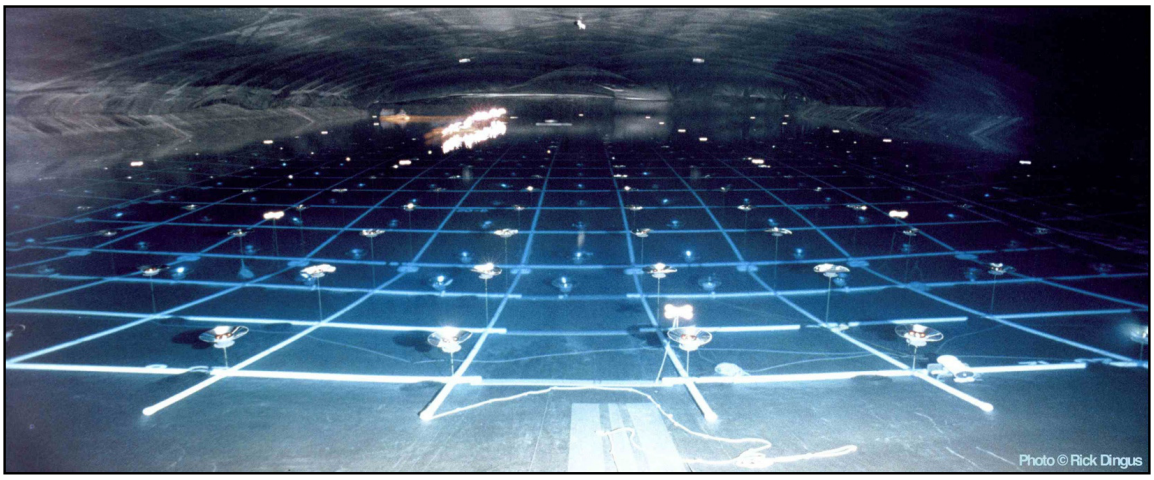

Figure 2.2: A view of the Milagro pond with the light-tight top cover inflated for maintenance and repairs. Clearly visible are the AS layer and Mu layer PMTs and the weighted lattice to which they are anchored.

the water. This cover could be inflated for access to the pond. A view of the pond with the cover inflated can be seen in Figure 2.2.

The AS layer depth was selected to balance the need for gamma ray pair conversion $\gamma \rightarrow e^+e^-$ above the PMTs, while keeping the time dispersion of the Cherenkov light relatively low and the instrumented area large. The spacing between the AS PMTs was dictated by the 41° half-opening angle of the Cherenkov light cone in water, and the minimum number of tubes required to keep the detection efficiency relatively high ($\sim$ 50%). The AS PMT layer is used primarily for timing and triggering purposes. The timing of the shower front gives the EAS major axis azimuthal and inclination angles which enables the reconstruction of the primary particle's direction. The Mu PMT layer was used for background rejection and for calorimetry. Hadron-initiated showers contain a relatively large number of energetic muons which penetrate deep

into the pond. The Mu PMTs could detect the Cherenkov radiation from these muons, but were located deep enough to not detect much light from the electrons and positrons in a non-hadronic EAS. As a result, the light detected in the Mu layer PMTs can be used to discriminate between hadron and lepton/photon generated EASs.

The Milagro pond was later surrounded by an array of 175, PMT-instrumented water tanks known as the "outrigger" array. Each outrigger tank was 2.4 m in diameter and 1 m high, filled with 2200 liters of purified water, and contained a single downward-facing PMT. Pictures of an outrigger tank, and the distribution of tanks around the Milagro pond can be seen in Figure 2.3. The outrigger array increased the physical area of Milagro dramatically, from 4800 m^2 to $\sim 40,000$ m^2. The increased area improved the sensitivity of Milagro by enabling a better determination of the shower core location for events when the core was located off the pond. To accurately reconstruct the direction of the EAS, timing corrections for the slight curvature of the shower front need to be made and these corrections depend strongly on the location of the shower core. The addition of the outriggers greatly improved the determination of the off-pond shower core locations which was particularly important since showers which had cores located off of the pond accounted for the vast majority of triggered events in the experiment. Furthermore, the background rejection for showers landing off of the pond was significantly better than for those showers landing on the pond because determining the muon content of showers far from the shower core (using the Mu layer PMTs in the pond) is a very good discriminator of hadron-initiated vs.

Figure 2.3: Left: A cut-away view of one of the Milagro outrigger tanks partially emptied of water but with the PMT still mounted inside. Right: An overhead view of the Milagro Observatory. The covered pond is in the center and the locations of the outrigger tanks marked in red.

gamma/lepton-initiated showers.

The tubes themselves were large (8" photocathode diameter) hemispherical Hamamatsu model #R5912SEL PMTs. Each was attached to a PMT base which was surrounded by a water-tight PVC enclosure. Each PMT was connected to the readout electronics in the counting house adjacent to the pond through a single RG-59 coaxial cable which carried both the power to, and the signal from the PMT. The PMT signal was extracted via capacitive coupling by the analog front-end electronics boards (FEBs). Each tube was surrounded by a conical baffle made of reflective polypropylene. The baffles served both to increase the light-collection of each PMT and, more importantly, to block unwanted scattered or reflected light. This reduced the number of noise triggers and also narrowed the PMT hit time distribution, increasing the angular resolution of the instrument.

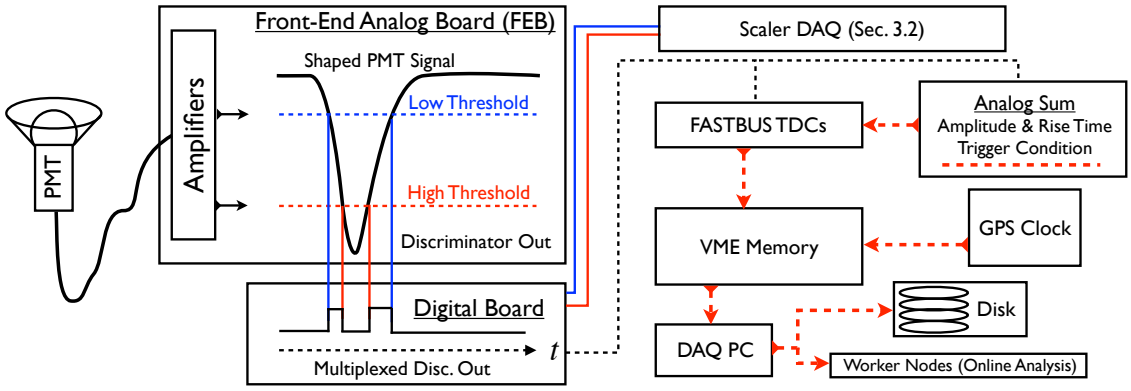

Figure 2.4: A simplified schematic of the Milagro standard DAQ pipeline

2.3.2 Data Acquisition System

During operation, Milagro ran two independent data acquisition (DAQ) pipelines: the standard DAQ and the scaler DAQ. The standard DAQ facilitated the triggering of the instrument on air showers along with the associated readout and transfer of data to the online analysis which was responsible for shower reconstruction. The scaler DAQ monitored the count rates of all of the PMTs in the experiment at a frequency of 1 Hz. A brief description of the standard DAQ system follows, while a detailed description of the scaler DAQ can be found in Section 3.2.

In both the standard air-shower and scaler DAQ pipelines the first step is the amplification and integration of the raw PMT pulses into a single shaped pulse some tens of ns wide. This amplitude of this shaped pulse is then compared to each of two discriminators: the low threshold corresponding to ~ 0.25 photoelectrons (pe) and the high threshold corresponding to ~ 5 pe. The time of each of the edges from the two discriminator outputs on the FEB are sent to a digital board, multiplexed, and

then passed to LeCroy FASTBUS time-to-digital converters (TDCs), where the time of each edge was recorded. All of this was done in parallel for each PMT. In addition to the multiplexing of the discriminator signals, the digital board also generated a 180 ns square pulse which was sent to an analog sum trigger. The details of the trigger condition are omitted here but a combination of the number of PMTs whose shaped signal crossed the discriminator thresholds and the proximity in time of these crossings, caused the experiment to trigger.

When a trigger occured, data acquisition was briefly stopped while the TDCs were read out for times within 1.5 μs of the trigger. This was recorded to VME memory along with the GPS time stamp of the event. This information was then sent to a PC which in turn gave the information to worker nodes that performed the online event reconstruction. The results from the online reconstruction were sent back to the DAQ PC which then recorded this information to disk. A simplified schematic of the standard DAQ is shown in Figure 2.4.

2.4 Standard Methods of Signal Reconstruction and Background Rejection

This section briefly describes the online event reconstruction as well as standard methods of data analysis for triggered air-shower events with Milagro. The details of these methods are quite complex and the reader is referred to Vasileiou (2008) for a

more complete description.

The raw data generated by Milagro amounted to ~ 250 GB each day. At the time this amount of data was impractical to store so real-time data reduction was done by worker nodes connected to the DAQ PC. This online analysis took the edge-timing information for all of the PMTs and used it to reconstruct properties of the shower event as a whole. In addition to the timing information, the light intensity detected by each PMT can be determined by calculating the time over threshold (TOT) of the shaped pulse, as the size of this pulse is directly correlated with the number of Cherenkov photons incident on the PMT photocathode.

Using the intensities from the all of the PMTs, the location of the shower core on the ground was determined. Sampling corrections based on PMT TOT and timing corrections for the curvature of the shower plane were made based on each PMT's distance from the shower core. From the PMT timing information and the calculated location of the shower core, the shower plane, and consequently the direction of the initial particle was fit. The last step of the online analysis consisted of calculating some gamma/hadron discrimination parameters. All event-based information from the online analysis was then saved to disk – at a much more manageable rate of 4 GB/day.

With the shower event-by-event information from the online analysis, searches for excess gamma-ray signals above background could be pursued. After cutting based on gamma/hadron discriminators, gamma-like events in an appropriate signal region

were counted. A suitable background region was defined and used to accumulate background gamma-like events. A statistical test of the significance of the number of signal events vs. background events determined whether a source is considered to be detected. For gamma-ray astronomy the value for detection is generally considered to be a signal that is 5 standard deviations (σ) above the background. Transient gamma-ray sources such as GRBs can be searched for using the standard shower event reconstruction method. These searches can be either triggered, when a detection by another instrument determines the putative location and time of the event (e.g. (Atkins *et al.*, 2005)), or untriggered, where significant gamma-ray excesses are searched for over the entire sky and various time windows (e.g. (Morales, 2002, Vasileiou, 2008)). Simulations of the detector response to air showers generated by primary particles of various species and energies are then used to translate the information on signal and background counts into information on the incident photon flux and spectrum.

Chapter 3

The Single-Particle (Scaler) Analysis Technique

3.1 Introduction & Application to Milagro

Alongside the standard shower-reconstruction DAQ and analysis methods used in Milagro, there was a parallel DAQ and associated analysis methods for measuring the singles' rates of the Milagro PMTs – the so-called scaler technique (Aglietta *et al.*, 1996, Morello *et al.*, 1984, Obrien and Porter, 1976, Vernetto, 2000). The essence of this method was to search for increases in the PMT rates above background fluctuations, which would be an indicator of an increased number of relativistic particles passing through the water volumes in the detector. For EAS-generating primary particles with energies above ~ 1 GeV, a small number of secondary particles from the

air shower would propagate down to the altitude of Milagro. Though the size of these low-energy air showers was much too small to trigger the detector, a sufficient flux of these primary GeV particles generated a notable increase in the count rate of the Milagro PMTs.

There were two inherent limitations to the scaler technique: no directional reconstruction and the inability of the method to detect steady sources. Since the scaler data contains little-to-no information on the individual air showers responsible for the increased PMT count rates, directional information about the primary particles is lost. The nature of the scaler analysis, a search for rate fluctuations, clearly made the method sensitive only to transient events. The primary benefit of the scaler analysis was that it significantly increased the sensitivity of Milagro to low-energy primary particles. Figure 3.1 shows the effective area, as a function of energy, of both the triggered air shower and scaler techniques. While the scaler effective area is much larger over all energies, the important aspect of the scaler technique was that the effective area remains quite high even down to low energies where the triggered air shower effective area became negligible.

This low-energy sensitivity was important for inherently lower-energy transient astrophysical phenomena such as solar flares, magnetar outbursts, etc., but also for inherently high-energy transient events that take place at cosmological distances – e.g. GRBs and AGN flares. As discussed in Section 1.5, the highest-energy gamma rays from sources at great distances, such as GRBs, are attenuated due to pair production

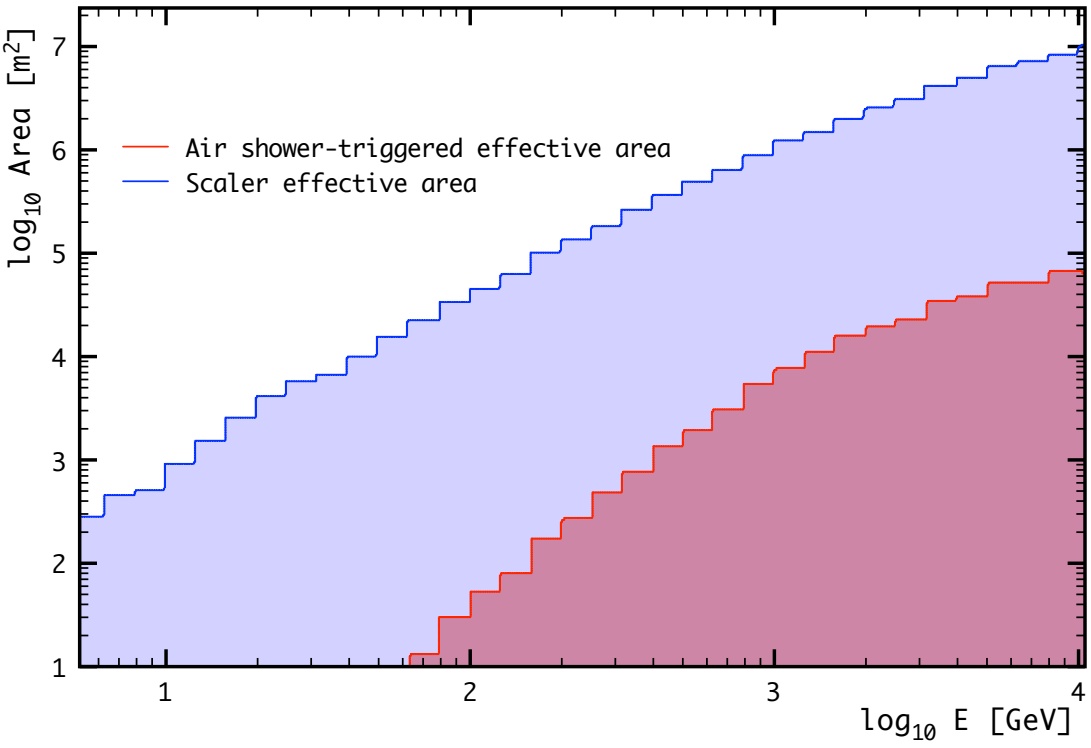

Figure 3.1: The Milagro triggered and scaler gamma-ray effective areas plotted as a function of energy. Both effective areas asymptotically approach a constant at high energies and are essentially flat above the maximum energy shown here. This is because the area on the ground covered by gamma ray-induced air showers is approximately independent of the primary gamma-ray energy and all showers at these energies are bright enough to be detected by Milagro.

with the EBL, thus making the low-energy sensitivity improvement offered by the scaler technique important when observing these objects. Furthermore, the high duty-cycle and large fields of view of EAS arrays like Milagro greatly improve the chances of transient source detection compared to alternative ground-based gamma-ray experiments.

The Milagro scaler system provided a largely independent and complementary source of data on transient events to the standard triggered operating mode. In addition to the science capabilities, the scaler system could be used for diagnostic purposes. Since it routinely monitored counting rates of all PMTs in the experiment, it could be used to identify dead or otherwise malfunctioning phototubes. In the rest of this chapter, the scaler DAQ system is described as are the methods used to reduce and analyze the scaler data for a transient event search.

3.2 The Scaler Data Acquisition System

In the scaler system, the first part of the data acquisition process was the same as that of the standard triggered process. Sixteen PMTs were attached to each front-end analog board which integrated pulses of the PMTs to create a shaped pulse. The low- and high-threshold discriminator crossing times of these shaped pulses were then sent to the digital front-end board (see Figure 2.4). At this point, the scaler and standard DAQ processes diverged. From every digital front-end board (DFEB, each of which handles sixteen PMTs) there were three types of scaler-specific output: low-threshold,

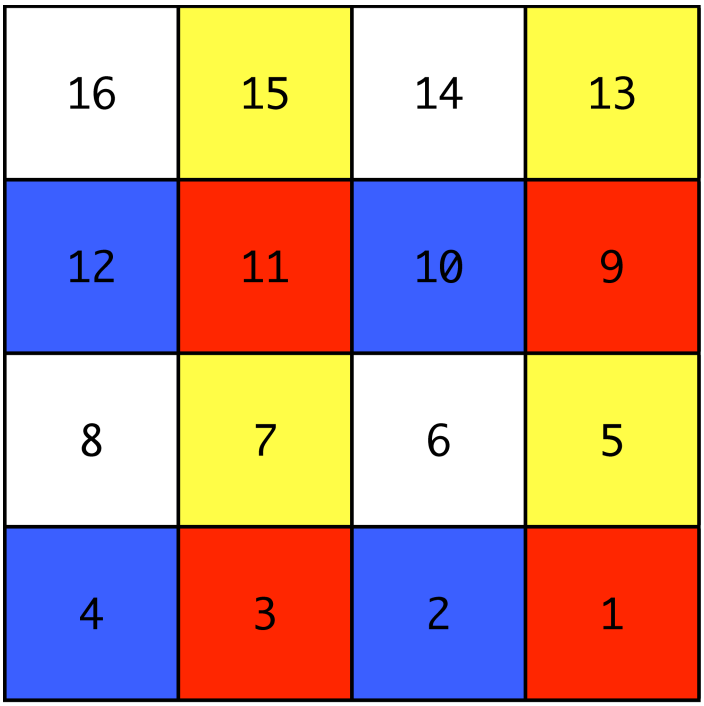

Figure 3.2: The PMT layout for a representative group of 16 tubes sharing the same front-end board. The colors indicate the four-fold logical-OR combination of the low-threshold DFEB output. The high-threshold output was simply a logical-OR of all 16 PMTs in the group. A diagram of how the outputs were combined and connected to the CAMAC scalers can be found in Figure 3.3.

high-threshold, and mask.

The sixteen PMTs connected to a single DFEB were selected such that they formed a four by four array of nearest-neighbors[1]. There were four low-threshold outputs on each DFEB, each of which consisted of four hardwired, logically OR-combined PMT discriminator signals from four non-adjacent PMTs in the group of sixteen. The layout and combination of PMTs for an arbitrary group of sixteen can be seen in Figure 3.2. The DFEB could determine separate counts from a logically-OR'd group

[1]At the edge of the pond and in the outrigger array this pattern could not always be followed exactly.

of PMTs only if the counts were at least $\sim$ 30 ns apart. If two tubes in the same OR-group were hit within 30 ns of one another, only 1 count would register in the output. In light of this limitation, maximizing the number of counts from a single particle triggering neighboring tubes required connecting the PMTs so that nearest neighbors were not in the same OR-group. Jumpers on the DFEB allowed for the four low-threshold outputs to be OR-combined further to reduce the overall number of scaler channels needed. For the AS PMT layer in Milagro, two of the four low-threshold outputs were OR-combined, giving eight non-neighboring PMTs per scaler channel. For both the Mu PMT layer and the PMTs in the outrigger array, all four low-threshold outputs on the DFEB were combined, resulting in sixteen neighboring PMTs per scaler channel. A diagram of the scaler connections is shown in Figure 3.3.

The high-threshold output from each DFEB was a logical OR of all of the high-threshold discriminator outputs in the 16-PMT group. For the high-threshold events, the DFEB minimum event separation was significantly longer – around 50 ns. The sixth output from the DFEB was the mask output. This output consisted of a logical OR of low-threshold counts from al 16 PMTs in a group, along with a programmable bit mask used to set which tubes are included. During normal operation, this masked output was used to record the low-threshold rate of one PMT in the group. After every readout of the scaler (which occurred once a second), the bit mask is changed to record the rate from the next tube in the group. In this fashion the rate from each individual tube in the experiment was recorded for one second, every sixteen seconds.

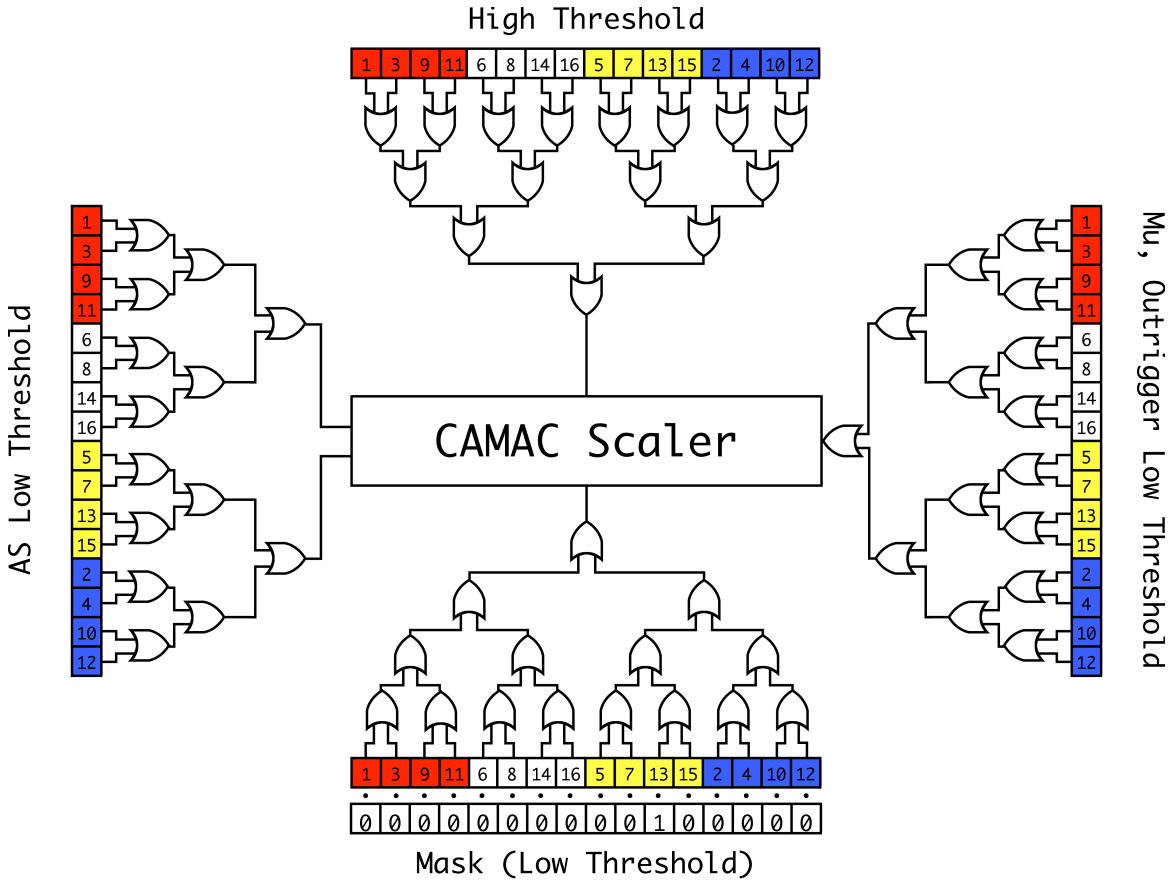

Figure 3.3: A diagram of the connections between the DFEB and the CAMAC scalers. The colored boxes represent the discriminator output from each PMT and their relative location in the group of sixteen PMTs sharing a front-end board (see Figure 3.2). The low-threshold output is combined into either 8 (AS) or 16 (Mu, Outrigger) PMTs per channel, while the high-threshold output contains all 16 OR-combined PMTs per scaler channel. The masked output was normally set to measure the rate from one PMT in the group at a time.

In addition to counting the PMT rates, there were also scalers used for monitoring trigger rates. One scaler counted the number of times the multiplicity requirement for a trigger was satisfied[2], while another scaler counted the number of times the TDCs were actually read out. This allows for the calculation of the live time of the experiment.

The scaler DAQ PC initiated the readout of the CAMAC scalers about once every second. Due to process scheduling on the PC, the readout interval was not exactly every second so in order to correct for this, a 10 MHz reference counter from the GPS clock was read concurrently with the scalers. During the readout, all scalers were stopped, each scaler was read and cleared, and then all scalers were instructed to resume counting again. Once the scaler data had been read out to the computer, it was compressed and stored to disk. The scaler data rate was a quite reasonable ~ 40 MB per day.

3.3 Improved Sensitivity and Data Cleaning

Once the raw scaler data had been collected and stored it was, in principle, possible to directly analyze the data to search for significant increases in rates that may have indicated that presence of a gamma ray signal from astrophysical source. In practice however, the deviations of the PMT count rate in Milagro were very strongly

[2]In the beginning of the Milagro experiment, a simple multiplicity trigger was used. This was later changed to a more sophisticated method which took into account the relative time of PMT hits in addition to the total number of hits.

correlated to instrumental and environmental effects. Such rate fluctuations were the largest background in the scaler analysis method and reducing the correlation between PMT rates and instrumental and environmental factors was the key to increasing the sensitivity of the analysis. This section describes the methods used to increase the sensitivity of the scaler analysis by reducing the correlation of PMT rates with environmental factors and by removing certain groups of PMTs that degraded sensitivity from the analysis.

3.3.1 Reducing Instrumental Effects

As was expected, with 730 PMTs operating continuously, underwater, and with limited maintenance, the failure rate was bound to be non-zero over the > 8 year lifespan of the Milagro observatory. The most common reason for PMT failure was water entering into the PMT housing. This problem was more prevalent during the early part of the experiment and mitigating steps were taken to prevent this as tubes were repaired and replaced. Nevertheless, at any time, several PMTs throughout the experiment were inoperative. Such a situation was easily dealt with since the search algorithms were not impacted by tubes with zero counts. The inoperative tubes did decrease the sensitivity of the instrument, however, and had to be taken into account when computing fluxes and upper limits (as is described in Section 4.3).

More problematic were PMTs that displayed highly erratic rates due to water shorting the circuitry in the PMT base or inherent problems with the PMT itself.

While the erratic rates were not sufficient to mimic a signal, such behavior could mask a weak excess of counting rates in the experiment. Figure 3.4 illustrates an instance of this behavior. Since the PMTs were not obviously dead, an automated algorithm was developed to exclude these PMTs from the scaler analysis before the search for transient count rate fluctuations was attempted. The sensitivity of the scaler method was largely determined by the stability the background counting rate. A measure of a PMT's stability was the root-mean-square (RMS) of its count rate over the time period of interest. The RMS is inversely proportional to the sensitivity of the PMT to real (i.e. not noise) fluctuations. The automated algorithm determined which PMTs had RMS's high enough that they increased the RMS (reduced the sensitivity) of the entire experiment and marked these for exclusion from the scaler analysis. The method is described below. Note, that since several PMTs were OR-combined into a single scaler channel, this exclusion could only be done on a group-by-group basis, that is removing 8 (AS low threshold) or 16 (AS high, Mu, Outrigger) PMTs at a time.

For each OR-group, the RMS of the average count rate was determined over a period of time[3] The RMS is defined as:

$$\text{RMS} = \sqrt{\langle r^2 \rangle - \langle r \rangle^2} \quad \text{where} \quad r = \frac{1}{n} \sum_{i=0}^{n} \frac{r_i}{t_i} \tag{3.1}$$

[3]This period of time was dependent on the signal interval of interest, and was chosen to sufficiently reduce background fluctuations. Details can be found in Section 3.4.

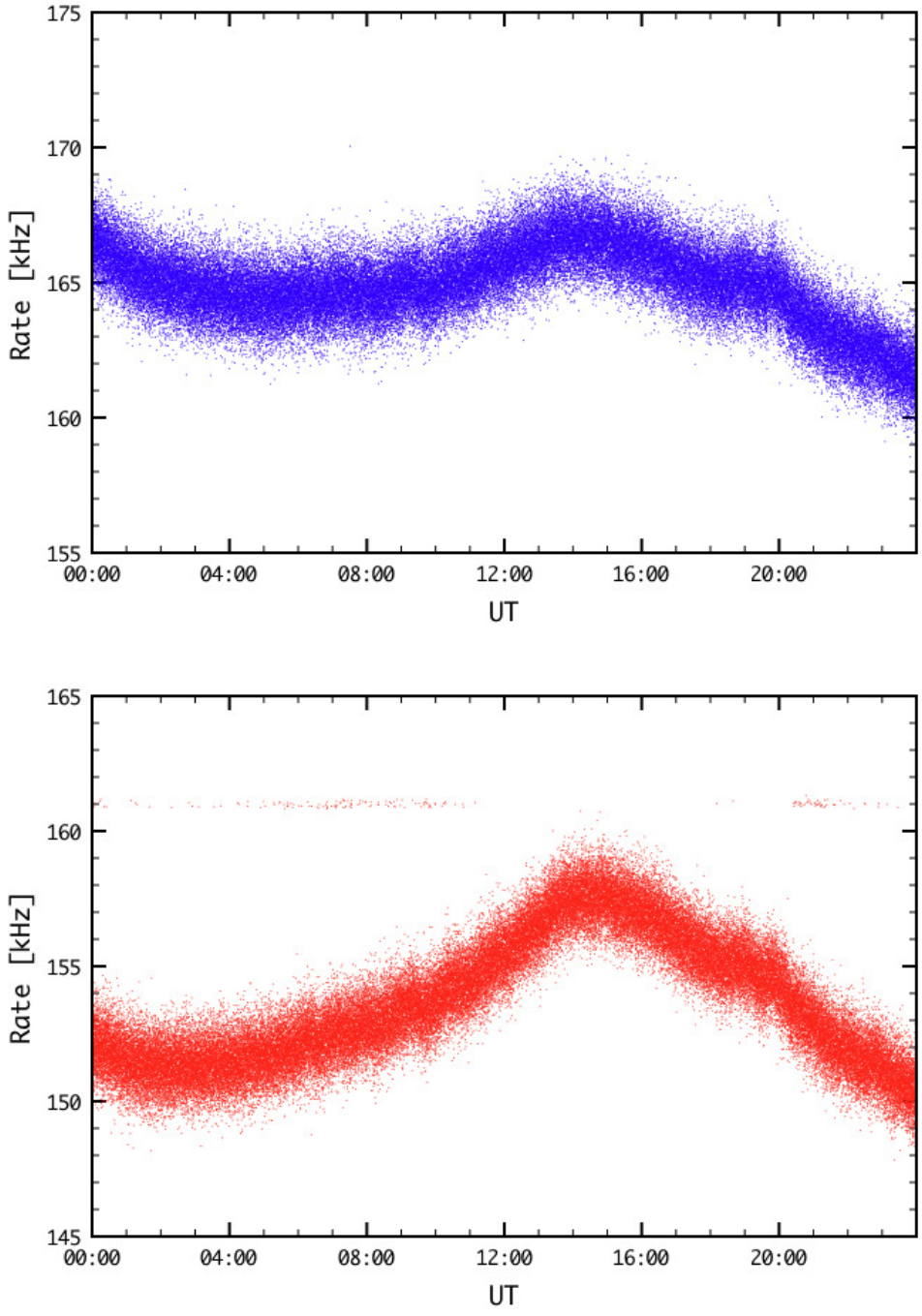

Figure 3.4: *Top:* Raw scaler rate from a functioning OR-group over the course of a day. *Bottom:* Raw scaler rate from an OR-group with one or more malfunctioning PMTs as is evident by the 161 kHz noise. Such an OR-group would be removed from the scaler analysis.

n being the number of times the scalers were read during the time interval specified, r_i the value of the scaler at that reading, and t_i the time over which the scaler had been counting. t_i was very close to 1 s, but small deviations due to hardware limitations (see Section 3.2) had to be taken into account. The next step was to determine the average RMS of all of the OR-groups in the array. Here, array refers to one physical PMT array (e.g. AS) and one threshold level (low or high). Finally the maximum acceptable RMS was determined by calculating, from the OR-groups in the sample, the RMS of any individual OR-group which increases RMS of the array as a whole. This RMS threshold was given by:

$$\mathrm{RMS}_{\mathrm{max}} = \sqrt{\left[2 - \frac{1}{n_{\mathrm{OR}}}\right] \overline{\mathrm{RMS}^2}} \tag{3.2}$$

where n_{OR} was the number of OR groups in the array and $\overline{\mathrm{RMS}^2}$ was the average of the sum of the squares of all of the OR groups in the same array. Any OR-groups with an RMS greater than $\mathrm{RMS}_{\mathrm{max}}$ were then excluded from the scaler analysis. A new determination of $\mathrm{RMS}_{\mathrm{max}}$ from this smaller sample of OR-goups was made and the OR-groups which had an RMS above the limit were again discarded. This procedure continued until the first iteration where no OR-groups are discarded. The remaining OR-groups made up the most sensitive combination possible and the scaler analysis was performed based on data from only these OR-groups. The effect of this procedure can be seen in Figure 3.5.

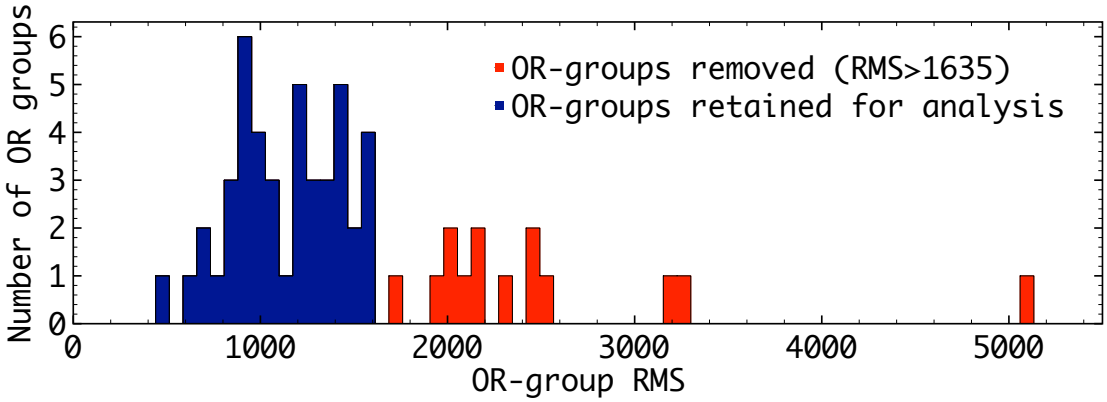

Figure 3.5: The removal of noisy PMT OR-groups based on a automated procedure for maximizing of array sensitivity. The blue histogram represents the subset of OR-groups which comprise the most-sensitive combination for this particular event.

3.3.2 Correcting for Environmental Conditions

As mentioned in the previous section, the sensitivity of the scaler analysis is directly related the stability of the background count rates. While instrumental effects account for some of the variations in the scaler rates, the environment, specifically pressure and temperature, also have a substantial influence. Milagro had several sensors to monitor and record various environmental conditions in and around the experiment. These included the outside temperature, outside pressure, counting house temperature and the temperatures of the digital and analog FEBs for all of the PMT arrays. The exact sampling period for these measurements varied based on what quantity was being measured, but was about 1 minute. Using the information from these measurements, the scaler count rate could be corrected for environmental fluctuations. The procedure is described below.

In practice, it was found that the outside temperature and outside pressure had the largest effect on the scaler rates. For similar reasons to those described in the previous subsection, the goal was again to minimize the RMS of the scaler rates, only in this case using linear corrections to the scaler rates based on measured environmental quantities. The corrected rate for a given measurement, $\hat{r}_i$ is the raw rate, r_i, modified by linear terms dependent on the measured environmental value(s):

$$\hat{r} = \sum_i^n \hat{r_i} = \sum_i^n r_i + c_1(x_{i,1} - \bar{x}_1) + c_2(x_{i,2} - \bar{x}_2) + \cdots \tag{3.3}$$

where the c's describe the dependence of the rate on the corresponding measured environmental quantity (x_i's) and $\bar{x}_j = \frac{1}{n}\sum_i^n x_{i,j}$ is the average of the environmental quantity over the period begin analyzed. The $\bar{x}$'s are not strictly necessary for the correction procedure but serve to keep the absolute normalization of the rate constant. To minimize the corrected rates, the RMS of the corrected rates,

$$\widehat{RMS} = \sqrt{\langle \hat{r}^2 \rangle - \langle \hat{r} \rangle^2} \tag{3.4}$$

or, equivalently $\widehat{RMS}^2$ was minimized as a function of the correction factors (c's):

$$\frac{d}{dc_1}\widehat{RMS}^2 = 0; \quad \frac{d}{dc_2}\widehat{RMS}^2 = 0; \cdots \tag{3.5}$$

This gave a set of equations that can be solved for the c's which minimize the RMS

of the corrected rate:

$$\begin{bmatrix} \sum_i^n x_{i,1}^2 - \frac{1}{n}(\sum_i^n x_{i,1})^2 & \sum_i^n x_{i,1}x_{i,2} - \frac{1}{n}\sum_i^n x_{i,1}\sum_i^n x_{i,2} & \cdots \\ \sum_i^n x_{i,1}x_{i,2} - \frac{1}{n}\sum_i^n x_{i,1}\sum_i^n x_{i,2} & \sum_i^n x_{i,2}^2 - \frac{1}{n}(\sum_i^n x_{i,2})^2 & \cdots \\ \vdots & \vdots & \ddots \end{bmatrix} \begin{bmatrix} c_1 \\ c_2 \\ \vdots \end{bmatrix}$$
$$= \begin{bmatrix} \frac{1}{n}\sum_i^n r_i \sum_i^n x_{i,1} - \sum_i^n r_i x_{i,1} \\ \frac{1}{n}\sum_i^n r_i \sum_i^n x_{i,2} - \sum_i^n r_i x_{i,2} \\ \vdots \end{bmatrix} \quad (3.6)$$

This system of equations can be solved for any number of correction factors, i.e. measured environmental quantities. Notice that the equations above have no dependence on the $\bar{x}$'s, however, including them in Equation 3.3 ensures that the average of the corrected scaler rates is equal to the average of the raw scaler rates.

Figure 3.6 illustrates the results from correcting for pressure and temperature on the scaler rates. It can be seen that the long-term fluctuations in the rates are strongly suppressed by these corrections. The RMS of the corrected rate in this example is reduced by $\sim 80\%$. Correcting for shorter-term temperature fluctuations inside the counting house was also studied, but it was found that correcting for these fluctuations had much less of an impact on reducing the RMS of the corrected scaler rates. Unfortunately, it is likely that the short-term fluctuations play the most important part in reducing sensitivity for short-term events (such as GRBs) and it would be desirable to reduce this effect of these fluctuations. For the results

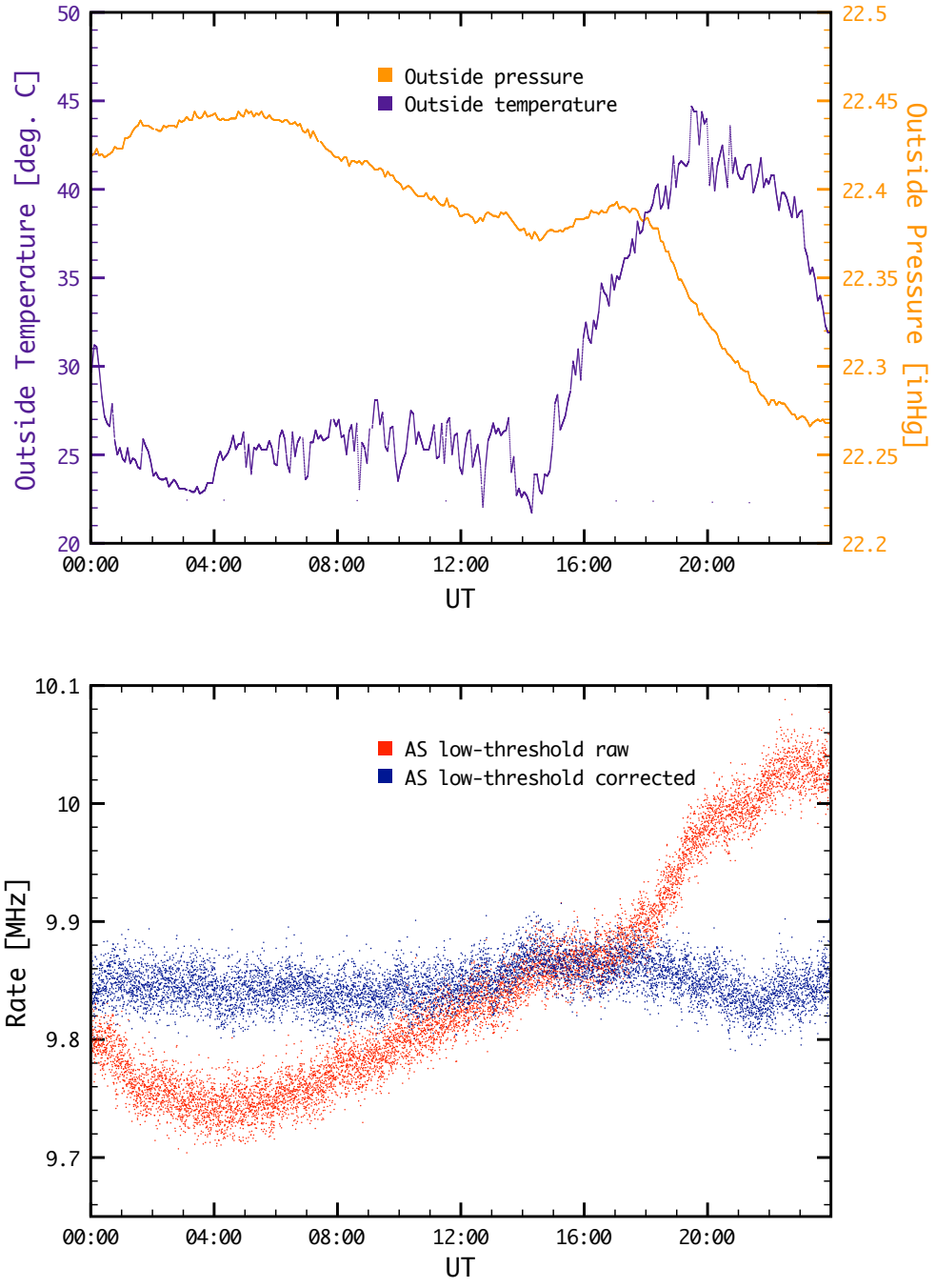

Figure 3.6: Plots showing the effect of environmental corrections on the raw scaler data (red). *Top:* The measured outside temperatures and pressures over the course of 4 July, 2006. *Bottom:* Raw and corrected scaler rates from the AS low-threshold array. Corrections were made based on the above temperature and pressure measurements.

discussed in the following section and chapter, corrections on the outside temperature and pressure were made on all scaler data analyzed.

3.4 Determining the Statistical Significance of Rate Fluctuations in the Presence of Systematic Effects

The overall purpose of the scaler analysis in the context of the work to be presented here was to determine whether or not there was a significant increase of high-energy particles passing through the Milagro detector coincident with an astrophysical event. To claim a detection, a positive statistical fluctuation of five standard deviations (σ) above background region count rates must be observed in the signal region of the data. This corresponds to a 0.00006 %, or $\sim 1/2000000$ chance of a false detection, and is the standard confidence level required for a detection in particle astrophysics. The first step is to define a signal region, which in principle can be any duration > 1 s, which is due to the limitations of the scaler data. Next a suitable background region must be chosen. The background region should be large enough to include sufficient statistics on the background rates, but not so large that it begins to encompass fluctuations in the background that have little to no effect on the signal region. In practice, the background region was defined to be ten times the duration of the signal region, centered, but not including the signal region (see Figure 3.7).

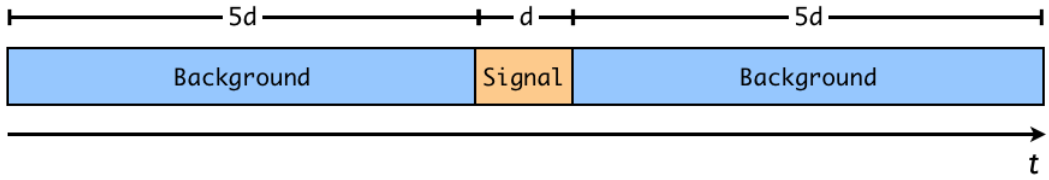

Figure 3.7: Orientation and durations of the background regions relative to the signal region for a transient analysis.

To determine the significance of the scaler count rate in the signal interval relative to the scaler count rate in the background interval, first the RMS of each region is calculated:

$$\mathrm{RMS}_x = \sqrt{\left[\frac{\sum_i^n r_{x,i}^2}{n} - \frac{\left(\sum_i^n r_{x,i}\right)^2}{n}\right]\frac{n}{n-1}} \tag{3.7}$$

where n is the number of times the scalers were readout in the interval of interest. From the RMS of each region, the significance of the signal region can be found by calculating the difference between the average rate of the signal region and the average rate of the background region, divided by the sum of the errors on the average rates:

$$\sigma = \frac{\frac{\sum_i^{n_{\mathrm{sig}}} r_{\mathrm{sig},i}}{n_{\mathrm{sig}}} - \frac{\sum_i^{n_{\mathrm{bkg}}} r_{\mathrm{bkg},i}}{n_{\mathrm{bkg}}}}{\sqrt{\frac{\mathrm{RMS}_{\mathrm{sig}}^2}{n_{\mathrm{sig}}} + \frac{\mathrm{RMS}_{\mathrm{bkg}}^2}{n_{\mathrm{bkg}}}}} \tag{3.8}$$

In the event that a signal region contained only one scaler readout, the Equation 3.7 is undefined. This arises from the fact that the factor of $n-1$, Bessel's correction, is used with small-to-moderate samples so that the RMS calculated above is unbiased. However, in a sample of one there is no bias in the RMS so the biased standard deviation of the sample ($n-1 \to n$) may be used.

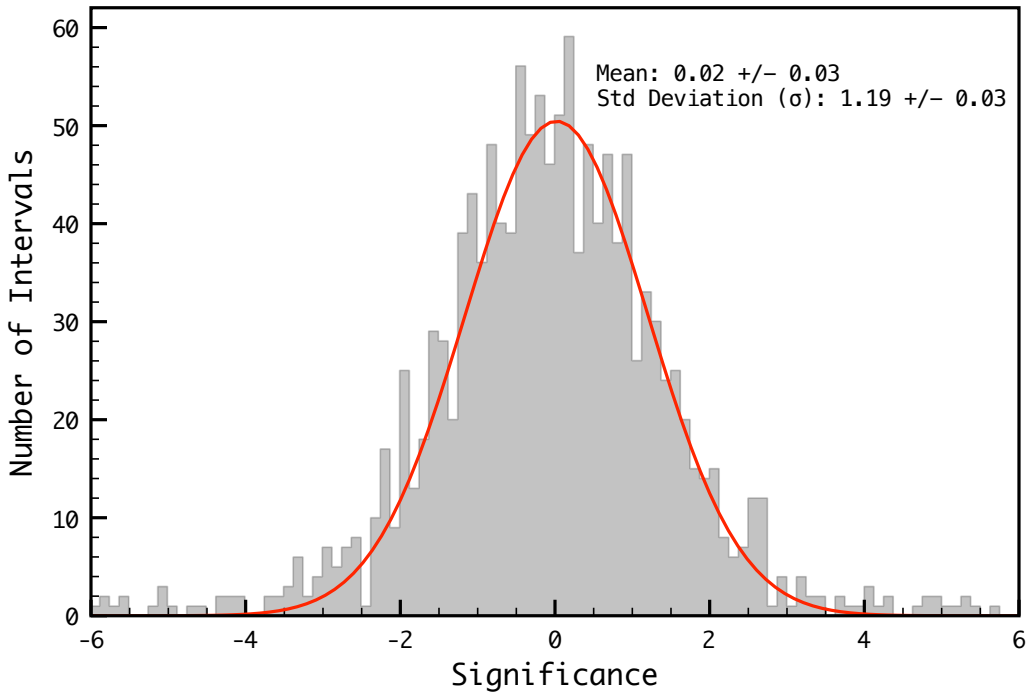

Figure 3.8: Distribution of significances for $\sim$ 1370 uncorrelated data intervals. The red line is the fit of a Gaussian that shows by the long tails that the fluctuations are not purely statistical but influenced by some systematic effects.

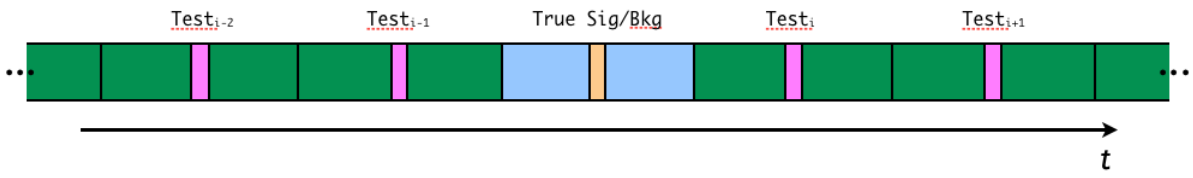

Figure 3.9: Illustration of how the test intervals are distributed around the true signal/background interval. For a standard transient analysis, roughly 15,000 test intervals are used to calculate the significance distribution (3.8).

In a system with only statistical variations in the data sampled, that is, in the absence of instrumental effects, a distribution of the significances calculated using Equation 3.8 on an uncorrelated data set, should follow the unit normal distribution. In the Milagro scaler data, however, it was found that while the mean of the distribution was consistent with zero, the variance of the distribution was substantially larger than 1. Figure 3.8 shows a distribution of significances for ~ 1370 uncorrelated significances from the AS low-threshold array. The longer tails in the distribution of significances are indicative of instrumental or other non-random noise in the scaler data. While there was significant effort made to combat instrumental and environmental effects on the data (see Section 3.3) there still remained some non-random effects influencing the data.

If the distribution of significances was unit normal, then the true significance of any measurement would simply be the significance obtained from Equation 3.8. The deviation of the significance distribution requires that we must correct the "raw" significance obtained with Equation 3.8 in order to obtain the true statistical significance of the count rate in the signal interval. To correct the raw significance value, a

"bootstrap" approach is used. With this approach, the significance values of a large number of "test" signal and background intervals around the true signal and background intervals (Figure 3.9) are used to generate a distribution similar to what is shown in Figure 3.8. From this distribution, a confidence level (CL) can be computed, which is simply the fraction of significances less than the signal significance:

$$\mathrm{CL} = \frac{N_{\sigma<\mathrm{signal}\,\sigma}}{N} \tag{3.9}$$

where N is the total number of test intervals used in the calculation. In practice, $\sim$ 15000 test intervals were used. For most signal intervals analyzed, this amounted to several days worth of test intervals, which was a good compromise between high statistics and avoiding long-term changes, such as PMT failure, in the detector. Once the confidence level has been determined, the corresponding significance can be found. The cumulative probability distribution of the standard normal distribution is:

$$\Phi(x) = \frac{1}{2} + \frac{1}{2}\mathrm{erf}(\frac{\sigma}{\sqrt{2}}) = \mathrm{CL} \tag{3.10}$$

which provides a relation between the CL found and the associated Gaussian significance desired. This "corrected" significance is then calculated:

$$\sigma = 2\mathrm{erfc}^{-1}(2(1-\mathrm{CL})) \tag{3.11}$$

It is this significance that is used to determine whether or not the count rate from a signal interval constitutes a detection. If there is not a significant detection ($\sigma < 5$) then a similar "bootstrap"-type approach can be used to determine the upper limit on the counts in the signal region. This procedure is described in Section 4.3.

Chapter 4

Satellite-Triggered Search for Prompt VHE Emission from GRBs with Milagro

The Milagro scaler data and analysis offer improved low-energy sensitivity compared to the air-shower reconstruction method. Since the high-energy spectra of gamma-ray sources at cosmological distances are attenuated by the EBL, the scaler method is ideal for use in searching for transient gamma-ray emission from extragalactic objects. This chapter describes the details of a search for gamma-ray emission > 1 GeV, using the Milagro scaler method, from GRBs that were detected by satellites at lower (keV – MeV) energies.

4.1 Satellite-detected GRBs Observed with Milagro

Over the lifetime of the Milagro experiment, there were many satellites designed to detect X rays and/or gamma rays in operation. Many of these satellites could detect and (either independently or collectively) localize the source of gamma rays from GRBs. The duration and intensity of the X- and soft gamma-ray (keV – MeV) emission could also be determined in wavebands particular to each satellite instrument. Much of this satellite-based GRB information was distributed in near-real-time to astronomers and observatories via the gamma-ray burst coordinates network (GCN),[1] enabling rapid follow-up observations. If the localization provided by one or more of these satellites was sufficiently constraining, follow-up observations in optical wavebands could sometimes be used to determine the distance, i.e. redshift, of the GRB.

Milagro was a large-field-of-view, unpointed, high-duty-cycle observatory, and as such, did not require intervention in the case of a GRB detection by satellite observatories. However, information provided by satellites was used to refine the search for high-energy emission from GRBs. Using the time of detection and GRB duration information, the Milagro scaler data could be analyzed over time periods coincident with the satellite-detected GRBs to search for an increased count rate, indicative of an increased gamma-ray flux at energies above ~ 1 GeV.

[1] http://gcn.gsfc.nasa.gov/

Table 4.1: Satellite-detected GRBs in the field of view of Milagro. All information taken from GCN circulars.

Name	Instrument[1]	Trig. Time[2]	Dur.[3](s)	R.A.[4](°)	Dec.[4](°)	Zen. Ang.[5](°)	z[6]
GRB 000113	BATSE	34202.36	370	163.27	19.89	20.9	···
GRB 000212	BATSE	81065.14	8	16.09	35.63	2.2	···
GRB 000226	BATSE	36772.60	10	330.03	16.89	31.5	···
GRB 000301C	BATSE/IPN	9234.36	14	3.69	72.68	37.6	2.03
GRB 000302	BATSE	10225.08	120	58.20	54.28	31.9	···
GRB 000317	BATSE	77953.79	550	27.22	32.66 6.39	···	
GRB 000330	BATSE	75449.40	0.2	358.31	39.26	30.0	···
GRB 000331	BATSE	85421.82	55	32.00	59.77	38.3	···
GRB 000408	BATSE/IPN	9348.22	2.5	138.51	67.22	31.1	···
GRB 000508	BATSE	77419.26	30	89.89	2.39	34.1	···
GRB 000615	BeppoSAX	22704	10	233.14	73.80	39	···
GRB 000630	IPN	1853	20	221.81	41.22	33.2	···
GRB 000727	IPN	70956	10	176.29	17.41	40.8	···
GRB 000730	IPN	255	7	191.29	19.27	7	···
GRB 000926	IPN	85773	25	256.06	51.78	15.9	2.04
GRB 001017	IPN	80347	10	272.18	-2.99	42.1	···
GRB 001018	IPN	61114	31	198.54	11.81	31.8	···
GRB 001019	IPN	86375	10	257.93	35.34	19.5	···
GRB 001105	IPN	59128	30	195.47	35.49	8.5	···
GRB 010104	IPN	62489	2	267.44	18.23	19.8	···
GRB 010220	BeppoSAX	82267	150	39.25	61.77	27	···
GRB 010613	IPN/HETE	59329	152	255.45	14.28	24.7	···
GRB 010921	IPN/HETE	18950.56	24.6	343.96	41.01	10.4	0.45
GRB 011130	HETE	22775.66	83.2	46.40	3.81	33.7	···
GRB 011212	HETE	14642.00	80	75.02	32.13	33.0	···

Continued on Next Page...

Table 4.1 – Continued

Name	Instrument[1]	Trig. Time[2]	Dur.[3](s)	R.A.[4](°)	Dec.[4](°)	Zen. Ang.[5](°)	z[6]
GRB 020625B	HETE	41149.32	125	310.9	7.1	38.1	···
GRB 021104	HETE	25262.9	19.7	58.53	38.02	13.3	···
GRB 021112	HETE	12495.9	7.1	39.16	49.95	33.6	···
GRB 021113	HETE	23936.9	20	23.64	40.58	17.6	···
GRB 021211	HETE	40714	6	122.26	6.71	34.8	1.01
GRB 030413	IPN	27277	15	198.62	62.50	27.1	···
GRB 030823	HETE	31960.64	322.73	22.01	33.4	···	
GRB 031026A	HETE	20143.25	114.2	49.723	28.493	33.0	···
GRB 031220	HETE	12596.74	23.7	69.95	7.420	43.4	···
GRB 040924	HETE	42731.36	0.6	31.63	16.05	43.3	0.859
GRB 041211	HETE	41507	30.2	100.87	20.423	43.0	···
GRB 041219A	INTEGRAL	6138	520	6.16	62.82	26.9	···
GRB 050124	*Swift*	41402.87	4.1	192.943	13.034	23.0	···
GRB 050319	*Swift*	34278.44	15	154.285	43.5	45.1	3.24
GRB 050402	*Swift*	22194.58	8	136.5	16.6	40.4	···
GRB 050412	*Swift*	20642.89	26	181.1	-1.3	37.1	···
GRB 050502	INTEGRAL	8037	20	202.4	42.7	42.7	3.793
GRB 050504	INTEGRAL	28852.5	80	201.0	40.7	27.6	···
GRB 050505	*Swift*	84141.09	60	141.8	30.3	28.9	4.3
GRB 050509B	*Swift*	14419.23	0.128	189.1	29.0	10.0	0.226?
GRB 050522	INTEGRAL	21621	15	200.1	24.8	22.8	···
GRB 050607	*Swift*	33082.80	26.5	300.2	9.1	29.3	···
GRB 050712	*Swift*	50427.51	35	77.7	64.9	38.8	···
GRB 050713B	*Swift*	43637.62	30	307.8	60.9	44.2	···
GRB 050715	*Swift*	81026.42	52	155.7	-0.07	36.9	···
GRB 050716	*Swift*	45363.63	69	338.6	38.7	30.3	···
GRB 050820	*Swift*	23693.11	20	337.4	19.6	21.9	2.612

Continued on Next Page...

Table 4.1 – Continued

Name	Instrument[1]	Trig. Time[2]	Dur.[3](s)	R.A.[4](°)	Dec.[4](°)	Zen. Ang.[5](°)	z[6]
GRB 051008	*Swift*	59601	16	202.9	42.1	34.2	···
GRB 051109	*Swift*	4340	36	330.3	40.8	9.6	2.346
GRB 051111	*Swift*	21581.5	20	348.2	18.4	43.7	1.55
GRB 051211B	INTEGRAL	79544	80	345.7	55.1	33.3	···
GRB 051221	*Swift*	6675.61	1.4	328.7	16.9	41.8	0.5465
GRB 051221B	*Swift*	72200.09	61	312.4	53.1	25.9	···
GRB 060102	*Swift*	76648	20	328.9	-1.8	39.9	···
GRB 060109	*Swift*	60881	10	282.7	32.0	22.4	···
GRB 060110	*Swift*	28877	15	72.7	28.4	43.0	···
GRB 060111B	*Swift*	72943	59	286.5	70.4	36.5	···
GRB 060114	INTEGRAL	45586.1	100	195.3	-4.7	40.6	···
GRB 060204B	*Swift*	52464	134	211.8	27.7	30.5	···
GRB 060210	*Swift*	17929.8	5	57.73	27.03	43.4	3.91
GRB 060218	*Swift*	12870.97	2000	50.40	16.87	43.7	0.0331
GRB 060306	*Swift*	2950	30	41.10	-2.16	46.2	···
GRB 060312	*Swift*	5772	30	45.77	12.82	43.6	···
GRB 060313	*Swift*	726.29	0.8	66.62	-10.86	46.7	···
GRB 060403	*Swift*	47537.12	30	282.33	8.33	27.6	···
GRB 060427B	IPN	85915.32	0.22	98.47	21.35	16.4	···
GRB 060428B	*Swift*	32078.83	58	235.38	62.03	26.6	···
GRB 060507	*Swift*	6792.23	185	89.94	75.24	47.1	···
GRB 060510B	*Swift*	30134.81	330	239.22	78.60	42.8	4.9
GRB 060515	*Swift*	8872.91	52	127.29	73.55	41.5	···
GRB 060712	*Swift*	76063.71	26	184.07	35.54	34.8	···
GRB 060814	*Swift*	82939.03	146	221.34	20.59	22.7	···
GRB 060904A	*Swift*	3846.20	80	237.73	44.98	14.2	···
GRB 060906	*Swift*	30767	43.6	40.75	30.35	28.8	3.685

Continued on Next Page...

Table 4.1 – Continued

Name	Instrument[1]	Trig. Time[2]	Dur.[3](s)	R.A.[4](°)	Dec.[4](°)	Zen. Ang.[5](°)	z[6]
GRB 060908	*Swift*	32242	2.43	31.84	0.37	38.8	2.43
GRB 061002	*Swift*	3809.59	20	220.35	48.74	44.6	···
GRB 061126	*Swift*	31676.42	191	86.62	64.20	28.4	···
GRB 061210	*Swift*	44439.33	0.8	144.52	15.61	23.4	0.41?
GRB 061222A	*Swift*	12532.11	115	358.26	46.53	30.1	···
GRB 070103	*Swift*	74799.41	19	352.58	26.82	38.7	···
GRB 070125	IPN	26445	60	117.85	31.14	9.5	1.547
GRB 070129	*Swift*	84910.26	460	37.00	11.73	30.7	···
GRB 070208	*Swift*	33034.28	48	197.90	61.95	31.7	1.165
GRB 070311	INTEGRAL	6770	50	87.54	3.37	32.6	···
GRB 070402	IPN	56915	12	311.2	27.4	11.9	···
GRB 070521	*Swift*	24670.86	60	242.7	30.3	8.7	0.55?
GRB 070529	*Swift*	46108.34	120	283.7	20.6	44.7	2.4996
GRB 070612B	*Swift*	22877.79	20	261.7	-8.75	46.2	···
GRB 070616	*Swift*	59373.97	402	32.15	56.95	22.8	···
GRB 071025	*Swift*	14933.68	109	355.07	31.78	6.7	···
GRB 071122	*Swift*	5005.62	68.7	276.58	47.10	44.0	1.14
GRB 080129	*Swift*	22005	50	105.3	-7.83	44.3	···
GRB 080205	*Swift*	28551	120	98.22	62.77	40.1	···
GRB 080218	*Swift*	72522	27.6	355.9	12.2	26.2	···
GRB 080310	*Swift*	31078	365	220.1	-0.17	44.9	2.42
GRB 080315	*Swift*	8701	65	155.1	41.7	40.7	···
GRB 080319	*Swift*	20742	40	206.4	44.1	38.2	···
GRB 080319B	*Swift*	22369	60	217.9	36.3	43.2	0.937
GRB 080319C	*Swift*	44757	20	258.97	55.41	19.6	1.95
GRB 080320	*Swift*	16658	25	177.78	57.14	32.5	···
GRB 080330	*Swift*	13276	60	169.3	30.57	27.8	1.51

Continued on Next Page...

Table 4.1 – Continued

Name	Instrument[1]	Trig. Time[2]	Dur.[3](s)	R.A.[4](°)	Dec.[4](°)	Zen. Ang.[5](°)	z[6]
GRB 080409	*Swift*	4977	10	84.33	5.09	39.8	···
GRB 080503	*Swift*	44773	170	286.7	68.8	33.9	···
GRB 080506	*Swift*	63981	200	329.5	39.0	43.4	···
GRB 080507	AGILE	27900	40	233.7	56.4	20.6	···
GRB 080513	IPN	18850	30	163.3	28.2	34.5	···
GRB 080517	*Swift*	76971	20	102.3	50.7	17.3	···
GRB 080521	*Swift*	14282	??	182.18	30.58	9.8	···
GRB 080603A	INTEGRAL	40712	180	279.4	62.7	34.7	1.688
GRB 080604	*Swift*	26821	82	236.97	20.55	24.1	1.416

Although the scaler method is insensitive to the directional characteristics of incoming primary particles, the GRB localization information from the satellites provided a measure of the burst's elevation with respect to Milagro. This was important because in order to transform a detection (non-detection) into a physical flux measurement (upper limit), the Milagro scaler detector response, which was dependent on gamma-ray source elevation, had to be taken into account. The redshift of the GRB could be used to constrain the overall energetics of the burst and was essential

[1]Satellite that detected and localized the GRB – see text for instrument descriptions

[2]Time of satellite trigger in seconds of the UT day.

[3]Duration of the GRB. The amount of time over which 90% of the satellite-detected gamma-ray emission occurred. (??) if unknown.

[4]Decimal degrees in J2000 epoch.

[5]Zenith angle of the burst with respect to Milagro, i.e. 90 - (GRB elevation)

[6]Redshift of the GRB, if successfully measured. (?) indicates a probable, but not conclusive measurement.

for testing physical models of emission mechanisms, etc.

A table of all satellite-detected GRBs in the field of view of Milagro and their basic characteristics can be found in Table 4.1. From 2000 January to 2008 June, 115 GRBs were detected above 40° elevation in the field-of-view of Milagro, including 30 with conclusive or tentative redshift measurements. The table includes GRB detections from six independent satellites: the Burst Alert and Transient Source Experiment (BATSE, (Fishman *et al.*, 1992)), the High Energy Transient Explorer (HETE, (Vanderspek *et al.*, 1999)), BeppoSAX (Boella *et al.*, 1997), the International Gamma-Ray Astrophysics Laboratory (INTEGRAL, (Winkler *et al.*, 2003)), *Swift* (Gehrels *et al.*, 2004), the Astro-rivelatore Gamma a Immagini Leggero (AGILE, (Tavani *et al.*, 2009)), as well as the Interplanetary Network (IPN, (Hurley *et al.*, 2010)), which consists of many satellites distributed throughout the Solar System.

4.2 Milagro Detector Response in Scaler Mode

The Milagro detector response was a function of many parameters. This was true for both the standard air shower triggered mode and in scaler mode. Since the details of the parameter dependencies are quite complex and often statistical in nature, an analytical description of the entire detector was not feasible. In order to understand and quantify the dependencies of the detector, Monte Carlo simulations of both EASs and the detector itself were used.

The first step in simulating the response of the Milagro detector to EASs was,

perhaps not surprisingly, to first simulate the EASs themselves. This was done using the Cosmic-Ray Simulations for KAskade (CORSIKA) EAS simulation software package (Heck *et al.*, 1998)[2]. CORSIKA was used to simulate showers created by both gamma-ray and hadronic primary particles. The hadronic primaries simulated were H and He nuclei, which make up the vast majority of EAS-inducing primary hadrons. Hadronic interactions with energies below 80 GeV were simulated with FLUKA (Battistoni *et al.*, 2007) while hadronic energies above 80 GeV were simulated using the NEXUS model (Bossard *et al.*, 2001). The electromagnetic simulations were done using the EGS4 model (Nelson *et al.*, 1985) within CORSIKA. A visualization of simulated CORSIKA air showers can be seen in Figure 2.1.

When converting measured quantities (e.g. scaler rate fluctuations) to physical fluxes and flux upper limits, the error on the final physical measurement is in part determined by how thoroughly the detector has been simulated. For this reason, hundreds of millions of CORSIKA showers were simulated, from primary particle interaction down to the particles incident on the detector. The gamma-ray-primary showers were simulated over a zenith angle range of $0^\circ \leq \theta \leq 45^\circ$, while the hadronic showers were simulated for zenith angles up to 70°. For the scaler simulations, primary particles with energies $500\,\mathrm{MeV} < E < 100\,\mathrm{TeV}$ were simulated, with an intrinsic primary particle energy spectrum of $\frac{dN}{dE} \propto E^{-2}$

The particles reaching the ground in the CORSIKA simulations were then used

[2]CORSIKA v6.5021 was used for the computations and results described here.

as inputs for a Monte Carlo simulation of the detector itself. The code first randomly distributed the cores of the CORSIKA showers over a circular area, 2 km in diameter, centered on the Milagro pond. The response of the detector was then simulated using the Geometry ANd Tracking (GEANT4) software toolkit (Agostinelli *et al.*, 2003). The interactions of the secondary shower particles, including Cherenkov photon generation, pair production, and various hadronic processes, were tracked throughout the detector volume. The number, energy, and timing of the Cherenkov photons as well as their location and angle of incidence on the photocathode was determined for each PMT.

From the number of Cherenkov photons hitting each PMT, the effective area of the detector can be calculated. For the analysis presented here, the effective area of Milagro in scaler mode to gamma rays is the quantity of interest and will be used in the calculating of flux upper limits from scaler data that is described in Section 4.3. The scaler gamma-ray effective area is a function of both the primary gamma-ray energy and the zenith angle of the source (i.e. the total amount of atmosphere the air shower must pass through) and is a measure of the efficiency of the detector. The effective area is defined as:

$$A_{\rm eff}(E,\theta) = \frac{N_{\rm det}(E,\theta)}{N_{\rm throw}(E,\theta)} A_{\rm throw} \tag{4.1}$$

where $N_{\rm det}$ and $N_{\rm throw}$ are the number of detected showers and number of thrown (simulated) showers, respectively. $A_{\rm throw}$ is area on the ground over which the primary

particles (i.e. main shower cores) were thrown. The Milagro effective areas, as a function of energy of low zenith angle ($\theta < 20^{\circ}$) gamma-ray primaries for both the standard and scaler methods can be seen in Figure 3.1. Note that the physical area of the Milagro pond is only about 4800 m^2 but the scaler effective area for the low-threshold AS PMT layer surpasses this value at $\sim$20 GeV. This is due to the fact that the successful detection of secondary particles from an EAS does not require the primary particle trajectory intersect the physical area of the detector.

When calculating the effective area, assumptions about the source spectrum must be made. For generic GRBs, a source spectrum of $\frac{dN}{dE} \propto E^{-2}$ is used, a choice based on the average high-energy Band function component measured by BATSE (Preece *et al.*, 2000). However, since GRBs are located at cosmological distances, gamma-rays at $\sim$GeV energies and above are attenuated through interaction with the EBL. The effect of the EBL is a function of source distance and photon energy and is taken into account when making the GRB spectral assumptions. Since GRBs are relatively short-lived (on the order of only a few seconds in duration), they effectively occur at one elevation angle with respect to Milagro, rather than transiting the field of view as a constant source would do. Simply from geometrical concerns, the majority of GRBs, which are distributed isotropically on the sky, occur at large (low) zenith angles (elevation).

The average Milagro scaler effective area, including the absorption effects of the

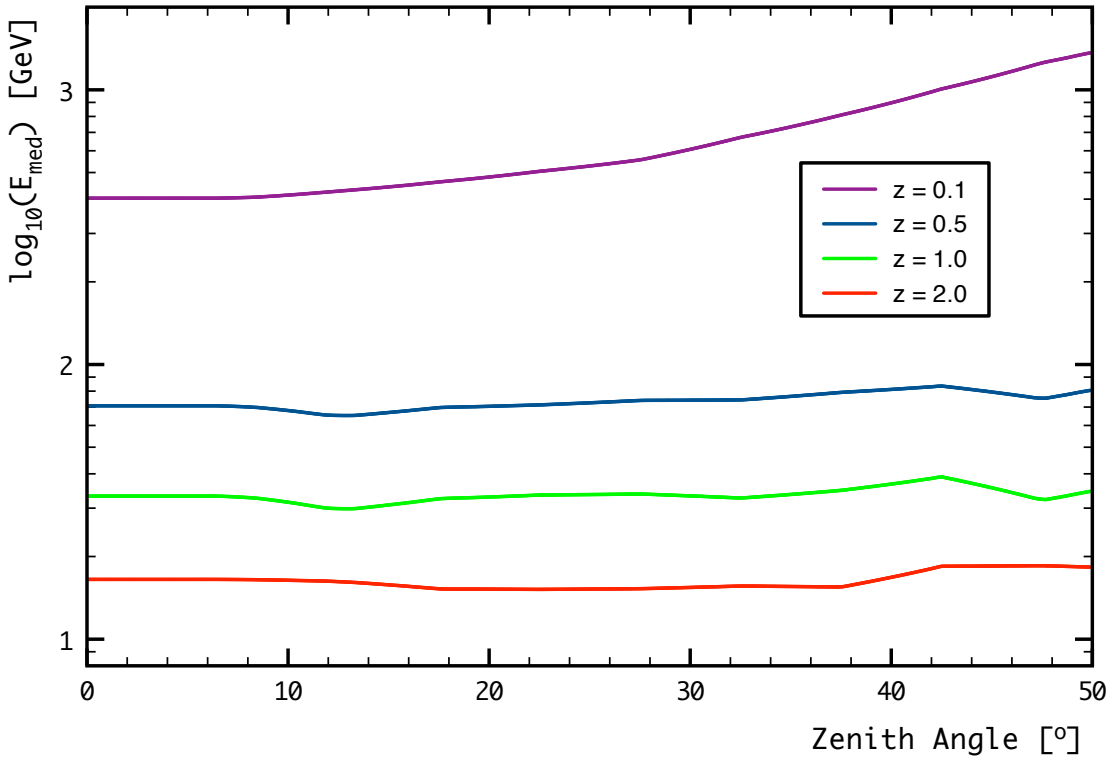

Figure 4.1: The median energy of detected events as a function of zenith angle for the Milagro scaler system. An intrinsic spectrum of $\frac{dN}{dE} \propto E^{-2}$ is assumed. This spectrum is then attenuated by the EBL using the model of Gilmore *et al.* (2009) assuming four different redshifts.

EBL is given by:

$$\langle A_{\text{eff}} \rangle = \frac{\int \frac{dN}{dE} e^{-\tau(E,z)} \cdot A_{\text{eff}}(E)\, dE}{\int \frac{dN}{dE}\, dE} \tag{4.2}$$

where $\tau(E, z)$ is the optical depth due to the interaction with the EBL as a function of energy and redshift (z). $\langle A_{\text{eff}} \rangle$ is obtained from the Monte Carlo simulations.

Simulated showers are thrown at random over some area A_{throw} and the fraction of showers detected by the scalers determines the effective area. The Monte Carlo events each have some weight w_i from how the events were generated. Most Milagro simulations were generated with the number of events $\propto \rho$, the radius from the center of the pond. To equally populate a circle, the events should have been distributed $\propto \rho^2$ but that would leave most of the events far from the pond, which wastes valuable computing time. The events near the pond were the most important ones to have in the sample. Thus, events were generated $\propto \rho$ and weighted by another factor of ρ when they are used to calculate the effective area. The Monte Carlo events are generated with $\frac{dN}{dE} \propto E^{-2}$ spectrum. If a different intrinsic spectrum is desired, e.g. one that takes the attenuation of the EBL into account, the events can be re-weighted accordingly:

$$\langle A_{\text{eff}} \rangle = \frac{\sum_i w_i e^{-\tau(E_i,z)} \cdot \mu_i}{\sum_i w_i} A_{\text{throw}} \tag{4.3}$$

where μ_i is the number of hits in event i. For shower triggers, $\mu_i = 0$ or 1. For the scalers, μ_i can be more than 1.

The median energy of detected events increases as a function of zenith angle. This

is due to the larger column density of atmosphere that the shower must pass through. However, the median energy decreases as a function of source redshift, as the highest energy photons are preferentially attenuated. The median energy of events detected by the Milagro scalers is plotted as a function of zenith angle assuming an intrinsic spectrum of $\frac{dN}{dE} \propto E^{-2}$ for several different redshifts in Figure 4.1. Note that the high energy spectral cutoff due to the EBL essentially negates the zenith-angle dependence of the median energy, but the overall effective area at high redshifts is much smaller. The effective area is used to calculate the physical fluxes and flux upper limits; the details of the latter are described in the following section (4.3).

4.3 Calculation of Flux Upper Limits from Scaler Data

The temporal information on each GRB from satellite observations, i.e. the start time and duration of the burst, is used to define a signal region over which the search for gamma-ray emission with Milagro is made. The interval is commonly referred to as the GRB T_{90}, which is defined as the time period over which 90% of the GRB emission is detected by a satellite. The T_{90} is dependent on the wave band, but for most gamma-ray satellites, the energies covered are in the 10s to 100s of keV. The T_{90} is considered the "prompt" phase of the GRB and is the phase for which the results described in the following chapter (Chapter 5) are derived. No evidence for

gamma-ray emission from any GRB was detected with Milagro. Upper limits on the gamma-ray flux in the Milagro energy band were computed, and the methods for this computation are described in this section.

To determine the upper limit on the excess rate (rate above background) with the scaler data, a procedure initially similar to the calculation of the statistical significance of rate fluctuations (Section 3.4) is used. The GRB T_{90} is used as the signal region and a background region of $5 \times T_{90}$ before and after the signal region (see Figure 3.7) is defined. The rate excess in the signal region is the defined as:

$$r_{\mathrm{ex}} = \left[\frac{\sum r_{\mathrm{sig}}}{n_{\mathrm{sig}}} - \frac{\sum r_{\mathrm{bkg}}}{n_{\mathrm{bkg}}} \right] \tag{4.4}$$

where r_{sig} and r_{bkg} and the scaler rates measured in the signal and background regions, respectively, and n_{sig} and n_{bkg} are the number of times the scalers were read in their respective intervals. The number of excess counts can be either positive or negative. This calculation of excess counts is repeated for several thousand test intervals, each of which has a similarly defined signal and background region, distributed around the true GRB signal/background region (Figure 3.9). Once the excess rates have been calculated for each of the test intervals, the excess rate from the true signal region is compared to those of the ensemble of test intervals. The upper limit, r_{UL}, on the rate in the signal region is calculated by adding signal counts to each of the test interval regions until the number of test intervals with excess rates greater than the excess

rate in the signal region make up $CL \times 100\%$ of the test intervals, where CL is the confidence level desired:

$$\frac{|\{r_{\mathrm{ex,test}} : r_{\mathrm{ex,test}} + r_{\mathrm{UL}} > r_{\mathrm{ex,sig}}\}|}{|\{r_{\mathrm{ex,test}}\}|} >= CL \tag{4.5}$$

where $r_{\mathrm{ex,test}}$ is the collection of excess rates in the test intervals and $r_{\mathrm{ex,sig}}$ is the excess rate in the signal interval. For the GRB upper limits presented in the following chapter, a 99% confidence level ($CL = 0.99$) is used.

Once the upper limit on the rate is computed, a conversion to an upper limit on physical quantities is necessary. To calculate the upper limit on the gamma-ray flux from an upper limit on rate, a spectral assumption and an energy range over which to quote the upper limit is required. With the exception of GRB 080319B, for which a more sophisticated analysis was done (see Section 5.2), the intrinsic source (GRB) spectrum was assumed to be a simple power law with a spectral index of 2:

$$\frac{dN}{dE} = N_0 E^{-2} \text{ cm}^{-2} \text{ s}^{-1} \text{ GeV} \tag{4.6}$$

The experiment detects events with a rate, r where:

$$r = \int \frac{dN}{dE} e^{-\tau(E,z)} \cdot A_{\mathrm{eff}}(E)\, dE \tag{4.7}$$

where $A_{\mathrm{eff}}(E)$ is obtained from Equation 4.1 and the integral is over all pertinent

energies (i.e. where the integral is non-zero).

With the effective area, combining Equations 4.6 and 4.7, gives the normalization of the integral (N_0) over the sensitive energy range of the experiment:

$$\int_a^b \frac{dN}{dE}\,dE = \int_a^b N_0 E^{-2}\,dE \text{ cm}^{-2}\text{ s}^{-1}\text{ GeV} = -\frac{N_0}{E/\text{GeV}}\text{ cm}^{-2}\text{ s}^{-1}\Big|_a^b \tag{4.8}$$

$$= N_0\text{ cm}^{-2}\text{ s}^{-1}\left[\frac{1}{a/\text{GeV}} - \frac{1}{b/\text{GeV}}\right] \approx \frac{N_0}{a/\text{GeV}}\text{ cm}^{-2}\text{ s}^{-1}\ (b \gg a) \tag{4.9}$$

$$\frac{N_0}{a/\text{GeV}}\text{ cm}^{-2}\text{ s}^{-1} = \frac{r_{\text{UL}}}{\langle A_{\text{eff}}\rangle} \Rightarrow N_0 = \frac{r_{\text{UL}}}{\langle A_{\text{eff}}\rangle}\text{ cm}^2\text{ s} \tag{4.10}$$

where r_{UL} is the upper limit on the rate, and the sensitive energy range is assumed to be $a = 1\,\text{GeV} < E < b = 100\,\text{TeV}$. The integral upper limit on the energy flux ($\mathcal{F}$) between energies E_l and E_h is then simply:

$$\mathcal{F}_{\text{UL}} = \int_{E_{\text{l}}}^{E_{\text{h}}} E\frac{dN}{dE}\,dE = \int_{E_{\text{l}}}^{E_{\text{h}}} N_0 E^{-1}\text{ cm}^{-2}\text{ s}^{-1}\text{ GeV}\,dE \tag{4.11}$$

$$= N_0 \cdot \ln\left(\frac{E_{\text{h}}}{E_{\text{l}}}\right)\text{ cm}^{-2}\text{ s}^{-1}\text{ GeV} \tag{4.12}$$

The calculation of flux upper limits was done for all GRBs observed with Milagro. The results of these calculations and what they can say about the physical mechanisms at work in GRBs are described in the following chapter.

Chapter 5

Results from GRB Observations with Milagro

The Milagro detector surveyed the VHE sky for eight and a half years, from 2000 January to 2008 June. During this time, 115 well-localized, satellite-detected GRBs occurred within the 2 sr field of view of the instrument, above an elevation of 40° (see Section 4.1). A search for gamma-ray emission at energies > 1 GeV was made over the prompt phase of these GRBs, using the scaler data from Milagro. This catalog represents the most comprehensive search for VHE emission from the prompt phase of GRBs yet made. Details of the results from the search are presented in this chapter with special attention focused on the unique "naked-eye" burst, GRB 080319B.

5.1 Milagro Observations of GRBs from 2000 – 2008

No statistically significant evidence of gamma-ray emission from any of the 115 GRBs observed with Milagro was found. The corrected significance distribution is shown in Figure 5.1. The distribution is, within errors, consistent with background fluctuations (a unit normal distribution). The burst with largest positive fluctuation was GRB 060204B with a significance of just 2.2σ, an unremarkable fluctuation, particularly in a sample of 115. Since no gamma-ray emission was found to be associated with any of the GRBs, upper limits on the gamma-ray fluence (flux $\times$ duration) are calculated.

The upper limits on GRB fluence are calculated as described in Section 4.3. An intrinsic power-law GRB spectrum of $\frac{dN}{dE} \propto E^{-2}$ is assumed. Effects of gamma-ray absorption by the EBL are taken into account assuming the model of Gilmore *et al.* (2009). For the majority of the GRBs observed with Milagro the redshift is unknown. For these bursts fluence upper limits are calculated assuming the GRB was at four arbitrary distances, $z = 0.1, 0.5, 1.0, 2.0$. For the 30 GRBs with measured (or tentatively measured) redshifts, these values are used in the upper limit calculation. The fluence upper limits on GRBs with $z > 3$ are omitted due to the fact that a more complete model of the EBL is needed to provide meaningful results. Furthermore, the effects of the EBL on the GRB spectrum when the burst is located at such a large

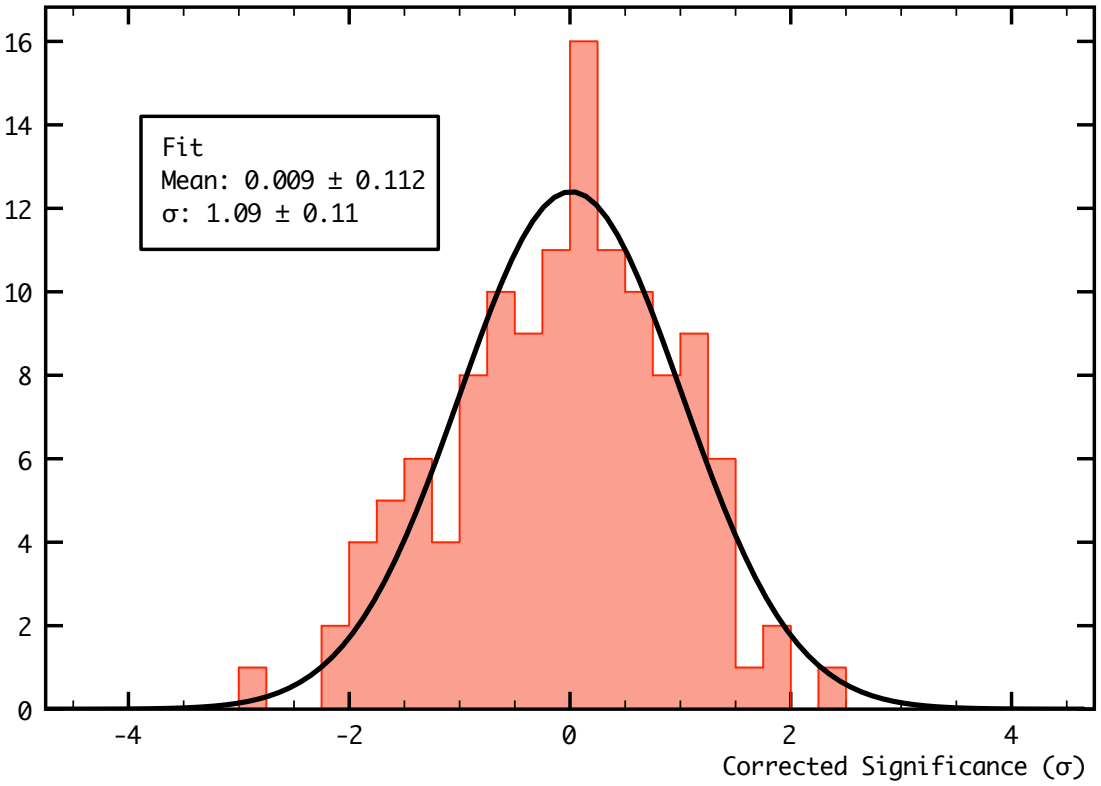

Figure 5.1: A histogram of the statistical significances of scaler rate fluctuations coincident with the prompt phase of GRBs observed with Milagro. The distribution is consistent with a unit normal distribution, indicating that the scaler rate fluctuations during the observations were purely background in nature.

distance is so severe as to make the upper limits non-constraining in any conceivable GRB model. The results for all of the GRBs can be found in Table 5.1.

Table 5.1: Upper limits on gamma-ray emission in the 1 – 100 GeV energy range for all satellite-detected GRBs in the Milagro field of view (above 40° elevation).

			1 – 100 GeV fluence upper limits (erg cm^{-2})				
Name	z	σ^1	$z = z_{\rm obs}$	$z = 0.1$	$z = 0.5$	$z = 1.0$	$z = 2.0$
GRB 000113	–	-1.5	–	2.6e-04	9.7e-04	1.9e-03	4.7e-03
GRB 000226	–	-0.4	–	2.2e-05	9.3e-05	1.9e-04	4.7e-04
GRB 000301C	2.03	0.0	1.3e-03	–	–	–	–
GRB 000302	–	-1.3	–	3.2e-04	1.4e-03	2.8e-03	7.0e-03
GRB 000317	–	1.1	–	2.4e-03	8.1e-03	1.6e-02	4.0e-02
GRB 000330	–	-0.1	–	3.6e-06	1.5e-05	3.1e-05	7.7e-05
GRB 000331	–	0.6	–	7.4e-04	3.7e-03	7.9e-03	2.0e-02
GRB 000408	–	-1.4	–	3.4e-06	1.4e-05	3.0e-05	7.3e-05
GRB 000508	–	-2.1	–	1.6e-05	7.1e-05	1.5e-04	3.6e-04
GRB 000615	–	-1.9	–	8.5e-06	4.3e-05	9.4e-05	2.5e-04
GRB 000630	–	0.9	–	9.9e-05	4.4e-04	9.2e-04	2.3e-03
GRB 000727	–	0.2	–	4.1e-05	2.2e-04	4.8e-04	1.4e-03
GRB 000730	–	-0.7	–	5.7e-06	2.1e-05	4.1e-05	1.0e-04
GRB 000926	2.04	-1.2	2.7e-04	–	–	–	–

Continued on Next Page...

Table 5.1 – Continued

			1 – 100 GeV fluence upper limits (erg cm^{-2})				
Name	z	σ^1	$z = z_{\rm obs}$	$z = 0.1$	$z = 0.5$	$z = 1.0$	$z = 2.0$
GRB 001017	–	-0.2	–	4.2e-05	2.3e-04	5.2e-04	1.5e-03
GRB 001018	–	1.1	–	6.2e-05	2.7e-04	5.5e-04	1.4e-03
GRB 001019	–	-1.3	–	4.6e-06	1.7e-05	3.4e-05	8.1e-05
GRB 001105	–	1.3	–	3.1e-05	1.0e-04	2.0e-04	5.1e-04
GRB 010104	–	0.7	–	3.5e-05	2.1e-04	4.5e-04	1.3e-03
GRB 010220	–	-1.3	–	6.5e-05	2.6e-04	5.4e-04	1.3e-03
GRB 010613	–	0.8	–	4.6e-04	1.8e-03	3.7e-03	8.9e-03
GRB 010921	0.45	0.6	3.0e-04	–	–	–	–
GRB 011130	–	-0.6	–	2.3e-04	1.0e-03	2.2e-03	5.3e-03
GRB 011212	–	0.1	–	2.1e-04	9.6e-04	2.0e-03	4.8e-03
GRB 020625B	–	-1.5	–	2.6e-04	1.3e-03	2.8e-03	7.2e-03
GRB 021104	–	1.1	–	3.9e-05	1.3e-04	2.5e-04	5.9e-04
GRB 021112	–	-0.4	–	1.8e-05	8.2e-05	1.7e-04	4.2e-04
GRB 021113	–	-1.2	–	1.7e-05	6.0e-05	1.2e-04	2.8e-04
GRB 021211	1.01	0.3	1.5e-04	–	–	–	–
GRB 030413	–	-1.7	–	8.5e-06	3.4e-05	7.1e-05	1.7e-04
GRB 030823	–	0.2	–	1.9e-04	8.4e-04	1.7e-03	4.3e-03
GRB 031026A	–	1.0	–	2.9e-05	1.7e-04	3.7e-04	1.0e-03
GRB 031220	–	0.1	–	9.6e-05	5.5e-04	1.2e-03	3.5e-03

Continued on Next Page...

Table 5.1 – Continued

			1 – 100 GeV fluence upper limits (erg cm^{-2})				
Name	z	σ^1	$z = z_{\rm obs}$	$z = 0.1$	$z = 0.5$	$z = 1.0$	$z = 2.0$
GRB 040924	0.859	-0.5	1.2e-04	–	–	–	–
GRB 041211	–	1.5	–	1.6e-04	8.9e-04	2.0e-03	5.8e-03
GRB 041219A	–	1.3	–	1.2e-03	5.0e-03	1.0e-02	2.5e-02
GRB 050124	–	-0.6	–	4.6e-06	1.8e-05	3.6e-05	8.6e-05
GRB 050319	3.24	1.3	–	–	–	–	–
GRB 050402	–	-1.0	–	1.8e-05	9.4e-05	2.1e-04	5.7e-04
GRB 050412	–	0.2	–	4.3e-05	2.1e-04	4.4e-04	1.1e-03
GRB 050502	3.793	-1.1	–	–	–	–	–
GRB 050504	–	0.5	–	1.5e-04	6.1e-04	1.3e-03	3.1e-03
GRB 050505	4.3	-2.0	–	–	–	–	–
GRB 050509B	0.226?	-0.5	3.3e-06	–	–	–	–
GRB 050522	–	-0.1	–	1.3e-05	5.2e-05	1.0e-04	2.5e-04
GRB 050607	–	1.0	–	4.4e-05	1.8e-04	3.8e-04	9.2e-04
GRB 050712	–	0.6	–	1.5e-04	7.7e-04	1.7e-03	4.4e-03
GRB 050713B	–	0.2	–	2.3e-04	1.3e-03	2.9e-03	8.2e-03
GRB 050715	–	0.2	–	2.2e-04	1.1e-03	2.3e-03	5.8e-03
GRB 050716	–	0.7	–	2.7e-04	1.1e-03	2.3e-03	5.7e-03
GRB 050820	–	–	Power Out				
GRB 051008	–	0.5	–	4.9e-05	3.3e-04	7.1e-04	1.9e-03

Continued on Next Page...

Table 5.1 – Continued

			1 – 100 GeV fluence upper limits (erg cm^{-2})				
Name	z	σ^1	$z = z_{\rm obs}$	$z = 0.1$	$z = 0.5$	$z = 1.0$	$z = 2.0$
GRB 051109	2.346	1.2	1.4e-03	–	–	–	–
GRB 051111	1.55	0.1	2.7e-03	–	–	–	–
GRB 051211B	–	0.2	–	3.0e-04	1.4e-03	2.8e-03	6.9e-03
GRB 051221	0.5465	0.2	1.2e-04	–	–	–	–
GRB 051221B	–	-1.0	–	1.2e-04	4.8e-04	9.7e-04	2.4e-03
GRB 060102	–	-1.0	–	4.0e-05	2.1e-04	4.6e-04	1.2e-03
GRB 060109	–	-0.8	–	7.3e-06	2.8e-05	5.6e-05	1.4e-04
GRB 060110	–	-1.0	–	3.9e-05	2.2e-04	5.0e-04	1.5e-03
GRB 060111B	–	1.0	–	3.3e-04	1.6e-03	3.3e-03	8.4e-03
GRB 060114	–	-1.8	–	1.8e-04	9.7e-04	2.1e-03	5.9e-03
GRB 060204B	–	2.2	–	6.1e-04	2.6e-03	5.3e-03	1.3e-02
GRB 060210	3.91	-0.6	–	–	–	–	–
GRB 060218	0.0331	-0.0	9.7e-02	–	–	–	–
GRB 060306	–	1.2	–	4.5e-04	2.7e-03	5.8e-03	1.6e-02
GRB 060312	–	0.0	–	3.0e-04	1.7e-03	3.8e-03	1.1e-02
GRB 060313	–	0.6	–	3.0e-05	1.8e-04	3.9e-04	1.0e-03
GRB 060403	–	-0.3	–	2.6e-05	1.1e-04	2.2e-04	5.4e-04
GRB 060427B	–	0.7	–	3.5e-06	1.2e-05	2.4e-05	5.8e-05
GRB 060428B	–	-1.0	–	9.3e-05	3.7e-04	7.6e-04	1.9e-03

Continued on Next Page...

Table 5.1 – Continued

			1 – 100 GeV fluence upper limits (erg cm^{-2})				
Name	z	σ^1	$z = z_{\rm obs}$	$z = 0.1$	$z = 0.5$	$z = 1.0$	$z = 2.0$
GRB 060507	–	0.6	–	7.1e-03	4.3e-02	9.1e-02	2.4e-01
GRB 060510B	4.9	-0.8	–	–	–	–	–
GRB 060515	–	0.2	–	3.8e-04	2.1e-03	4.6e-03	1.3e-02
GRB 060712	–	0.3	–	6.2e-05	2.9e-04	6.0e-04	1.5e-03
GRB 060814	–	-0.8	–	1.0e-03	4.0e-03	8.0e-03	1.9e-02
GRB 060904A	–	0.8	–	4.5e-04	1.6e-03	3.0e-03	7.0e-03
GRB 060906	3.685	-0.2	–	–	–	–	–
GRB 060908	–	–	Power Out				
GRB 061002	–	-0.3	–	8.0e-05	4.7e-04	1.0e-03	2.9e-03
GRB 061126	–	-0.2	–	7.5e-04	3.4e-03	6.2e-03	1.1e-02
GRB 061210	0.41?	1.2	1.7e-05	–	–	–	–
GRB 061222A	–	-0.7	–	3.6e-04	1.5e-03	3.1e-03	7.6e-03
GRB 070103	–	0.7	–	4.7e-05	2.4e-04	5.1e-04	1.3e-03
GRB 070125	1.547	-0.2	4.9e-04	–	–	–	–
GRB 070129	–	0.1	–	7.4e-04	3.1e-03	6.4e-03	1.6e-02
GRB 070208	1.165	-0.2	3.6e-04	–	–	–	–
GRB 070311	–	0.3	–	8.2e-05	3.6e-04	7.5e-04	1.8e-03
GRB 070402	–	-1.3	–	3.7e-06	1.3e-05	2.4e-05	5.7e-05
GRB 070521	0.55?	1.2	6.8e-04	–	–	–	–

Continued on Next Page...

Table 5.1 – Continued

			1 – 100 GeV fluence upper limits (erg cm^{-2})				
Name	z	σ^1	$z = z_{\rm obs}$	$z = 0.1$	$z = 0.5$	$z = 1.0$	$z = 2.0$
GRB 070529	2.5	-0.1	2.7e-01	–	–	–	–
GRB 070612B	–	1.8	–	2.0e-04	1.2e-03	2.5e-03	6.9e-03
GRB 070616	–	-0.3	–	1.1e-03	4.3e-03	8.6e-03	2.1e-02
GRB 071025	–	-1.4	–	2.9e-05	9.9e-05	2.0e-04	4.9e-04
GRB 071122	1.14	-0.8	1.4e-02	–	–	–	–
GRB 080129	–	0.3	–	2.0e-04	1.2e-03	2.5e-03	7.2e-03
GRB 080205	–	0.0	–	2.5e-04	1.3e-03	2.9e-03	7.8e-03
GRB 080310	2.42	1.0	1.5e-01	–	–	–	–
GRB 080315	–	0.1	–	8.2e-04	4.4e-03	9.6e-03	2.7e-02
GRB 080319	–	-0.5	–	2.0e-04	9.9e-04	2.1e-03	5.5e-03
GRB 080319B	0.937	-0.4	7.2e-03	–	–	–	–
GRB 080319C	1.95	0.4	5.3e-04	–	–	–	–
GRB 080320	–	0.2	–	5.8e-05	2.6e-04	5.3e-04	1.3e-03
GRB 080330	1.51	0.0	1.4e-03	–	–	–	–
GRB 080409	–	-0.5	–	3.5e-05	1.8e-04	4.0e-04	1.1e-03
GRB 080503	–	0.3	–	5.5e-03	2.5e-02	5.2e-02	1.3e-01
GRB 080506	–	-0.6	–	1.2e-02	6.9e-02	1.5e-01	4.4e-01
GRB 080507	–	0.1	–	1.8e-04	6.7e-04	1.3e-03	3.2e-03
GRB 080513	–	0.5	–	2.8e-04	1.3e-03	2.7e-03	6.7e-03

Continued on Next Page...

Table 5.1 – Continued

			1 – 100 GeV fluence upper limits (erg cm^{-2})				
Name	z	σ^1	$z = z_{\rm obs}$	$z = 0.1$	$z = 0.5$	$z = 1.0$	$z = 2.0$
GRB 080517	–	0.4	–	7.0e-05	2.5e-04	5.0e-04	1.2e-03
GRB 080521	–	–	Unknown Duration				
GRB 080603A	1.688	-0.5	1.8e-02	–	–	–	–
GRB 080604	1.416	2.5	8.1e-03	–	–	–	–

Although the fluence limits are quoted in the 1 – 100 GeV band, the contribution to the Milagro sensitivity from photons > 100 GeV is used when setting the limit on the normalization of the spectrum. For low redshifts, where the power-law spectrum is not much attenuated above 100 GeV, this contribution is substantial, and results in lower fluence limits than if all the emission were restricted to the 1 – 100 GeV energy interval. The upper limits presented here are comparable to those obtained with other EAS arrays, e.g. Aielli *et al.* (2009).

[1] Corrected significance of the scaler rate fluctuation associated with the GRB. Units are standard deviations.

5.2 The "naked-eye" burst: GRB 080319B

On 2008 March 19 one of the most energetic GRBs to date was detected by the Burst Alert Telescope (BAT) onboard *Swift* (Cummings *et al.*, 2008) and by the Konus GRB spectrometer onboard the *Wind* spacecraft (Golenetskii *et al.*, 2008). With a peak visual magnitude of 5.3, GRB 080319B was dubbed the "naked-eye" GRB, as an observer under dark skies could have seen the burst without the aid of an instrument. Due in part to the burst's proximity (10° separation) to GRB 080319A, which was detected < 30 minutes earlier, the prompt phase of GRB 080319B was observed in the optical band by several wide-field robotic optical telescopes. These fortuitous circumstances led to GRB 080319B having the best broadband coverage of any GRB to date.

With a measured redshift of $z = 0.937$ (Vreeswijk *et al.*, 2008), this was the most distant astronomical object known to be observable with the naked eye. Contemporaneous gamma-ray and optical data for GRB 080319B appear to be at least mildly correlated (Figure 5.2), leading to the conclusion that both the optical and gamma-ray emission are most likely produced in the same physical region (Racusin *et al.*, 2008). Perhaps the most natural explanation of the observed emission of GRB 080319B comes from the synchrotron self-Compton (SSC) model of GRB emission. The SSC interpretation in the context of correlated optical and gamma-ray emission and a strong first order inverse Compton (IC) peak, as observed in the case of GRB 080319B, predicts a strong second order IC peak in the hundreds of GeV (Kumar and Panaitescu,

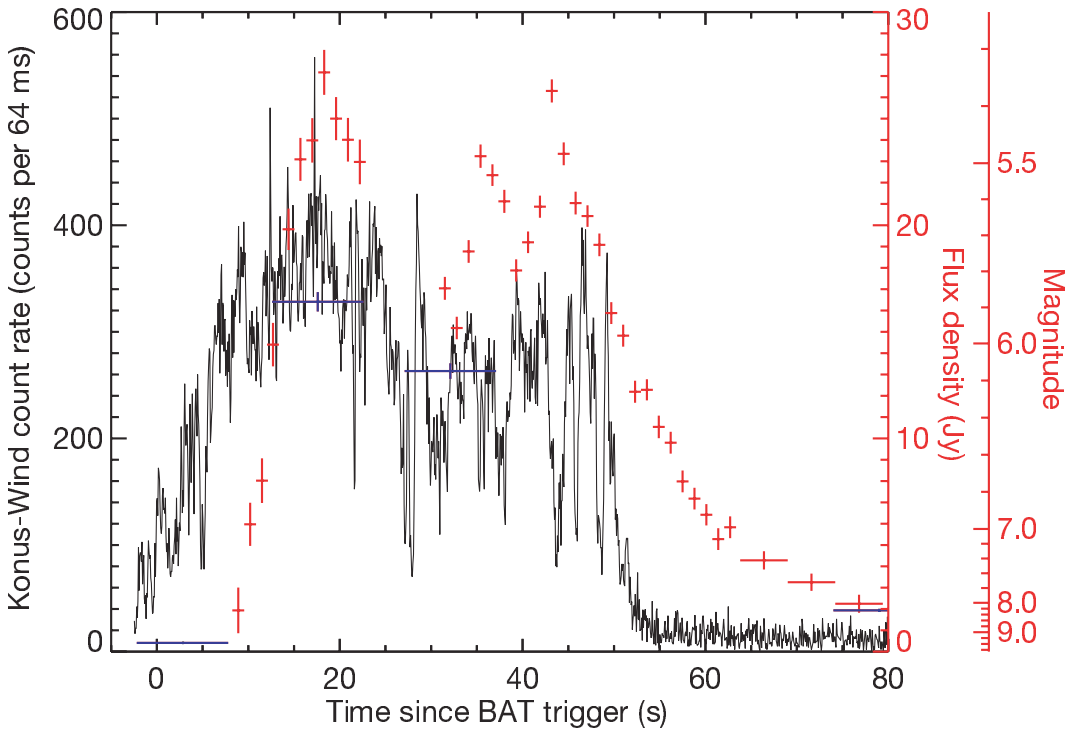

Figure 5.2: The background-subtracted gamma-ray light curve as measured by Konus (black; 181,160 keV), plotted relative to the GRB trigger time measured with *Swift*-BAT. Optical data from Pi of the Sky (blue) and TORTORA (red) are also plotted. The optical emission begins within seconds of the onset of the burst and ends at roughly the same time, providing strong evidence that both originate at the same site. Figure from Racusin *et al.* (2008).

2008), within the energy range and sensitivity of the Milagro gamma-ray observatory (Atkins *et al.*, 2004b).

GRB 080319B occurred in the Milagro field of view at an elevation angle of 47°. Analyses of the Milagro data during the prompt phase of GRB 080319B using two independent techniques, the scaler and standard air-shower reconstruction, show no indication of gamma-ray emission. For the results presented here, the prompt phase of GRB 080319B is considered to begin at $T_0 = 22370.339$ s (06:12:50.339) UT and

extend for a duration of 60 s, both quantities selected based on the main pulse observed by the Konus instrument (Golenetskii *et al.*, 2008). In the standard analysis, Milagro observed 30 events during this burst interval, with a predicted background of 29.7 events. This gives a 99% confidence-level upper limit of 17.3 events.

The scaler analysis of the data collected coincident with GRB 080319B shows no significant excess in the scaler count rate associated with the prompt phase of the burst. Using the scaler analysis procedure described above to calculate the significance of the time interval coincident with the main gamma-ray pulse observed by the Konus instrument, a 0.35σ deficit with respect to the background rate is found in the Milagro data. This results in a 99% confidence-level upper limit on the scaler rate of 11.8 kHz. The Milagro light curves obtained from both the scaler and standard analyses are shown in Figure 5.3

To calculate the corresponding upper limit on the photon flux above some threshold energy, $E_{\rm th}$ a monochromatic GRB spectrum at the threshold energy is assumed. Because the sensitivity of Milagro improves with energy, this procedure gives the most conservative limit on the integral flux above $E_{\rm th}$. The gamma-ray burst spectrum is assumed to be attenuated by the EBL according to the model of Gilmore *et al.* (2009). The effective area of Milagro is computed as describe in Section 4.2. With the effective area, EBL-attenuated GRB spectrum, and an upper limit on events, an upper limit on the integral photon flux above various values of $E_{\rm th}$ is calculated. These limits are shown for both the standard analysis and the scaler analysis in Figure 5.4.

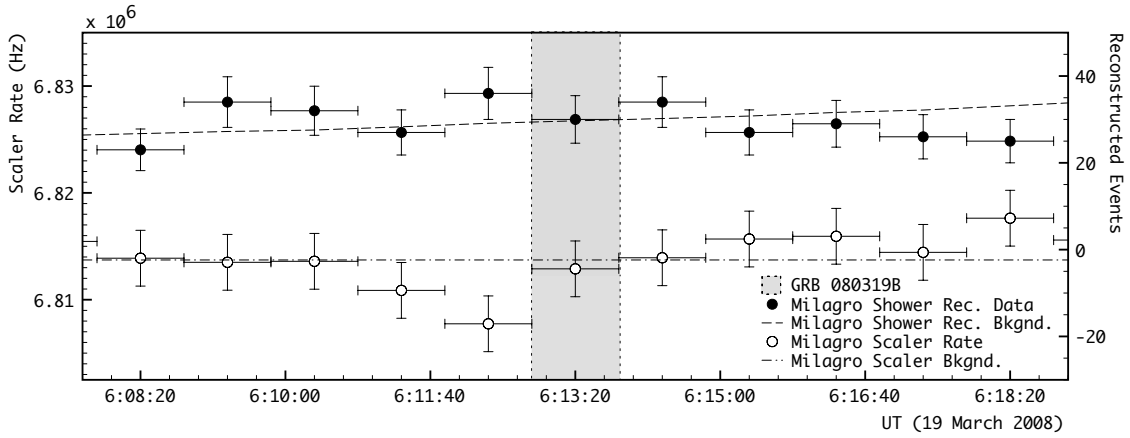

Figure 5.3: Light curve of both the scaler and reconstructed air shower count rates coincident with GRB 080319B and the time immediately before and after the prompt phase of the burst. The lightcurve is binned in intervals of the burst duration, which for GRB 080319B was 60 seconds. No significant excess of events associated with the prompt phase of GRB 080319B is observed.

In addition to calculating upper limits on the conservative, but rather non-physical assumption of a monochromatic GRB spectrum, a more realistic spectral hypothesis can be used. If one assumes that the optical emission detected during the prompt phase of GRB 080319B is due to synchrotron radiation from a population of energetic electrons and that the keV – MeV gamma rays detected by Konus arise from IC scattering of these synchrotron photons by this same population of electrons, it follows that gamma rays with energies in the tens to hundreds of GeV should be produced by secondary IC scattering of the keV – MeV gamma rays.

The shape of this high-energy, second-order spectral feature should resemble that of the keV – MeV spectrum, which is fit well by a Band function (Band *et al.*, 1993) with spectral indices $\alpha = -0.833$, $\beta = -3.499$ (Racusin *et al.*, 2008). Using

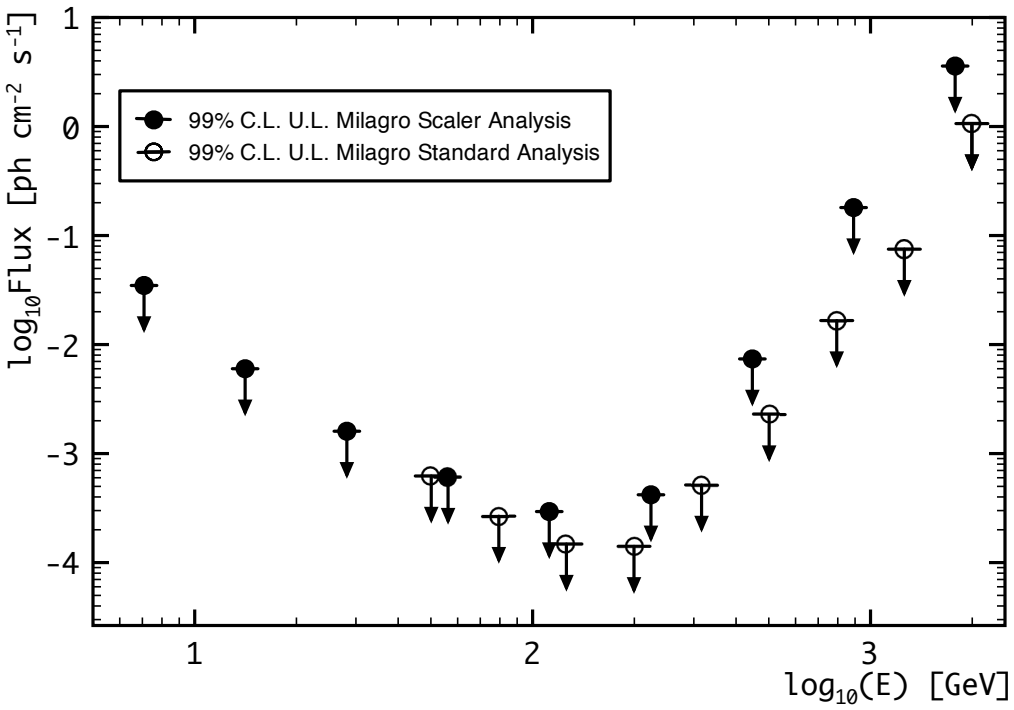

Figure 5.4: 99% confidence-level upper limits on the integral photon flux above various values of $E_{\rm th}$ assuming a monochromatic (δ-function) intrinsic GRB spectrum at $E_{\rm th}$. This spectrum is then attenuated by the EBL using the model of Gilmore *et al.* (2009). The upper limits from both the scaler and standard analyses are plotted here.

the TORTORA measurement as an anchor point, we assume several synchrotron spectra, again with a Band function form with $\alpha = -0.833$, $\beta = -3.499$, with 0.4 eV $\leq E_{p,\mathrm{sync}} \leq 40$ eV, where $E_{p,\mathrm{sync}}$ is the Band function peak energy of the synchrotron spectrum. According to the SSC model, each of these assumed synchrotron spectra, in the context of the keV – MeV peak, give rise to a corresponding Band-function spectral feature in the GeV energy range.

Using this GeV-Band function as the spectral assumption together with the 99% confidence-level upper limits on the scaler count rate from Milagro, we calculate the corresponding limit on νF_ν at the GeV Band function peak energy ($E_{\mathrm{p,GeV}}$) for several different values of $E_{\mathrm{p,sync}}$. These limits are shown in Figure 5.5 together with the average flux observed by TORTORA (Racusin *et al.*, 2008) and the gamma-ray spectrum obtained with Konus. The Milagro upper limits are computed assuming attenuation of the high-energy gamma rays by both Klein-Nishina suppression at the source and by the intervening EBL based on the model of Gilmore *et al.* (2009). The Klein-Nishina suppression is included as an exponential cutoff at the Klein-Nishina limit, which is a conservative approximation to the true shape of the Klein-Nishina cutoff. Details on the origin and characteristics of the Klein-Nishina suppression can be found in Section 1.3.1. As can be seen in Figure 1.19, the dependence of the gamma-ray opacity on the choice of EBL model is quite small, at least among the currently favored EBL models.

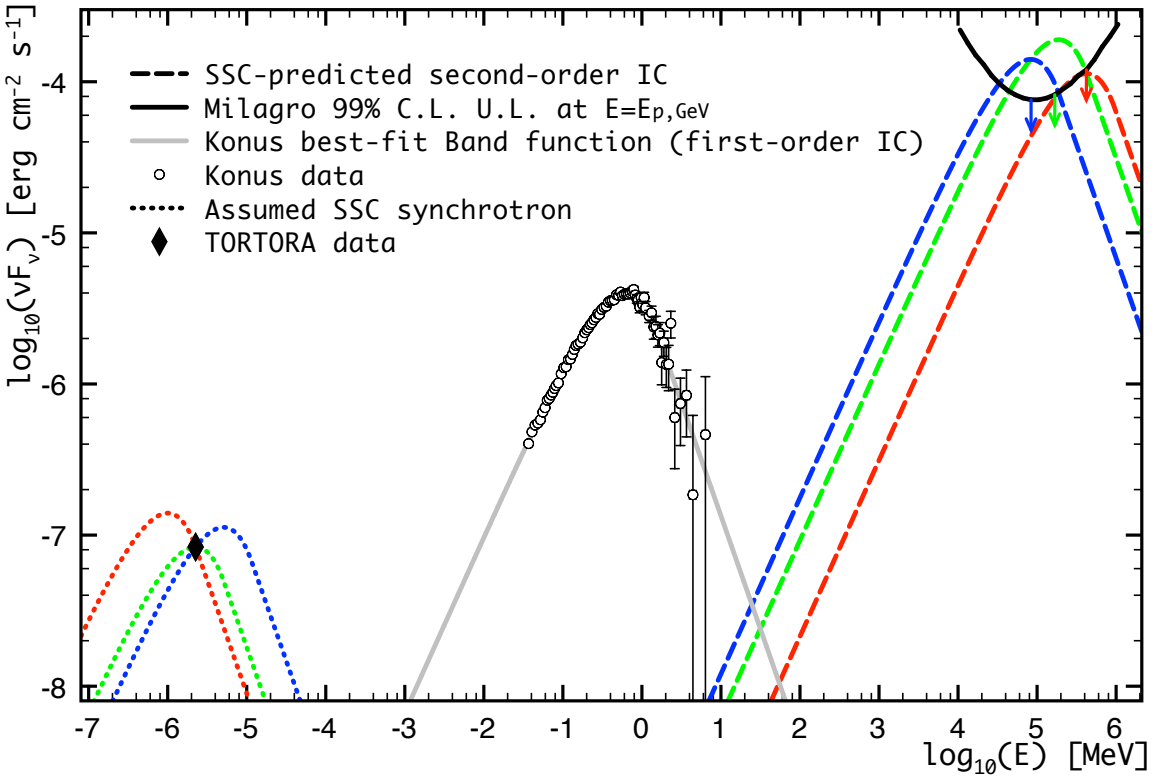

Figure 5.5: 99% confidence-level upper limits on the prompt νF_ν flux obtained using the scaler analysis method described in the text. The limits are quoted at $E = E_{\rm p,GeV}$ where $E_{\rm p,GeV}$ is the peak energy for various intrinsic Band-function GRB spectra. Also shown are the data obtained simultaneously by Konus and TORTORA. The dotted lines show three assumed synchrotron spectra ($E_{\rm p,syn} = 1, 2.26, 5.1$ eV). The corresponding second-order IC spectral features predicted by the SSC model are shown with dashed lines. The Milagro upper limits are compared to the unattenuated second-order IC spectral components since the limits plotted here already account for gamma-ray attenuation from both Klein-Nishina suppression and attenuation via pair production with the EBL.

5.3 Constraints on the synchrotron self-Compton model of prompt GRB Emission

From the observations of GRB 080319B by Konus and TORTORA, a Compton parameter of $Y \lesssim 100$ is found, this parameter being defined as the ratio between the amount of energy carried in the first-order IC (keV – MeV gamma ray) component and the synchrotron (optical) component. Assuming that the SSC mechanism is responsible for the emission observed in the optical and keV – MeV gamma-ray bands and following the discussion in Kumar and Panaitescu (2008), it is predicted that there should exist a second-order IC spectral feature and that it should peak at $\sim 400(\nu_{\rm io}/1{\rm eV})^{-1}$ GeV ($\nu_{\rm io} \lesssim 1$ eV being the peak of the synchrotron spectrum) and carry a fluence of $Y_2 = Y = 100$ times that carried in the first-order IC (i.e. Konus-detected) component. The upper limits obtained by Milagro indicate that $Y_2 \leq 20$, a factor of 5 less than predicted. This result is the only direct experimental constraint on the SSC mechanism and strongly disfavors this scenario in the case of GRB 080319B, assuming the GeV peak lies in the ~ 20 – 200 GeV energy range.

This is illustrated in Figure 5.6 where the Milagro scaler 99% confidence-level upper limits at various $E_{\rm p,GeV}$ are plotted with the predicted SSC-model-predicted flux at $E_{\rm p,GeV}$. In deriving these limits, the assumed GRB spectrum is a Band function with peak energies varying between 10 GeV $< E_{\rm p,GeV} = E_{\rm p,IC2} <$ 1 TeV, that is then attenuated due to Klein-Nishina suppression assuming a bulk Lorentz factor $\Gamma = 500$.

This spectrum is assumed to be further attenuated at high energies due to interaction with the EBL. The upper limits then, are limits on the unattenuated flux of the second order IC peak and these limits are compared with the SSC model-predicted fluxes in Figure 5.6. The synchrotron peak energy, $E_{\rm p,syn}$ is determined by the energy of the first and second order IC peak energies ($E_{\rm p,IC}$, $E_{\rm p,IC2}$) in the SSC model through $E_{\rm p,syn} \approx E^2_{\rm p,IC1}/E_{\rm p,IC2}$, where $E_{\rm p,IC1}$ is the peak of the Band function measured by Konus. Since Milagro limits exclude the 20 – 200 GeV peak energies of the second order IC component, the corresponding $E_{\rm p,syn}$ in the 2 – 16 eV range is equivalently excluded.

Due to the apparent correlation in time and different spectral properties of the optical and gamma-ray emission from GRB 080319B (i.e. the extrapolation of the gamma-ray spectrum to lower energies under-predicts the optical emission by several orders of magnitude), the SSC model offers a "natural" explanation but is not without problems. One such problem is that the first-order IC spectrum is predicted to follow $F_\nu \propto \nu$ below the self-absorbed photon energy ($\sim$ 100 keV) whereas a significantly softer spectrum $F_\nu \propto \nu^{0.2}$ was measured by Konus. Considering the constraints from synchrotron self-absorption in GRB 080319B, Zou *et al.* (2009a) show that for reasonable assumptions of the bulk Lorentz factor ($\Gamma \sim 500$ – 1000), small values ($\lesssim 30$) of the Compton parameter Y are forbidden. On the other hand, the Milagro upper limits presented here serve to directly rule out the possibility of large values of Y. Consequently, the SSC model cannot explain the observed properties of

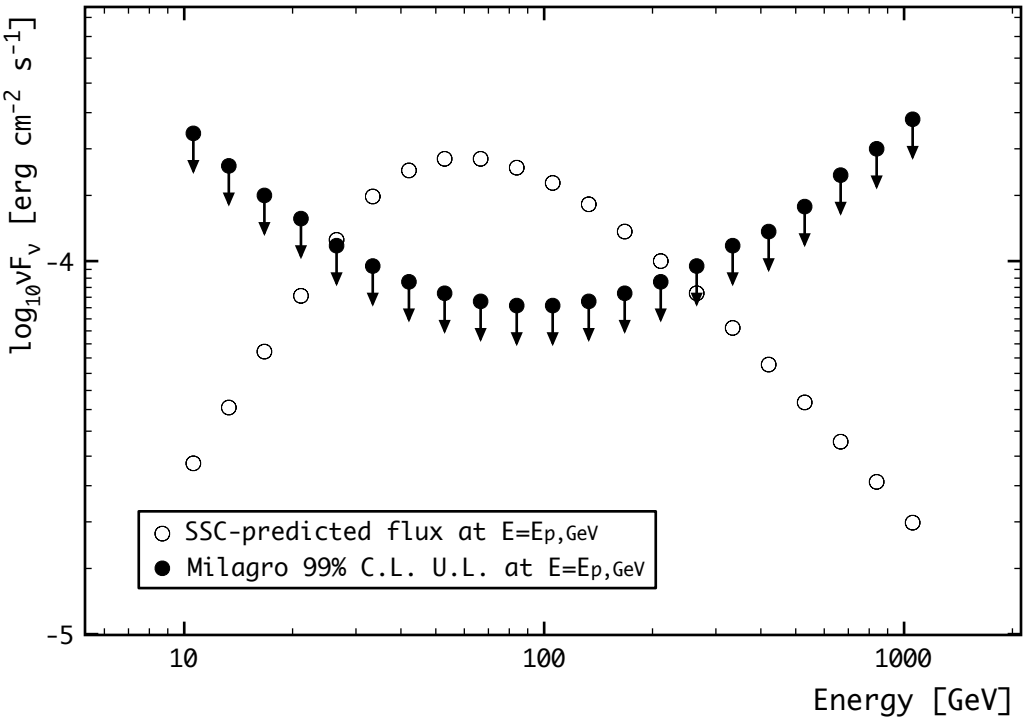

Figure 5.6: SSC-model-predicted prompt νF_ν flux at $E = E_{\rm p,GeV}$ (open points) plotted for several assumed values of $E_{\rm p,GeV}$ and the corresponding 99% confidence level upper limits obtained with Milagro using the scaler method described in the text (filled points). The Milagro limits account for attenuation of the high-energy gamma-ray flux by both Klein-Nishina suppression at the source and from the EBL using the model of Gilmore *et al.* (2009).

GRB 080319B. However, if one instead supposes that the prompt optical and gamma-ray photons are produced in separate physical regions (i.e. not correlated), then the observed spectra may be reproduced while additionally allowing for a reasonable, but not extreme high-energy component (Zou *et al.*, 2009a).

The unique qualities of GRB 080319B, particularly the intensity of optical emission associated with the prompt phase of the event, challenge some of the standard theoretical models of GRBs. Perhaps the most natural explanation of the emission detected from GRB 080319B is provided by the SSC model, where the gamma rays and optical photons are produced in the same physical region. Such a model, however, predicts the existence of a bright spectral peak in the 10s to 100s of GeV, within the energy range and sensitivity of the Milagro detector. The Milagro data associated with GRB 080319B show no significant gamma-ray signal using either the standard air-shower or scaler analyses. The resulting upper limits on the gamma-ray flux constrain the second order Compton parameter, Y_2, to be well below that predicted by the SSC model across a broad range of energies, disfavoring this scenario in these cases.

This result is the only direct experimental constraint on the high-energy emission from GRB 080319B and demonstrates the power of a large-area, wide field of view, continuously-operating VHE observatory with respect to GRB observations. A next-generation extensive air shower array dubbed the High Altitude Water Cherenkov (HAWC) observatory is currently under construction and is expected to provide a 15-

fold increase in sensitivity compared to that of Milagro (Abeysekara *et al.*, 2011). It is predicted that HAWC could detect GRBs with characteristics similar to some *Fermi*-LAT-detected bursts (e.g. GRB 090510 (De Pasquale *et al.*, 2010) and GRB 090902B (Abdo *et al.*, 2009b)) and information provided by HAWC on the high-energy spectrum of GRBs could greatly improve our understanding of GRB physics.

Chapter 6

Very Energetic Radiation Imaging Telescope Array System (VERITAS)

6.1 Introduction

VERITAS, the Very Energetic Radiation Imaging Telescope Array System, is an array of four optical reflectors, 12 m in diameter, located at the Fred Lawrence Whipple Observatory in southern Arizona (31°40′30″ N, 110°57′07″ W) at an altitude of 1268 m above sea level (Figure 6.1). At the focus of each of the four telescopes is an imaging camera consisting of 499 PMTs maximally sensitive to blue – UV photons. The array detects gamma rays using the imaging atmospheric Cherenkov technique,

Figure 6.1: The VERITAS array at the Fred Lawrence Whipple Observatory. The array configuration seen here is the new (post-Summer, 2009) configuration which leads to relatively uniform separation distances (roughly 100 m) between the telescopes.

which is described in further detail in the following section (6.2). The first VERITAS telescope started observations in early 2005 and the experiment has been operating in its full, four telescope configuration since April, 2007. In Summer, 2009, one of the four telescopes was moved in order to improve the base-line spacing of the array which in turn led to better sensitivity primarily through improved angular resolution.

VERITAS is a second-generation IACT system, the field of ground-based IACT astronomy having been pioneered with the Whipple 10 m reflector (Weekes *et al.*, 1989) and later with the stereoscopic High Energy Gamma-Ray Astronomy (HEGRA) array (Pühlhofer *et al.*, 2003). The VERITAS array has a sensitive energy range extending from $\sim$ 100 GeV to several tens of TeV, with an energy resolution of 15% at 1 TeV. The field of view of the instrument is 3.5° with an angular resolution

of approximately 0.1°. Although IACT instruments like VERITAS are much more sensitive than EAS arrays (e.g. Milagro), they have much lower duty cycle, ($\sim 11\%$) due to the need for darkness and good weather conditions for operation. In a typical calendar year, VERITAS currently obtains about 1000 h of observations.

In this chapter the imaging atmospheric Cherenkov technique and its implementation with respect to VERITAS is explained. The VERITAS telescopes and data acquisition systems are described with an emphasis on the system performance with respect to GRB follow-up observations.

6.2 The Imaging Atmospheric Cherenkov Technique

The imaging atmospheric Cherenkov technique is a method to detect EASs using images of the Cherenkov light generated by the relativistic particles in the shower as they pass through the atmosphere and to reconstruct the energy, direction, and species of the primary particle. The distribution of Cherenkov radiation reaching the ground from an EAS is dependent on several characteristics of the primary particle including energy, interaction height and inclination angle relative to the Earth's surface. While the Cherenkov emission is beamed strongly along the trajectory of the primary particle, the emission angle (relative to the trajectory of the primary particle) of the radiation is actually a function of the refractive index of the medium through which the relativistic particles are passing. The atmosphere becomes denser as the particles penetrate deeper and the emission angle increases. If one assumes a

primary particle traveling directly downwards, the distribution of Cherenkov light on the ground will be a circle with a radius of ~ 120 m. The edge of this light pool will be brighter due to the elevation-dependent index of refraction of the atmosphere (see Figure 6.2).

The duration of the Cherenkov light pulse from a typical EAS is about 4 ns. The photon density of this pulse on the ground is again dependent on several characteristics of the primary particle, but is usually a few tens of ph/m^2. For comparison, the photon density of the night sky background (NSB) in roughly the same waveband as the Cherenkov light produced by the shower is $\sim 10^9$ ph m^{-2} s^{-1}. In order to pick out the flash of Cherenkov light from the shower, the detector must be able to integrate the light pulses on the timescale of the shower. For example, VERITAS samples the photon flux at the camera every 2 ns and is thus able to resolve the light produced by the EAS from the NSB. For IACT instruments like VERITAS it is desirable to maximize the collection area of the mirror and the photon detector sensitivity while minimizing the integration time. If the time resolution is sufficiently good, information on the temporal qualities of the air shower can be used to better quantify the properties of the primary particle. Shower timing information is not yet used in VERITAS, however, and is beyond the scope of this work.

In addition to resolving the shower light from the NSB, there is another background that must be dealt with when attempting to detect gamma rays using the imaging atmospheric Cherenkov technique. Much like EAS arrays, IACT instru-

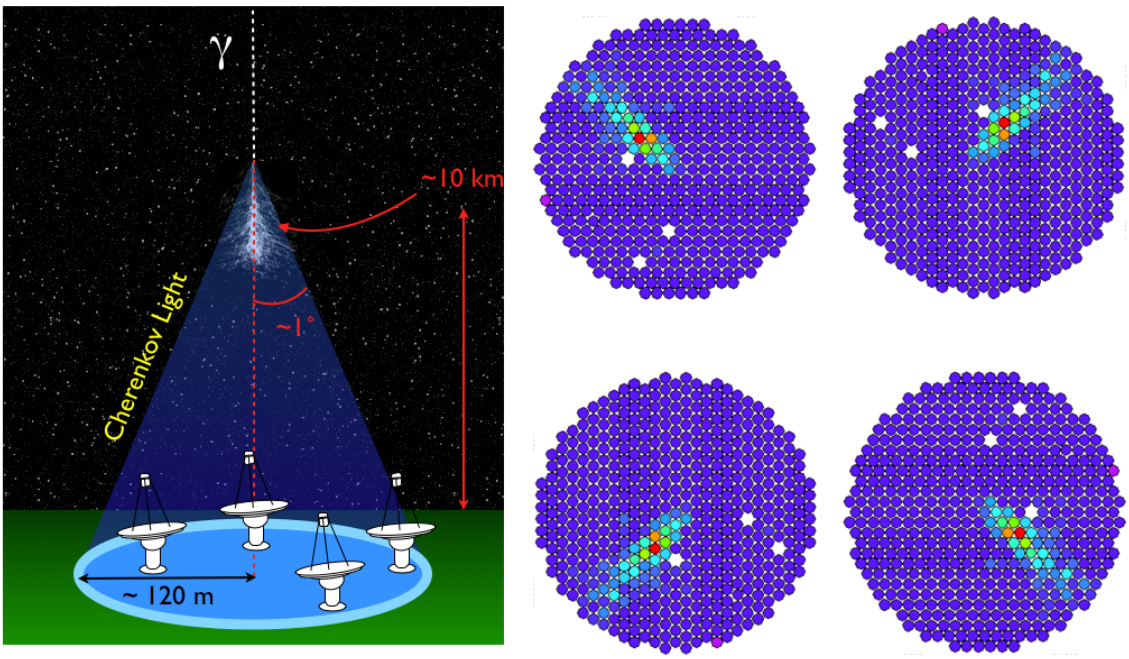

Figure 6.2: *Left:* A cartoon illustrating the distribution of Cherenkov light on the from a gamma-ray-generated EAS. The figure is not to scale but it illustrates the effect of the varying refractive index of the atmosphere and the subsequent creation of the Cherenkov ring. *Right:* Resulting camera images from a gamma-ray shower similar to the one shown in the cartoon, that is, with the axis of the shower intersecting the Earth's surface roughly in the middle of the array.

ments must be able to distinguish the showers produced by gamma-ray primaries from those produced by the much more ubiquitous hadronic primaries. This is accomplished in two ways: classification based at the shape of the shower image and by the image orientation relative to the putative source direction. A brief description of the differences between gamma-ray-initiated and hadron-initiated air showers can be found in Section 2.2. With respect to the distribution of Cherenkov light, air showers produced by gamma-ray primaries create images that are more compact and regular than images resulting from showers produced by hadronic primaries. The sub-showers present in hadronic showers give a substantial lateral spread of the light-producing relativistic particles, which in turn produce much more irregular images.

Air showers that have their major axis parallel to the optical axis of the telescope (and hence may be from the putative source being observed), produce a roughly elliptical image in the camera (Figure 6.2). The axis of the image intersects the location of the observed source in the camera. Since the flux of hadronic primaries is isotropic, the elliptical shower images produced by these particles are oriented randomly in the camera. By filtering out the images whose major axis does not intersect the source position in the camera, much of the hadronic background can be eliminated. A more technical and detailed explanation of the method of hadron rejection can be found in Section 8.1.

The use of multiple Cherenkov telescopes to simultaneously image air showers offers a significant improvement in sensitivity over using just a single telescope and

all current-generation IACT instruments utilize arrays of Cherenkov telescopes. In addition to increasing the effective area of the system, stereoscopic shower imaging provides improved low-energy sensitivity due to the elimination of triggers from NSB fluctuations in a single camera. It also improves hadronic background rejection by providing different views of the shower and by eliminating triggers from relativistic muons local to a single telescope which are common in hadronic showers.

A typical Cherenkov telescope consists of a large, segmented mirror mounted on a drive system to enable pointing and tracking. The angular resolution of the telescope is quite poor compared to optical telescopes since the EASs being imaged are relatively extended (on the order of several arc minutes). The mirror reflects the Cherenkov light onto a camera consisting of UV/blue-sensitive, fast photon detectors (typically PMTs). While the angular resolution of these instruments need not be very good, a high reflectivity and a large reflector are important and allow for imaging of smaller, dimmer showers from lower-energy primary particles. A description of the VERITAS telescopes and data acquisition systems is provided in the following section.

6.3 The Telescopes and Data Acquisition System

6.3.1 Telescopes

Each of the four VERITAS telescopes consists of a positioner system capable of moving the telescope in altitude and azimuth independently. The positioned system is

located at the top of a $\sim$ 6 m tall pedestal. The segmented mirrors of the reflector are mounted on a tubular steel, custom-manufactured optical support structure (OSS). The camera is mounted on a steel quadrupod at the 12 m focus of the mirror. The torque on the system from the camera is balanced by counterweights located behind the OSS. The system is currently configured to slew at 1° s^{-1} independently in altitude and azimuth. The orientation of the altitude and azimuth positioners is recorded four times a second and used by the tracking software (described in more detail in Section 7.2) to adjust telescope pointing speed and acceleration. This system gives an overall pointing accuracy of $\lesssim 0.01^{\circ}$.

The optical principles of the shape and orientation of the segmented mirrors used in VERITAS follow the Davies-Cotton design (Davies and Cotton, 1957). On the OSS of each telescope, 342 identical, hexagonal mirror facets are mounted which results in a total mirror area of $\sim$ 110 m^2 (Figure 6.3). Each mirror facet has a radius of curvature of 24 m and is constructed from slumped, ground, and polished glass with an anodized aluminum overcoating. The mirror reflectance is better than 80% over the wavelength range relevant to Cherenkov light (280 nm – 450 nm) and is better than 90% at the peak Cherenkov radiation wavelength of 320 nm (Figure 6.4). The reflectivity of the mirrors degrades over time due to weathering so a schedule of regular re-coating and replacement of mirror facets is followed which results in $\sim$ 350 mirrors being reconditioned annually.

The PMTs (with light concentrators) in the VERITAS camera subtend an angle of

Figure 6.3: A picture of one of the VERITAS telescopes which shows the segmented mirror facets and the tubular steel OSS.

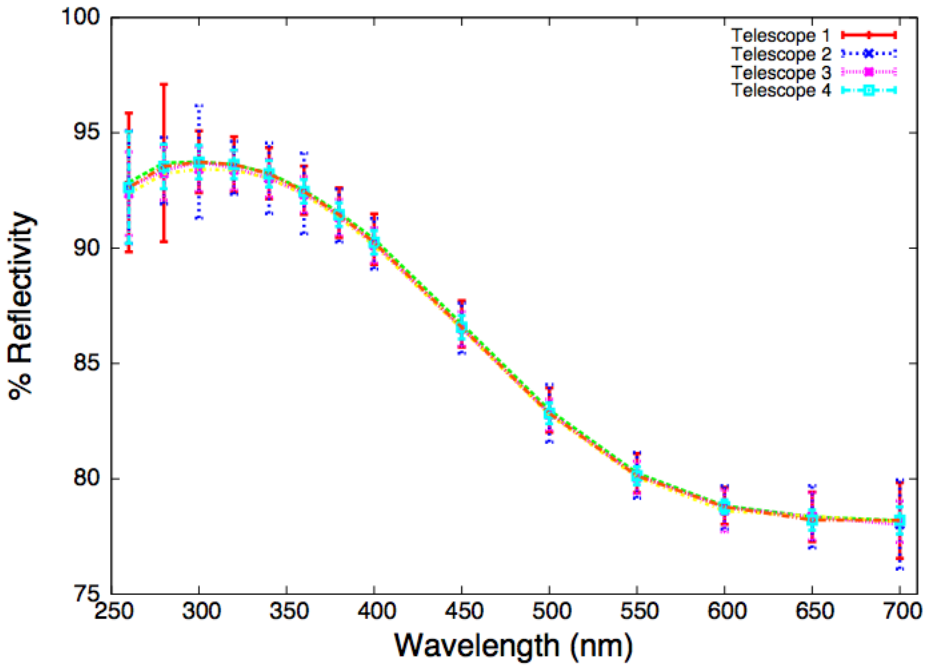

Figure 6.4: Reflectivity of the VERITAS telescopes as a function of wavelength (Roache *et al.*, 2008).

0.15° on the sky. This sets the maximum tolerance for mirror misalignment. In other words, the mirrors just need to be aligned well enough to focus a point source of light at infinity to a spot small enough to be contained in a single camera pixel (PMT). Optical aberrations in both the individual facets and the composite mirror (coma and astigmatism) contribute to the optical point spread function (PSF) of the telescope, but these effects are often small, however, compared to the effect of misaligned mirror facets. Mirror facets become misaligned when they are replaced and also from flexure in the OSS. Misaligned mirrors are found by installing a wide-FOV CCD camera in front of the PMTs, facing the mirror facets. The telescope is then pointed at a bright (mag. < 3) star and images of the mirror facets are taken while the telescope scans around the region of the star. Software that analyzes the illumination of each mirror facet as a function of telescope pointing then determines the required adjustments for each facet. The adjustments to each facet are then done by hand. The effect of the alignment procedure can be seen in Figure 6.5 and is described in detail in McCann *et al.* (2010).

At the focus of each reflector is a camera consisting of 499 Photonis XP 2970/02 PMTs. The angular separation between the PMTs is 0.15° and in front of each PMT is a concentrating light cone which reduces dead space between the PMTs and focuses the light on the center of the PMT photocathode (Figure 6.6). Each PMT has a nominal gain of 2×10^5 at potential difference of 850 V. The quantum efficiency of the PMT photocathode peaks at 320 nm which was chosen to match closely with

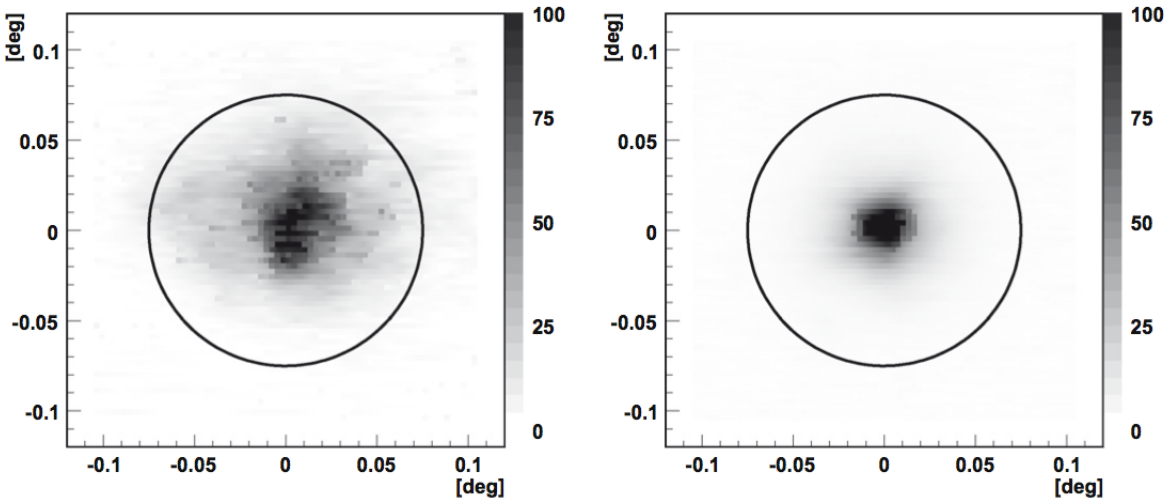

Figure 6.5: Improvement (before: left, after: right) of the VERITAS PSF from mirror alignment. The solid circle represents the size of a VERITAS pixel (McCann *et al.*, 2010)

the peak of the Cherenkov spectrum from air showers at ground level. A PMT base including a low-noise transimpedance preamplifier AC couples and converts the PMT current signal to a voltage signal with a gain of $\sim$ 7 and bandwidth of 300 MHz. The DC current of each PMT is monitored with a resolution of 0.5 μA ten times a second. The system is designed to automatically suppress the PMT voltage of any pixel whose current is above 40 μA or above 30 μA for several seconds in order to prevent damage to the PMTs. The voltage signals from the PMT preamplifiers are connected to the trigger electronics and the data acquisition systems.

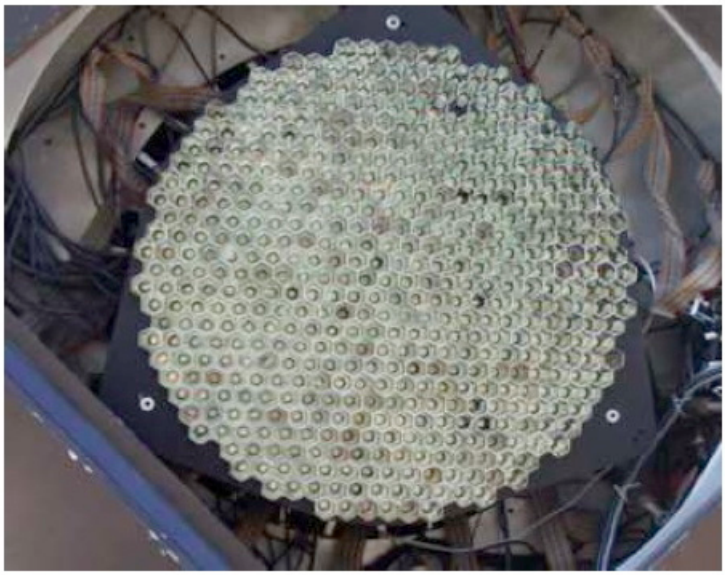

Figure 6.6: The VERITAS camera with concentrating light-cones installed (Nagai *et al.*, 2008).

6.3.2 Trigger and Data Acquisition Systems

The VERITAS trigger system is designed to distinguish light from potential air-shower events from ambient and NSB light as well as local muons. The trigger consists of three hierarchical conditions at the pixel, camera, and array level (L1, L2, L3), respectively. A simplified diagram of the trigger systems is shown in Figure 6.7. An array-level (L3) trigger constitutes an event and initiates a readout by the data acquisition system.

The pixel-level (L1) trigger is a programmable constant-fraction discriminator (CFD) which generates a logic pulse whenever a PMT signal exceeds the set voltage. The VERITAS CFD design (Figure 6.8) differs from a standard CFD as it has a rate feedback circuit that changes (the amount is programmable) the zero-crossing

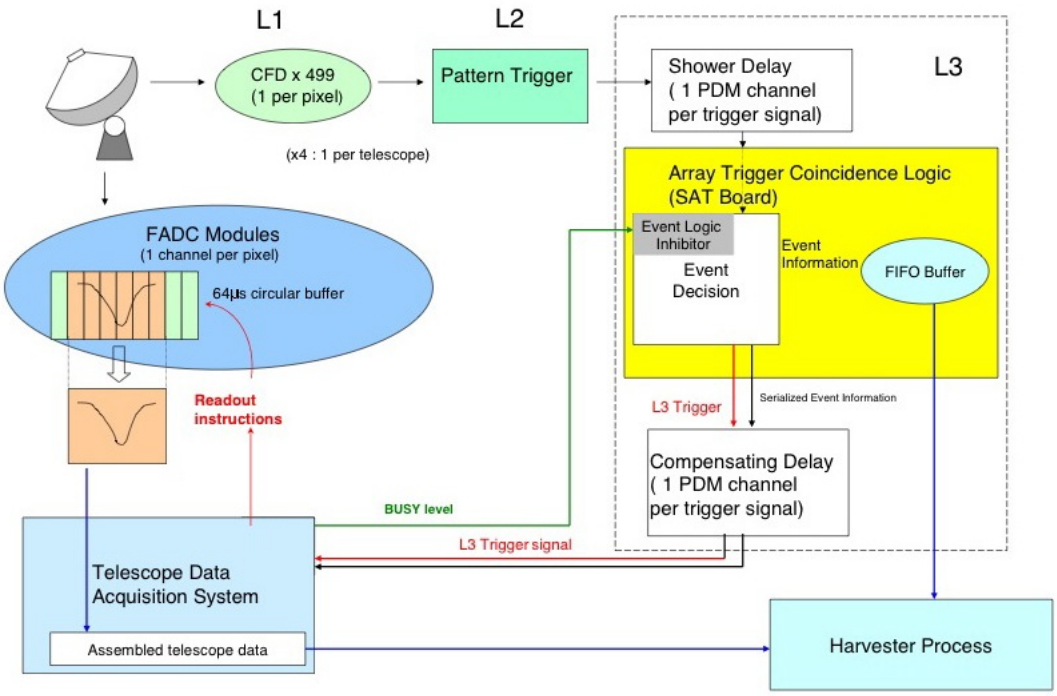

Figure 6.7: Diagram of the VERITAS trigger levels and data acquisition systems (Weinstein, 2008). The components are described in the text.

discriminator (ZCD) offset based on the ZCD trigger rate. This extra circuit reduces timing jitter and stabilizes the pixel trigger rate in the presence of changing NSB levels (e.g. a galactic vs. extragalactic field). For standard, dark sky VERITAS operation the threshold discriminator (TD) is set to 50 mV (corresponding to 4 – 5 photoelectrons). When the CFD is triggered, a 10 ns logic pulse is generated and these pulses are the input for the camera-level (L2) trigger.

The camera-, or telescope-level trigger (L2) is designed to trigger on Cherenkov-light images of air showers. Fluctuations in the NSB or PMT after pulsing can cause spurious L1 triggers in a telescope camera, sometimes even in several pixels simultaneously. In order to help differentiate these spurious L1 triggers, which occur randomly across the camera, from L1 triggers that occur due to air showers and which appear as clusters of triggered pixels, the L2 trigger condition is met only when several adjacent pixels trigger.[1] The logic signals from each of the PMTs in a camera are split into 3 slightly overlapping camera regions and each of these regions is searched simultaneously for N adjacent pixels (for standard VERITAS operation, $N = 3$). If such a condition is satisfied a logic signal is then sent to the array-level (L3) trigger.

The L3 trigger condition is satisfied when the L2 is triggered in some (programmable) combination of telescopes. For normal VERITAS operation the L3 trigger is set for a combination of any 2 telescopes in the array. Timing is everything in the L3 trigger, and a programmable delay of the incoming L2 signals ensures that

[1]The L2 trigger was recently upgraded and the brief description that follows is of the new system. The prior system implemented the same adjacent pixel requirement in a different fashion. The results presented later in this work were obtained using both the old and new L2 systems.

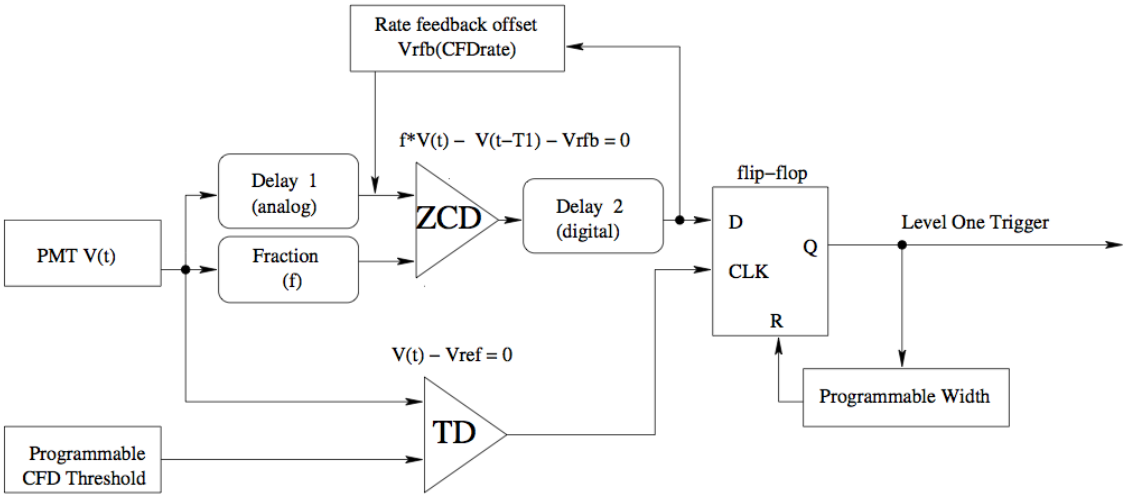

Figure 6.8: Schematic of the pixel-level (L1) trigger, which includes a novel rate-feedback circuit for improved performance in the presence of NSB light (Hall *et al.*, 2003). ZCD and TD are explained in the text.

a single shower is responsible for the array trigger. These delays are applied by the pulse delay module (PDM) which has a 2 ns resolution and delay range from 100 ns to 6 μs (Weinstein, 2008). Delays for the relative distance between the telescopes and the physical location of the L3 and a pointing-dependent delay which compensates for the propagation of the shower front are required. When an L3 trigger occurs, a logic signal is sent back to each telescope which in turn signals the DAQ systems to begin readout. Since an L3 trigger constitutes an event, diagnostic information such as trigger rates and deadtimes can be (and are) calculated and recorded by the L3 system. Data from the L3 system is also sent to the array-level DAQ system (the harvester). The L3 trigger and associated system is quite complicated and a more

complete description can be found in Weinstein (2008).

In parallel with the triggering system, the analog signal from each PMT is continuously digitized by a 500 megasample per second flash analog to digital converter (FADC). A 16000 sample ring buffer holds the digitized information for the previous 32 μs. The signal from each PMT preamplifier is amplified by a factor of 7.25 and offset by $\sim$ 180 mV before being digitized. If the signal saturates the 8-bit range of the FADC, an automatic low-gain setting is implemented in which a copy of the original PMT signal, amplified by a factor of only 1.25 (vs. 7.25 for high-gain), is digitized. When an L3 trigger occurs, digitization is halted and a portion of the FADC memory, determined by a programmable lookback time and window size, is read to RAM for readout by the VME Data Acquisition (VDAQ) software. During readout of the FADCs (400 μs) a busy signal inhibits further L3 triggers. The digitized PMT signal information, L1 trigger status, and High/Low gain status from each PMT is recorded.

This information is then collected by the event builder software process which combines all of the data into a telescope event. Telescope events from all four telescopes in the array are then sent to the array-level DAQ software, the harvester. The harvester combines the individual telescope events into array level events. The data are then compressed and stored to disk in a custom disk format, the VERITAS Bank Format (VBF). For typical observing conditions, the stored data rate is about 15 GB/hr. This description of the DAQ system is quite abbreviated and a more detailed

explanation can be found in Hays (2008).

Chapter 7

Rapid Follow-Up Observations of GRB Afterglows with VERITAS

Since beginning operation, the VERITAS telescopes have been used to search for gamma-ray emission from satellite-detected GRBs. During this time, observations of more than 50 GRBs were made. These observations are among the most sensitive probes of the characteristics of the prompt to early afterglow emission of GRBs at energies above $\sim$ 100 GeV. The motivation for searching for gamma-ray emission during the prompt and early afterglow phases of GRBs with instruments like VERITAS is outlined in Sections 1.4 and 1.6. It is predicted that very high energy photons with relatively late emission times (up to several hours) may be produced by SSC processes in GRB shocks. These photons would be prime candidates for detection by ground-based, imaging atmospheric Cherenkov telescope (IACT) systems (Xue

et al., 2009, Zou *et al.*, 2009a) such as VERITAS. Though detection of VHE afterglow emission with IACTs is predicted to be possible, observations by both previous (Connaughton *et al.*, 1997, Padilla *et al.*, 1998) and current-generation (Acciari *et al.*, 2011, Aharonian *et al.*, 2009, Albert *et al.*, 2007) observatories have yielded no significant detections. This chapter describes VERITAS GRB observations as well as the strategy behind and technical details of performing these observations.

7.1 Satellite-triggered Observations

Observations of GRBs take priority over all others in the VERITAS observing plan. Since VERITAS has a relatively narrow FOV and limited duty cycle (Chapter 6), the telescope array must be repointed to observe the GRB, to the exclusion of all other observations. The odds of a burst occurring serendipitously in the VERITAS FOV is extremely low and is not expected to occur in the lifetime of the experiment.

VERITAS takes follow-up observations for GRBs detected by several gamma-ray satellites including *Swift*, *Fermi*, AGILE, and INTEGRAL. VERITAS observations are triggered if the satellite-detected GRB is above 20° elevation and the conditions are sufficiently dark to allow VERITAS operation. The duration of GRB observations by VERITAS is dependent on the quality of the GRB localization. If the localization of the GRB by the satellite is sufficiently good, i.e. smaller than the FOV of VERITAS, the observing window lasts for three hours after the burst trigger, subject to observing constraints, such as elevation. If the localization is poor but is better than

10° (68% containment radius), VERITAS observes the center of the error circle for 1 hour, again subject to observing constraints. This is the situation for most GRBs detected by the Gamma-ray Burst Monitor (GBM) instrument onboard *Fermi*. If the 68% containment radius of the localization is greater than 10°, the GRB is not observed with VERITAS.

The transition from the prompt to the afterglow phase of a GRB, which can occur hundreds to thousands of seconds after the initial burst, is often accompanied by X-ray flares (Chincarini *et al.*, 2007). These flares can be very bright and may be associated with extended activity from the GRB central engine (Burrows *et al.*, 2005) or be from delayed external shocks that could produce a relatively large flux of gamma rays in the $\sim$ 100 GeV energy range. For GRBs, the VERITAS strategy of rapid follow-up observations that continue for several hours allows for good temporal coverage of X-ray flare phenomena. Even in the absence of flare activity, it is suggested that a significant flux of high-energy photons from IC processes associated with the GRB afterglow may extend to more than 10 ks after the beginning of the GRB prompt emission (Galli and Piro, 2008) and so an observation window of several hours is warranted.

The results from GRB observations by VERITAS which are presented later in this work will be confined to well-localized GRBs. Most of these bursts are detected and localized by the *Swift* Burst Alert Telescope (BAT) a CdZnTe coded mask instrument with a relatively large (1.4 sr) FOV and sensitive to gamma rays in the

15 – 150 keV energy range (Gehrels *et al.*, 2004). Upon a repointing of the *Swift* satellite, further positional refinement and lower-energy observations are made using the X-ray Telescope (XRT) and Ultraviolet and Optical Telescope (UVOT) onboard the spacecraft. Table 7.1 lists the characteristics of the well-localized GRBs observed above 25° elevation since 2007 January up to this writing. The weather conditions during observations of the burst presented here were good to fair (some high clouds present) and with dark skies or low moonlight illumination. GRB observations with VERITAS are ongoing and are expected to continue for several more observing seasons, contingent upon approval of observing time from the VERITAS time allocation committee.

Time is of the essence with GRB observations and minimizing the time between satellite GRB trigger and the beginning of VERITAS GRB observations is of paramount importance. Using the GCN, the VERITAS observers on duty are notified as quickly as possible of the satellite detection of a GRB and are instructed to repoint the telescopes to the location of the GRB immediately barring circumstances that would risk the safety of observers or the instrument. The details of the rapid GRB alert software and telescope pointing and tracking subsystems are described in detail in the following section.

Table 7.1: Details of *Swift*-detected GRBs triggering observations by VERITAS since 2007 January

GRB	*Swift* trigger	T_{90}(s)$^{\alpha}$	Fluence $^{\beta}$	T^{γ}_{trig}	RA	Dec	Error	z
070223	261664	89	17	01:15:00	$10^h13^m48^s.39$	$+43°08'00.70''$	$0.30''$	...
070419A	276205	116	5.6	09:59:26	$12^h10^m58^s.83$	$+39°55'34.06''$	$0.15''$	0.97^{δ}
070521	279935	37.9	80	06:51:10	$16^h10^m38^s.59$	$+30°15'21.96''$	$1.70''$	$0.553?^{\epsilon}$
070612B	282073	13.5	17	06:21:17	$17^h26^m54^s.49$	$-08°45'06.3''$	$4.0''$	...
071020	294835	4.2	23	07:02:26	$07^h58^m39^s.78$	$+32°51'40.4''$	$0.250''$	2.145^{ζ}
080129	301981	48	8.9	06:06:45	$07^h01^m08^s.20$	$-07°50'46.3''$	$0.3''$	...
080310	305288	365	23	08:37:58	$14^h40^m13^s.80$	$-00°10'29.60''$	$0.6''$	2.43^{η}
080330	308041	61	3.4	03:41:16	$11^h17^m04^s.50$	$+30°37'23.53''$	$0.7''$	1.51^{θ}
080409	308812	20.2	6.1	01:22:57	$05^h37^m19^s.14$	$+05°05'05.4''$	$2.0''$	...
080604	313116	82	8.0	07:27:01	$15^h47^m51^s.70$	$+20°33'28.1''$	$0.5''$	1.416^{ι}
080607	313417	79	240	06:07:27	$12^h59^m47^s.24$	$+15°55'08.74''$	$0.5''$	3.036^{κ}
081024A	332516	1.8	1.2	05:54:21	$01^h51^m29^s.71$	$+61°19'53.04''$	$1.9''$	...
090102	338895	27	68	02:55:45	$08^h32^m58^s.54$	$+33°06'51.10''$	$0.5''$	1.55^{λ}
090418A	349510	56	46	11:07:40	$17^h57^m15^s.17$	$+33°24'21.1''$	$0.5''$	1.608^{μ}
090429B	350854	5.5	3.1	05:30:03	$14^h02^m40^s.10$	$+32°10'14.6''$	$1.8''$	9.4^{ν}
090515	352108	0.036	0.04	04:45:09	$10^h56^m36^s.11$	$+14°26'30.3''$	$2.7''$	...
090929B	371050	360	59	10:09:07	$07^h50^m52^s.84$	$-0°39'27.5''$	$1.8''$	...
091024	373674	110	61	08:56:01	$22^h36^m59^s.70$	$+56°53'23.4''$	$0.5''$	1.092^{ξ}
100205A	411248	26	4	04:18:43	$09^h25^m33^s.00$	$+31°44'25.8''$	$1.7''$	...
100420A	419932	48	5.7	05:22:42	$19^h44^m30^s.57$	$+55°46'10.0''$	$0.3''$	...
100615A	424733	39	50	01:59:03	$11^h48^m49^s.25$	$-19°28'52.2''$	$1.7''$	...
110201A	444230	13	7.0	09:35:08	$09^h08^m16^s.12$	$+88°36'27''$	$2.3''$	$< 1^{o}$
110205A	444643	257	170	02:02:41	$10^h58^m31^s.13$	$+67°31'30.8''$	$1.5''$	2.22^{π}
110928A	504215	26.7	6.9	01:51:31	$17^h10^m55^s.91$	$+36°32'08.5''$	$2.2''$	...
111029A	506519	7.6	3.9	09:44:40	$02^h59^m08^s.10$	$+57°06'40.4''$	$2.5''$	...
111225A	510341	106.8	13	03:50:37	$00^h57^m32^s.34$	$+51°34'17.6''$	$2.2''$	...
120119A	512035	253.8	170	04:04:30.21	$08^h00^m06^s.90$	$+09°04'54.4''$	$1.4''$	1.728^{ρ}
120215A	515015	26.5	4.0	00:41:15	$02^h00^m11^s.41$	$+08°48'06.4''$	$2.0''$	...

All information was taken from GCN circulars (http://gcn.gsfc.nasa.gov/gcn3_archive.html) except where cited. $^{\alpha}$Duration over which 90% of the emission in the 15–350 keV energy band occurs, as measured by the *Swift*-BAT. $^{\beta}$15–150 keV fluence, as measured by the *Swift*-BAT (erg cm^{-2} s^{-1}). $^{\gamma}$ UT time of the GRB trigger determined by the *Swift*-BAT. $^{\delta}$Cenko *et al.* (2007). $^{\epsilon}$Hattori *et al.* (2007). $^{\zeta}$Jakobsson *et al.* (2007). $^{\eta}$Prochaska *et al.* (2008a). $^{\theta}$Malesani *et al.* (2008). $^{\iota}$Wiersema *et al.* (2008). $^{\kappa}$Prochaska *et al.* (2008b). $^{\lambda}$de Ugarte Postigo *et al.* (2009). $^{\mu}$Chornock *et al.* (2009). $^{\nu}$Cucchiara *et al.* (2011). $^{\xi}$Cucchiara *et al.* (2009). ^{o}Rumyantsev *et al.* (2011). $^{\pi}$Cenko *et al.* (2011a). $^{\rho}$Cucchiara and Prochaska (2012).

7.2 The VERITAS GRB Alert and Tracking Subsystems

At VERITAS, the rapid response to satellite-detected GRBs is facilitated by the GRB alert and tracking software subsystems. The ability to obtain fast notification of GRBs detected by other instruments is made possible by the Gamma-ray bursts Coordinate Network (GCN - see Figure 7.1). The GCN notifications are the result of information received in real-time by the GCN system from the various spacecraft, processed into a standard format and automatically distributed to various ground-based instruments and observatories. No humans are involved in the GCN portion of the sequence, and for most satellite missions there is no human interaction required for the satellite response to GRBs. This automation minimizes the time delay between when the gamma-rays hit the instrument detectors and when the GRB position information is available to the follow-up instruments. A computer at the VERITAS site is constantly connected to the GCN via a TCP/IP socket connection and processes the GCN notices immediately as they become available.

Currently, the GRB alert software at VERITAS is configure to process GRB location notifications from the *Swift*, *Fermi*, AGILE, and INTEGRAL missions. When such a notification from one of these missions arrives at VERITAS, the grbalert daemon process parses the contents of the notification and performs a rudimentary filtering of the GRB information. If the GRB has a declination of less than $-30°$, the

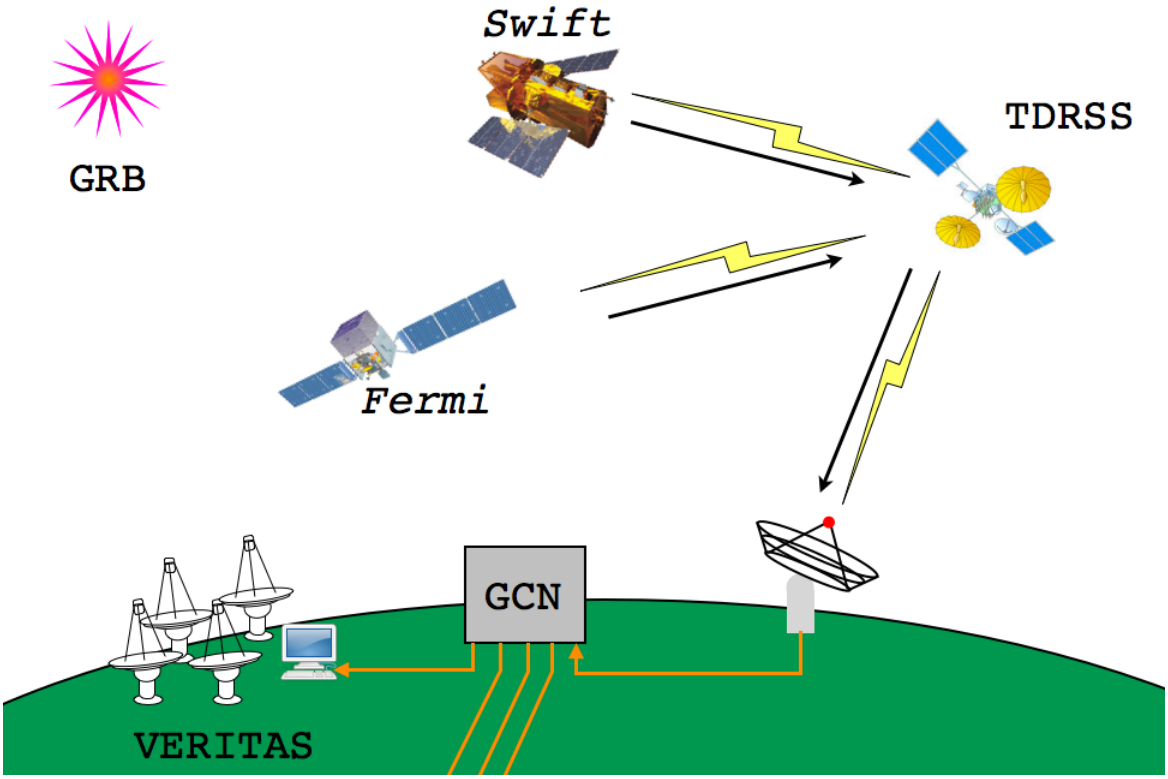

Figure 7.1: A diagram illustrating the communication of GRB detections from satellite-based instruments through the Tracking and Data Relay Satellite System (TDRSS), to the ground and through the GCN system to ground-based telescopes including VERITAS.

notice is thrown out, as this is too far south for VERITAS to successfully observe a GRB. The grbalert daemon also checks the error in the GRB localization from the satellite and ignores the burst if the 68% containment radius of the localization is greater than 10°. The *Fermi* and *Swift* missions also provide information on the likelihood of the triggering event actually being a GRB. The grbalert ignores notifications where the satellite-reported GRB probability is less than 50%.

If a GRB notification passes the filtering by the grbalert daemon, the position and other information on the burst is compiled into a common object research broker architecture (CORBA) object and passed between systems to the VERITAS pointing control software as well as to system in the control room that plays an audio alert that notifies the observers on duty that a possibly-observable GRB has been detected. The pointing control software then computes the elevation of the GRB at the VERITAS location and if the burst is above 20° elevation, the coordinates of the GRB are loaded automatically and the observers are given the option to immediately slew to the GRB position after they have confirmed that it is safe to do so. The observers are also instructed to extend the current run duration for an additional 20 minutes (a standard data run has a nominal 20 minute duration). A diagram of the GRB alert process is shown in Figure 7.2.

The pointing control system comprises a complex set of interconnected components whose purpose is to allow the telescope to track celestial objects accurately, and to ensure the integrity of the positioner, drive system, optical support structure

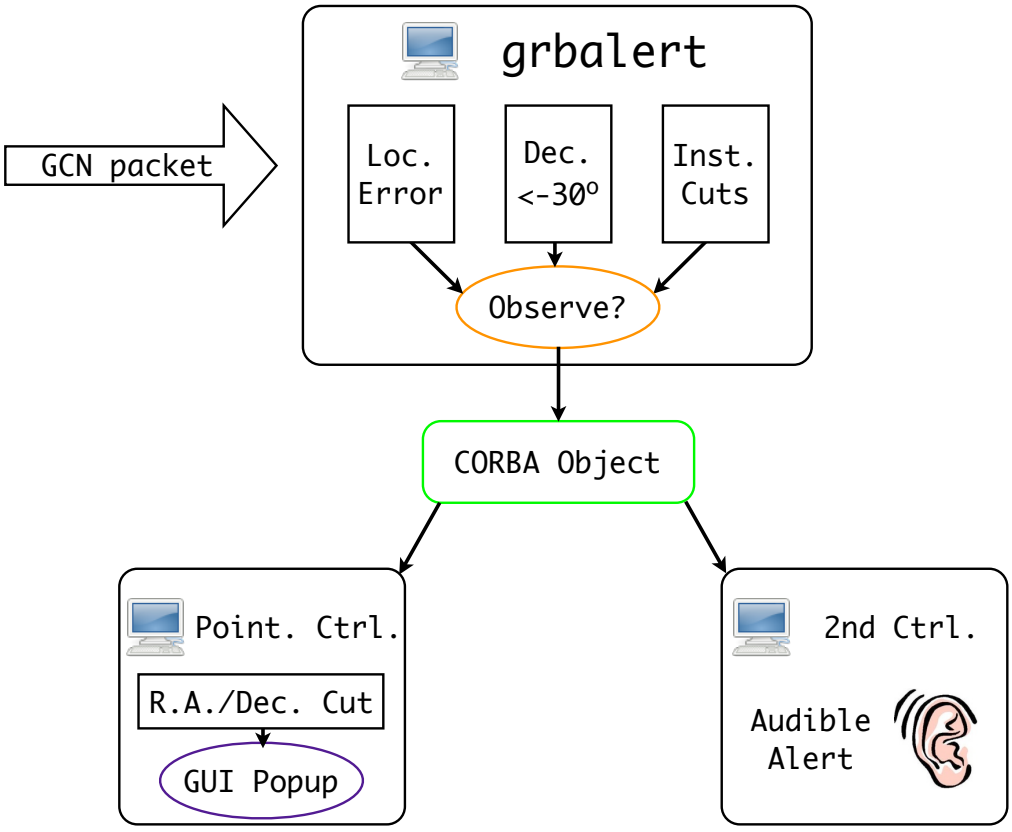

Figure 7.2: Diagram of GRB alert processing by the systems at VERITAS.

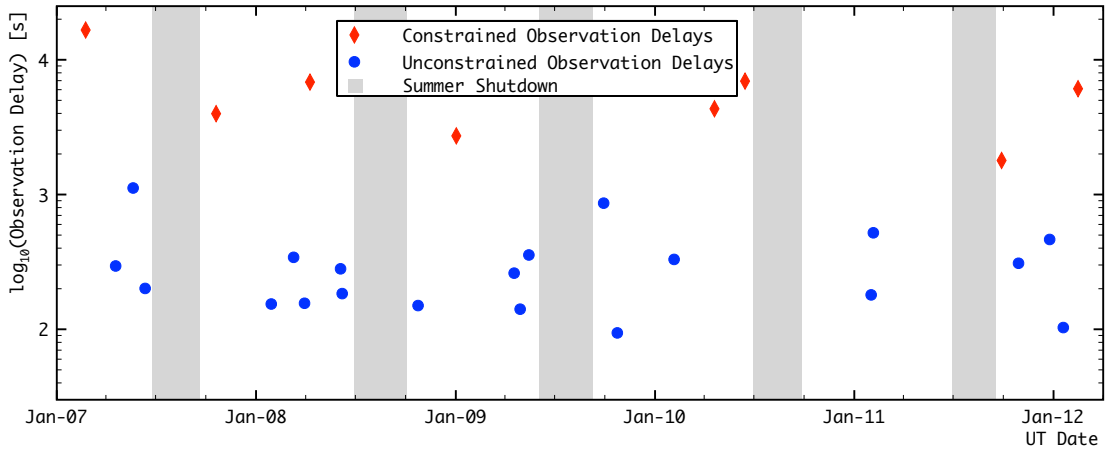

Figure 7.3: Plot of observation delays of the VERITAS-observed GRBs listed in Table 7.1. The red diamonds indicate bursts where the delays were affected by elevation, light level, or other environmental factor. The blue dots show unconstrained response times which incorporate time for satellite downlink, GCN distribution, and VERITAS processing of the GRB alert. The grey bands indicate the time during which VERITAS is shut down for the Summer monsoons.

and all components attached to the telescope such as the mirrors and focus box. At one end of the control system is the servo amplifier which provides current to the motors driving each axis and the encoders and tachometers which provide feedback of the mount position and speed. At the other end of the control chain is the tracking software which is responsible for communicating the operator's commands to the positioner, for monitoring and displaying the positioner status and for proving timely updates of the target position to the positioner if it is commanded to track a celestial object.

The VERITAS telescopes are currently configured to slew at a rate of 1°/s independently in altitude and azimuth. The time required to slew to a GRB is usually

the largest factor in the overall VERITAS GRB observation delays. Efforts are underway to increase the slewing speed of the VERITAS telescopes in order to reduce observing delays and these are briefly outlined in Section 7.4. Figure 7.3 shows the observation delays for the GRBs listed in Table 7.1. The delay between the satellite trigger and the beginning of GRB observations is usually less than 300 s if the burst is immediately observable. In several cases this delay is less than 100 s.

7.3 Observing GRBs under non-optimal conditions

For typical VERITAS observations of constant, or putatively constant gamma-ray sources, plans are made in advance and observing times are scheduled to coincide with dark, moonless nights and the times when the source is near culmination. High-elevation observations in dark skies and good weather give the highest sensitivity and lowest energy threshold for a given target. Since GRB observations cannot be planned in advance, these observations are taken in whatever conditions are present when the GRB occurs. By simple phase-space considerations, most GRBs will occur at relatively low elevations at the VERITAS location. The absolute intensity of GRBs in the VERITAS waveband is unknown and could conceivably be quite bright, so the loss of sensitivity due to moonlight or less-than-perfect weather conditions does not preclude GRB follow-up observations. These conditions do need to be taken into account, however, when analyzing these data. Finally, some GRB alerts have relatively poor localizations and an observing strategy for rapidly tiling large error

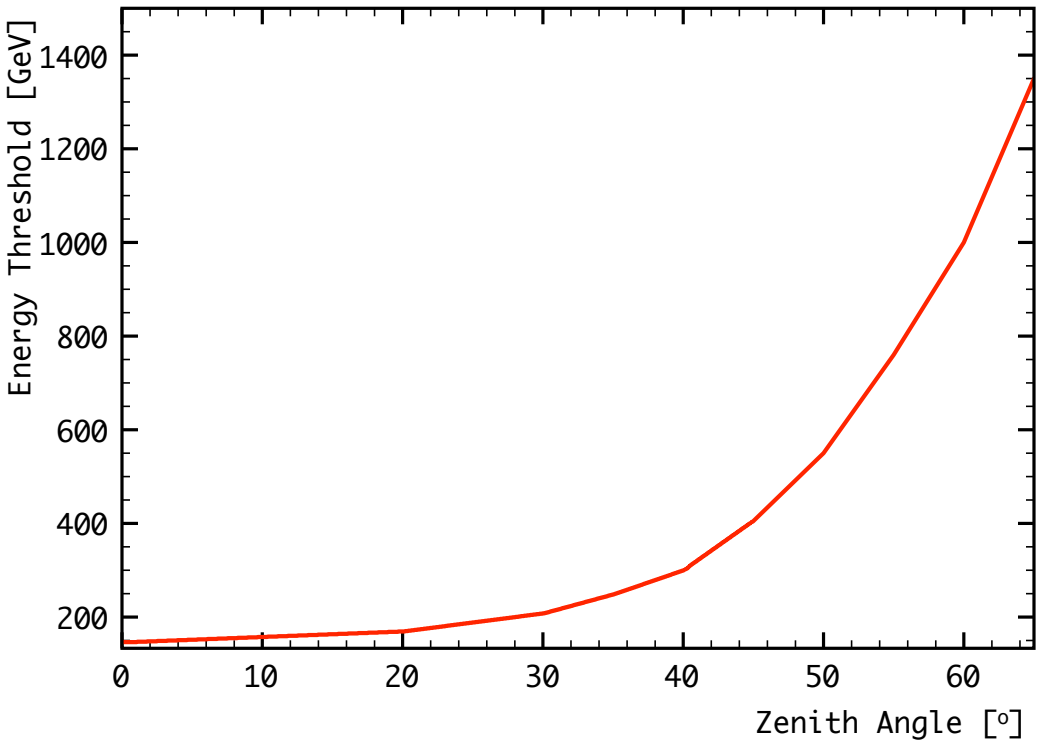

Figure 7.4: The VERITAS energy threshold as a function of zenith angle. The energy threshold is defined as the maximum of the differential counting rate of a Crab-like ($\frac{dN}{dE} \propto E^{-2.5}$) spectrum.

circles must be considered. This section describes the methods for dealing with the non-optimal conditions often present during GRB observations.

The most common and detrimental condition for GRB observations is low elevation. There are several compounding factors that affect low-elevation observations which serve both to raise the energy threshold of observations (which is particularly important for EBL-attenuated, extragalactic sources like GRBs), and reduce the overall sensitivity. Figure 7.4 shows the VERITAS energy threshold as a function of zenith angle. This effect is unavoidable as it is the result of the air showers

passing through more atmosphere which results in shower images appearing smaller for a given energy. Improving the low-energy response of VERITAS generally greatly improves the prospects for GRB observations since such improvements would enable a GRB of a given intensity to be detected at lower elevations or at greater cosmological distances. In addition to increased energy thresholds, low elevation observations also result in reduced sensitivity due to poor angular reconstruction of air showers. The ability to distinguish an excess flux of gamma rays from the cosmic-ray background is made more difficult if the point-source flux is smeared over a larger area of the sky. The advantages of stereoscopic observations become increasingly negligible as the individual telescopes' lines of sight become more parallel as is the case during low-elevation observations. The effect of zenith angle and energy on the angular resolution of VERITAS is shown in Figure 7.5.

Two other factors that can adversely impact GRB observations are weather conditions and moonlight illumination. In previous-generation IACT experiments and in the earlier days of VERITAS, observations were taken only during moonless nights. Over the last several observing seasons, VERITAS has begun taking observations in low-moonlight conditions. The increased night-sky background (NSB) from ambient moonlight raises the threshold and reduces the sensitivity of observations in these conditions. In cases when the moonlight is very bright, an adjustment of the CFD thresholds is required. Instrument simulations of high NSB conditions and non-standard CFD settings enables the accurate reconstruction of source flux and flux

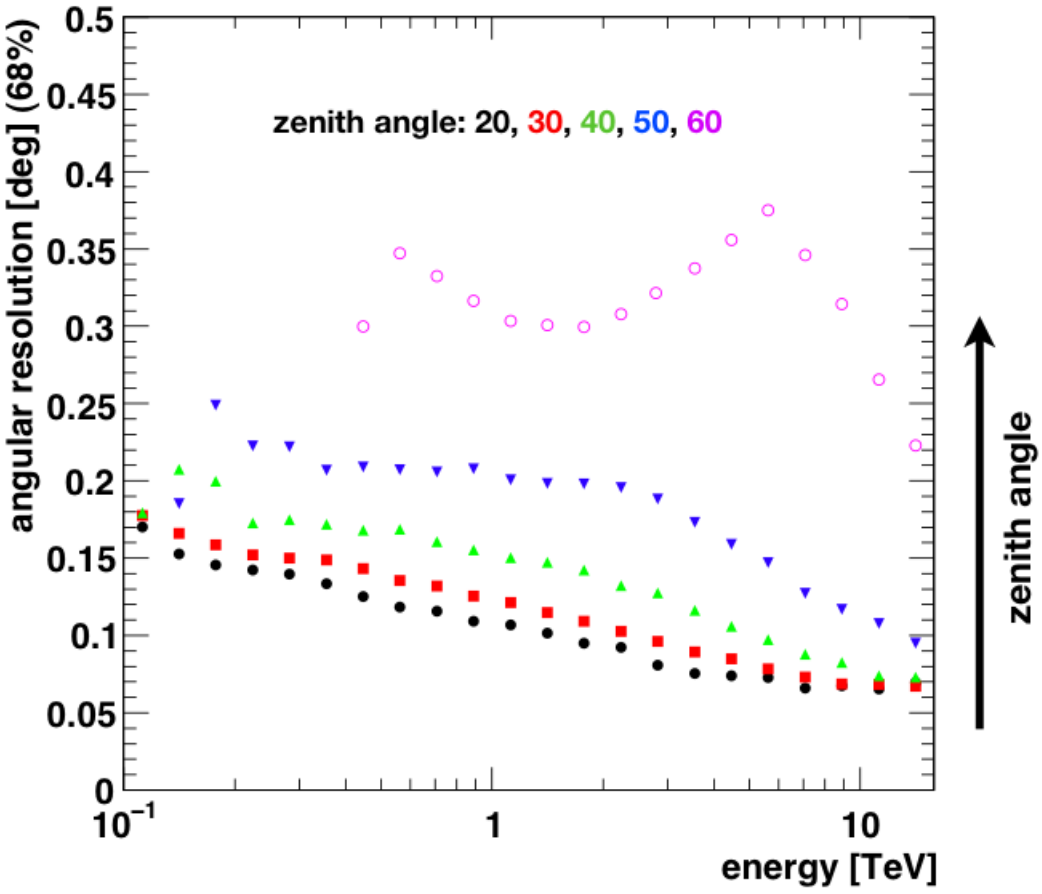

Figure 7.5: Angular resolution of VERITAS as a function of energy and zenith angle (90°− elevation). Figure credit: G. Maier

upper limits. While high-NSB observing conditions are not ideal, the increased observing time significantly increases the number of GRBs able to be observed annually.

Weather conditions at the VERITAS site are usually quite favorable for observations, though there are times when clouds may be present. If clouds are too thick, observations are impossible as light from the air showers is absorbed and scattered. To deal with scattered clouds VERITAS has several infrared radiometers that measure sky temperature and can indicate the presence of clouds. Since the amount of GRB data gathered in a single observing season is small, cutting out just the segments of cloudy data, rather than throwing out whole runs, is standard procedure. The development and installation of a LIDAR system at VERITAS should further improve weather and transparency measurements at VERITAS in the future but such a system was not yet in operation when the observations presented here were taken.

Finally, a majority of GRB alerts received at VERITAS are from the GBM instrument on *Fermi*. The localization capabilities of this instrument are limited and the location of a GRB often cannot be confined to a 3.5° diameter field (the FOV of VERITAS) on the sky (Paciesas *et al.*, 2012). When looking for potential gamma-ray sources over an entire field rather than at a point, there are special considerations regarding statistical trials factors and the method of background calculation at large source offsets. To better cover the large GBM error boxes, a raster observing method is being currently being developed and details are discussed in the following section.

7.4 Improving GRB Observations with VERITAS

To improve the instrument performance of VERITAS with respect to GRBs, several steps have been taken to reduce GRB observation delays, to thoroughly characterize the instrument response at low elevations, and to develop observing strategies and analysis methods for rapid observations of large areas of sky. In this section, a description of the current and future enhancements to the VERITAS hardware and software systems for GRB observations is provided.

As discussed previously, the most common undesirable condition affecting GRB observations is low elevation. For this reason, understanding and improving the VERITAS instrument response at low elevations is of paramount importance. To this end, more than 20 hours of low-elevation observations of the Crab Nebula, the most well-measured VHE gamma-ray source, have been taken since 2007. Using these data, the VERITAS instrument simulations and effective area calculations can be evaluated. Figure 7.6 shows the reconstruction of the Crab Nebula spectrum at various elevation ranges. The consistency of the VERITAS-measured Crab Nebula flux across elevation ranges and with the spectrum measured by the MAGIC telescope confirms that GRB observations and low elevations produce valid results.

Improving the VERITAS sensitivity to gamma-ray sources observed at low elevations is accomplished through implementation of the displacement air-shower reconstruction method (disp method) (Hofmann *et al.*, 1999). The details of this method are described in detail in Section 8.2. For observations of sources at zenith angles

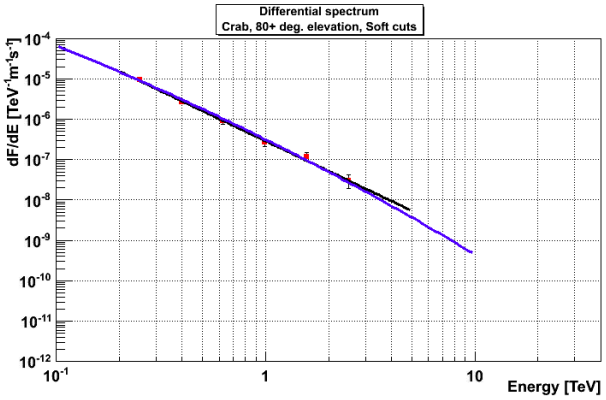

(a) Elevation $> 80°$

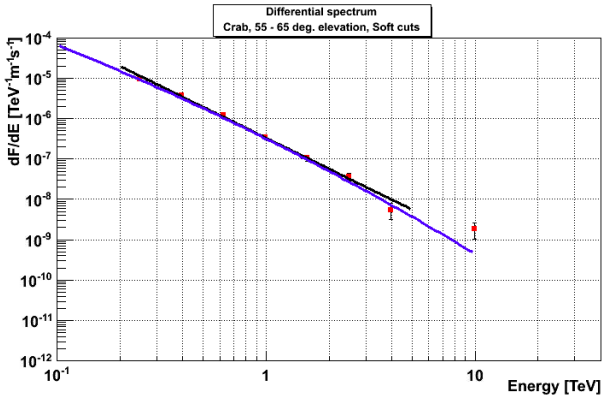

(b) $55° >$ Elevation $> 65°$

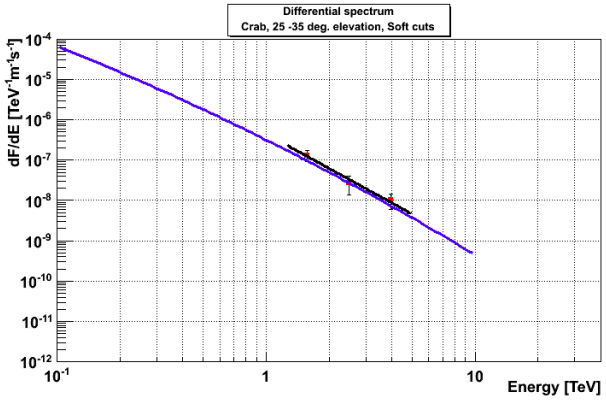

(c) $25° >$ Elevation $> 35°$

Figure 7.6: Reconstruction of the Crab spectrum at different elevation ranges. The blue spectrum is a fit of the Crab spectrum as measured by the MAGIC collaboration (Albert *et al.*, 2008) and the red points are the VERITAS measurements. The black line is a power-law fit to the VERITAS points. The VERITAS spectral points are self-consistent and consistent with the MAGIC measurements across all elevations. The analysis cuts used for this study are the same used for GRB analysis.

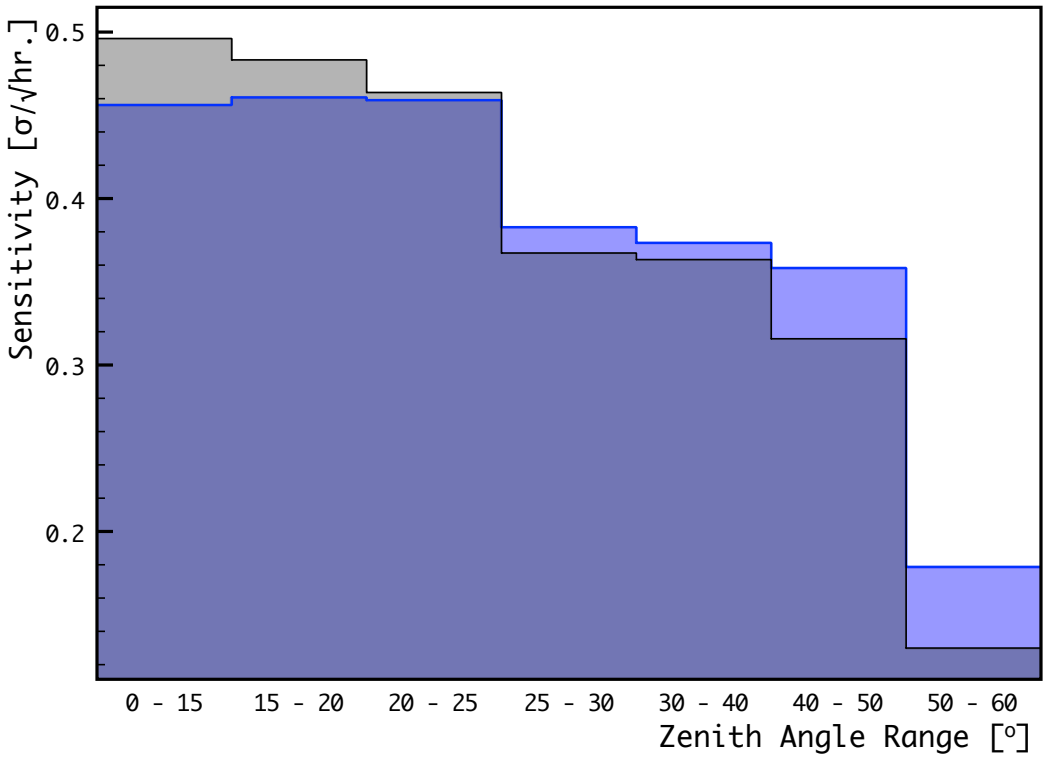

Figure 7.7: The VERITAS sensitivity to a 1% Crab Nebula source over various zenith angle ranges. The blue histogram indicates the disp method sensitivity, and the grey histogram the standard reconstruction method. Both methods are described in Section 8.1.

below $\sim 30°$, i.e. those that constitute the vast majority of GRB observations, the disp method results in improved sensitivity. A plot of the sensitivity versus zenith angle for a 1% Crab Nebula source is shown in Figure 7.7.

In addition to the analysis improvements to understand improve low-elevation observations with VERITAS, hardware modifications and novel observing strategies are planned for future GRB observations. The current telescope slewing speed is $1°/s$ though increasing this value to $1.5°/s$ with the current hardware is feasible and inves-

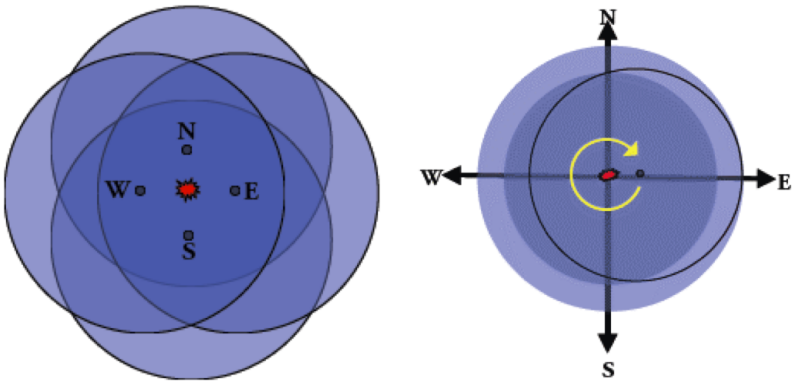

(a) Wobble Mode (b) Orbit Mode

Figure 7.8: Illustration of the wobble and orbit observing modes employed by VERITAS. In both cases the putative source position is offset from the center of the VERITAS FOV, enabling the simultaneous measurement of signal and background regions at a minimal loss of sensitivity. Figure credit J. Christiansen.

tigations are currently proceeding along these lines. The effect of increased torques on telescope components including the OSS and positioners needs to be carefully considered. It is conceivable that any improvement in slewing time would lead to a directly proportional reduction in GRB delays.

The *Fermi*-GBM detects 250 – 300 GRBs per year, the most of any satellite currently in operation and nearly 3 times as many detected by *Swift* annually. The relatively poor GRB localizations provided by the GBM present a challenge for VERITAS follow-up observations since the errors on the GRB position are often larger than the VERITAS FOV. To effectively cover the large position errors from the GBM, a strategy to rapidly tile extended region of interest is being developed. Currently, typical VERITAS data runs are taken with the center of the FOV offset 0.5° from the putative source position. The offset is alternated between North, South, East,

and West offsets. This observing mode enables a simple and robust calculation of the background simultaneous with source observation and is dubbed the "wobble" mode (Figure 7.8(a)). Recent upgrades to the pointing control software have included the addition of an "orbit" mode in which the center of the FOV is continuously rotated around the source position (Figure 7.8(b)) – a sort of continuous wobble mode. A modified orbit mode, in which after each complete orbit around the source position the offset is increased, results in concentric tiling of large sky areas, ideal for GRB follow-up observations. Work towards developing the software required to analyze the orbit mode data is currently underway.

Chapter 8

Analysis of VERITAS GRB Data

The analysis of VERITAS data consists of several steps: calculation and application of pixel-level corrections (calibration), cleaning and parameterization of air-shower images on the telescope-level, and rejection of hadron-initiated EASs, background estimation and signal extraction all on the array-level. The input of this procedure is the raw VERITAS data, stored in VBF (Section 6.3) files by the data acquisition processes and the result is a characterization of the putative gamma-ray source observed, including source intensity, spectral characteristics, and morphology. The analysis of GRB data often differs from a standard source analysis due to the low elevation of observed GRBs that necessitates augmented shower-reconstruction methods (Section 8.2) and the cosmological ($z > 0.5$) distances of GRBs that require deconvolution of the EBL to determine intrinsic sources fluxes (or flux upper-limits). This chapter outlines the VERITAS data analysis procedure as implemented by the

software used to obtain the results presented in the following chapter: the VERITAS Gamma-ray Analysis Suite (VEGAS), details of which are presented in Cogan (2008).

8.1 VERITAS Data Analysis – Event Reconstruction & Background Rejection

This section describes the standard process by which voltage variations from $\sim$ 2000 pixels recorded by the VERITAS FADCs are used to reconstruct the properties of observed air showers and subsequently to search for the existence of astrophysical gamma-ray sources.

8.1.1 Pixel Calibration & Image Cleaning

The first step in the analysis of VERITAS data is calculating and applying calibration corrections on a pixel-by-pixel basis. These corrections involve the characterization of pixel behavior in the absence of Cherenkov light signals, the relative gains between pixels, and timing corrections. NSB photons incident on the PMTs generate a baseline component that fluctuates on nanosecond timescales. Since each PMT is AC coupled at the preamplifier, the direct current (DC) offset generated by the NSB is filtered out – that is, fluctuations of the PMT voltage are around the zero-point. The VERITAS FADCs can only measure negative polarity analog signals, so in order to capture the positive and negative fluctuations from the NSB, an artificial negative

offset is added to the analog PMT signal. This offset, fluctuating signal is called the pedestal. The pedestal for each FADC channel is determined from "pedestal events" artificially triggered by the L3 system at a rate of 1 Hz. These pedestal events contain virtually no contamination from Cherenkov light and provide a baseline measurement of each pixel's response to the current NSB conditions.

From the pedestal events, the mean value of the pedestal for pixel i is calculated:

$$\bar{p_i} = \frac{1}{Nt} \sum_{j}^{N} p_{ij} \tag{8.1}$$

where N is the number of pedestal events, t is the length of the readout window, and p_{ij} is the j'th pedestal event of pixel i. Once the mean value of the pedestal has been determined, the RMS of the pedestal distribution for each pixel can be calculated:

$$\sigma_i = \sqrt{\frac{1}{N} \sum_{j}^{N} (p_{ij} - \bar{p_i} t)^2} \tag{8.2}$$

The mean value of the pedestal for each pixel remains constant between runs since it is only dependent on the artificial offset added to the analog PMT signal. The RMS, or "pedvar," calculated in Equation 8.2 can vary substantially depending on the brightness of different fields of view (e.g. galactic vs. extragalactic). The pedvar can be used to diagnose and remove problem pixels as a noisy, malfunctioning pixel will have a relatively large pedvar, while a dead pixel will have an inordinately small

pedvar value. The primary use of the pedvar is as a baseline pixel characterization in the absence of Cherenkov light. When determining whether a given pixel should form part of a shower image, a cut on the amount by which a pixel's value exceeds its pedestal value in units of pedvar is used.

To ensure that shower images are not distorted, a uniform response of each pixel to a given amount of light is desired. To this end, adjustments to PMT voltages are calculated and applied to maintain as constant a gain across the camera as possible. This procedure, called flat-fielding, is done approximately once a month, but variations in pixel gains over shorter timescales do occur. To correct for these variations, special calibration runs called "flasher" runs are taken each night. During flasher runs, the telescopes are externally triggered to coincide with flashes of light from UV LEDs that uniformly illuminate the cameras (Hanna *et al.*, 2010). From these runs, corrections to each pixel's gain can be computed:

$$\Delta G_i = \frac{1}{N} \sum_{j}^{N} (s_{ij} - \bar{p_i})/\bar{g} \tag{8.3}$$

where N is the number of flasher triggers, s_{ij} the signal measured for pixel i, and $\bar{g}$ is the camera-averaged gain. Applying this correction to the VERITAS data compensates for the relative gain differences between pixels in a given camera. At this stage of the analysis, the baseline PMT behavior has been determined, noisy and dead pixels have been discarded (based on their pedvar values), and the relative gain differences between pixels minimized. The next step is to identify and clean the

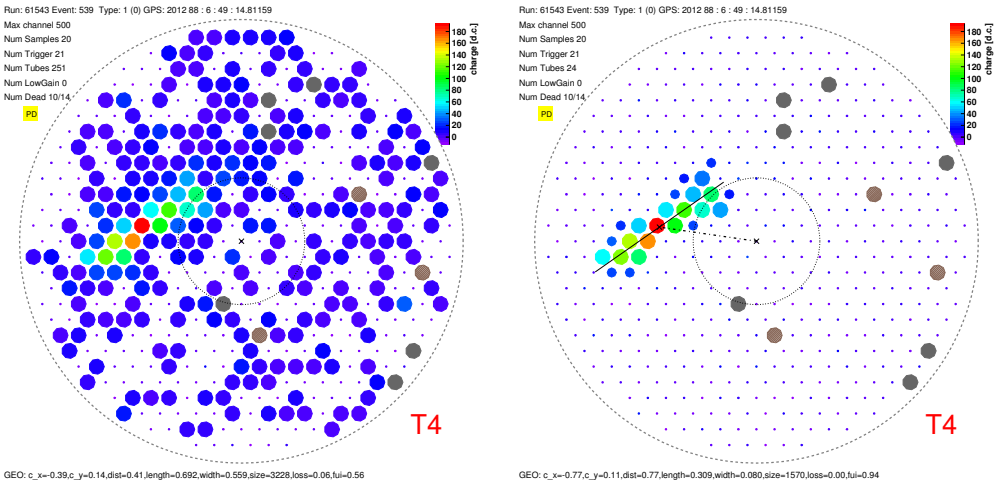

(a) Before Image Cleaning (b) After Image Cleaning

Figure 8.1: Illustration of the effect of the image cleaning procedure described in the text. Image pixels have a threshold of $5 \times \sigma_i$ and the boundary pixels have a threshold of $2.5 \times \sigma_i$.

shower images in the VERITAS data.

When a shower image is recorded, many pixels that do not record Cherenkov photons from the air shower do record photons from the NSB. In order to separate the NSB-activated pixels from the shower-activated pixels, a cleaning algorithm is used. The first step in this algorithm is the identification of shower-image pixels as those pixels which have a signal-to-noise ratio (SNR) ≥ 5, where the SNR is defined as $\mathrm{SNR}_i = (s_i - \bar{p}_i)/\sigma_i$. Once the shower-image pixels have been identified, any adjacent pixels with SNR ≥ 2.5 are identified as boundary pixels. All other pixels are removed from the image. The shower-image and boundary pixels constitute the cleaned image and it is this image that is parameterized and used for the event reconstruction described in the following subsection. The effect of the cleaning algorithm can be seen in Figure 8.1.

Table 8.1: Image parameters obtained from a moment analysis of light distribution

Name	Parameter
Size	Zeroth moment of the image. Total amount if integrated charge in pixels that passed the cleaning procedure
Distance	Distance (in degrees) of the centroid (first moment) of the image from the center of the field of view
α	Angle between the major axis (eigenvector of the second central moment of the image) and the line between the centroid and source position
Length	Extension of the image along the major axis (eigenvalue of the second central moment tensor)
Width	Extension of the image along the minor axis

8.1.2 Image Parameterization & Shower Reconstruction

Once the shower images have been calibrated and cleaned, each image is parametrized based on the first three moments of the light distribution in the image (Hillas, 1985). The parameters extracted from each shower image are described in Table 8.1. The parameters obtained from each telescope image are then combined to determine the properties of the shower, as observed by all of the telescopes in the array. A diagram of the Hillas parameters derived from an elliptical shower image can found in Figure 8.2.

At this point in the analysis, that is, before the individual shower images are combined, quality cuts, based on the image distance, image size, and number of pixels passing the image cleaning procedure, are made. The purpose of these cuts is to ensure that each image positively contributes to the reconstruction of the shower. The cut on image distance from the center of the camera reduces the chance of including showers where part of the image is off of the camera. These truncated images result in erroneous size and direction measurements for a given shower and in some cases

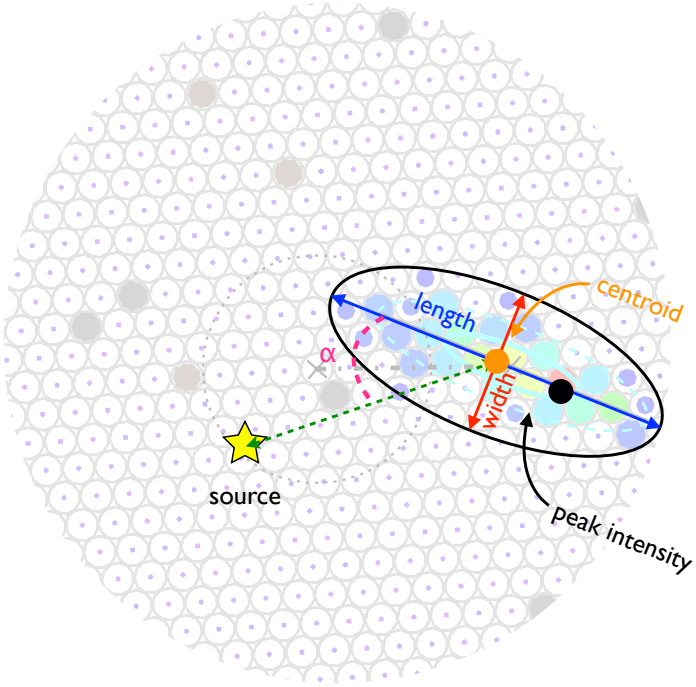

Figure 8.2: A diagram showing the parameterization of a Cherenkov shower image. The quantities noted are defined in Table 8.1.

may cause hadronic showers to appear more like showers generated by gamma-ray primaries. The cuts on total image size and the number of pixels passing the cleaning procedure are made to ensure that the images are large enough to be meaningfully parameterized. For the results presented later in this work, the image cuts used were Size $\geq$ 200 digital counts (dc) which corresponds to $\sim$ 40 photoelectrons, number of pixels in cleaned image (n_{pix}) $\geq$ 5, and Distance $\leq 1.43^{\circ}$. These cuts are chosen because they result in improved low-energy sensitivity which is very desirable for EBL-attenuated sources such as GRBs.

Once the images have passed through calibration, parameterization, and image

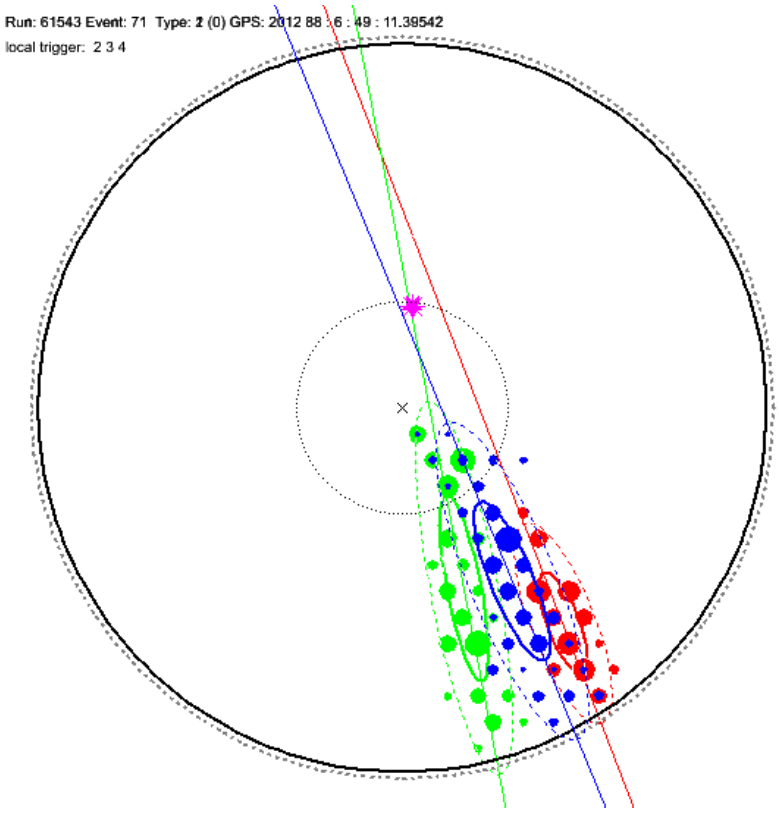

Figure 8.3: Reconstruction of the shower source location in the mirror plane using 3 telescope images. The pink star represents the reconstructed position calculated from a weighted minimization of the distance from the 3 shower image major axes.

quality cuts, information from them is combined and used to reconstruct the properties of the shower. In the focal plane, the source of the shower-generating primary particle lies along the major axis of the shower image. Without stereoscopic information, i.e. if the shower is only observed by a single telescope, the location of the shower source is ambiguous. With multiple telescopes the shower source is much more constrained and is computed based on the intersection of the major axes of multiple images (see Figure 8.3).

In addition to reconstructing the source location the directional information ob-

tained from the shower images can be used to reconstruct the intersection of the shower axis with the mirror plane. The distance between a telescope and this intersection point is referred to as the impact distance. Since a shower of a given size developing closer to a telescope will generate a brighter image in the camera than a shower developing further away, accurately reconstructing the impact distance of a shower for each telescope is crucial for determining the intrinsic brightness of the shower, which is directly correlated with the shower-generating primary particle's energy. Figure 8.4 shows a reconstruction of an air shower's impact location in mirror plane of the array.

To determine a primary particle's energy based on measurements of shower parameters, comparisons to simulated gamma-ray events are made. Simulations of the development of the EAS and Cherenkov light-generation, the VERITAS telescope optics, PMTs, and DAQ electronics provide shower images from which the Hillas parameters may be extracted. Simulations of millions of gamma-ray-initiated air showers covering a large range of primary particle energies, source locations, and observing configurations facilitates the creation of lookup tables which contain the information relating the characteristics of the primary particle and air shower with the Hillas parameters extracted from images observed by the telescopes.

There are several methods available for determining the shower source and impact point based on Hillas parameters (Table 8.1). For the GRB analysis presented in this work, two directional reconstruction methods are used. For observations occurring

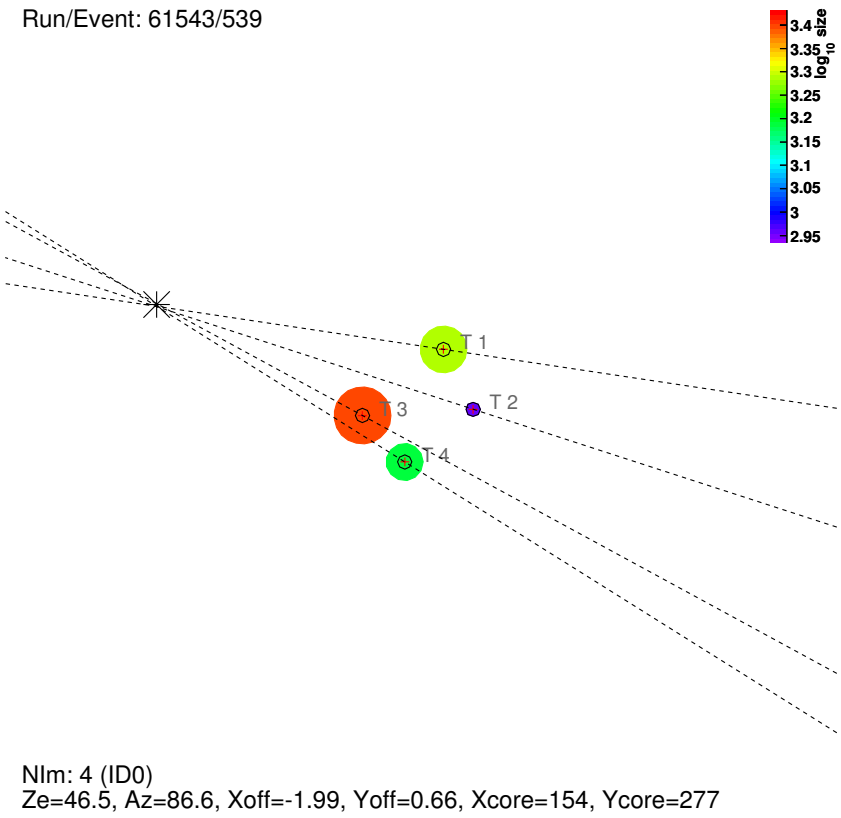

Figure 8.4: Reconstruction of the impact point in the telescope mirror plane for an event recorded by all four VERITAS telescopes. The size and color of the circle surrounding each telescope indicates the size of the image measured by that telescope.

at high elevations ($> 60°$), the minimization of the perpendicular distance from the reconstructed source location to each image major axis weighted by $\log_{10}$(Size) of the image is used to reconstruct the shower source. For GRB observations below $60°$ elevation, the displacement, or *disp* method is used. This method significantly improves sensitivity of the array at low elevations and is described in detail in Section 8.2.

8.1.3 Gamma-Hadron Separation

Even after Cherenkov light images of EASs have been successfully acquired and parameterized, there remains the challenge of separating the signal showers generated by gamma-ray primaries from much more numerous background showers generated by hadrons. This procedure is referred to as gamma-hadron separation. One straightforward way to clean many of the hadronic showers out of a data sample is to make use of the fact that the flux of hadronic primaries is essentially isotropic, while the signal gamma rays are assumed to be emitted from the source in the sky being observed. A cut on θ (or equivalently θ^2), defined as the angle on the sky between the putative source position and the reconstructed shower position, removes much of the isotropic background from hadronic cosmic rays.

The sample of showers passing the cut on θ^2 is still dominated by the hadronic background. To reduce the number of hadronic showers in this sample, the intrinsic differences in the development, morphology, and consequently the images of air

showers initiated by gamma-rays and those initiated by hadrons are examined. As mentioned in Section 6.2, showers generated by gamma rays produce compact, elliptical images while the shower images of hadronic EASs are much more irregular. The information on the shape of the shower image is contained in the length, $l(d,s)$, and width, $w(d,s)$, Hillas parameters. The length and width of an image for a given shower is dependent on both the distance d and the size s Hillas parameters. In order to quantify how "gamma-like" a given shower is (i.e. how likely it was to have been generated by a gamma-ray primary), the length and width of that shower is compared to the average length, $\langle l_{\rm sim}(d,s)\rangle$ and width, $\langle w_{\rm sim}(d,s)\rangle$, of simulated gamma-ray showers for that size and distance as expressed by the scaled width sw and scaled length sl:

$$sw = \frac{w(d,s)}{\langle w_{\rm sim}(d,s)\rangle} \tag{8.4}$$

$$sl = \frac{l(d,s)}{\langle l_{\rm sim}(d,s)\rangle} \tag{8.5}$$

For a shower that generates images in multiple telescopes, the mean scaled width and mean scaled length (msw, msl) can be computed by, perhaps not surprisingly, taking the mean of the scaled length and scaled width values from all participating telescopes ($N_{\rm tel}$):

$$msw = \frac{1}{N_{\rm tel}} \sum_{i}^{N_{\rm tel}} sw_i \tag{8.6}$$

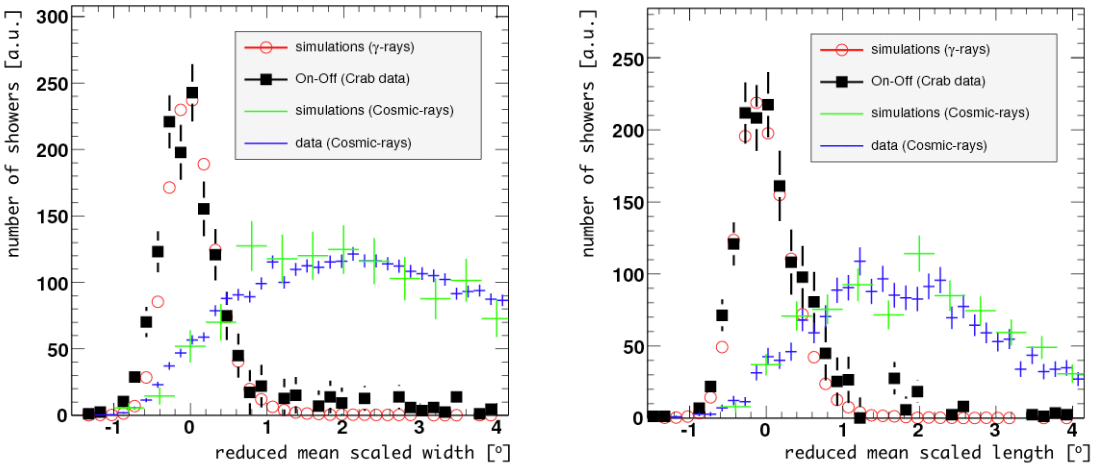

(a) $\widehat{msw}$ (b) $\widehat{msl}$

Figure 8.5: Reduced mean scaled width and reduced mean scaled length distributions for hadronic cosmic-ray showers and gamma-ray showers. Image credit: G. Maier.

$$msl = \frac{1}{N_{\text{tel}}} \sum_{i}^{N_{\text{tel}}} sl_i \tag{8.7}$$

Similar quantities, the reduced mean scaled width ($\widehat{msw}$) and reduced mean scale length ($\widehat{msl}$) take into account the uncertainties of the image lengths and widths in the simulated showers and may also be used:

$$\widehat{msw} = \frac{1}{N_{\text{tel}}} \left[\sum_{i}^{N_{\text{tel}}} \frac{w_i - \langle w_{\text{sim},i}(d,s) \rangle}{\sigma_{w,\text{sim},i}} \right] \tag{8.8}$$

$$\widehat{msl} = \frac{1}{N_{\text{tel}}} \left[\sum_{i}^{N_{\text{tel}}} \frac{l_i - \langle l_{\text{sim},i}(d,s) \rangle}{\sigma_{l,\text{sim},i}} \right] \tag{8.9}$$

Since the hadronic showers appear less compact and more irregular then gamma-ray showers, the msw and msl distributions of these showers are quite different, sufficiently different that placing a cut at simulation-determined values on these pa-

rameters significantly reduce the contamination of hadronic background showers in the data sample. Figure 8.5 shows the difference between the $\widehat{msw}$ and $\widehat{msl}$ distributions for hadronic and gamma-ray shower images. The values of the msw, msl, θ^2 cuts are all optimized by studying the effect of the cuts on the sensitivity to well measured gamma-ray sources (e.g. the Crab Nebula). For the GRB analysis, $msw \leq 1.08$, $msl \leq 1.19$, and $\theta^2 \leq 0.02$ cuts were used for gamma-hadron separation.

8.1.4 Background Estimation & Signal Extraction

Once most of the hadronic background showers have been removed, the search for a statistical excess of gamma rays at the putative source position can begin. Maps of the distribution of shower source locations in celestial coordinates are created. The dominant feature in these sky maps is the relatively smooth and isotropic background due to the residual hadronic showers that survived the gamma-hadron selection process. To determine whether or not a statistically significant gamma-ray signal is present at the putative source location, this residual background must be well-characterized. There are several combinations of observing modes and analysis methods by which this goal may be attained. For most VERITAS GRB observations, the wobble observation mode is used. In this mode the putative source location is observed offset (nominally 0.5°) at four discrete positions (N,S,E,W) from the center of the camera. The search for a statistical excess at a given point in a sky map is a two step process. First a camera acceptance function is generated by fitting the back-

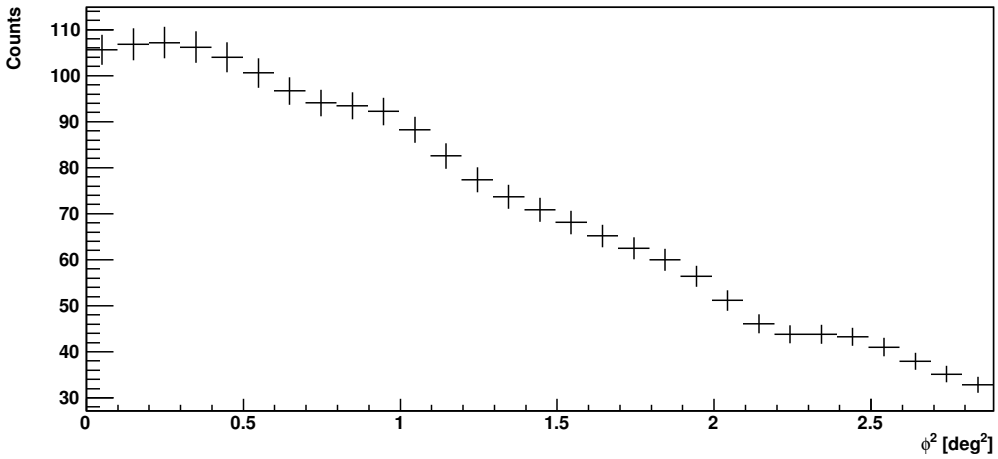

Figure 8.6: Smoothed acceptance function for a 20-minute run on GRB 080310. The histogram is plotted as a function of ϕ^2, the squared angle from the center of the FOV.

ground distribution, explicitly excluding data from the putative gamma-ray source position. The next step is to determine the significance of the excess number of events in the source region. This is accomplished by using either the reflected region method (RRM) or the ring-background method (RBM).

The event reconstruction efficiency of VERITAS is not constant across the field of view of the instrument as events with large impact distances are poorly reconstructed. Quantifying this variation in efficiency is critical for correct signal and background calculations and is done by creating a histogram binned in units of ϕ^2 where ϕ is the angular separation between the center of the FOV (the telescope pointing) and the position in the sky map. Regions of the sky map which include bright stars or known gamma-ray sources are excluded and compensated for to prevent overestimation of the background when generating the acceptance histogram. Note that this method of

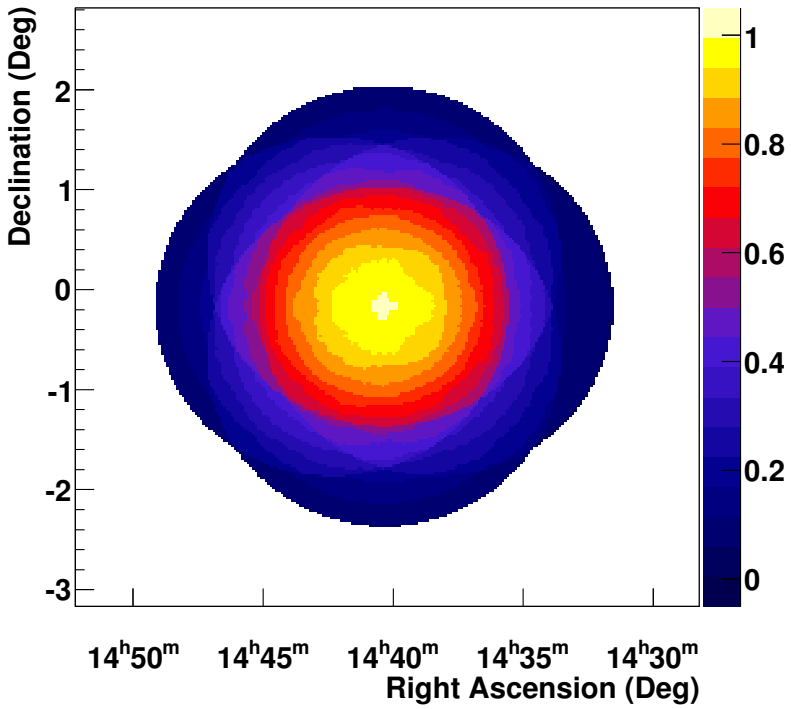

Figure 8.7: Relative acceptance map for all runs taken on GRB 080310. The shape of the map is due to the observations being taken over all four wobble positions (Figure 7.4).

acceptance function generation assumes azimuthal symmetry. A typical acceptance function is shown in Figure 8.6. The acceptance function is calculated on a run-by-run basis, usually of $\sim$ 20 minute duration. For observations incorporating multiple runs, a 2-D acceptance map is generated which illustrates the gamma-ray response of VERITAS over the region observed (Figure 8.7).

With the acceptance map, the significance of the excess counts at the putative source position is computed using either the RRM or RBM. With the RRM, the signal region is defined as a circular region of radius θ centered on the source position

which is located at a distance δ from the center of the FOV. The circle at distance δ from the center of the FOV is populated with non-overlapping background regions of equal size (Figure 8.8(a)). The significance of the excess counts in the signal region is computed from the number of counts in the signal region (N_s), the total number of counts in all of the non-excluded background regions (N_b), and the ratio of the area covered by the signal region to the the area covered by the background region (α). Using the likelihood ratio method, the significance of the number of counts in the signal region is given by $-2\ln\lambda$ where λ is the maximum likelihood ratio (Li and Ma, 1983):

$$\sigma = \sqrt{-2\ln\lambda} = \sqrt{2\left\{N_s \ln\left[\frac{1+\alpha}{\alpha}\left(\frac{N_s}{N_s+N_b}\right)\right] + N_b \ln\left[(1+\alpha)\left(\frac{N_b}{N_s+N_b}\right)\right]\right\}} \tag{8.10}$$

The RRM does not make use of the acceptance function (it assumes a radial symmetry) and so it is prone to systematic errors in the case of large asymmetries in the background. The use of the wobble technique significantly reduces such a systematic error as an excess or deficit in the background estimation in the presence of large scale asymmetries will cancel out at the source position. In certain circumstances, e.g. the source is observed at the center of the FOV (which was indeed the case for many older GRB observations), use of the RRM is not possible or not desirable. For these situations, the RBM is used. The RBM makes use of the camera

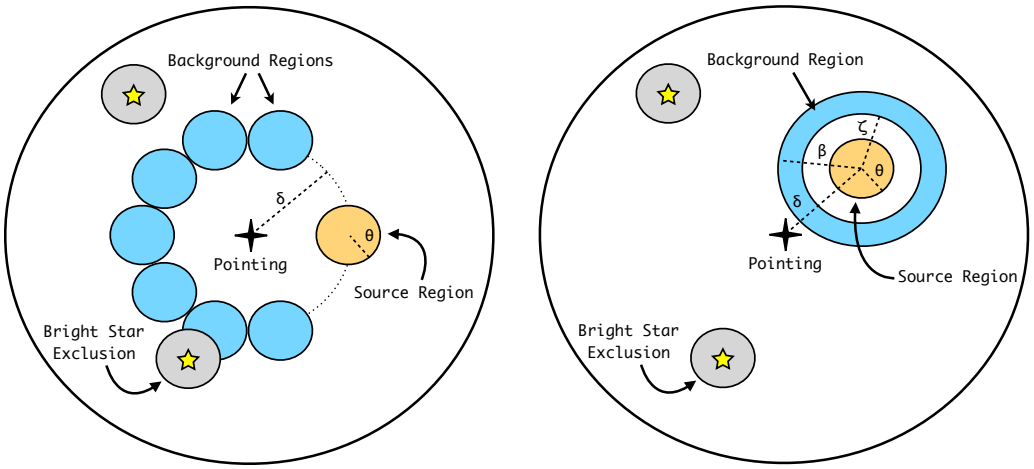

(a) Reflected-Region Method (RRM) (b) Ring-Background Method (RBM)

Figure 8.8: The two methods of background estimation and signal extraction used in this work. See text for explanation.

acceptance function and calculates the acceptance-corrected background using counts from an annulus surrounding the source position (see Figure 8.8(b)). The RBM can be used for sources at the center of the FOV and is less prone to systematic errors due to large asymmetries or other structure in the residual background map. With the (acceptance-corrected) counts from the signal region and background ring, the significance of the number of excess counts is again computed using Equation 8.10.

8.2 Low-Elevation Observations: The "Displacement" Reconstruction Method

As most GRB observations take place at low-elevations (large zenith angles), improving the performance of the instrument under these conditions is of great impor-

tance for GRB science with VERITAS. Aside from the inherent loss of sensitivity at low energies for sources observed at low elevations due to the increased column density of atmosphere, significant sensitivity is also lost due to the degradation of the VERITAS angular resolution at these elevations (Fiugre 7.5). The use of an alternative method of shower source location reconstruction, the displacement method, greatly ameliorates this situation. In this section the displacement method, how it differs from the standard shower source location reconstruction method, and the effect it has on VERITAS sensitivity to sources observed at low elevations, is described.

For both the standard and displacement (disp) methods, a minimum of two telescopes with images passing the cleaning cuts is required. The standard shower source location reconstruction method (standard method) performs a χ^2 minimization on the size-weighted perpendicular distance squared from each of the axes. A diagram of such a reconstruction with three telescopes participating is shown in Figure 8.9. If there are only two telescopes participating, the location is simply the intersection of the two image length axes. For showers with large impact distances, the major axes of the shower images become very close to parallel. In such a situation a small change in the major axis angle results in a huge change in source location reconstruction. This problem is particularly acute when only two telescopes are participating in an event so if there are only two telescopes with shower images, and the image major axes differ in orientation by less than 10°, these events are thrown out.

The disp method used with VERITAS is described as algorithm 3 in Hofmann

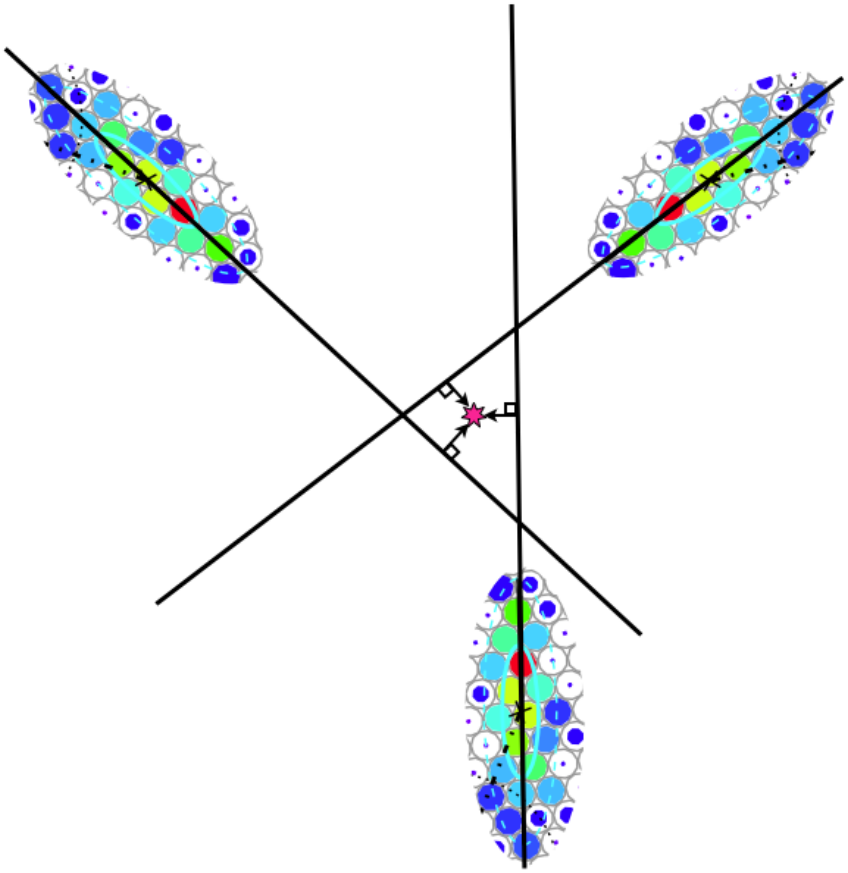

Figure 8.9: Diagram of the standard shower source location reconstruction involving the three telescopes. The reconstructed source location is determined by a minimization of size-weighted perpendicular distance.

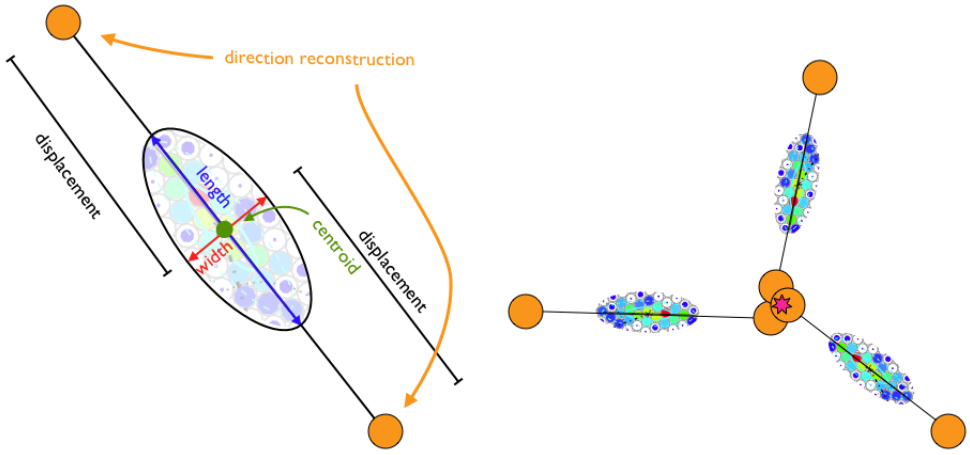

(a) Displacement calculated from *length*/*width* for a single image.

(b) Disp method source location reconstruction

Figure 8.10: Diagrams illustrating the calculation of the image displacement and the use of this information to reconstruct source locations in a stereoscopic event.

et al. (1999) and is basically an extension of the method used by non-stereoscopic IACT systems (Akerlof *et al.*, 1991). At the heart of this method is the fact that a given shower will have an increased ellipticity ($\sqrt{\frac{\text{length}^2-\text{width}^2}{\text{length}^2}}$) with increased impact distance. This relationship is quantified using simulations and it is found that the displacement, that is, the distance along the major axis between the image centroid and the reconstructed source position (Figure 8.10(a)), is dependent not only on image length and width but also on image size. The displacement is a scalar value and for a single telescope image it is not possible to determine which direction along the image major axis the true source location lies. With multiple telescope images, it is assumed that the N source locations in closest proximity (where N is the number of telescopes participating in the event reconstruction) represent the true source location and these locations are used for the weighted source location reconstruction.

When combining the source locations from multiple telescopes, the weight for each telescope is determined based on the uncertainty of the telescope source location determination. This overall uncertainty is a product the uncertainty in the orientation of the image major axis and the RMS of the displacement ($\mathrm{RMS_{disp}}$) calculated from the simulations for a given width, length, and size. The uncertainty of the image orientation ($\Delta\zeta$) as a function of image width (W), image length (L), and image size (S) was determined from the simulations:

$$\Delta\zeta \propto \frac{(W/L)^4}{S} \tag{8.11}$$

The total uncertainty is then given by $\sigma = \sqrt{\Delta\zeta^2 + \mathrm{RMS_{disp}}^2}$. Each image is then weighted by a factor of σ^{-2} and the combination of the weighted source locations from all telescopes is used as the reconstructed source position for the event.

The effect of the disp reconstruction method on the angular resolution of VERITAS is shown in Figure 8.11. The angular resolution of the array is important since a tighter θ^2 cut can be used which reduces the number of hadronic showers contaminating the signal region. The sensitivity improvement to the Crab Nebula as a function of zenith angle is shown in Figure 7.7. Due to the improved sensitivity obtained from observations at low elevations, the disp method is used for GRB analysis for all bursts occurring at elevations at or below 60° in elevation.

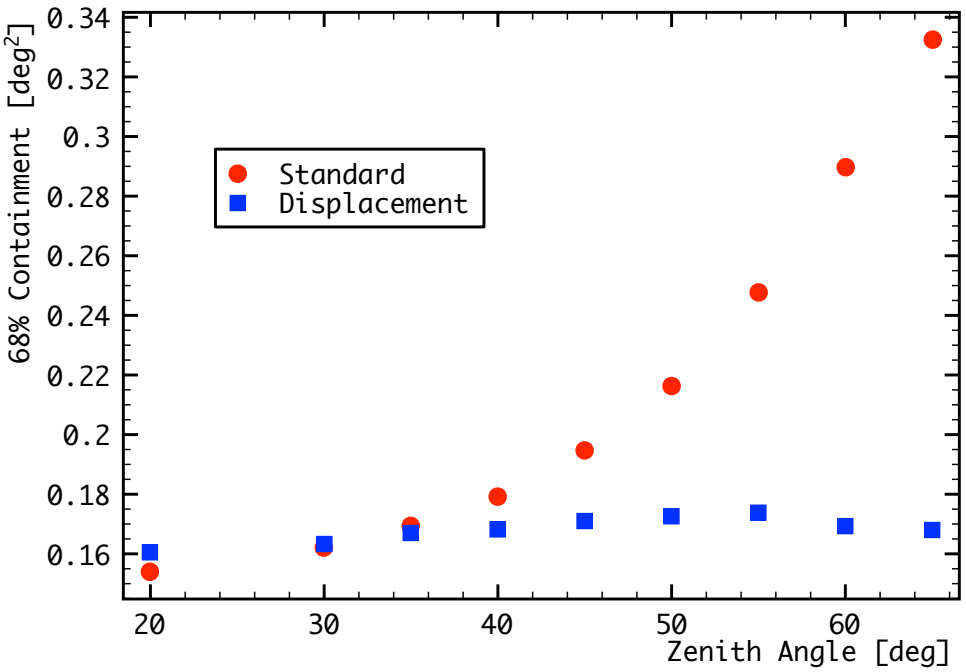

Figure 8.11: A comparison of the angular resolution of VERITAS as a function of zenith angle obtained using the standard reconstruction method and the displacement reconstruction method.

8.3 Spectral Reconstruction and Upper Limit Calculations

As discussed in Section 2.4, the standard statistical threshold for claiming a detection is a signal with amplitude at or above 5 times the standard deviation of the background (5σ). In the case of a detection, a spectrum is computed. In the case of a non-detection, an upper limit on the number of counts in the signal region is computed and, with an assumption on the spectral characteristics of the source, a corresponding upper limit on the flux can be determined. In either case a model of the VERITAS instrument response to gamma rays as a function of energy as well as the dead-time-corrected duration of observation is required.

While VERITAS is collecting data, there is a fraction of time during which the experiment is essentially "off" because the data acquisition systems are processing and recording information from an event and not sensitive to any new triggers. This dead-time is monitored by the L3 system and is largely due to the time required to read out event information from a telescope ($\sim 400\,\mu$s). For the typical VERITAS trigger rate of ~ 250 Hz, this gives a dead-time fraction of about 10%. The live time (τ = [total observing time] - [dead-time]), is used to determine the flux measured by VERITAS.

The VERITAS response function or effective area to gamma rays, is computed via Monte Carlo simulations. The effective area (A) is a function of the primary

gamma-ray energy (E), but also of several observing and analysis conditions ($\mathbf{x}$) such as zenith angle, azimuth angle, NSB, and gamma-hadron separation cuts. The true gamma-ray source flux ($\frac{dN}{dE}$) is related to the source flux measured by VERITAS (F) via:

$$F = \tau \int A(E, \mathbf{x}) \frac{dN}{dE} dE \tag{8.12}$$

The VERITAS effective area as a function of energy for analysis cuts optimized for a weak, soft-spectrum, point source is shown in Figure 8.12 for a variety of elevation angles. Details of the method used to reconstruct the source spectrum are numerous and are not covered in detail here, but more information about several methods of spectral fitting can be found in Section 3.6 of Wood (2010).

For the computation of upper limits on the source flux, the first step is to calculate the upper limit on the number of counts in the signal region. For the analysis presented here, the maximum likelihood method as described in Rolke *et al.* (2005) is used to compute the 99% confidence level upper limits on source counts (N_{UL}). Once this limit has been determined, the upper limit on the flux can be computed in the same fashion as outlined in Section 4.3. The upper limits on the flux are calculated using the entire sensitive energy range of VERITAS, i.e. the entire energy range over which the effective area is non-zero. For the GRB results presented here the upper limits are typically quoted on the νF_ν (differential) flux at the threshold energy (E_{th}) which is defined as the peak of the differential count spectrum (effective area times

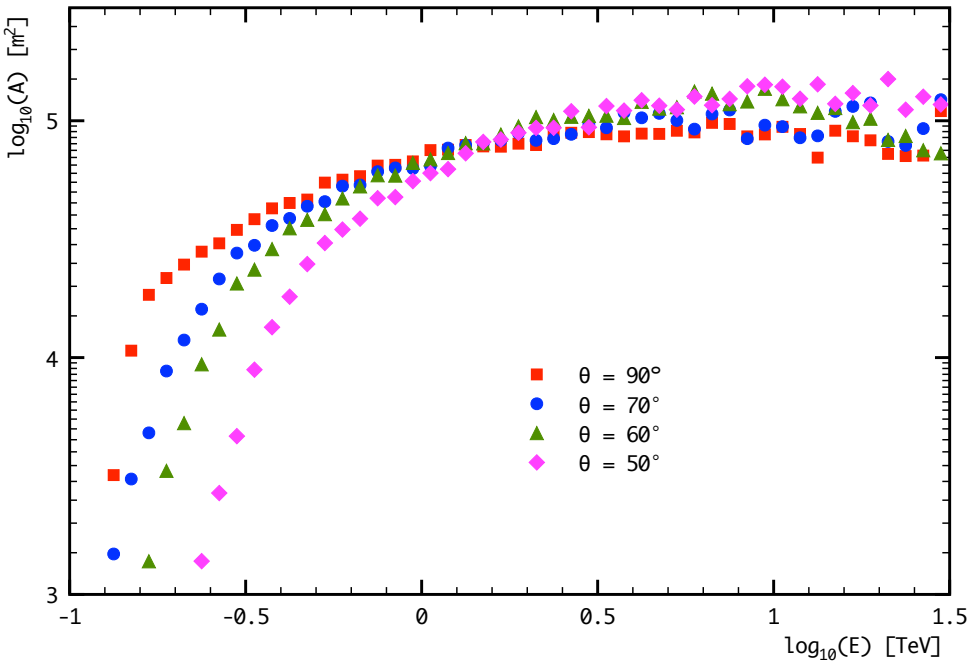

Figure 8.12: The effective area of VERITAS as a function of energy for several different elevation angles, (θ). These effective areas were generated using cuts optimized for a weak, soft-spectrum point source and the standard shower location reconstruction method.

assumed source spectrum).

8.4 Correcting the Absorption of VHE Gamma-Rays by the EBL

When determining flux measurements or flux upper limits for GRBs, it is desirable to do so with respect to the intrinsic properties of the burst. The mechanisms and physical processes by which GRBs accelerate particles and produce gamma rays are not fully understood and constraining the intrinsic qualities of burst spectra can provide valuable information. One significant impediment to determining a GRB's true spectrum is the attenuation of high-energy photons by the EBL as they traverse great distances from the GRB to Earth. In order to remove the effects on the GRB spectrum, a model of the EBL is used to de-absorb the assumed spectrum. For de-absorption calculations presented in this work, the model of Gilmore *et al.* (2009) is used.

Disentangling one unknown (GRB physics and emission characteristics) from another unknown (the spectrum and cosmological evolution of the EBL) is a difficult business. The photons detected at Earth from an observation of a GRB at high energies contains information on both the GRB and the EBL and determining whether a cutoff in the GRB spectrum, for instance, is due to inherent processes in the burst or the absorption of these photons by the EBL is not possible without understanding

reasonably well the properties of one or the other. Fortunately, models of the EBL (e.g. (Franceschini *et al.*, 2008, Gilmore *et al.*, 2009, Kneiske and Dole, 2010)) seem to be converging and at the moment it appears the the EBL is much better understood than the high-energy emission characteristics of GRBs.

When calculating the upper limit for a GRB, a spectral shape is assumed, typically a power law $\frac{dN}{dE} \propto E^{-\Gamma}$ and the upper limit is first computed using this spectral assumption without regard to attenuation from the EBL. To determine the factor by which the unattenuated upper limits increase due to effects of the EBL, one must calculate the effective attenuation of VHE photons over the VERITAS waveband, taking into account the spectral response of the instrument. For each VERITAS GRB observation, the effective area of VERITAS is multiplied by the assumed intrinsic spectrum of the burst (black curve in Figure 8.13(a)). The total flux is then calculated by integrating the intrinsic differential flux of the GRB multiplied by the effective area of VERITAS, over all energies at which the product is non-negligible (black curve in Figure 8.13(b)). This process is repeated, substituting an EBL-attenuated burst spectrum (red curve in Figure 8.13(a)) for the intrinsic burst spectrum. The ratio of the total photon flux obtained using the intrinsic burst spectrum to the total photon flux obtained using the EBL-attenuated burst spectrum (essentially the ratio of areas under the black and red curves in Figure 8.13(b)) gives the attenuation factor for that particular GRB observation.

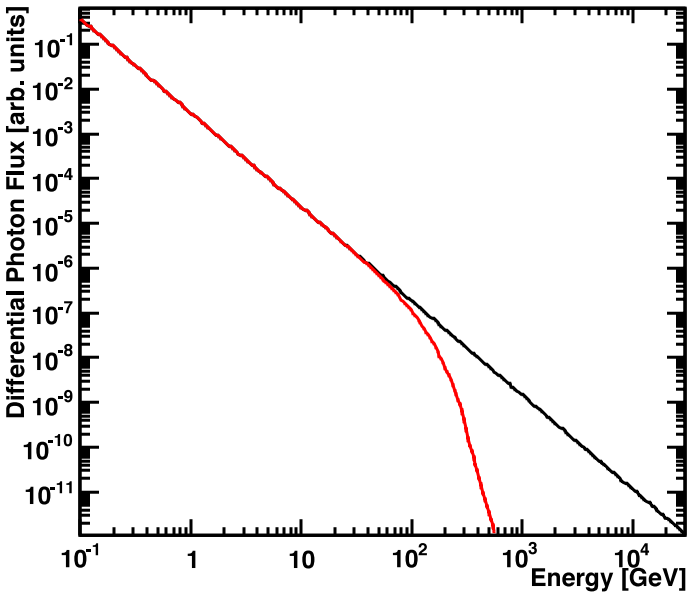

(a) Intrinsic (black) and EBL-attenuated (red) GRB spectra

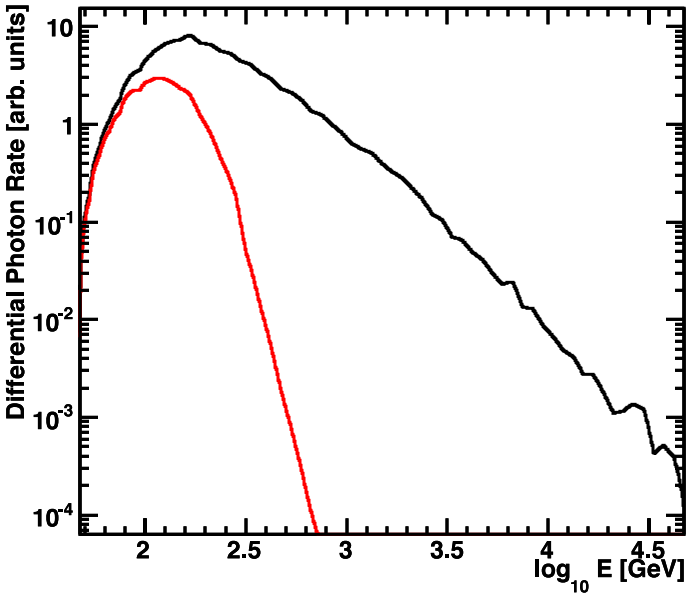

(b) Spectra from Figure 8.13(a) multiplied by the VERITAS effective area

Figure 8.13: Effects of EBL attenuation on a hypothetical GRB with a power-law spectrum ($\Gamma = -2.1$) located at a redshift of $z = 1$. The observation elevation when factoring in the VERITAS effective area (Figure 8.13(b)) is assumed to be 70° in this case.

Chapter 9

Results from GRB Observations with VERITAS

9.1 VERITAS Observations of GRBs: 2007 – 2012

During the period beginning January, 2007 and ending February, 2012, VERITAS took follow-up observations of 53 GRBs. 25 of these bursts were detected only by the Gamma-ray Burst Monitor (GBM) on board the *Fermi* satellite and the errors on the localizations were larger than the VERITAS field of view. Analysis of these bursts will not be presented here. Table 7.1 lists the general properties of the remaining 28 well-localized *Swift*-detected bursts. The VERITAS observations of GRBs presented here took place under dark skies or low-moonlight conditions.

The data were collected in runs with nominal durations of twenty minutes with

roughly thirty seconds of dead time between runs. At the beginning of each run the best source localization to arrive via the GCN socket connection is used as the target for the duration of that run. 24 of the bursts were observed in "wobble mode," but in the cases of GRB 070419A, GRB 070521, GRB 070612B, and GRB 080604, observations were taken in a tracking mode in which the source is placed at the center of the camera. Historically, GRB observations were taken in tracking mode but wobble mode is now the default method of observation with VERITAS and all GRB observations are currently taken in this fashion. The use of the tracking mode does offer a marginal increase in "raw" sensitivity over the wobble mode but with a significant increase in the uncertainty of the background. The cuts used for this analysis were optimized for a weak soft-spectrum point source and are listed in Table 9.1. For data runs taken at elevations below 60°, the displacement reconstruction method is used, which improves the angular resolution of the array at large zenith angles.

An analysis of VERITAS data associated with the 28 GRB positions listed in Table 7.1 shows no significant excess of VHE gamma-ray events compared to the expected background for any GRB over the entire duration of VERITAS observations. Table 9.2 summarizes the details and results of the VERITAS GRB observations for these bursts. The significance distribution is shown in Figure 9.1. The sensitivity of the VERITAS array, and the small observation delays with respect to the GRB T_{trig} (half of the burst observations had delays of less than five minutes) combine to give some

Table 9.1: Analysis Cuts

Cut Parameter	Value
Size	> 200 dc
nTubes	> 4 PMTs
Mean Scaled Width	1.08
Mean Scaled Length	1.19
θ^2	0.02
Shower Maximum	> 8 km
Distance	$< 1.43°$

Cut values used for the analysis presented here. The definition of each cut parameter can be found in Chapter 8. These cuts were chosen to optimize the VERITAS sensitivity to weak, soft spectrum point source, though their use does not preclude the detection of a source with different characteristics.

of the most constraining limits on VHE gamma-ray emission from GRB afterglows.

The VHE photon fluxes from objects at cosmological distances are attenuated due to absorption by the EBL (Section 1.5). Of the 28 bursts for which results are presented here, 13 had redshifts determined by optical followup observations. For these bursts, a limit on the intrinsic photon flux of the GRB can be set if one assumes a model of the EBL. For all calculations requiring a model of the EBL, the model described in Gilmore *et al.* (2009) is used. To determine the factor by which the upper limits in Table 9.2 increase due to effects of the EBL, one must calculate the effective attenuation of VHE photons over the VERITAS waveband, taking into account the spectral response of the instrument. For each GRB observation, the effective area of VERITAS is multiplied by the assumed intrinsic spectrum of the burst, which is taken to be $\Gamma = 2.5$. The total flux is then calculated by integrating the intrinsic differential flux of the GRB multiplied by the effective area of VERITAS, over all

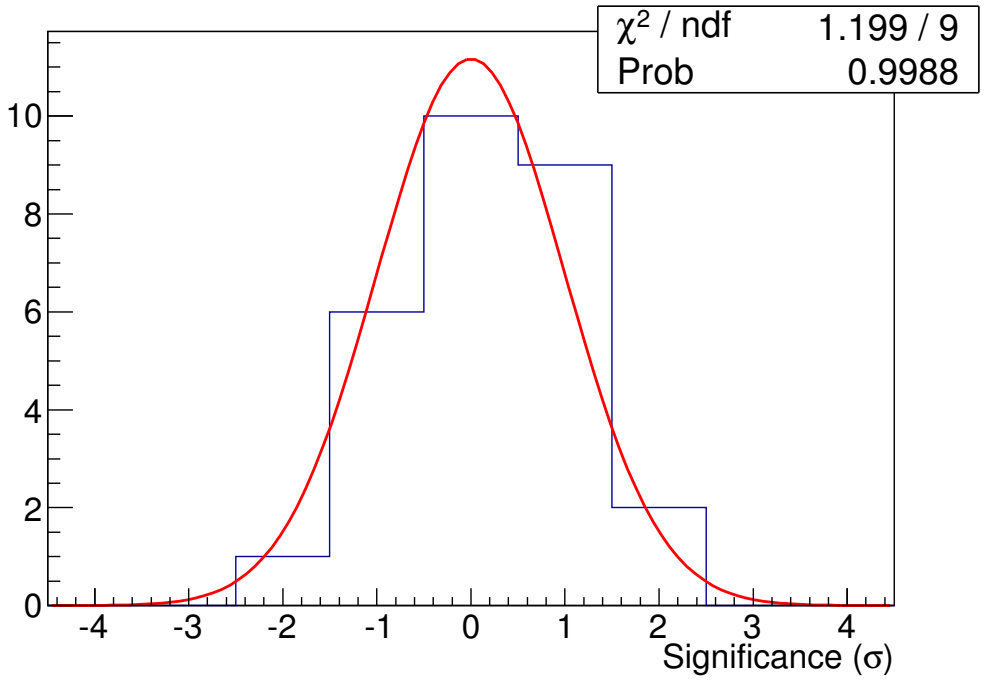

Figure 9.1: Significance histogram of the 28 GRBs in the sample listed in Table 9.2. Included in the figure is the normalized Gaussian distribution of mean zero and variance one that the significance histograms should follow if no signal is present. The GRB significances are consistent with having been drawn from the aforementioned Gaussian distribution indicating that no VHE gamma-ray emission was observed from this set of GRBs.

Table 9.2: VERITAS Observations of Gamma-Ray Bursts

GRB	T_{delay} (s)$^{\alpha}$	T_{obs} (min)$^{\beta}$	Elevation ($^{\circ}$)$^{\gamma}$	E_{th} (GeV)$^{\delta}$	σ^{ζ}	Upper Limit
070223	1.7×10^4	74.1	67–78	150	0.8	2.0×10^{-11}
070419A	295	37.7	32–36	420	−1.0	1.0×10^{-11}
070521	1118	75.4	63–88	120	−0.3	9.6×10^{-11}
070612B	201	131.9	46–50	230	0.6	7.1×10^{-12}
071020	5259	92.2	24–45	550	0.4	1.4×10^{-11}
080129	1456	31.4	47–50	220	1.4	1.2×10^{-11}
080310	342	196.0	46–53	260	−0.1	4.2×10^{-12}
080330	156	107.8	64–88	120	−0.7	6.3×10^{-12}
080409	6829	57.4	23–35	1100	2.1	3.7×10^{-11}
080604	281	151.8	33–70	160	0.9	1.2×10^{-11}
080607	184	94.0	26–48	500	0.1	1.2×10^{-11}
081024A	150	160.1	54–59	290	−1.7	3.8×10^{-12}
090102	5344	121.1	23–49	420	1.0	1.2×10^{-11}
090418A	261	30.4	86–88	120	1.7	3.0×10^{-11}
090429B	141	158.8	70–88	120	1.0	9.6×10^{-12}
090515	356	87.7	38–57	380	1.3	1.9×10^{-11}
090929B	863	78.7	21–41	600	−1.5	1.6×10^{-11}
091024	214	73.1	22–33	660	−0.4	5.1×10^{-11}
100205A	330	119.1	47–81	260	−1.2	5.4×10^{-12}
100420A	5082	76.1	23–35	600	−0.4	3.7×10^{-11}
100615A	6943	57.2	21–30	600	1.1	1.1×10^{-10}
110201A	180	151.3	32–33	550	−0.2	1.5×10^{-11}
110205A	520	174.4	23–41	500	−0.9	1.3×10^{-11}
110928A	1790	120.2	34–62	290	−0.9	7.0×10^{-12}
111029A	309	110.9	39–57	290	−0.4	9.7×10^{-12}
111225A	464	129.6	36–61	220	−0.3	8.5×10^{-12}
120119A	103	157.2	26–48	320	0.9	1.2×10^{-11}
120215A	6097	94.6	26–48	500	−0.2	9.6×10^{-12}

Upper limits are given at the 99% confidence level in terms of νF_{ν} at E_{th}, assuming a spectral index of 3.5, in units of erg cm^{-2} s^{-1}. $^{\alpha}$Time between the GRB trigger time (T_{trig}) and the beginning of VERITAS GRB observation. $^{\beta}$Duration of VERITAS observation. $^{\gamma}$Elevation range of the VERITAS observation. $^{\delta}$The VERITAS energy threshold. $^{\zeta}$Statistical significance (standard deviations) of signal counts observed by VERITAS at the GRB position.

Table 9.3: Redshift-corrected VERITAS upper limits on VHE emission from nine *Swift*-detected GRBs

GRB	Redshift	Attenuation Factor	Upper Limit
070419A	0.97	1.5×10^{-4}	2.8×10^{-8}
070521	0.553	0.2	2.9×10^{-11}
071020	2.145	1.2×10^{-8}	7.0×10^{-4}
080310	2.43	3.1×10^{-4}	1.4×10^{-8}
080330	1.51	0.027	1.2×10^{-10}
080604	1.4	4.7×10^{-3}	9.9×10^{-10}
080607	3.036	1.6×10^{-7}	6.8×10^{-5}
090102	1.55	7.1×10^{-5}	8.1×10^{-8}
090418A	1.608	0.03	6.0×10^{-10}
090429B	9.4^{α}	N/A	N/A
091024	1.092	1.51×10^{-6}	2.3×10^{-5}
110201A	1^{β}	4.8×10^{-6}	1.8×10^{-6}
110205A	2.22	5.9×10^{-8}	$.0 \times 10^{-4}$
120119A	1.728	1.9×10^{-4}	6.2×10^{-8}

Upper limit and threshold energy (E_{th}) of each GRB defined as in Table 9.2. The attenuation factor is explained in the text. $^{\alpha}$Attenuation was not calculated for this burst, but is presumably extremely large. $^{\beta}$Redshift is tentatively found to be less than 1 for this burst, but the limit is calculated here assuming $z = 1$.

energies at which the product is non-negligible. This process is repeated, substituting an EBL-attenuated burst spectrum for the intrinsic burst spectrum. The ratio of the total photon flux obtained using the intrinsic burst spectrum to the total photon flux obtained using the EBL-attenuated burst spectrum gives the attenuation factor for that particular GRB observation. The attenuation factors and redshift-corrected upper limits for GRBs with known redshift are shown in Table 9.3. Not surprisingly, the attenuation depends strongly on both the redshift and the energy threshold for a particular observation, but under good observing conditions, specifically at small zenith angles, sensitivity sufficient to detect some *Fermi*-LAT-detected GRBs out to $z \sim 2$ is attainable with VERITAS (see Section 10.2).

9.2 Search for VHE Gamma-Ray Emission Optimized on the *Fermi* "Super-Bursts"

In addition to a search for VHE emission performed over the entire duration of the VERITAS observations, a search over a shorter timescale that optimizes the sensitivity of VERITAS to a source with a flux that decays as a power-law in time is investigated. The *Fermi*-LAT has detected more than a dozen gamma-ray bursts with emission above 100 MeV. This high-energy emission is seen to persist after the flux in the GBM band has ceased and shows weak spectral evolution with a spectral index between the α and β indices of the Band function fit to the GBM data (Ghisellini *et al.*, 2010). The temporal behavior of the brightest four *Fermi*-LAT detected bursts: GRB 080916C (Abdo *et al.*, 2009c), GRB 090510 (De Pasquale *et al.*, 2010), GRB 090902B (Abdo *et al.*, 2009b), and GRB 090926A (Ackermann *et al.*, 2011), shows a common $\frac{\mathrm{d}N}{\mathrm{d}E} \sim t^{-\Delta}$ decay, where $1.2 < \Delta < 1.7$ in the observer frame. If it is assumed that the temporal and spectral characteristics of a GRB detected by the *Fermi*-LAT extend to the VHE energy range, the observed power law temporal decay of the high energy emission consequently defines an optimal duration over which the search for VHE emission is maximally sensitive.

This optimal duration is determined solely by the high-energy temporal power law index of the GRB, the delay from the GRB trigger time ($\mathrm{T_{trig}}$) to the beginning of VERITAS GRB observations, and by, to a lesser extent, the observational

Table 9.4: A search for VHE emission on timescales optimized on VERITAS sensitivity to a power law afterglow decay $\sim t^{-1.5}$.

GRB	Duration(s)	$N_{\rm on}$	$N_{\rm off}$	σ^{α}	$E_{\rm th}$ (GeV)	Upper Limit
070223	2.7×10^4	–	–	–	–	–
070419A	477	2	42	−0.9	420	4.6×10^{-11}
070521	1809	23	364	−0.9	110	1.6×10^{-11}
070612B	325	7	58	1.1	270	9.3×10^{-11}
071020	8509	–	–	–	–	–
080129	2356	–	–	–	–	–
080310	553	13	55	1.4	290	7.9×10^{-11}
080330	252	6	43	−0.2	170	1.4×10^{-10}
080409	1.1×10^4	–	–	–	–	–
080604	455	9	128	−0.3	140	3.6×10^{-11}
080607	298	7	46	0.3	250	1.1×10^{-10}
081024A	242	4	29	0	190	1.9×10^{-10}
090102	8647	–	–	–	–	–
090418A	422	8	46	0.4	120	6.9×10^{-11}
090429B	228	4	27	0.1	140	1.5×10^{-10}
090515	576	11	72	0.8	210	6.2×10^{-11}
090929B	1396	24	205	−0.4	600	1.4×10^{-10}
091024	346	6	48	0.0	660	2.0×10^{-10}
100205A	534	8	88	−1.0	320	2.3×10^{-11}
100420A	8223	–	–	–	–	–
100615A	1.1×10^4	–	–	–	–	–
110201A	291	3	37	−1.0	550	1.4×10^{-10}
110205A	841	20	123	1.0	600	6.9×10^{-10}
110928A	2896	44	223	−0.2	220	1.4×10^{-11}
111029A	500	10	105	−1.0	290	2.8×10^{-11}
111225A	751	21	171	0.3	200	4.0×10^{-11}
120119A	167	5	11	1.7	550	7.3×10^{-9}
120215A	9865	–	–	–	–	–

Upper limits defined as in Table 9.2. $^{\alpha}$Due to the low statistics, the calculation of the Gaussian significance by equation 17 of Li and Ma (1983) is not valid. The ratio of Poisson means, as discussed in the text, is employed instead.

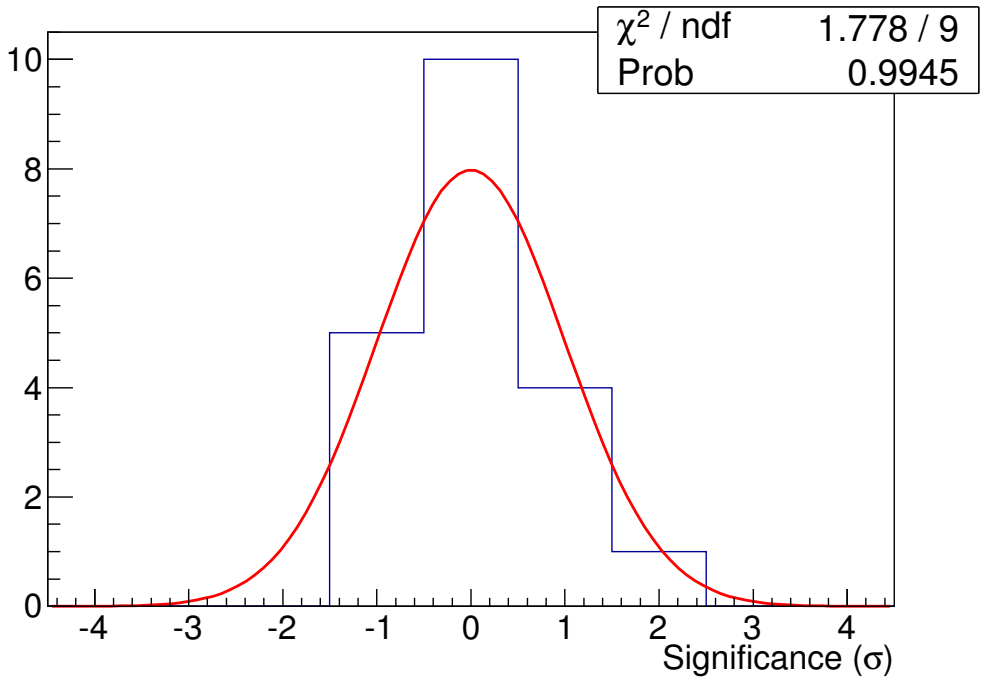

Figure 9.2: Significance histogram obtained from an analysis of the GRBs in the sample over timescales for which VERITAS is maximally sensitive to a burst with a $t^{-1.5}$ power-law afterglow. Included in the figures is the normalized Gaussian distribution of mean zero and variance one that the significance histogram should follow if no signal is present. The GRB significances are consistent with having been drawn from the aforementioned Gaussian distribution.

backgrounds. For a VERITAS observation beginning 100 s after the GRB T_{trig}, the observation window that gives maximum sensitivity is $\sim$ 2 – 5 minutes for GRBs similar to the brightest LAT-detected bursts. For bursts with unknown high-energy behavior, the determination of an optimal time window for VHE observations is not straightforward. However, the maximum sensitivity of a VHE instrument such as VERITAS to a GRB with a power-law decay in time is likely to be on the order of a few minutes.

Table 9.4 shows the results of this search. No emission associated with any GRB in the sample of 28 is found. In almost all cases the integration time is sufficiently short as to reduce the on and off counts to values less than ~ 10. In this case, the profile likelihood method for calculating the significance as employed in Li and Ma (1983) undercovers, that is it overestimates the significance, though only by a few percent Zhang and Ramsden (1990). To combat this problem, the use of the ratio of Poisson means (also known as Fisher's exact test) is used, which is guaranteed by construction not to undercover and gives the most accurate and conservative results (Cousins *et al.*, 2008).

The distribution of significances for the optimum time analysis is shown in Figure 9.2. For eight of the bursts, the maximally sensitive duration of observation is greater than the length of time spent observing the burst and these bursts are omitted from this analysis. This occurred when the delay to the beginning of VERITAS observations was sufficiently long.

9.3 Looking for VHE Gamma-Rays from X-Ray Flares During GRB Afterglows

In the case of GRB 080310, the *Swift*-XRT detected a large X-ray flare beginning ~ 475 s after the beginning of the burst as measured by the *Swift*-BAT. VERITAS was on target 342 s after T_{trig} for this burst and observed throughout the X-ray flare.

Figure 9.3 shows the VERITAS observing window for this burst relative to the XRT lightcurve (Evans *et al.*, 2007, 2009). A search for VHE emission is made coincident with the X-ray flare.

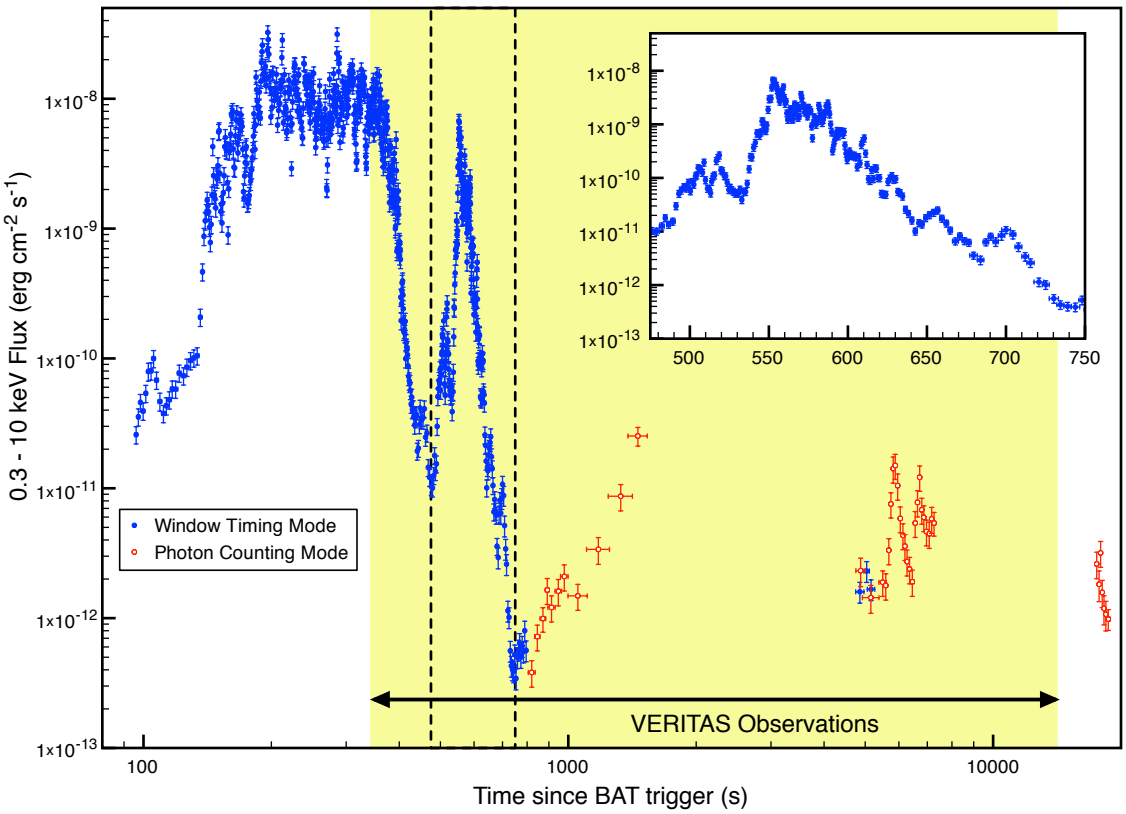

Figure 9.3: VERITAS observation window of GRB 080310 superimposed on the *Swift*-XRT lightcurve (Evans *et al.*, 2007, 2009). The inset shows the structure of the X-ray flare (between the dashed lines) and is the time window over which the search for VHE emission was performed. No significant excess of VHE gamma rays coincident with the X-ray flare ($475\ \mathrm{s} < t - \mathrm{T_{trig}} < 750\ \mathrm{s}$) was found.

No significant excess of VHE gamma-ray events coincident with the large X-ray flare corresponding to the interval $\mathrm{T_{trig}} + 475$ s to $\mathrm{T_{trig}} + 750$ s during the afterglow of GRB 080310 (see Figure 9.3) is found. After accounting for gamma-ray attenuation

by the EBL, an integral upper limit of 9.8×10^{-8} ph cm^{-2} s^{-1} above 310 GeV is calculated. Though the flare was quite bright in the XRT band, increasing by ~ 3 orders of magnitude relative to the underlying afterglow, the burst was at a moderate redshift ($z = 2.4$) so the VHE gamma-ray attenuation is significant.

Over the time period of the flare observed during the afterglow of GRB 080310, the VERITAS upper limits constrain the integral of F_ν above 300 GeV, corrected for absorption by the EBL, to be less than 9.4×10^{-8} erg cm^{-2} s^{-1}, which is a factor of ~ 12 above the peak flux observed by the *Swift*-XRT in the 0.3 – 10 keV band. In light of the fact that GRB 080310 was at a redshift of nearly 2.5, it is clear that VHE observations of a strong X-ray flare from a low redshift GRB could challenge some models in which SSC processes produce VHE emission simultaneously and with comparable intensity to the X-ray emission during the flare (Fan *et al.*, 2008) and add detail to our understanding of the processes occurring in GRB afterglows.

9.4 Constraints on VHE Emission During the Early Afterglow Phase of GRBs

After the VERITAS upper limits are corrected for EBL effects, the VHE upper limits on the fluence above 200 GeV are compared with the fluences of the GRBs as measured by the *Swift*-BAT in the 15 – 350 keV energy range (Butler *et al.*, 2010, 2007), that is taken as a proxy for the overall intensity of the burst. To account for

the different delays and durations of the VERITAS observations, t_{med} is calculated, the time since the beginning of the VERITAS observations of the GRB at which VERITAS is expected to detect half of the photon signal, assuming a time profile of the GRB afterglow of $\frac{dN}{dE} \propto t^{-1.5}$ that is motivated by the high-energy afterglows observed by the *Fermi*-LAT.

The ratio of VERITAS upper limit on the fluence above 200 GeV to the BAT fluence versus t_{med}, is plotted in Figure 9.4(a) for each burst. Since a time-dependence of the VHE afterglow is assumed, this ratio may be calculated for any time period after the start of the GRB, which is taken to be $t - T_{trig} > 300$ s. Then for each GRB, we calculate the fractional upper limit on the VHE gamma-ray fluence over the entire afterglow ($300 < t - T_{trig} < \infty$) relative to the fluence measured by the BAT. A histogram of this quantity is plotted in Figure 9.4(b). It should be noted that if the bursts with unknown redshift are assumed to have the mean redshift of the GRBs in our sample ($z = 1.9$) as opposed to mean redshift detected by *Swift* ($z = 2.5$), then the distribution of bursts with unknown redshift moves to the left and more closely follows the distribution of known-z bursts.

These results show that for several bursts the VHE component of the GRB afterglow is less than the energy released in the *Swift*-BAT band during the prompt phase of the burst. With observation delays often on the order of a few hundred seconds, the VERITAS upper limits begin to restrict theoretical models in which the afterglow from the forward external shock contains an SSC component in addition to

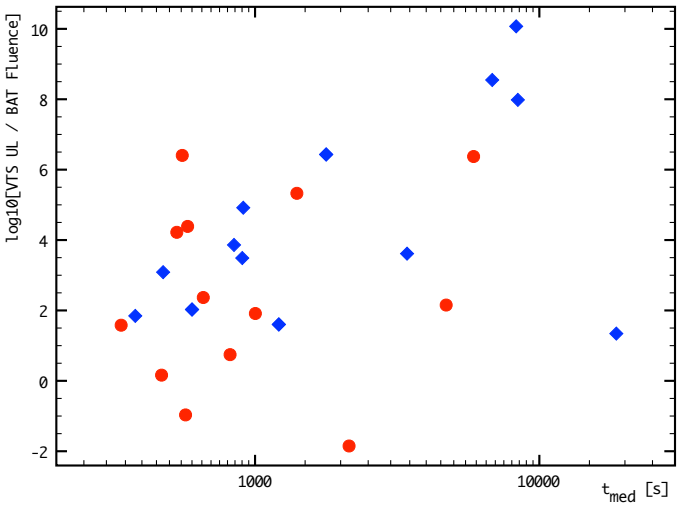

(a)

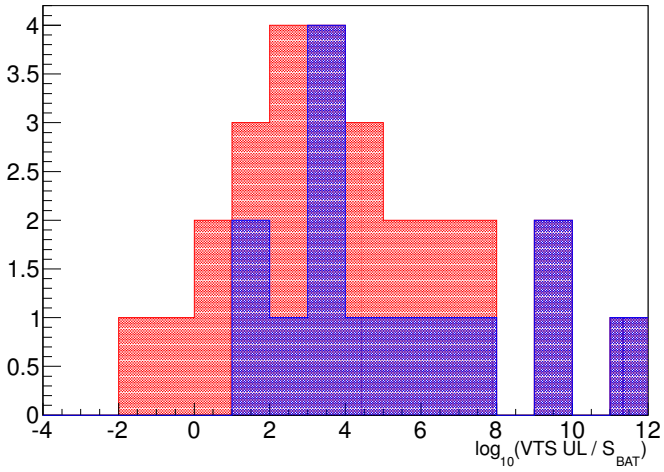

(b)

Figure 9.4: (a) EBL-corrected VERITAS integral fluence upper limits above 200 GeV, divided by the fluence measured by the *Swift*-BAT in the 15 – 350 keV energy band as a function of t_{med} as defined in the text. (b) A histogram of the ratio of the VERITAS integral fluence upper limit above 200 GeV, now integrated over the time period $t - T_{trig} > 300$ s, to the Swift-BAT fluence. In both figures the red entries indicate GRBs with measured redshifts, while the blue entries represent GRBs without measured redshifts and for which a fiducial redshift of $z = 2.5$ is assumed.

the synchrotron component (Xue *et al.*, 2009).

VERITAS continues to take follow-up observations of GRBs. In the summer of 2009 one of the telescopes in the VERITAS array was moved to a new position that resulted in an improvement in sensitivity of $\sim 30\%$. Last summer (2011), an upgraded implementation of the telescope-level trigger system was installed and by Fall 2012 the replacement of existing PMTs with a more sensitive PMT will significantly increase the low energy response of the instrument. This is particularly important for GRB observations as the EBL significantly attenuates the high-energy component of sources with appreciable redshifts.

Additionally, work is ongoing to improve the sensitivity of the array with respect to low elevation targets, which make up the majority of GRB observations. Response times for immediately observable bursts have been gradually decreasing and efforts are underway to increase the slewing speed of the telescope motors to reduce these times further. Such efforts are increasing the GRB science capability of VERITAS and will lead to a more thorough characterization of the highest energy emission from gamma-ray bursts.

Chapter 10

Discussion

10.1 Constraints from VHE Observations on GRB Environment, Particle Populations, & Shock Acceleration

The observations of GRBs with Milagro and VERITAS provide information on the nature of of the highest-energy processes occurring during GRBs. The non-detection of any GRB with these or similar instruments is due to some combination of intrinsic GRB emission properties, VHE instrument performance, and photon-photon attenuation of VHE gamma rays by the EBL. The instruments are well understood and a general consensus is developing on the properties of the EBL, particularly at low to moderate redshifts and at energies of interest to VHE gamma-ray telescopes. The

intrinsic emission characteristics of GRBs, then, can be constrained to some degree by VHE observations, even with the current non-detections so far acquired.

The Milagro limits on the prompt emission from more than 100 GRBs provide a relatively large catalog of VHE limits, which in turn provides a robust upper limit on the energy released by GRBs at energies above a few GeV. Though Milagro is significantly less sensitive than the IACT instruments currently in operation, the ability to observe many bursts during their prompt phases allows for constraints on the gamma-ray emission of internal shocks and the bulk Lorentz factor and opacity in the relativistic outflow immediately after acceleration phase. In addition to large numbers of GRB observations, the wide FOV and high duty cycle of Milagro increases the odds of observing an exceptional burst that may challenge the current understanding of GRB physics. This was the case with GRB 080319B.

GRB 080319B was exceptional for its optical luminosity and the extremely good instrumental coverage. The interpretation of the optical and keV – MeV emission as correlated, naturally leads to the assumption that the same particle population was responsible for producing both. The failure of the extrapolation of the Band function gamma-ray spectrum down to optical energies implies that different physical mechanisms were responsible for the gamma-ray and optical emission and the SSC mechanism would seem to naturally explain the observations. The fact that no significant flux of second-order IC scattered photons was detected with Milagro strongly disfavors the SSC model of gamma-ray emission over a broad range of characteristic

synchrotron photon energies. It is therefore likely that the gamma rays and optical photons do not arise from a common origin (Abdo *et al.*, 2012, Zou *et al.*, 2009b). GRBs are quite a heterogeneous group and the results from an exceptional burst like GRB 080319B may not be expected to apply to all GRBs, but it is important to note the wealth of information provided when a GRB is observed under favorable circumstances.

Observations of the GRB early afterglow with VERITAS have placed strong limits on the VHE emission from IC processes in the forward shock. Constraining the emission properties at VHE energies on minute timescales has direct implications on the ambient density and equipartition fraction of the magnetic field in the fireball model (Pe'er and Waxman, 2005). The lack of a VERITAS detection and the corresponding upper limits favor the scenario where the magnetic field in the GRB outflow is at or near equipartition and/or that a wind environment is preferred over a constant-density ISM. In this context, simultaneous observations of a *Fermi*-LAT-detected GRB by an IACT under reasonably good observing conditions would be exceptionally informative. It is clear from VERITAS (and other IACT) upper limits on VHE GRB emission that, while IC and SSC mechanisms may produce VHE emission, this component, if it is observable, contains much less energy than the prompt emission produced in the lower energy (X-ray – soft gamma-ray) regime. This suppression of VHE gamma-rays relative to X-rays may also be true during X-ray flares in GRB afterglows, as evidenced by VERITAS observations of the afterglow of GRB 080310

(Acciari *et al.*, 2011), which runs contrary to the expectations of some models (Pe'er and Waxman, 2005, Wang *et al.*, 2001). A comprehensive search for VHE gamma-ray flares associated with X-ray flares has yet to be performed but could be an interesting study, particularly in the context of the LAT-detected emission concurrent with X-ray flares in GRB 100728A (Abdo *et al.*, 2011).

Observing unpredictable, transient objects such as GRBs is difficult at any energy, but particularly at high energies where the emission is generally expected to be relatively short lived ($<$ hr). The failure of any ground-based VHE experiment to detect GRB emission is almost certainly due in some part to the sensitivity and overall performance of current-generation VHE instruments. In particular, current-generation IACTs have been shown to possess the sensitivity required to detect bright *Fermi*-LAT-detected GRBs, assuming no severe internal suppression of VHE gamma rays in the GRB itself (Acciari *et al.*, 2011). In the following section a brief discussion of the sensitivity and detection prospects for current-generation VHE observatories, particularly VERITAS, is discussed.

10.2 Sensitivity of Current-Generation Ground-Based VHE Observatories to GRBs

The most sensitive VHE experiments in operation today are the IACTs. The largest drawbacks to GRB observations with these instruments are their low duty

cycle and small fields of view which make GRB observations relatively infrequent and delayed (due to the re-point requirement). The odds of a GRB occurring in the FOV of an IACT over the duration of their operation is quite small but may have occurred once already (Aharonian *et al.*, 2008), however, see Wijnands *et al.* (2009). In most cases, the observations of GRBs with IACTs will take place minutes to hours after the initial satellite detection and occur at less than optimal elevations. Broadly speaking, the results from GRB observations by the currently-operating IACT experiments (VERITAS (Acciari *et al.*, 2011), HESS (Aharonian *et al.*, 2009), and MAGIC (Albert *et al.*, 2007)) typically constrain the photon flux above a few hundred GeV to be $< 10^{-7}$ m^{-2} s^{-1}, a value which is comparable to flux values measured by the *Swift*-XRT in the X-ray band.

The detection of VHE emission from GRBs in light of recent observations by the *Fermi* and *Swift* space telescopes remains a challenging, though not unreasonable, prospect. The number of GRBs found by the LAT to emit GeV radiation is small, with a detection rate on the order of one every few months. Combined with the $\sim$10 – 15% duty cycle of an IACT array such as VERITAS, the probability of simultaneous observation of such bursts is not high. On the other hand, >30 GeV emission has been detected from both short (Abdo *et al.*, 2009a) and long (Abdo *et al.*, 2009b) GRBs and, in the latter case, persists well after the prompt phase of the burst. Furthermore, these observations indicate that the high-energy photon absorption due to the EBL is not so severe (Abdo *et al.*, 2010b) as to rule out ground-based VHE detections that

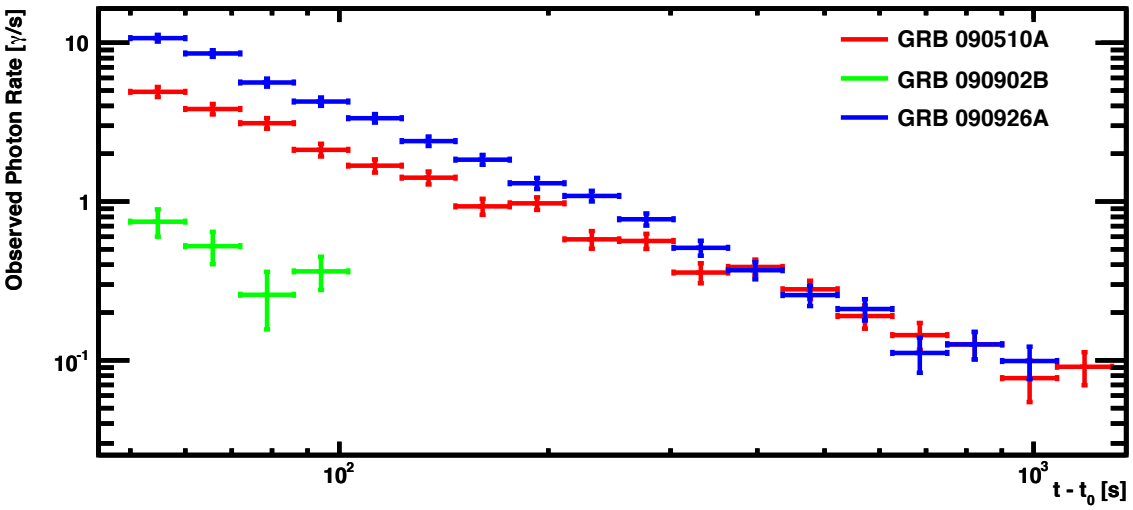

Figure 10.1: Predicted VERITAS lightcurves for three of the four brightest *Fermi*-LAT GRBs. The fourth, GRB 080916C had a redshift of nearly 4.4 and VHE emission is predicted to be too attenuated by the EBL to be detectable by VERITAS. The EBL model of Gilmore *et al.* (2009) is used to estimate the attenuation of the VHE γ-rays. The elevation of the burst with respect to VERITAS is chosen to be 70° and no intrinsic spectral cutoff of the high energy emission is assumed. Each point signifies a detection of at least three standard deviations (σ) in that time bin.

in turn could strongly constrain models of GRB physics (Cenko *et al.*, 2011b), as well as those of the EBL.

Approximately one of every twenty-five GRBs detected by the *Fermi*-GBM is detected by the LAT (provided the burst also falls in the LAT FOV). Though they are rare, some luminous, LAT-detected GRBs should be detectable by VERITAS. Taking the spectral and temporal characteristics of the high energy emission from the four brightest *Fermi*-LAT bursts: GRB 080916C (Abdo *et al.*, 2009c), GRB 090510 (De Pasquale *et al.*, 2010), GRB 090902B (Abdo *et al.*, 2009b), and GRB 090926A (Swenson *et al.*, 2010) we estimate the expected flux of VHE photons in the energy

range of VERITAS as a function of time. Figure 10.1 shows the lightcurves of three of these four bursts that we predict to have been detectable by VERITAS. GRB 090510 and GRB 090926A produce significant signal in the VERITAS band for roughly a thousand seconds. GRB 080916C had a redshift of $z > 4$ and the VHE emission is extremely suppressed through interaction with the EBL. It is observed that even for bursts with redshift between 1 and 2, some exceptional GRBs may be quite bright in the VERITAS energy band. However, in the absence of delayed activity (e.g. that associated with X-ray flares) the power law temporal decay of the late-time, high-energy emission necessitates relatively rapid follow-up observations. VERITAS has made several GRB follow-up observations with delays of less than 100 seconds and has a median response time of ~ 5 minutes and therefore may be capable of detecting the same high-energy component that the *Fermi*-LAT detects, provided it extends to > 100 GeV energies.

In addition to IACTs there are several currently- or recently-operating EAS arrays that have put upper limits on GRB emission. Although these instruments are much less sensitive that IACTs, their high duty cycles and wide fields of view enable the observation of GRBs much more frequently. This increases the odds of observing *Fermi*-LAT-detected GRBs and enables the observation of the prompt phase of GRBs. Results from Milagro (Abdo *et al.*, 2007, 2012, Atkins *et al.*, 2004a, 2005), ARGO-YBJ (Aielli *et al.*, 2009), Auger (Bertou, 2008), and LAGO (Allard *et al.*, 2008) have put upper limits on prompt emission from GRBs. Though these limits are several

orders of magnitude higher than those from IACTs, the limit on prompt emission for some extraordinary bursts (e.g. GRB 080319B) can strongly constrain some models of GRB emission.

The High Altitude Water Cherenkov (HAWC) detector (DeYoung *et al.*, 2010) is currently being constructed, and along with the next-generation IACT experiment, the Cherenkov Telescope Array (CTA) (Actis *et al.*, 2011), will greatly increase the capabilities of ground-based VHE astronomy both generally and with respect to GRBs. The prospects for GRB science with these instruments is briefly reviewed in the following section.

10.3 Prospects For Future VHE GRB Observations

Recent results from *Fermi* show that current-generation IACTs most likely have the sensitivity to detect the highest-energy emission from some hyper-energetic GRBs. The odds of such a detection are not great however, due to the rarity of these events and to the low duty cycles of IACT instruments. Wide-field EAS instruments such as Milagro have almost certainly observed at least a few hyper-energetic GRBs, but the sensitivity of these types of instruments has not been good enough to claim a conclusive detection. Milagrito, a prototype of Milagro, did claim a tentative detection of GRB 970417A at the $\sim 3\sigma$ level (Atkins *et al.*, 2000). It is conceivable that this burst

was similar to some of the *Fermi*-LAT-detected hyper energetic GRBs and/or very nearby in which case attenuation by the EBL may have been relatively small. This particular GRB was detected by BATSE and not localized well enough to facilitate optical follow-up observations. No redshift was determined for this burst. Milagrito was ∼4–8 times less sensitive than Milagro was, so if Milagrito did in fact marginally detect GRB 970417A, such a burst would have been easily detectable by Milagro.

Both IACTs and EAS arrays have their own advantages with respect to GRB observations and GRB science with the next generation of both of these types of instruments looks promising. The next-generation EAS array, HAWC, is under construction and offers the most exciting prospects for ground-based VHE GRB science in the near future.

10.3.1 High Altitude Water Cherenkov (HAWC) Observatory

Expected to be completed in 2014, HAWC is currently the most promising instrument for VHE GRB science (Abeysekara *et al.*, 2011). The observatory will consist of 300 large cylindrical tanks, each instrumented with 4 PMTs. These tanks will be distributed in a close-packed array near the peak of the Volcán Sierra Negra in Mexico at an altitude of 4100 m, 1500 m above the elevation at which Milagro was situated. HAWC will be 15 times more sensitive than Milagro to a Crab-like point source and the sensitivity increase is even more pronounced for lower-energy gamma

rays due to the significantly larger fraction of particles in the EAS that make it down to HAWC altitudes. Much like Milagro, HAWC will be operated in both a standard air-shower reconstruction mode and a scaler mode, though for GRB science it is the scaler system that will most likely be the most interesting. The scaler rates from all 1200 HAWC PMTs will be monitored in 10 ms time windows, a frequency increase of 100 over Milagro which only had 1 s resolution with the scaler system. This dense sampling in time offers the possibility of reconstructing high-energy GRB light curves which could provide valuable insight into GRB emission processes.

The wide FOV and high duty cycle of HAWC make it ideal for observing the prompt phase of GRBs but also greatly increases the probability of observing the hyper-energetic bursts similar to those observed by the *Fermi*-LAT. Figure 10.2 shows the sensitivity of the scaler system as a function of several variables and also includes a few of the *Fermi* hyper-energetic GRBs for comparison. Depending on the details of the nature of the GRB, it is likely that HAWC would detect emission from such bursts. HAWC observations of the prompt phases of GRBs simultaneous to satellite-based observations at lower energies will be able to constrain the nature of the extra-hard power-law component seen by *Fermi* in bursts like GRB 090902B (Abdo *et al.*, 2009b) and provide information on intrinsic spectral cutoffs. The fact that HAWC will most likely be operating concurrently with *Swift* and *Fermi* significantly enhances the quality of GRB science results produced by all of the experiments.

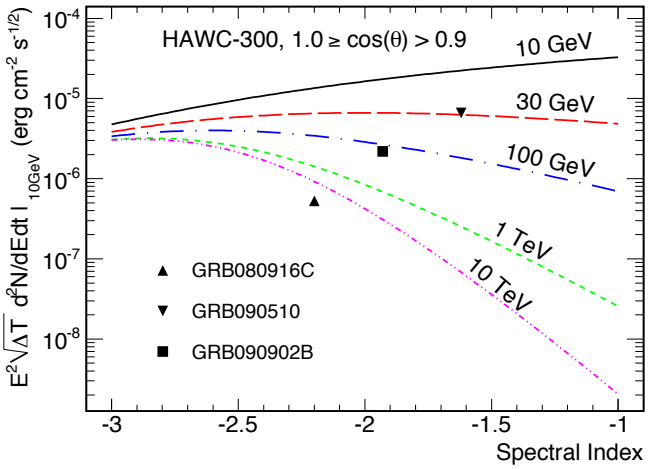

(a)

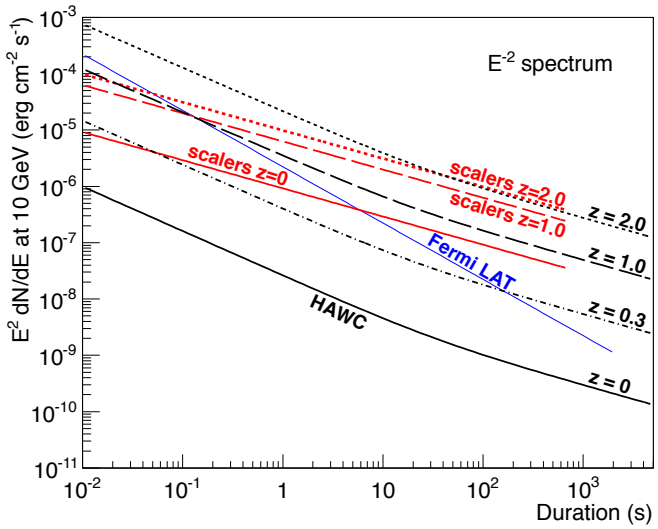

(b)

Figure 10.2: Senstivity of HAWC to GRBs. Figure 10.2(a) shows the necessary flux at 10 GeV multiplied by the square root of the duration of the GRB required to produce a 5σ detection from the HAWC scaler data. This is for the full HAWC array and for a burst with high elevation. The energies plotted indicate an assumed exponential spectral cutoff. The data from 3 bright LAT-detected GRBs are included. Figure 10.2(b) shows the 5σ detection level (discovery potential) for the HAWC scaler (air-shower reconstruction) analysis as a function of duration for various redshifts. Included is the flux necessary for the observation of 1 photon above 10 GeV by the *Fermi*-LAT. Figures from Abeysekara *et al.* (2011).

10.3.2 The Cherenkov Telescope Array (CTA)

CTA is the proposed next-generation IACT facility now in the planning stages (Actis *et al.*, 2011). It is expected that CTA will provide at least an order of magnitude sensitivity improvement over current-generation IACTs (e.g. VERITAS, MAGIC, and HESS), with particular improvement at low (< 100) GeV energies. While the characteristics of the observatory have not yet been fixed, studies of the predicted GRB detection efficiency and results from GRB observations have already been made (Gilmore *et al.*, 2012). While CTA will still suffer from some of the inherent limitations of existing IACTs with respect to GRB observations (small FOV, delays, etc.), it is expected that the increased sensitivity of CTA will significantly improve the chances of a GRB detection.

Using the BATSE and *Swift* GRB catalogs and taking into account the projected performance of CTA, information from high energy observations of GRBs with the *Fermi*-LAT, and the non-detections of current-generation IACTs, Gilmore et al. (Gilmore *et al.*, 2012) determine that CTA should detect a GRB once every 30 months or so, assuming satellite GRB triggers at a rate similar to that provided today primarily from *Fermi* and *Swift*. While not expected to be a common occurrence, a GRB detection at VHE energies with CTA's sensitivity could have a large influence on GRB science. Furthermore, a non-detection with CTA of a GRB simultaneously detected by the *Fermi*-LAT could constrain the properties of the EBL at high redshifts.

The prospects for GRB science with ground-based VHE gamma-ray observatories

are bright. HAWC and CTA will offer significant improvements over their predecessors with increased sensitivity and reduced energy thresholds. GRB detections with these instruments will provide data that can constrain some of the most fundamental physical properties of GRBs including the nature of the radiation production mechanisms, the bulk Lorentz factor of material in GRB jets, and the overall energy released in these spectacular events.

Bibliography

R Abbasi, *et al.* An absence of neutrinos associated with cosmic-ray acceleration in γ-ray bursts. *Nature*, **484**(7394):351, 2012.

A A Abdo, *et al.* Milagro Constraints on Very High Energy Emission from Short-Duration Gamma-Ray Bursts. *ApJ*, **666**(1):361, 2007.

A A Abdo, *et al.* A limit on the variation of the speed of light arising from quantum gravity effects. *Nature*, **462**(7):331, 2009a.

A A Abdo, *et al.* Fermi Observations of GRB 090902B: A Distinct Spectral Component in the Prompt and Delayed Emission. *ApJL*, **706**(1):L138, 2009b.

A A Abdo, *et al.* Fermi Observations of High-Energy Gamma-Ray Emission from GRB 080916C. *Science*, **323**(5):1688, 2009c.

A A Abdo, *et al.* Fermi Detection of Delayed GeV Emission from the Short Gamma-Ray Burst 081024B. *ApJ*, **712**:558, 2010a.

A A Abdo, *et al.* Fermi Large Area Telescope Constraints on the Gamma-ray Opacity of the Universe. *ApJ*, **723**(2):1082, 2010b.

A A Abdo, *et al.* Detection of High-energy Gamma-Ray Emission During the X-Ray Flaring Activity in GRB 100728A. *ApJL*, **734**:L27, 2011.

A A Abdo, *et al.* Constraints on the emission model of the "Naked-Eye Burst" GRB 080319B. *ApJL*, **submitted**, 2012.

A U Abeysekara, *et al.* On the sensitivity of the HAWC observatory to gamma-ray bursts. *arXiv*, **1108**:6034, 2011.

V A Acciari, *et al.* VERITAS Observations of Gamma-Ray Bursts Detected by Swift. *ApJ*, **743**(1):62, 2011.

M Ackermann, *et al.* Fermi Observations of GRB 090510: a Short-Hard Gamma-Ray Burst with an Additional, Hard Power-Law Component From 10 keV to GeV Energies. *ApJ*, **716**(2):1178, 2010.

M Ackermann, *et al.* Detection of a Spectral Break in the Extra Hard Component of GRB 090926A. *ApJ*, **729**(2):114, 2011.

M. Actis, *et al.* Design concepts for the Cherenkov Telescope Array CTA: an advanced facility for ground-based high-energy gamma-ray astronomy. *Experimental Astronomy*, **32**(3):193, 2011.

M. Aglietta, *et al.* Search for Gamma-Ray Bursts at Photon Energies E >= 10 GeV and E >= 80 TeV. *ApJ*, **469**:305, 1996.

S. Agostinelli, *et al.* Geant4-a simulation toolkit. *NIM A*, **506**:250, 2003.

F Aharonian, *et al.* HESS Observations of the Prompt and Afterglow Phases of GRB 060602B. *ApJ*, **690**(2):1068, 2008.

F Aharonian, *et al.* HESS observations of -ray bursts in 2003-2007. *A&A*, **495**:505, 2009.

G Aielli, *et al.* ARGO-YBJ constraints on very high energy emission from GRBs. *APh*, **32**:47, 2009.

C W Akerlof, *et al.* Locating very high energy gamma-ray sources with arcminute accuracy. *ApJ*, **377**:L97, 1991.

J Albert, *et al.* MAGIC Upper Limits on the Very High Energy Emission from Gamma-Ray Bursts. *ApJ*, **667**:358, 2007.

J Albert, *et al.* VHE Ray Observation of the Crab Nebula and its Pulsar with the MAGIC Telescope. *ApJ*, **674**(2):1037, 2008.

D Allard, *et al.* Use of water-Cherenkov detectors to detect Gamma Ray Bursts at the Large Aperture GRB Observatory (LAGO). *NIM A*, **595**(1):70, 2008.

G Amelino-Camelia, *et al.* Tests of quantum gravity from observations of γ-ray bursts. *Nature*, **393**(6687):763, 1998.

Katsuaki Asano, Sylvain Guiriec, and Peter Mészáros. Hadronic Models for the Extra Spectral Component in the Short GRB 090510. *ApJL*, **705**(2):L191, 2009.

R Atkins, *et al.* Evidence for TeV Emission from GRB 970417A. *ApJ*, **533**(2):L119, 2000.

R Atkins, *et al.* Limits on Very High Energy Emission from Gamma-Ray Bursts with the Milagro Observatory. *ApJ*, **604**(1):L25, 2004a.

R Atkins, *et al.* TeV Gamma-Ray Survey of the Northern Hemisphere Sky Using the Milagro Observatory. *ApJ*, **608**(2):680, 2004b.

R Atkins, *et al.* Constraints on Very High Energy Gamma-Ray Emission from Gamma-Ray Bursts. *ApJ*, **630**(2):996, 2005.

W B Atwood, *et al.* The Large Area Telescope on the Fermi Gamma-Ray Space Telescope Mission. *ApJ*, **697**(2):1071, 2009.

D Band, *et al.* BATSE observations of gamma-ray burst spectra. I - Spectral diversity. *ApJ*, **413**:281, 1993.

Matthew G. Baring. Temporal Evolution of Pair Attenuation Signatures in Gamma-Ray Burst Spectra. *ApJ*, **650**(2):1004, 2006.

S D Barthelmy, *et al.* An origin for short -ray bursts unassociated with current star formation. *Nature*, **438**(7):994, 2005.

G Battistoni, *et al.* The FLUKA code: description and benchmarking. In *Hadronic Shower Simulation Workshop*, pages 31–49. AIP, 2007.

X Bertou. Search for Gamma Ray Bursts using the single particle technique at the Pierre Auger Observatory. In *Proceedings of the 30th International Cosmic Ray Conference. July 3 - 11*, pages 441–444. 2008.

P N Bhat and S Guiriec. An overview of the current understanding of Gamma Ray Bursts in the Fermi era. *Bulletin of the Astronmical Society of India*, **39**:471, 2011.

Elisabetta Bissaldi, *et al.* First-Year Results of Broadband Spectroscopy of the Brightest Fermi-GBM Gamma-Ray Bursts. *ApJ*, **733**(2):97, 2011.

R D Blandford and D. G. Payne. Hydromagnetic flows from accretion discs and the production of radio jets. *MNRAS*, **199**:883, 1982.

J S Bloom, D A Frail, and S R Kulkarni. GammaRay Burst Energetics and the GammaRay Burst Hubble Diagram: Promises and Limitations. *ApJ*, **594**(2):674, 2003.

G Boella, *et al.* BeppoSAX, the wide band mission for X-ray astronomy. *Astron. Astrophys. Suppl. Ser.*, **122**(2):299, 1997.

Ž. Bošnjak, F. Daigne, and G Dubus. Prompt high-energy emission from gamma-ray bursts in the internal shock model. *A&A*, **498**(3):677, 2009.

G Bossard, *et al.* Cosmic ray air shower characteristics in the framework of the parton-based Gribov-Regge model NEXUS. *Phys. Rev. D*, **63**(5), 2001.

Markus Bottcher and Charles D Dermer. High-energy Gamma Rays from Ultra–high-energy Cosmic-Ray Protons in Gamma-Ray Bursts. *ApJ*, **499**(2):L131, 1998.

D N Burrows, *et al.* Bright X-ray Flares in Gamma-Ray Burst Afterglows. *Science*, **309**(5):1833, 2005.

Nathaniel R Butler, Joshua S Bloom, and Dovi Poznanski. The Cosmic Rate, Luminosity Function, and Intrinsic Correlations of Long Gamma-Ray Bursts. *ApJ*, **711**:495, 2010.

Nathaniel R Butler, *et al.* A Complete Catalog of Swift Gamma-Ray Burst Spectra and Durations: Demise of a Physical Origin for Pre-Swift High-Energy Correlations. *ApJ*, **671**(1):656, 2007.

S B Cenko, J. L. Hora, and J S Bloom. GRB 110205A: FAST redshift. *GCN*, **1163**, 2011a.

S B Cenko, *et al.* GRB 070419: Keck/LRIS absorption redshift. *GCN*, **6322**:1, 2007.

S B Cenko, *et al.* Afterglow Observations of Fermi Large Area Telescope Gamma-Ray Bursts and the Emerging Class of Hyper-Energetic Events. *ApJ*, **732**(1):29, 2011b.

G Chincarini, *et al.* The First Survey of X-Ray Flares from Gamma-Ray Bursts Observed by Swift: Temporal Properties and Morphology. *ApJ*, **671**:1903, 2007.

R Chornock, *et al.* GRB 090418 Lick redshift. *GCN*, **9151**:1, 2009.

P Cogan. VEGAS, the VERITAS Gamma-ray Analysis Suite. In *Proceedings of the 30th International Cosmic Ray Conference. July 3 - 11*, pages 1385–1388. 2008.

V Connaughton, *et al.* A Search for TeV Counterparts to BATSE Gamma-Ray Bursts. *ApJ*, **479**:859, 1997.

R Cousins, J Linnemann, and J Tucker. Evaluation of three methods for calculating statistical significance when incorporating a systematic uncertainty into a test of the background-only hypothesis for a Poisson process. *NIM A*, **595**:480, 2008.

A Cucchiara, D Fox, and N Tanvir. GRB 091024 gemini-north redshift. *GCN*, **1006**, 2009.

A Cucchiara and J X Prochaska. GRB 120119A: gemini-s redshift. *GCN*, **1286**, 2012.

A Cucchiara, *et al.* A Photometric Redshift of $z \sim 9.4$ for GRB 090429B. *ApJ*, **736**(1):7, 2011.

J Cummings, *et al.* GRB 080319B, Swift-BAT refined analysis. *GCN*, **7462**:1, 2008.

F. Daigne and R. Mochkovitch. Gamma-ray bursts from internal shocks in a relativistic wind: temporal and spectral properties. *MNRAS*, **296**(2):275, 1998.

Frédéric Daigne and Robert Mochkovitch. The physics of pulses in gamma-ray bursts: emission processes, temporal profiles and time-lags. *MNRAS*, **342**(2):587, 2003.

JM Davies and ES Cotton. Design of the Quartermaster Solar Furnace. *Solar Energy*, 1957.

M De Pasquale, *et al.* Swift and Fermi Observations of the Early Afterglow of the Short Gamma-Ray Burst 090510. *ApJL*, **709**:L146, 2010.

A de Ugarte Postigo, *et al.* GRB 090102: NOT redshift. *GCN*, **8766**:1, 2009.

Charles D Dermer. AIP Conference Proceedings. In *GAMMA-RAY BURSTS IN THE SWIFT ERA: Sixteenth Maryland Astrophysics Conference*, pages 97–102. AIP, 2006.

Charles D Dermer. Rapid X-Ray Declines and Plateaus in Swift GRB Light Curves Explained by a Highly Radiative Blast Wave. *ApJ*, **664**:384, 2007.

Charles D Dermer, James Chiang, and Kurt E Mitman. Beaming, Baryon Loading, and the Synchrotron Self-Compton Component in Gamma-Ray Bursts. *ApJ*, **537**(2):785, 2000.

L. Dessart, *et al.* Neutrino Signatures and the Neutrino-Driven Wind in Binary Neutron Star Mergers. *ApJ*, **690**(2):1681, 2009.

Tyce DeYoung, *et al.* The HAWC Observatory. *38th COSPAR Scientific Assembly.* Held 18-15 July 2010, **38**:2319, 2010.

P A Evans, *et al.* An online repository of Swift/XRT light curves of gamma-ray bursts. *A&A*, **469**(1):379, 2007.

P A Evans, *et al.* Methods and results of an automatic analysis of a complete sample of Swift-XRT observations of GRBs. *MNRAS*, **397**:1177, 2009.

A D Falcone, *et al.* The Giant X-Ray Flare of GRB 050502B: Evidence for Late-Time Internal Engine Activity. *ApJ*, **641**:1010, 2006.

A D Falcone, *et al.* The First Survey of XRay Flares from GammaRay Bursts Observed by Swift: Spectral Properties and Energetics. *ApJ*, **671**(2):1921, 2007.

Yi-Zhong Fan, *et al.* High-energy afterglow emission from gamma-ray bursts. *MNRAS*, **384**:1483, 2008.

Justin D Finke, Soebur Razzaque, and Charles D Dermer. Modeling the Extragalactic Background Light from Stars and Dust. *ApJ*, **712**(1):238, 2010.

C Firmani, *et al.* Discovery of a tight correlation among the prompt emission properties of long gamma-ray bursts. *MNRAS*, **370**(1):185, 2006.

G J Fishman, *et al.* The BATSE experiment on the Compton Gamma Ray Observatory: Status and some early results. *NASA Conference Publication*, **3137**:26, 1992.

A. Franceschini, G. Rodighiero, and M. Vaccari. Extragalactic optical-infrared background radiation, its time evolution and the cosmic photon-photon opacity. *A&A*, **487**(3):837, 2008.

T J Galama, *et al.* An unusual supernova in the error box of the [γ-ray burst of 25 April 1998. *Nature*, **395**(6703):670, 1998.

A Galli and L Piro. High energy afterglows and flares from gamma-ray burst by inverse Compton emission. *A&A*, **475**(2):421, 2007.

A Galli and L Piro. Prospects for detection of very high-energy emission from GRB in the context of the external shock model. *A&A*, **489**:1073, 2008.

M. Gedalin, M. A. Balikhin, and D. Eichler. Efficient electron heating in relativistic shocks and gamma-ray-burst afterglow. *Physical Review E*, **77**(2):26403, 2008.

N Gehrels, E Ramirez-Ruiz, and D B Fox. Gamma-Ray Bursts in the Swift Era. *Annual Review of Astronomy & Astrophysics*, **47**:567, 2009.

N Gehrels, *et al.* The Swift Gamma-Ray Burst Mission. *ApJ*, **611**(2):1005, 2004.

Giancarlo Ghirlanda, *et al.* Gamma-Ray Bursts: New Rulers to Measure the Universe. *ApJ*, **613**(1):L13, 2004.

G Ghisellini, *et al.* GeV emission from gamma-ray bursts: a radiative fireball? *MNRAS*, **403**(2):926, 2010.

R. Gilmore and E Ramirez-Ruiz. Local Absorption of High-energy Emission from Gamma-ray Bursts. *ApJ*, **721**(1):709, 2010.

Rudy C Gilmore, Francisco Prada, and Joel Primack. Modelling gamma-ray burst

observations by Fermi and MAGIC including attenuation due to diffuse background light. *MNRAS*, **402**(1):565, 2010.

Rudy C Gilmore, *et al.* GeV gamma-ray attenuation and the high-redshift UV background. *MNRAS*, **399**:1694, 2009.

Rudy C Gilmore, *et al.* IACT observations of gamma-ray bursts: prospects for the Cherenkov Telescope Array. *arXiv*, **1201.0010**, 2012.

S Golenetskii, *et al.* Konus-wind observation of GRB 080319B. *GCN*, **7482**:1, 2008.

M M Gonzalez, *et al.* A -ray burst with a high-energy spectral component inconsistent with the synchrotron shock model. *Nature*, **424**(6950):749, 2003.

Robert Gould and Gérard Schréder. Pair Production in Photon-Photon Collisions. *Phys. Rev.*, **155**(5):1404, 1967.

Jonathan Granot, Johann Cohen Tanugi, and Eduardo do Couto e Silva. Opacity Buildup in Impulsive Relativistic Sources. *ApJ*, **677**(1):92, 2008.

Sylvain Guiriec, *et al.* Detection of a Thermal Spectral Component in the Prompt Emission of GRB 100724B. *ApJ*, **727**(2):L33, 2011.

Jon Hakkila and Robert D Preece. Unification of Pulses in Long and Short Gamma-Ray Bursts: Evidence From Pulse Properties and Their Correlations. *ApJ*, **740**(2):104, 2011.

J Hall, *et al.* Veritas CFDs. In *Proceedings of the 28th International Cosmic Ray Conference. July 31-August 7*, page 2851. 2003.

D Hanna, *et al.* An LED-based flasher system for VERITAS. *NIM A*, **612**(2):278, 2010.

T Hattori, K Aoki, and N Kawai. GRB 070521: subaru observations and possible host detection. *GCN*, **6444**:1, 2007.

Michael G. Hauser and Eli Dwek. The Cosmic Infrared Background: Measurements and Implications. *Annual Review of Astronomy & Astrophysics*, **39**:249, 2001.

E Hays. VERITAS Data Acquisition. In *Proceedings of the 30th International Cosmic Ray Conference. July 3 - 11*, pages 1543–1546. 2008.

D. Heck, *et al. CORSIKA: a Monte Carlo code to simulate extensive air showers.* Forschungszentrum Karlsruhe, 1998.

A Heger, *et al.* How Massive Single Stars End Their Life. *ApJ*, **591**(1):288, 2003.

A M Hillas. Cerenkov light images of EAS produced by primary gamma. *In NASA. Goddard Space Flight Center 19th Intern. Cosmic Ray Conf.*, **3**:445, 1985.

W Hofmann, *et al.* Comparison of techniques to reconstruct VHE gamma-ray showers from multiple stereoscopic Cherenkov images. *APh*, **12**(3):135, 1999.

K Hurley, *et al.* The Third Interplanetary Network. In *Deciphering the Ancient Unvierse with Gamma-Ray Bursts*, pages 330–333. AIP, 2010.

P Jakobsson, *et al.* GRB 071020: VLT spectroscopy. *GCN*, **6952**:1, 2007.

Ray W. Klebesadel, Ian B. Strong, and Roy A. Olson. Observations of Gamma-Ray Bursts of Cosmic Origin. *ApJ*, **182**:L85, 1973.

O. Klein and T. Nishina. Über die Streuung von Strahlung durch freie Elektronen nach der neuen relativistischen Quantendynamik von Dirac. *Zeitschrift für Physik*, **52**(1):853, 1929.

T. M. Kneiske and H. Dole. A lower-limit flux for the extragalactic background light. *A&A*, **515**:19, 2010.

T. M. Kneiske, *et al.* Implications of cosmological gamma-ray absorption. II. Modification of gamma-ray spectra. *A&A*, **413**:807, 2004.

P Kumar and R Barniol Duran. On the generation of high-energy photons detected by the Fermi Satellite from gamma-ray bursts. *MNRAS*, **400**:L75, 2009.

P Kumar and R Barniol Duran. External forward shock origin of high-energy emission for three gamma-ray bursts detected by Fermi. *MNRAS*, **409**(1):226, 2010.

P Kumar and A Panaitescu. What did we learn from gamma-ray burst 080319B? *MNRAS*, **391**(1):L19, 2008.

William H Lee and Enrico Ramirez-Ruiz. Accretion Modes in Collapsars: Prospects for Gamma-Ray Burst Production. *ApJ*, **641**(2):961, 2006.

William H Lee, Enrico Ramirez-Ruiz, and Jonathan Granot. A Compact Binary Merger Model for the Short, Hard GRB 050509b. *ApJ*, **630**(2):L165, 2005.

Amir Levinson and David Eichler. Hydrodynamic Collimation of Gamma-Ray-Burst Fireballs. *Phys. Rev. Lett.*, **85**(2):236, 2000.

T Li and Y Ma. Analysis methods for results in gamma-ray astronomy. *ApJ*, **272**:317, 1983.

Yoram Lithwick and Re'em Sari. Lower Limits on Lorentz Factors in GammaRay Bursts. *ApJ*, **555**(1):540, 2001.

A I MacFadyen and S E Woosley. Collapsars: Gamma-Ray Bursts and Explosions in "Failed Supernovae". *ApJ*, **524**(1):262, 1999.

D Malesani, *et al.* GRB 080330: NOT redshift. *GCN*, **7544**:1, 2008.

R. S. Mallozzi. BATSE Web - http://f64.nsstc.nasa.gov. 2010.

A McCann, *et al.* A new mirror alignment system for the VERITAS telescopes. *APh*, **32**(6):325, 2010.

Jonathan C McKinney. General relativistic magnetohydrodynamic simulations of the jet formation and large-scale propagation from black hole accretion systems. *MNRAS*, **368**(4):1561, 2006.

Charles Meegan, *et al.* The Fermi Gamma-Ray Burst Monitor. *ApJ*, **702**(1):791, 2009.

P Mészáros and M J Rees. Delayed GEV Emission from Cosmological Gamma-Ray Bursts - Impact of a Relativistic Wind on External Matter. *MNRAS*, **269**:L41, 1994.

P Mészáros and M J Rees. Optical and LongWavelength Afterglow from GammaRay Bursts. *ApJ*, **476**(1):232, 1997.

B D Metzger, A L Piro, and E Quataert. Time-dependent models of accretion discs formed from compact object mergers. *MNRAS*, **390**(2):781, 2008.

M R Metzger, *et al.* Spectral constraints on the redshift of the optical counterpart to the γ-ray burst of 8 May 1997. *Nature*, **387**(6636):878, 1997.

M. Michalowski, *et al.* GRB 111005A: ATCA 18 GHz detection. *GCN*, **12422**, 2011.

M Morales. *A Search for TeV Gamma-Ray Burst Emission with the Milagro Observatory* . Ph.D. thesis, University of California, Santa Cruz, 2002.

C Morello, L Periale, and G Navarra. A search for high-energy cosmic gamma-ray bursts. *Il Nuovo Cimento C*, **7**(6):682, 1984.

Kohta Murase, *et al.* High-energy cosmic-ray nuclei from high- and low-luminosity gamma-ray bursts and implications for multimessenger astronomy. *Phys. Rev. D*, **78**(2):23005, 2008.

T Nagai, *et al.* Focal Plane Instrumentation of VERITAS. In *Proceedings of the 30th International Cosmic Ray Conference. July 3 - 11*, pages 1437–1440. 2008.

E. Nakar and T Piran. Gamma-Ray Burst Light Curves—Another Clue on the Inner Engine. *ApJ*, **572**(2):L139, 2002.

Ramesh Narayan, Tsvi Piran, and Pawan Kumar. Accretion Models of GammaRay Bursts. *ApJ*, **557**(2):949, 2001.

W R Nelson, H Hirayama, and D W O Rogers. EGS4 code system. *SLAC-265*, 1985.

J A Nousek, *et al.* Evidence for a Canonical GammaRay Burst Afterglow Light Curve in the SwiftXRT Data. *ApJ*, **642**(1):389, 2006.

S. Obrien and N A Porter. Upper limits for high energy gamma-rays in association with VELA bursts. *Astrophys Space Sci*, **42**:73, 1976.

William S Paciesas, *et al.* The Fermi GBM Gamma-Ray Burst Catalog: The First Two Years. *ApJS*, **199**(1):18, 2012.

B. Paczynski. Gamma-ray bursters at cosmological distances. *ApJL*, **308**:L43, 1986.

L Padilla, *et al.* Search for gamma-ray bursts above 20 TeV with the HEGRA AIRO-BICC Cherenkov array. *A&A*, **337**:43, 1998.

A Panaitescu and P Mészáros. Gamma-Ray Bursts from Upscattered Self-absorbed Synchrotron Emission. *ApJ*, **544**(1):L17, 2000.

Asaf Pe'er and Eli Waxman. Prompt GammaRay Burst Spectra: Detailed Calculations and the Effect of Pair Production. *ApJ*, **613**(1):448, 2004.

Asaf Pe'er and Eli Waxman. High-Energy Photon Emission in the Early Afterglow of GRBs. *ApJ*, **633**(2):1018, 2005.

T Piran. Gamma-ray bursts and the fireball model. *Physics Reports*, **314**(6):575, 1999.

T Piran and A Shemi. Fireballs in the Galactic halo and gamma-ray bursts. *ApJL*, **403**:67, 1993.

Tsvi Piran. Astronomy: Glowing embers. *Nature*, **422**(6929):268, 2003.

Tsvi Piran. The physics of gamma-ray bursts. *Rev. Mod. Phys.*, **76**(4):1143, 2005.

Cristiano Porciani and Piero Madau. On the Association of Gamma-Ray Bursts with Massive Stars: Implications for Number Counts and Lensing Statistics. *ApJ*, **548**(2):522, 2001.

R D Preece, *et al.* The BATSE GammaRay Burst Spectral Catalog. I. High Time Resolution Spectroscopy of Bright Bursts Using High Energy Resolution Data. *ApJS*, **126**(1):19, 2000.

J X Prochaska, *et al.* GRB 080310: Lick/Kast spectroscopy. *GCN*, **7388**:1, 2008a.

J X Prochaska, *et al.* GRB 080607: Keck/LRIS spectroscopy and redshift. *GCN*, **7849**:1, 2008b.

G Pühlhofer, *et al.* The technical performance of the HEGRA system of imaging air Cherenkov telescopes. *APh*, **20**(3):267, 2003.

J L Racusin, *et al.* Broadband observations of the naked-eye γ-ray burst GRB080319B. *Nature*, **455**(7):183, 2008.

E Ramirez-Ruiz. Neutrino-cooled accretion flows. *Il Nuovo Cimento B*, **121**(1):1261, 2006.

Soebur Razzaque, Charles D Dermer, and Justin D Finke. The Stellar Contribution to the Extragalactic Background Light and Absorption of High-Energy Gamma Rays. *ApJ*, **697**(1):483, 2009.

M J Rees and P Mészáros. Relativistic fireballs - Energy conversion and time-scales. *MNRAS*, **258**:41P, 1992.

M J Rees and P Mészáros. Unsteady outflow models for cosmological gamma-ray bursts. *ApJ*, **430**:L93, 1994.

E Roache, *et al.* Mirror Facets for the VERITAS Telescopes. In *Proceedings of the 30th International Cosmic Ray Conference. July 3 - 11*, pages 1397–1400. 2008.

Wolfgang A Rolke, Angel M López, and Jan Conrad. Limits and confidence intervals in the presence of nuisance parameters. *NIM. A*, **551**:493, 2005.

Stephan Rosswog, Enrico Ramirez-Ruiz, and Melvyn B. Davies. High-resolution calculations of merging neutron stars - III. Gamma-ray bursts. *MNRAS*, **345**(4):1077, 2003.

V. Rumyantsev, *et al.* GRB 110201A: optical observations. *GCN*, **1168**, 2011.

Felix Ryde and Asaf Pe'er. Quasi-blackbody Component and Radiative Efficiency of the Prompt Emission of Gamma-ray Bursts. *ApJ*, **702**(2):1211, 2009.

Re'em Sari and Ann A. Esin. On the Synchrotron Self-Compton Emission from Relativistic Shocks and Its Implications for Gamma-Ray Burst Afterglows. *ApJ*, **548**(2):787, 2001.

Re'em Sari, Tsvi Piran, and Ramesh Narayan. Spectra and Light Curves of Gamma-Ray Burst Afterglows. *ApJL*, **497**:L17, 1998.

F. Schmidt. CORSIKA Shower Images, http://www.ast.leeds.ac.uk/ fs/showerimages.html. 2009.

K Z Stanek, *et al.* Spectroscopic Discovery of the Supernova 2003dh Associated with GRB 030329. *ApJ*, **591**(1):L17, 2003.

F W Stecker, M. A. Malkan, and S. T. Scully. Intergalactic Photon Spectra from the Far-IR to the UV Lyman Limit for $0 < z < 6$ and the Optical Depth of the Universe to High-Energy Gamma Rays . *ApJ*, **648**(2):774, 2006.

Boris E. Stern and Juri Poutanen. Gamma-ray bursts from synchrotron self-Compton emission. *MNRAS*, **352**(3):L35, 2004.

Yudai Suwa and Kunihito Ioka. Can Gamma-ray Burst Jets Break Out the First Stars? *ApJ*, **726**(2):107, 2011.

C A Swenson, *et al.* GRB 090926A and Bright Late-time Fermi Large Area Telescope Gamma-ray Burst Afterglows. *ApJL*, **718**:L14, 2010.

N R Tanvir, *et al.* Late-time Observations of GRB 080319B: Jet Break, Host Galaxy, and Accompanying Supernova. *ApJ*, **725**(1):625, 2010.

M Tavani, *et al.* The AGILE Mission. *A&A*, **502**(3):995, 2009.

C Thompson, P Mészáros, and M J Rees. Thermalization in Relativistic Outflows and the Correlation between Spectral Hardness and Apparent Luminosity in GammaRay Bursts. *ApJ*, **666**(2):1012, 2007.

K Toma, X F Wu, and P Mészáros. Photosphere-internal shock model of gamma-ray bursts: case studies of Fermi/LAT bursts. *MNRAS*, **415**(2):1663, 2011.

J A van Paradijs, *et al.* Discovery of transient optical emission from the error box of the gamma-ray burst of february 28, 1997. *Nature*, **386**:686, 1997.

R Vanderspek, *et al.* GRB observations with the HETE soft X-ray cameras. *Astron. Astrophys. Suppl. Ser.*, **138**(3):565, 1999.

Vlasios Vasileiou. *A Search for Bursts of Very High Energy Gamma Rays with Milagro.* Ph.D. thesis, University of Maryland, College Park, 2008.

S Vernetto. Detection of gamma-ray bursts in the 1 GeV–1 TeV energy range by ground-based experiments. *APh*, **13**(1):75, 2000.

P M Vreeswijk, *et al.* VLT/UVES redshift of GRB 080319B. *GCN*, **7444**:1, 2008.

X Y Wang, Z G Dai, and T Lu. The Inverse Compton Emission Spectra in the Very Early Afterglows of GammaRay Bursts. *ApJ*, **556**(2):1010, 2001.

Xiang-Yu Wang, Zhuo Li, and Peter Mészáros. GeV-TeV and X-Ray Flares from Gamma-Ray Bursts. *ApJ*, **641**(2):L89, 2006.

Eli Waxman. HighEnergy Cosmic Rays from GammaRay Burst Sources: A Stronger Case. *ApJ*, **606**(2):988, 2004.

T C Weekes, *et al.* Observation of TeV gamma rays from the Crab nebula using the atmospheric Cerenkov imaging technique. *ApJ*, **342**:379, 1989.

A Weinstein. The VERITAS Trigger System. In *Proceedings of the 30th International Cosmic Ray Conference. July 3 - 11*, pages 1539–1542. 2008.

K Wiersema, *et al.* GRB 080604: Gemini-North spectroscopy. *GCN*, **7818**:1, 2008.

R. Wijnands, *et al.* GRB060602B = Swift J1749.4-2807: an unusual transiently accreting neutron-star X-ray binary. *MNRAS*, **393**(1):126, 2009.

C Winkler, *et al.* The INTEGRAL mission. *A&A*, **411**(1):L1, 2003.

Matthew Wood. *An Indirect Search for Dark Matter with VERITAS* . Ph.D. thesis, veritas.sao.arizona.edu, UCLA, 2010.

S E Woosley. Gamma-ray bursts from stellar mass accretion disks around black holes. *ApJ*, **405**:273, 1993.

R R Xue, *et al.* Very High Energy -Ray Afterglow Emission of Nearby Gamma-Ray Bursts. *ApJ*, **703**:60, 2009.

Bing Zhang, *et al.* Physical Processes Shaping GammaRay Burst XRay Afterglow Light Curves: Theoretical Implications from the SwiftXRay Telescope Observations. *ApJ*, **642**(1):354, 2006.

S N Zhang and D Ramsden. Statistical data analysis for gamma-ray astronomy. *Experimental Astronomy (ISSN 0922-6435)*, **1**:145, 1990.

Weiqun Zhang, S E Woosley, and A Heger. The Propagation and Eruption of Relativistic Jets from the Stellar Progenitors of Gamma-Ray Bursts. *ApJ*, **608**(1):365, 2004.

Yuan-Chuan Zou, Yi-Zhong Fan, and Tsvi Piran. The possible high-energy emission from GRB 080319B and origins of the GeV emission of GRBs 080514B, 080916C and 081024B. *MNRAS*, **396**(2):1163, 2009a.

Yuan-Chuan Zou, Tsvi Piran, and Re'em Sari. Clues from the Prompt Emission of GRB 080319B. *ApJL*, **692**(2):L92, 2009b.